UNIVERSITY OF OKLAHOMA

GRADUATE COLLEGE

THERMOGRAVIMETRY-MASS SPECTROMETRY AND VARIABLE TEMPERATURE INFRARED SPECTROSCOPY INVESTIGATIONS OF AROMATIC ACID INTERACTIONS WITH MONTMORILLONITE CLAYS AND ACID/BASE PROPERTIES OF DIIRON COORDINATION COMPLEXES

A DISSERTATION

SUBMITTED TO THE GRADUATE FACULTY

in partial fulfillment of the requirements for the

Degree of

DOCTOR OF PHILOSOPHY

By

AUDREY LYNN INGRAM
Norman, Oklahoma
2015

THERMOGRAVIMETRY-MASS SPECTROMETRY AND VARIABLE TEMPERATURE INFRARED SPECTROSCOPY INVESTIGATIONS OF AROMATIC ACID INTERACTIONS WITH MONTMORILLONITE CLAYS AND ACID/BASE PROPERTIES OF DIIRON COORDINATION COMPLEXES

A DISSERTATION APPROVED FOR THE
DEPARTMENT OF CHEMISTRY AND BIOCHEMISTRY

BY

Dr. Robert L. White, Chair

Dr. Mark A. Nanny

Dr. Kenneth M. Nicholas

Dr. Wai Tak Yip

Dr. Zhibo Yang

For my wonderful husband, Dr. Kyle Ingram, and for my family:

Dr. Dwight Myers, Nancy Myers, and Karen Myers.

My achievements would not have been possible without them.

Acknowledgements

First and foremost, I would like to thank my mentor, Dr. Robert White, for all of his guidance and support. He is a brilliant chemist and teacher, and his enthusiasm for research and for helping his students to succeed are truly inspiring. I appreciate that he is always happy to take time to talk about the "why" instead of just caring about results.

I would also like to thank my former research advisor, Dr. Robert Houser, for his guidance and patience as I learned how to perform research in the graduate setting. I appreciated that he always made time to talk about my project, even when he was busy with his departmental duties as Assistant Chair.

I am grateful for the enthusiasm and constructive feedback provided by my committee members, Dr. Mark Nanny, Dr. Kenneth Nicholas, Dr. Wai Tak Yip, and Dr. Zhibo Yang. I am also especially grateful for help with pK_a calculations provided by my former committee member, Dr. Richard Taylor.

My research group members, Dalia Maraoulaite and Dr. Tara Nickels, have been wonderful colleagues and friends to me. Our brainstorming sessions have been invaluable to our research and writing progress. I am also grateful for the help and friendship provided by my former research group members: Dr. Anna Jozwiuk, Dr. Mike McClain, Dr. Zhaodang Wang, Dr. Rajendra Shakya, and Adam Campbell. Additionally, my friend Dr. Katie Branscum Foster started the Ph.D. program in this department at the same time that I did, and now she defended her dissertation the same week that I defended mine. It has been so helpful to have a close friend whose career is on a parallel track with mine. Katie's friendship and support have been indispensable, and I'm very grateful for her.

I wish to thank my dad, Dr. Dwight Myers, who was also my undergraduate research advisor. He provided a great deal of advice and guidance, especially during my college years, but all throughout my life as well. His pride in my achievements has been a huge source of encouragement over the years.

My mom, Nancy Myers, was my very first teacher, and she taught me everything at home, starting in kindergarten and continuing all the way through my senior year of high school. She was an extremely well-rounded person and a very enthusiastic teacher. She inspired me to do my best at everything, especially science. She was also my confidant for personal matters; I could always trust her advice. Without her unconditional love and support I would not be the person that I am today. I am eternally grateful that I got to spend so much time with her during my school years, and that I lived at home while I went to college, because she passed away shortly after I started graduate school in 2008. Even though she isn’t here with me now, I know that she would be bursting with pride to see me graduating with my Ph.D. To have had two such loving parents that were also incredible role-models is rare, but it doesn’t end there. My sister, Karen Myers, has been a great friend and support to me over the years. I cannot imagine a better sister, mother, or father than mine.

I also can’t say enough about my husband, Dr. Kyle Ingram. He is so much more than I ever imagined that I would find in a husband. He is one of the smartest people I know, and he has an incredible work ethic and a great sense of humor. His support for me has been phenomenal. He celebrates my achievements with me, he comforts me when times are hard, and he always makes me laugh. I am so grateful to have him, and I look forward to spending the rest of my life with him.

Table of Contents

List of Tables

List of Figures

Abstract

Thermogravimetry-Mass Spectrometry (TG-MS) and Variable-Temperature Diffuse Reflection Infrared Fourier Transform Spectroscopy (VT-DRIFTS) were used to investigate interactions of benzoic acid, salicylic acid, and acetylsalicylic acid with potassium, sodium, and calcium montmorillonite clays. The presence of adsorbates perturbed the environments of interlayer water molecules. Below 60 ^{o}C, heating adsorbate/clay samples resulted in changes to both the adsorbate and water molecule local environments. Results described here show that TG-MS m/z 18 ion signal temperature profiles can be employed to selectively monitor water molecule desorption, which can provide information regarding thermal stabilities of interlayer water molecule environments. VT-DRIFTS measurements below 60 ^{o}C also provided selective tracking of sample changes associated with water loss. Absorbance band changes that occur in the O-H stretching vibration regions of infrared spectra reflected local environment changes to adsorbate and inorganic oxide hydroxyl groups and to interlayer water molecules. VT-DRIFTS C=O stretching and O-H bending vibration band changes are more dramatic and provide greater selectivity with respect to the nature of adsorbate molecule environment changes. Dehydration by heating samples from ambient temperature to 60 ^{o}C resulted in complex changes to adsorbate acid group environments that depended on the structure of the adsorbate and the clay interlayer cation. Above 60 °C, TG-MS results for samples containing acetylsalicylic acid indicated that it decomposed by reaction with water to form salicylic acid and acetic acid. Salicylic acid also decomposed, but at higher temperatures than acetylsalicylic acid, producing phenol and carbon dioxide. Results obtained at higher sample

temperatures provided information regarding adsorbate interactions with dehydrated environments as well as measures of relative adsorbate stabilities. Studies described here provide detailed characterizations of adsorbate environments within clay substrates and how these environments change as a result of dehydration.

Additionally, the acid-base properties of $[(\mathrm{FeL})_2(\mu\text{-OH})]\mathrm{BPh}_4$, $[(\mathrm{FeL})_2(\mu\text{-O})]$, and [FeLCl] (where L = the dianion of 2,2'-(2-Methyl-2-(pyridin-2-yl)-propane-1,3-diyl)bis(azanediyl)-bis(methylene)diphenol) were characterized in acetonitrile. $[(\mathrm{FeL})_2(\mu\text{-OH})]\mathrm{BPh}_4$ was reversibly deprotonated by strong bases such as 1,8-Diazabicyclo[5.4.0]undec-7-ene (DBU). $[(\mathrm{FeL})_2(\mu\text{-O})]$ was titrated with benzoic acid under inert conditions, and the $\mathrm{p}K_a$ of the hydroxo bridge in $[(\mathrm{FeL})_2(\mu\text{-OH})]^+$ was estimated to be 20.4, which is remarkably high compared to literature reports for other hydroxo-bridged diiron complexes.

Chapter 1 : Introduction

1.1 Pharmaceuticals and Personal Care Products

1.1.1 Use and Environmental Release of Pharmaceuticals and Personal Care Products

Pharmaceuticals and Personal Care Products (PPCPs) encompass a wide range of chemical compounds. Pharmaceuticals include prescription and over-the-counter (OTC) drugs for humans and animals.[1] Personal care products include such external-use items as shampoo, toothpaste, facial washes, moisturizers, and cosmetics, as well as agricultural pesticides and food preservatives, and many more.[2] The compounds found in these commodities are generally water soluble and very stable, which causes them to be persistent in the environment. Many of these are washed down the drain during use and find their way to municipal sewage or septic tanks.[2] Unused or out-of-date prescription or OTC drugs are often flushed down toilets and so enter municipal sewage and septic tanks by that means, as do drug metabolites excreted by humans.[2] Septic tank overflow can lead to direct environmental contamination, while municipal sewage passes through waste water treatment plants (WWTPs). Unfortunately, WWTPs are not equipped to remove all of these types of contaminants, so they are able to enter the environment, either via reclaimed water or from sludge used for agricultural purposes.[1, 3-9] Additionally, PPCPs disposed in landfills may enter surface or groundwater via landfill effluent.[10-12] Concerns began to be raised as early as 1961 regarding the potential impact of PPCPs on the environment, but at that time the instruments available were not capable of detecting the low concentrations of PPCPs in water sources.[13] As instrumental sensitivity and limit of detection have improved, research has increased in this area to elucidate the fates of PPCPs in the environment, and within the past twenty years, this has become an area of intense research activity.[10, 14-16] The world population increased by approximately 0.8 billion people just between the years of 1999 and 2009.[17, 18] As the population increases, so does the worldwide production of PPCPs, so there is an urgent need to understand the effects they may have on the environment, as well as the extent of human exposure.[1, 10, 19]

1.1.2 Investigations of PPCPs in the Environment

Studies have been conducted to test levels of PPCPs in waste water effluent, as well as in surface and ground waters. Currently, the levels of PPCPs in drinking water do not seem to pose a problem because they are very dilute and are quickly broken down in water, although not much is known yet regarding the possible chronic effects of long-term exposure to low doses of contaminants under these conditions.[10, 15, 16, 20] Additionally, PPCPs have been found to concentrate in soils, where they can be protected from degradation.[21] This could be a serious problem for several reasons. First, if PPCPs are washed back out of soils during heavy rainfall, they may be reintroduced to our water supplies during such times. Second, there is evidence that they may be taken up by plants, including crops, especially in cases where reclaimed water is used for irrigation.[22, 23] Humans may be exposed to PPCPs by eating contaminated crops, or by eating food produced from livestock exposed to PPCPs through crops. Additionally, if bacteria are exposed to antibiotics in soils, it may aggravate the already growing problem of antibiotic resistance.[5, 24] For these reasons, much research on PPCPs in the environment has focused on their interactions with soils.[25-27] The way that these interactions are typically studied is by batch experiments or soil column experiments. In batch experiments, a small amount of soil is suspended in a solution containing the compound of interest, and the mixture is agitated. After a period of time, the concentration of the solution is tested to see how much of the compound was absorbed by the soil.[28] Soil column experiments involve pumping a solution of the compound of interest through a column packed with soil. The liquid that comes out the other end of the column is tested for the compounds, so the retention of various PPCPs by different soil types can be determined.[28, 29] These methods allow correlations to be established. For example, polar (hydrophilic) organic compounds have been found to be more strongly retained by soils containing higher percentages of clay,[30, 31] whereas nonpolar (hydrophobic) compounds are generally retained more strongly by soil samples which contain more natural organic matter (NOM).[29] One drawback to these approaches, however, is that they only allow correlations to be made, and do not shed any light on the actual mechanisms of contaminant-soil interactions at a molecular level.

Other techniques which have been used to study contaminant-soil interactions are X-ray diffraction (XRD), nuclear magnetic resonance (NMR) spectroscopy, and thermal analysis methods, including thermogravimetry (TG), differential scanning calorimetry (DSC), and thermo-IR. Each of these techniques are able to provide some valuable information, but still have various limitations. XRD can be used to measure swelling of soil components upon adsorption of organic contaminants, but does not provide information as to the identity of the contaminant or its interactions with soils.[32-34] NMR can provide a great deal of information about soils, because it is capable of detecting both organic and inorganic components of soil.[35, 36]

Additionally, it is sensitive to the orientation of the adsorbate relative to the soil component. However, NMR signals are significantly disrupted by the presence of iron, which is a very common component of soil, and NMR requires the use of deuterated solvents, which are expensive.[37] Some NMR experiments also require long acquisition times.[35] TG and DSC can reveal temperatures at which reactions or desorption occur, but unless the evolved volatiles are captured and analyzed, it is not always clear exactly what processes are taking place.[38-40] Thermo-IR analysis of contaminant-soil interactions can provide useful insight into the environment and orientation of adsorbates. However, this technique utilizes thin films for analysis, which are extremely delicate and sensitive to heat, or pellets pressed with salts, which can interfere with the contaminant-soil interactions of interest.[41-45] Clearly, additional methods of analysis are needed to further our understanding of anthropogenic contaminant interactions with soils in the environment.

1.1.3 Overview of Research Goals

The goal of this research is to take a systematic approach to studying this problem by investigating the interactions of PPCPs with soil components on a molecular level. If we can determine the mechanisms that govern the behavior of PPCPs in the environment, then we will be better equipped to predict the fate of given PPCPs based on their characteristics and on the characteristics of the soils. This type of understanding is essential for developing appropriate remediation actions. In order to adopt a more systematic approach, we have chosen to start with polar organic compounds, specifically aromatic acids. Batch experiment studies of the sorption of small aromatic acids to goethite conducted by Evanko, et al.,[46, 47] suggested that the nature and number of functional groups have a significant impact on organo-clay interactions. Research on benzoic acid, the simplest aromatic acid, has already been undertaken by our research group, and now our studies continue with salicylic acid and acetylsalicylic acid (aspirin) in order to provide a more detailed understanding of the effects that small structural differences have upon the interactions of these compounds with soils.

We have chosen montmorillonite clay as the specific soil component for our studies because, as previously mentioned, polar compounds such as aromatic acids are more likely to be retained by the clay component of a given soil sample. The next sections outline the environmental significance of acetylsalicylic acid, salicylic acid, and montmorillonite, as well as the analysis techniques that we are using to study this problem.

1.2 Salicylic Acid and Acetylsalicylic Acid

1.2.1 Structure and Properties of Salicylic Acid and Acetylsalicylic Acid

The structures of salicylic acid and acetylsalicylic acid are shown in Figure 1.1, and the structure of benzoic acid is also shown for comparison.[48]

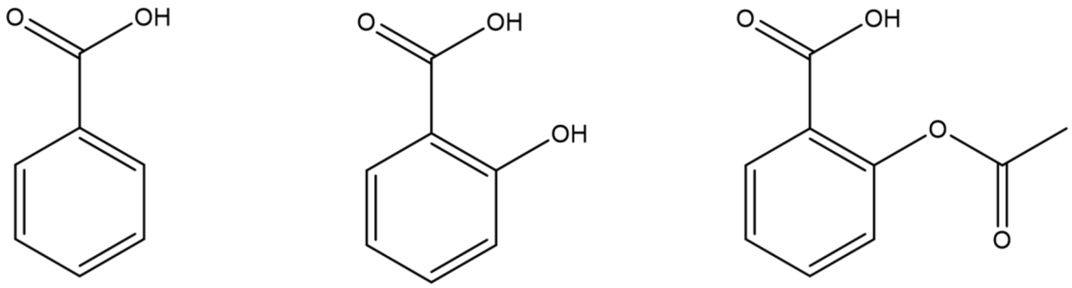

Figure 1.1 – Left to right: benzoic acid, salicylic acid, acetylsalicylic acid (aspirin).

Benzoic acid is the simplest aromatic acid, containing only two functional groups: an aromatic ring, or benzene group, and a carboxylic acid group, which consists of a carbon that is double-bonded to one oxygen and single-bonded to a hydroxyl (OH) group. Salicylic acid has the same structure with an additional hydroxyl group *ortho* to the carboxylic acid group. Acetylsalicylic acid has a similar structure, but instead of a hydroxyl group, it has an acetyl group in the *ortho* position. Figure 1.1 emphasizes the step-wise increase in complexity of structure from benzoic acid to salicylic acid to acetylsalicylic acid. This is important for our studies, because as complexity of molecular structure increases, complexity of spectral data increase significantly. Therefore it is important to compare data for similar structures in order to identify trends.

Salicylic acid and acetylsalicylic acid are both white, crystalline solids at room temperature. Salicylic acid has a molecular weight of 138.12 grams/mole (g/mol), a melting point of 158.6 °C, a boiling point of 211 °C, and a density of 1.433 g/cm^3. The molecular weight of acetylsalicylic acid is 180.16 g/mol, and its melting point is 136 °C.[48] The pK_a of salicylic acid is 2.98, and its solubility is 1.89 g/kg H_2O. It is interesting to note that the pK_a of salicylic acid is lower than that of most organic acids, which are typically around 4. This can be attributed to the hydroxyl group of salicylic acid stabilizing the carboxylate group by intramolecular hydrogen-bonding. The pK_a of acetylsalicylic acid is 3.48, and its solubility is 2.5 g/kg H_2O.[48]

1.2.2 History and Use of Salicylic Acid and Acetylsalicylic Acid

As long ago as 2400 years, the extract of willow bark was used to ease the pain of childbirth or a prolapsed uterus, as recommended by Hippocrates.[49] We now know that the compound responsible for the effectiveness of this treatment is salicylic acid. In fact, the Latin word for willow tree, “Salix,” provided the root for the name salicylic acid.[50] There is evidence of similar uses of plant extracts for pain relief throughout history, across several countries and continents, including Europe, Asia, and America. The first known synthesis of salicylic acid was performed by the German chemist, K. J. Lowig, by the oxidation of salicylaldehyde.[49] The modern procedure used to synthesize salicylic acid is more similar to that developed by Kolbe and Lautemann in 1860, and further refined by Kolbe in 1874. This procedure involves the carboxylation of sodium phenoxide by carbonic acid. One of the common uses for salicylic acid at that time was as a replacement for phenol as an antiseptic during surgeries.[49] Phenol is quite foul-smelling, so replacing it with salicylic acid was a significant improvement.

In 1875, a Swiss medical assistant named Buss began to study the application of salicylic acid and other salicylates as antipyretics.[49] This was the topic of his thesis for his State Medical Exam, which he followed up by performing experiments on animals and patients with various maladies, including typhoid fever. In 1876, physicians in Edinburgh and Berlin reported the use of salicylic acid to treat rheumatoid arthritis and rheumatic fever. While salicylic acid was generally found to be efficacious in these applications, Buss and others did notice some side effects. Salicylic acid is a gastric irritant, though this effect can be reduced by taking sodium bicarbonate together with salicylic acid. Currently, sodium bicarbonate is taken with acetylsalicylic acid, which is milder than salicylic acid, in order to reduce gastric distress.[49] Before it was replaced by acetylsalicylic acid, salicylic acid was the best-selling drug in the world.[50]

Acetylsalicylic acid was first synthesized in 1853 by a French chemist, Charles Federich von Gerhardt.[49] He achieved this by reacting sodium salicylate with acetyl chloride. In 1869, a chemist named Kraut improved upon the procedure. By extracting the product with ether, he was able to obtain acetylsalicylic acid with greater purity.[49] Acetylsalicylic acid did not become widely used as a drug until 1899, when it was introduced by the Bayer company, and given its trademark name, “aspirin.” This name was chosen because “acetylsalicylic acid” was considered too long and too similar to the name “salicylic acid,” so its first letter, “a” was taken, and the rest of the name, “spirin,” was derived from the fact that salicylic acid was first isolated from plants in the *Spirea* family.[49] Aspirin became extremely popular, partly because its name was so well chosen, but also because it is a very effective antipyretic and anti-inflammatory agent. Because it is much milder on the stomach than salicylic acid, it has effectively replaced salicylic acid for this market. Today, aspirin is one of the most popular over-the-counter pain medications, rivaled only by acetaminophen. In Germany alone, for example, more than 500 tons of aspirin are sold per year,[51] and approximately 40,000 tons of aspirin are produced worldwide.[52] According to the Aspirin Foundation, this is enough to make 100 billion tablets.[53] Roughly one-third of men over the age of 65 take aspirin every day in order to reduce their risk of a heart attack.[54]

1.2.3 Salicylic Acid and Acetylsalicylic Acid in the Environment

In a preliminary risk assessment study published in 2008, acetylsalicylic acid was given an overall environmental risk ranking of 43 out of 313 based on multiple factors, including number of annual prescriptions dispensed, effluent concentration, surface water concentration, biological half-life, environmental half-life, and solubility.[5] In the presence of water, acetylsalicylic acid is easily deacetylated to form salicylic acid and acetic acid, as shown in Figure 1.2.

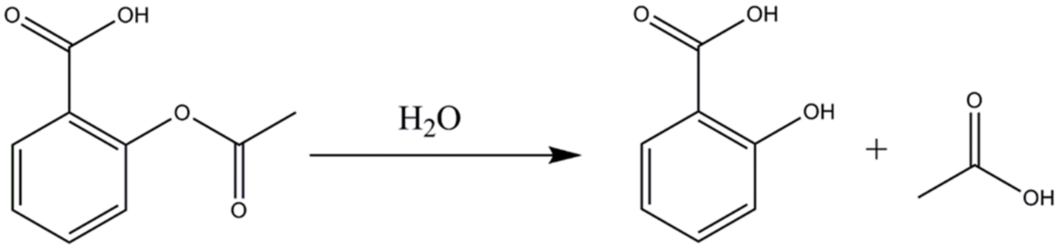

Figure 1.2 – Decomposition of acetylsalicylic acid to form salicylic acid and acetic acid.

Because of the ease of this transformation, acetylsalicylic acid’s impact on the environment has to be gauged primarily by the observation of salicylic acid. However, salicylic acid is still widely used in its own right, and therefore is also released directly into the environment, even though it is no longer used as a pain reliever. Modern uses of salicylic acid include treatment for acne and various other skin conditions.[55] It is also used in some dandruff shampoos, as it expedites the loss of dead skin cells.[56]

Salicylic acid also occurs naturally in the environment; as mentioned previously, it was first extracted from willow bark. It is found in many different plants, and is considered to be a plant hormone, as it plays important roles in the regulation of plant metabolism. Concentrations of salicylic acid in the range of 10^{-8} to 10^{-6} M (1.38 – 138 μg/L) have been found to increase plant growth.[50] Salicylic acid has been detected in sewage influent at concentrations as high as 54 μg/L, and in sewage effluent at concentrations reaching 13 μg/L,[51] which is well within the range found to have an effect on plant growth.

1.2.4 Retention of Salicylic Acid by Soils and Clays

Celis, et al., utilized batch experiments to investigate the sorption and leaching of salicylic acid, phthalic acid (2,2-benzenedicarboxylic acid), and picloram (4-amino-3,5,6-trichloropicolinic acid).[57] They concluded that aromatic acids can have highly varying sorption behaviors depending on the other functional groups present, and depending on the soil type. Of the acids investigated, salicylic acid was the least mobile and displayed the highest sorption. The trends observed also showed that salicylic acid adsorbs less strongly to soils containing more organic matter, suggesting that the mineral component is a more important contributor to sorption of polar molecules by soils.

Kubicki, et al., deposited acetic, salicylic, and benzoic acid, among others, and their sodium salts, onto montmorillonite and other types of clay, and used infrared spectroscopy to observe their interactions.[58] They recorded spectra after adsorption, and then washed the samples with water and recorded spectra again. Results varied for different clays, but for montmorillonite, most of the acids desorbed completely after rinsing, although they speculated that they might not be able to detect species remaining in the clay interlayer. Only salicylic acid still gave a weak spectrum after rinsing, which agrees with the findings reported by Celis, et al., that salicylic acid tends to be more strongly retained by clays than similar compounds.

1.3 Montmorillonite

1.3.1 Classification and Structure of Montmorillonite

Montmorillonite is a member of the smectite subgroup of the Phyllosilicate class.[59] In previous years, the name “montmorillonite” was also used to describe the group, but more recently it has been replaced with the name “smectite,” and now the name “montmorillonite” is generally reserved only for the species.[60] Montmorillonites consist of tetrahedral and octahedral layers in a 2:1 ratio, having the formula $(Al_{3.33}Mg_{0.67})Si_8O_{20}(OH)_4$.[60] The substitution of magnesium ions (Mg^{2+}) for aluminum ions (Al^{3+}) in this formula causes the layers to have a residual negative charge. The space between the layers is referred to as the “interlayer.” The interlayer contains cations of variable charge which balance the residual negative charge of the layers. The number of charges needed for balance varies somewhat, but for smectites it is generally in the range of 0.6 – 1.3 milliequivalents per gram (meq/g) of clay.[60] This value is called the “cation exchange capacity” (CEC). Samples of montmorillonite are usually distinguished based on the identity of the interlayer cation. For example, if a given sample of montmorillonite contains primarily sodium ions in the interlayer, it will be called “sodium montmorillonite.” The structure of montmorillonite is depicted in Figure 1.3.

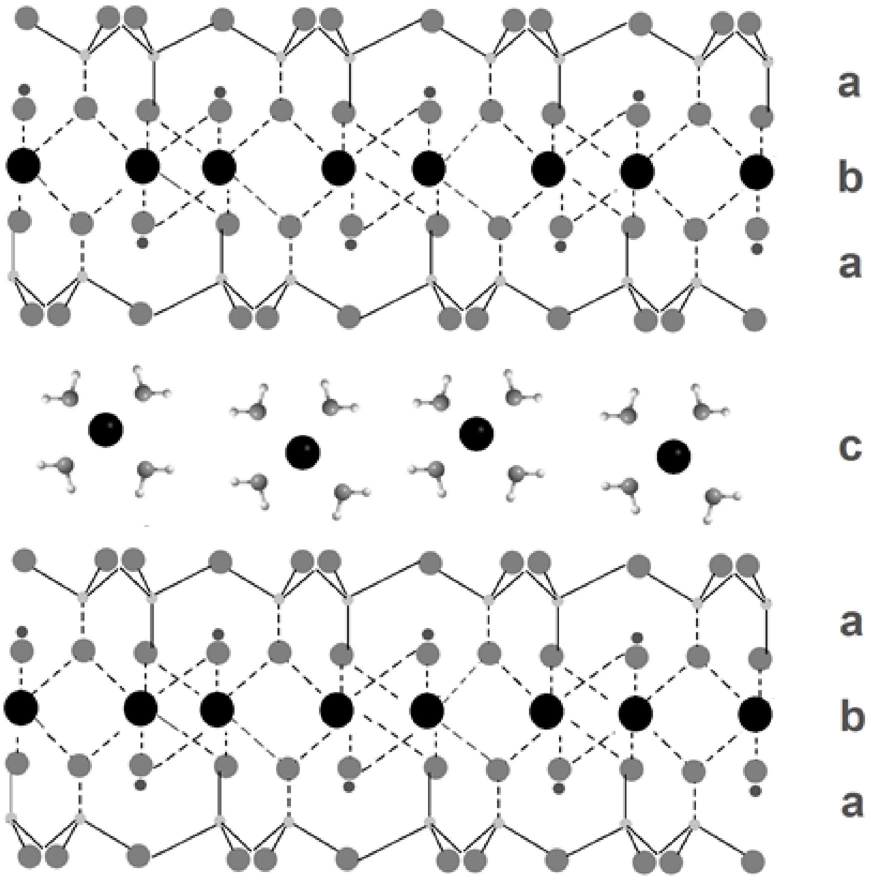

Figure 1.3 - Representation of the montmorillonite structure, with alternating tetrahedral (a) and octahedral (b) layers, surrounding the interlayer (c) which contains cations (large circles) interacting with water molecules.

1.3.2 Cation Exchange and its Effect on Interlayer Water

The identity of the interlayer cation has a significant impact on the properties of a given sample of montmorillonite; in particular it affects the amount of water contained between the layers.[61] The water content also depends on the relative humidity, because clays act as desiccants and can absorb water from the air. The identity of the cation and the water content together determine the width of the interlayer space, also known as the basal spacing. The basal spacing of a completely dehydrated sample of montmorillonite is generally about one nm, or ten angstroms (Å), and it increases with increasing water content.[60] Water content and basal spacing of montmorillonites have been found to increase in discrete steps, corresponding to addition of single layers of water within the interlayer.[62]

Ferrage, et al.,[63] studied the hydration properties of montmorillonites containing various interlayer cations using X-ray diffraction (XRD), and they reported that in a range from 0 – 80% relative humidity (RH), a given sample of montmorillonite could consist of a mixture of hydration states, from 0 – 2 water layers. According to their results, potassium montmorillonite consisted of a mixture of 0 and 1 water layer states between 0 and 80% relative humidity, gradually increasing from mostly 0 water layers at 0% RH to mostly 1 water layer at 80% RH. At 40% RH, potassium montmorillonite consisted of about 60% 0 water layer states and about 40% 1 water layer states, corresponding to a basal spacing between 11 and 12 Å. Sodium montmorillonite varied from 0 to 2 water layer states over the range of 0 – 80% RH, but over most of that range it consisted primarily of the 1 water layer state, with a basal spacing of 12.5 Å. Calcium montmorillonite also varied from 0 to 2 water layers over that humidity range, but at 40% humidity and higher, it consisted of primarily the 2 water layer state, with a basal spacing of around 15 Å.

These effects can be attributed to several factors. First, calcium ions are doubly charged, whereas sodium and potassium ions are singly charged. Doubly charged ions coordinate water more tightly, and so montmorillonite samples containing doubly charged ions generally tend to be more hydrated.[64] The difference between sodium montmorillonite and potassium montmorillonite can be attributed to the larger size of the potassium ion. Because the charge of the potassium ion is spread out over a larger area, it attracts water even more weakly than the sodium ion does. Additionally, the potassium ion happens to be just the right size to fit neatly into the hexagonal holes of the montmorillonite layers, so only one side of the ion is available to interact with water.[65, 66] These factors cause the layers of potassium montmorillonite to be held together more tightly than other types of montmorillonite, stabilizing low hydration states.

1.4 Interactions of Aromatic Acids with Montmorillonite

1.4.1 Benzoic Acid

Some research has already been conducted on the interactions of benzoic acid with montmorillonite. In a thermogravimetry study of benzoic acid/clay interactions, Lu et al. reported that benzoic acid desorption from sodium montmorillonite maximized at 140 ^{o}C, which was lower than when the clay contained calcium interlayer cations (179 ^{o}C).[38] They attributed the higher desorption temperature to stronger interactions between calcium ions and benzoic acid molecules.

The thermogravimetry-mass spectrometry (TG-MS) studies previously conducted by our research group for benzoic acid adsorbed on sodium and calcium montmorillonites yielded results that agreed with the results reported by Lu, et al., regarding the effect of the cation charge on the desorption temperatures of benzoic acid.[67] Namely, the higher charge of the calcium ion caused benzoic acid to desorb at a higher temperature. However, Lu and coworkers claimed that the desorption maxima of benzoic acid at 140 and 179 °C for sodium and calcium montmorillonites, respectively, represented the loss of all benzoic acid from the sample, but our TG-MS results suggested that this was not correct. We observed that some benzoic acid stayed on the clay to such high temperatures that it decomposed to form benzene and carbon dioxide, as evidenced by the appearance of MS signatures for both of those products.

By using thermo-IR, Yariv et al. reported that the -C=O stretching vibration frequency of benzoic acid adsorbed on montmorillonite was dependent on the cation present in the clay interlayer space and the extent of clay dehydration.[41, 68] They found that singly charged cations, such as Na^+, perturbed the -C=O stretching vibration the least relative to neat benzoic acid (dimer), whereas multiply charged cations, such as Ca^{2+}, produced the largest wavenumber shifts. They proposed a model to explain their spectroscopic findings in which a water molecule bridges between the acid and cation. After prolonged heating in vacuum, the -C=O stretching vibration band was found to shift to lower wavenumbers and ultimately split into two peaks that were assigned to benzoic anhydride. Yariv et al. reported that benzoic acid was still bound to clay even after heating in vacuum to temperatures above 150 ^{o}C, suggesting the presence of strong interactions.[68] Thermo-IR and thermogravimetry studies both reached the same general conclusion, that benzoic acid more strongly interacts with interlayer cations carrying higher charge.

Our variable temperature FTIR studies of benzoic acid on sodium and calcium montmorillonite confirmed the mechanism proposed by Yariv, et al., in which benzoic acid interacts with interlayer cations through water bridges.[69] We also confirmed that the charge of the interlayer cation significantly affects interactions with benzoic acid. Additionally, we heated our samples to higher temperatures (260 °C) than Yariv and coworkers, which provided some interesting results that are in agreement with their findings, but provide additional details regarding molecular interactions.[70] We concluded that benzoic acid interactions with montmorillonite are primarily determined by the polar carboxylic acid functionality, and not the aromatic ring, because montmorillonite had very little effect on the vibrational frequencies associated with the aromatic ring. We also found that benzoic acid was still interacting with the interlayer cations through water bridges even at temperatures significantly above the boiling point of water, indicating that benzoic acid – water – cation interactions are very strong.

1.4.2 Salicylic Acid and Acetylsalicylic Acid

The literature regarding salicylic acid and acetylsalicylic acid interactions with montmorillonite is more sparse. Bonina, et al.,[71] observed the adsorption and release of salicylic acid by bentonite (which is 85% montmorillonite), and found that after soaking a 30 g sample of bentonite in a 0.0253 M solution of salicylic acid for two days, the clay contained 8.0% salicylic acid by weight. They also conducted thermal analysis of salicylic acid adsorbed on bentonite, and plotted the derivative thermogravimetric curve. They observed three reaction peaks at 181 °C, 260 °C, and 408 °C, but they did not assign these peaks or explain what reactions were occuring. They also observed that clay dehydroxylation shifted from 691 °C for the neat clay to 648 °C for the salicylic acid loaded clay.

Nakai, et al., used X-ray diffraction, DSC, and IR to study adsorption and decomposition of acetylsalicylic acid on sodium montmorillonite.[72] The focus of their study was on the use of these clays as fillers for drugs, and their main concern was the stabilities of the drugs on the clays at various humidities. Sample preparation simply involved grinding the crystalline drug together with the clay using a mortar and pestle, which was a logical approach for their applications, but probably does not allow significant intercalation into the clay interlayer, so it is not representative of typical environmental conditions. However, their results are still of some interest. For samples of 5% acetylsalicylic acid on sodium montmorillonite stored at 40°C and 0, 31.3, and 79% relative humidity, they monitored the decomposition of acetylsalicylic acid over a period of nine days. Acetylsalicylic acid decomposed most slowly at 0% humidity, and most of the decomposition occurred in the first day, probably because the only water available was that adsorbed by the clay. X-ray diffraction was used to observe swelling of the clay at higher humidities, and it was thought that greater surface area would facilitate more rapid acetylsalicylic acid decomposition. In fact, less than 50% of the initial amount of acetylsalicylic acid was left after 9 days, *vs*. nearly 80% remaining after 9 days at 0% relative humidity.[72]

These studies provide some preliminary information, but it is clear that not much is known about the interactions of salicylic acid or acetylsalicylic acid with montmorillonite.

1.5 Research Goals

1.5.1 Thermogravimetry-Mass Spectrometry Studies

Thermogravimetric (TG) analysis involves constant monitoring of sample mass during heating. Samples generally lose mass while being heated, but different rates of mass loss during different temperature intervals provide insight into the thermochemical processes that occur during the experiment. This technique has been used extensively to study clays in the past.[73] The thermal behavior of montmorillonite has been well characterized by this method, so it makes sense to conduct TG studies of clay samples with adsorbed organic acids and compare to thermal analysis data obtained for neat clay samples. In a 2011 review of thermal analysis approaches used to study organo-clay interactions, Yariv, et al., predicted that evolved gas analysis methods, such as thermogravimetry coupled with mass spectrometry, would be important moving forward in this field.[74] Combining the TG technique with mass spectrometry (MS) provides additional information, specifically regarding the evolution of volatiles from the clay surface. By profiling the intensities of species-specific mass-to-charge (m/z) values, we can determine exactly which species are desorbing at any given temperature.

The thermogravimetry-mass spectrometry (TG-MS) studies previously conducted by our research group for benzoic acid adsorbed on sodium and calcium montmorillonites illustrated the utility of TG-MS studies; the MS data gave much more specific information than what has previously been reported for these systems. By continuing our TG-MS studies for salicylic acid and acetylsalicylic acid adsorbed on montmorillonite, we hope to elucidate trends that can be correlated with molecular structure.

1.5.2 Diffuse Reflection Infrared Fourier Transform Spectroscopy Studies

Diffuse Reflection Infrared Fourier Transform Spectroscopy (DRIFTS) is a technique that involves shining infrared (IR) light on a powder sample. Because a powder sample consists of many tiny particles, it does not reflect all of the light at the angle of incidence, like a mirror would. Instead, each particle reflects, scatters, and absorbs some of the light, causing the phenomenon known as diffuse reflection. The scattered and reflected light is collected by an arrangement of mirrors and focused on a detector, allowing us to determine which wavelengths of light were absorbed by the sample. Molecular vibrations exhibit distinctive IR absorptions which are characteristic of their environment. This information allows us to determine the molecular interactions between salicylic acid and acetylsalicylic acid with montmorillonite.

When using DRIFTS for soil constituent analyses, spectral subtractions can be employed to isolate selected infrared spectral features from large bulk sample absorbances. This is typically accomplished by subtracting mineral reference spectra from spectra obtained for the same material, but also containing substances of interest. Often, pretreatment processes (e.g. extractions) are employed to remove these substances from the reference samples. As pointed out by Thomas and Kelley,[75] careful reference and adsorbate spectrum measurements are critical for obtaining accurate difference spectra. For this reason, they reportedly avoided studies with montmorillonites. Unlike many other minerals, montmorillonite structures consist of two inorganic sheets around a variable thickness water layer. In order to measure an appropriate reference spectrum, it is necessary to precisely control the water content, which is difficult to accomplish. Thus, depending on environmental conditions, samples may contain different amounts of water and infrared spectra would therefore contain varying water absorbance contributions, which would be difficult to remove by using spectral subtractions.

To avoid difference spectrum artifacts not associated with substances of interest, a sample perturbation analysis method can be employed.[76] This approach can be explained with the aid of the diagram shown in Figure 1.4.

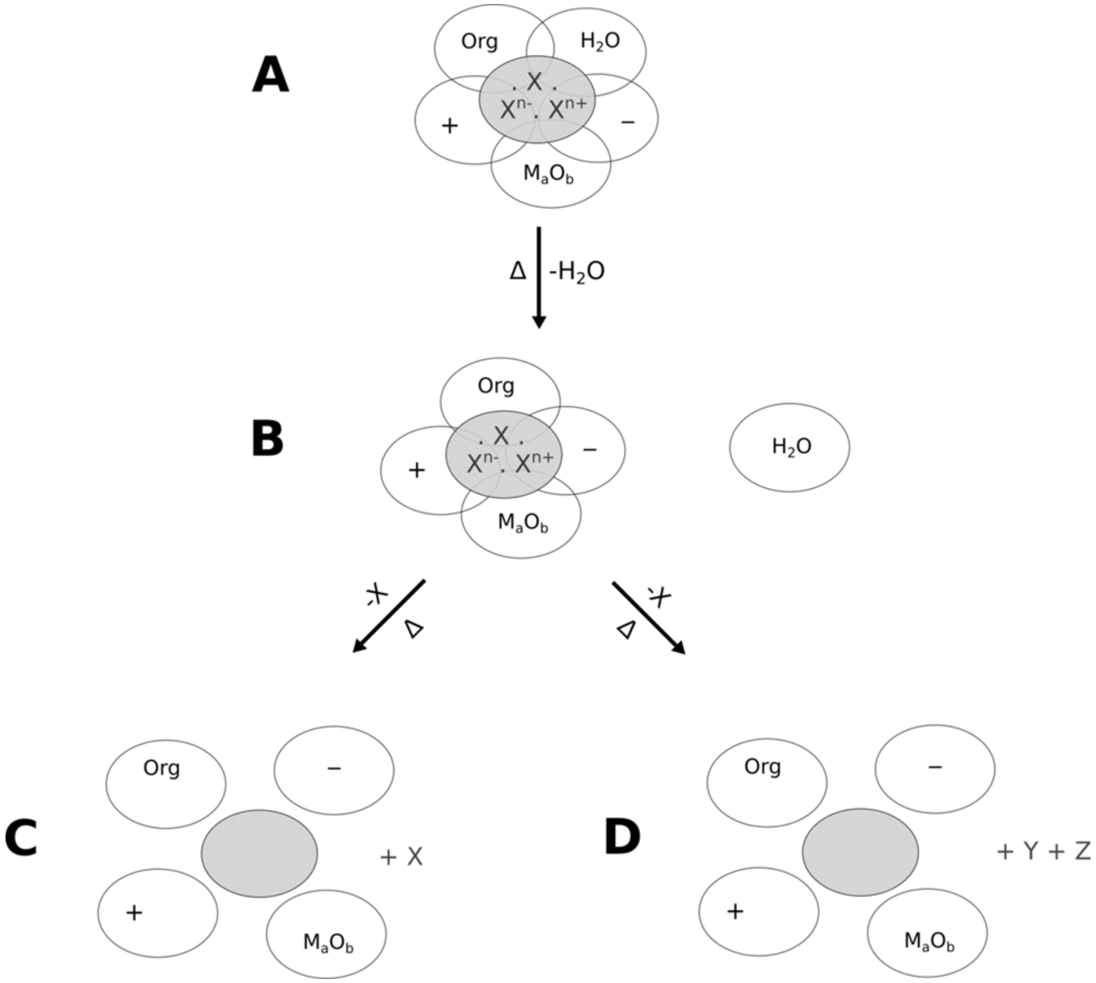

Figure 1.4 - Representation of the X local environment (A) before heating, (B) after dehydration, (C) after X desorption and (D) after X decomposition.

At the top of the diagram (A), the species of interest is represented by X, which may also exist in charge carrying forms (X^{n+} and X^{n-}), depending on its acid/base properties and local pH. Each form may interact differently with its surroundings, contributing different absorbance features to measured infrared spectra. The overlapping ellipses in Figure 1.4 represent X interactions with other organic substances (Org), water (H_2O), cations (+), anions (-), and inorganic oxides (M_aO_b) that may be present in the sample. The solid-state infrared spectrum measured for the system denoted in (A) will contain information regarding the vibrational modes of all constituents. After heating the sample represented by (A) to remove water (i.e. the perturbation), the resulting spectrum will represent a slightly different solid-state configuration (B). A difference spectrum computed by subtracting the infrared spectrum obtained for (A) from the spectrum measured for (B) will contain spectral features representing the changes that occurred as a result of heating. Specifically, the difference spectrum will contain positive features representing vibrations formed after water removal (i.e. related to new interactions) and negative features corresponding to vibrational modes that were lost due to the configuration change. The size of the spectral features in difference spectra will depend on the number of perturbed species and the absorptivities of the affected absorbance bands. Negative spectral features provide insight into the interactions between X and water in the initial configuration (A). By continuing to heat the sample while measuring infrared spectra, the difference spectrum representing (C) – (B) sample configuration changes would contain negative features corresponding to vibrational modes associated with the dehydrated X molecule and its environment that were lost when it desorbed from the sample and the (D) – (B) difference spectrum would provide similar vibrational mode information, but for instances when X decomposed rather than desorbing. Additional information regarding decomposition mechanisms may be obtained by determining the amounts and identities of decomposition products (Y and Z). In summary, this approach effectively removes the problems associated with using a different sample to obtain the reference spectrum. When we perturb the system by the addition of heat, the reference sample is the same material, but at a different temperature; therefore the only differences observed are the sample changes caused by heating, and not artifacts introduced by using a different material to obtain the reference spectrum. This application of DRIFTS analysis is called variable temperature diffuse reflection infrared Fourier transform spectroscopy (VT-DRIFTS).[76]

Figure 1.5 shows examples of difference spectra that might be obtained by using the perturbation method depicted in Figure 1.4. In Figure 1.5a, spectrum changes caused by sample heating result in a hypothetical band shift from 1685 cm^{-1} to 1715 cm^{-1}. This shift occurs without a change in band absorptivity, so band intensities do not change with temperature. The resulting difference spectrum has a characteristic "derivative" shape, with a negative band minimum located at a slightly lower wavenumber and a positive band minimum at a slightly higher wavenumber than the shifting band maxima. Figure 1.5b shows a hypothetical difference spectrum that might result from the same band shift, but with a reduction in band absorptivity with increased sample temperature. Difference spectrum negative and positive band locations appear at about the same wavenumbers as shown in Figure 1.5a, but the positive band intensity is greatly reduced. In addition to band shifting due to molecular environment changes, difference spectra may reflect the loss of sample components or the gain of new functionalities formed by chemical reactions. In general, difference spectrum band shapes reflect net spectral variations associated with any sample changes that result in absorbance gains and losses. Because of this, care must be taken when assigning difference spectra band constituents. When loss of functional groups over the selected temperature range can be confirmed, negative band intensities can in part be attributed to these losses. Positive bands may result from band shifts, or may appear as a result of new functionalities produced by temperature-dependent solid-state reactions.

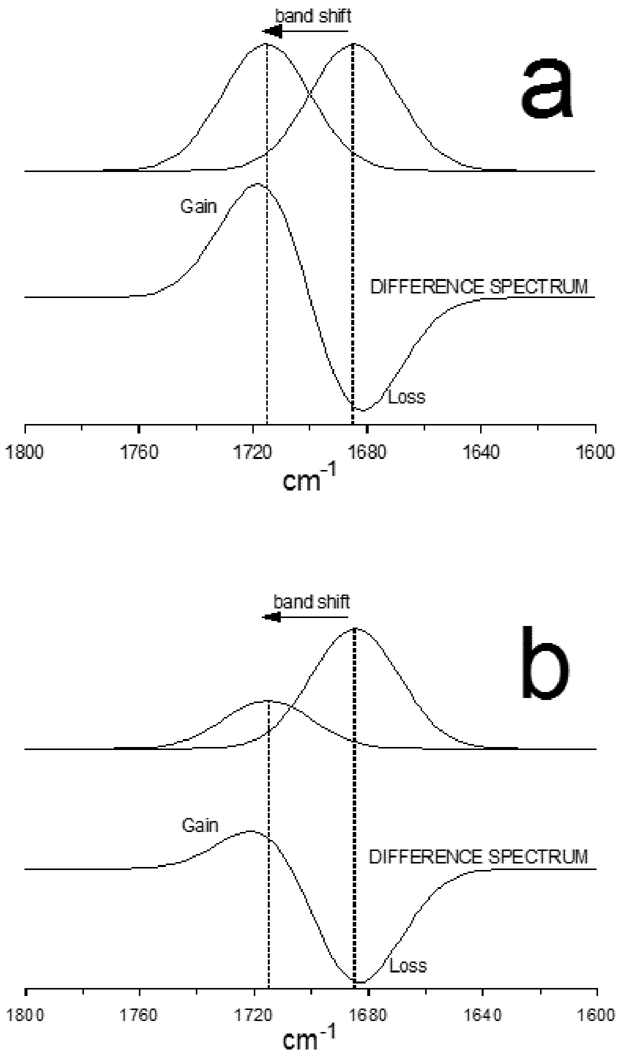

Figure 1.5 - Effect of band shift on difference spectrum shape for (a) no absorptivity change and (b) absorptivity decrease after shift. Dotted lines denote band center locations at 1715 and 1685 cm^{-1}.

Figure 1.4 (A) potentially represents a very complicated system of simultaneous interactions. Soils typically contain numerous organic molecules, cations, anions, and inorganic oxides in differing amounts. This is why our studies are focused on a simplified system, consisting only of montmorillonite and a single adsorbate, such as benzoic acid, salicylic acid, and acetylsalicylic acid.

1.5.3 Summary of Research Goals

By using TG-MS and VT-DRIFTS analysis of salicylic acid and acetylsalicylic acid adsorbed on sodium and calcium montmorillonite and comparing these results with those previously obtained for benzoic acid, we hope to elucidate adsorbate-clay interaction trends that can be correlated with molecular structure. We will also expand the previous studies to include samples of benzoic acid, salicylic acid, and acetylsalicylic acid adsorbed on potassium montmorillonite, in order to understand the effects of differing clay interlayer water contents on these interactions, because potassium montmorillonite contains significantly less water than sodium or calcium montmorillonite. The information derived from these studies will further our understanding of the transport mechanisms and fates of PPCPs in the environment.

Chapter 2 : Experimental

2.1 Materials and Reagents

Benzoic acid, salicylic acid, acetylsalicylic acid (aspirin), and K10 montmorillonite were purchased from Sigma-Aldrich. Silver powder (100 mesh, 99.95%) was purchased from Alfa Aesar. Sodium chloride and potassium chloride were purchased from Mallinckrodt. Calcium chloride and glacial acetic acid were purchased from Fischer Scientific. Chloroform and carbon tetrachloride were purchased from JT Baker Chemical Company. Phenol was purchased from EM Science (associate of Merck). All reagents were used as received without additional purification.

2.2 Sample Preparation

2.2.1 Preparation of Montmorillonite Samples by Cation Exchange

Procedures for preparing montmorillonite samples containing predominantly the cation of interest (either K^+, Na^+, or Ca^{2+}) were based upon published protocols.[77-79] K10 montmorillonite (4.9 g) was suspended in 100 mL of a 1 M solution containing the appropriate metal chloride. The suspension was stirred overnight, then allowed to settle. In suspension, clay particles form quasi-crystals, with structures that depend upon the cation.[80] The metal chloride solution was decanted, and the clay was resuspended and stirred in distilled water for several hours. Finally, the clay was washed with 300 mL of distilled water in small portions using vacuum filtration, then allowed to air dry. During the drying process, quasi-crystals in the solution coalesce to form larger particles.[79]

2.2.2 Loading of Clay Samples with Adsorbates

The cation-exchanged clays were loaded with benzoic acid, salicylic acid, or acetylsalicylic acid by incipient wetness. Benzoic acid (0.01 – 0.03 g) was dissolved in carbon tetrachloride (10-20 mL) and salicylic acid (0.01 – 0.03 g) and acetylsalicylic acid (0.02 – 0.04 g) were dissolved in chloroform (10 – 20 mL), and the clay was suspended and stirred in the solution for 30 minutes at room temperature. The solvent was then removed by roto-evaporation for 90 minutes at room temperature. The CEC for K10 montmorillonite was reported to be 0.8 meq/g.[81] A montmorillonite sample containing 10% (w/w) benzoic acid, 11% (w/w) salicylic acid, or 15% (w/w) acetylsalicylic acid would have a ratio of approximately 1:1 adsorbate molecules to sodium or potassium ions, or 2:1 adsorbate molecules to calcium ions.

2.2.3 Dilution of Samples in Silver Powder for VT-DRIFTS Analysis

Silver powder diluent, which is highly scattering and inert for this application, was employed to eliminate spectral artifacts that appear in infrared spectra when neat samples are analyzed by DRIFTS. Samples were prepared for VT-DRIFTS analysis by diluting with silver powder in a 5-95 ratio by weight (e.g. 5% (w/w)). Typically 20 mg of the clay sample was diluted with 380 mg of silver powder. Approximately 15 mg of the resulting samples were employed for VT-DRIFTS analysis. DRIFTS measurements of neat clays exhibit artifacts caused by the Reststrahlen effect,[82, 83] resulting in loss of spectral features over the affected wavelength range. Specifically, increased sample reflectance occurs near the intense 1050 cm^{-1} inorganic oxide absorption band due to high sample refractive index, which results in an apparent loss of absorbance (i.e. an increase in reflectance). As shown in Figure 2.1, this phenomenon results in a distorted reflectance spectrum when the neat clay is analyzed by DRIFTS. Fortunately, as illustrated by the dashed line spectrum in Figure 2.1, sample dilution can reduce the sample refractive index and eliminate this artifact. Thus, to avoid complications caused by Reststrahlen effects, samples used for VT-DRIFTS studies were diluted in silver powder.

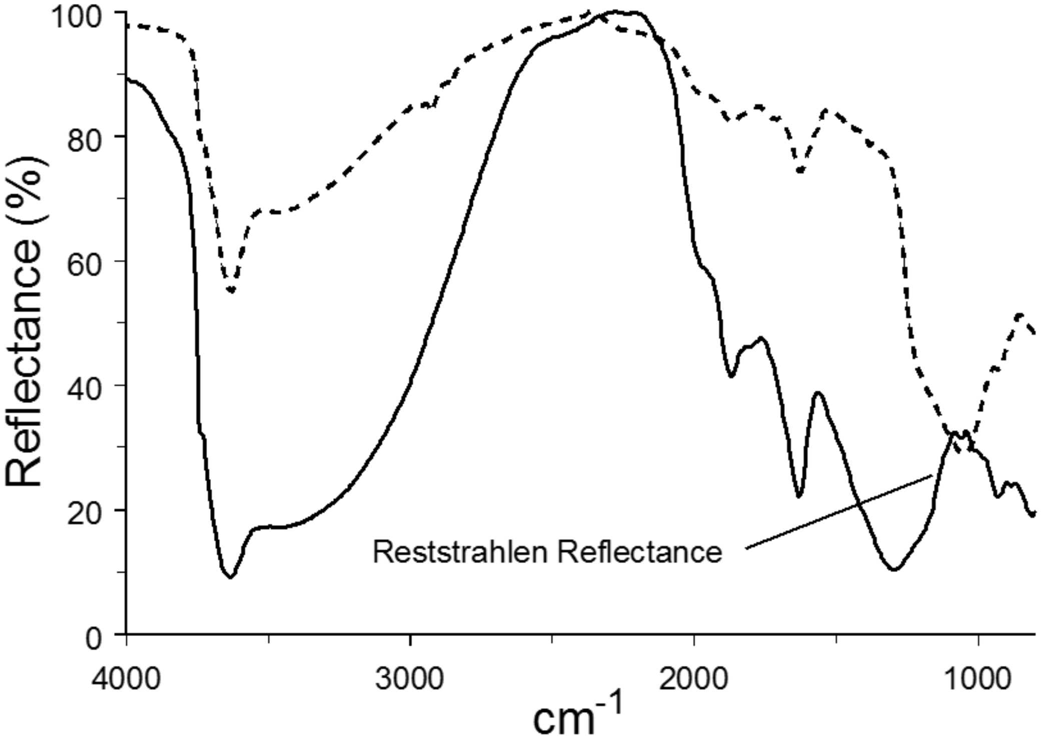

Figure 2.1 - Reflectance spectra measured for neat (solid line) and 5% (w/w) CaMMT diluted in silver powder (dashed line).

2.3 Instrumentation

2.3.1 General

A Mettler-Toledo balance, model AB104-S/FACT, was used for weighing dry samples to the nearest 0.1 mg. A Lab-Line Instruments, Inc. L-C oven set to ~100 °C was employed for drying glassware before use with organic solvents. A Corning Stirrer/Hot Plate was used to stir solutions of adsorbates (*e.g.*, benzoic acid, etc.) prior to adsorption on clays, and also to stir clays in metal chloride solutions for cation exchange. A Buchler Instruments VV-micro roto-evaporator was employed to stir and evaporate mixtures of clays with adsorbate solutions.

2.3.2 Thermogravimetry-Mass Spectrometry

Thermogravimetry – mass spectrometry (TG-MS) measurements were made by using a Du Pont Instruments 951 Thermogravimetric Analyzer (TGA) controlled by an IBM Personal System/2 Model 55 SX with Thermal Analyst software. TG-MS measurements were facilitated by connecting the TGA effluent output to a Hewlett Packard 5973 MSD quadrupole mass spectrometer, which was operated by a PC with Agilent ChemStation software. For TG-MS analyses, approximately ten mg clay samples were loaded into TG platinum balance pans and then heated in 50 mL/min helium with a 5 ºC/min temperature ramp from ambient temperature to at least 650 ºC. A flow splitter valve was used to divert some of the TG effluent into the mass spectrometer (~15 mL/min). For TG measurements in air, approximately two mg clay samples were employed with 50 mL/min air and a 5 ºC/min temperature ramp from ambient temperature to 800 ºC. A diagram of the sample environment within the TGA is shown in Figure 2.2.

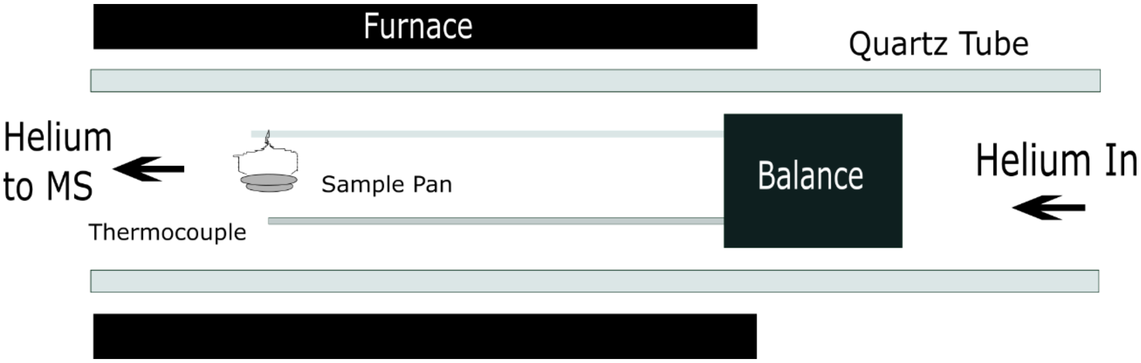

Figure 2.2 – Diagram of the sample environment within the TGA.

2.3.3 Variable Temperature Diffuse Reflection Infrared Fourier Transform Spectroscopy

Infrared spectra were collected by using a Mattson Instruments Inc. Nova Cygni 120 FTIR. The apparatus is described in detail elsewhere[84] and a schematic is provided in Figure 2.3. A Madison Instruments, Inc. 0200-0004 (Middleton, WI) water-cooled globar (silicon carbide) infrared radiation source was used because it allows for better signal-to-noise ratio at high wavenumbers than do air-cooled sources.

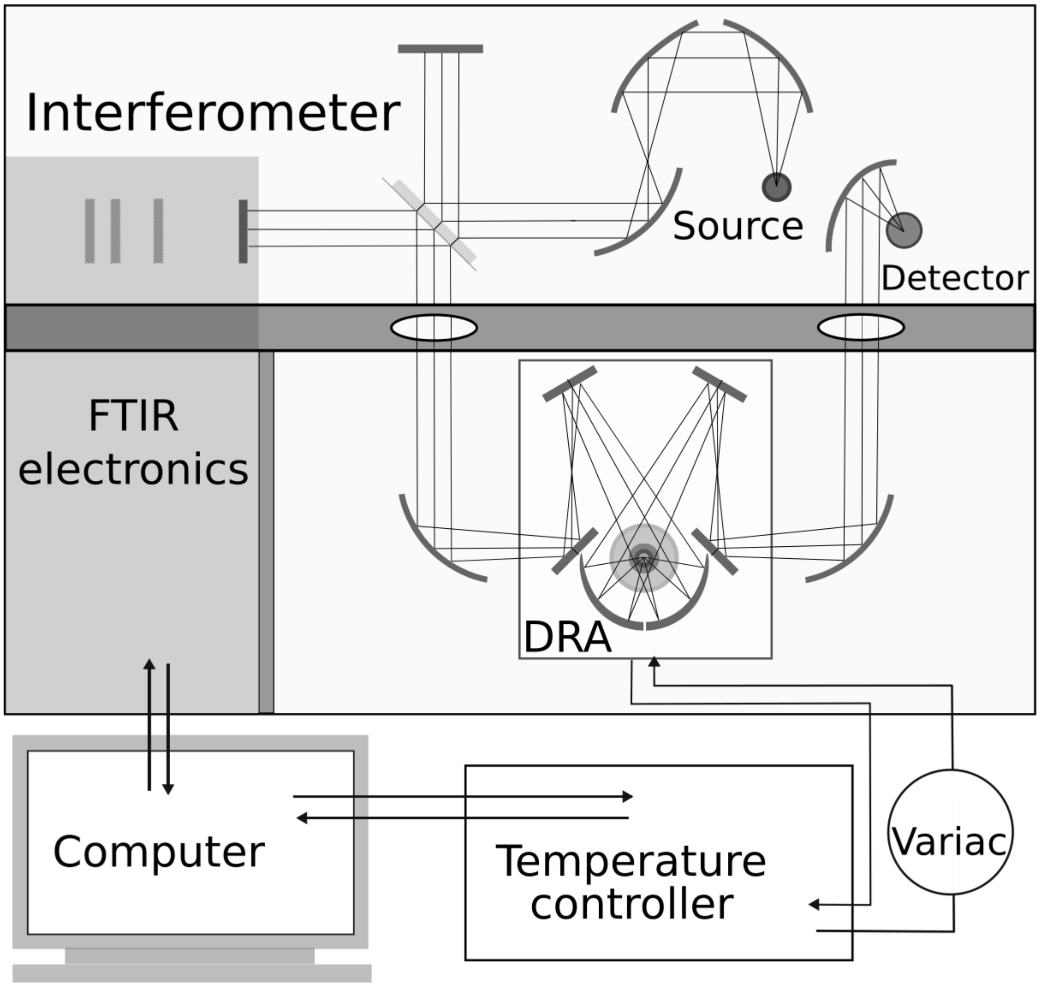

Figure 2.3 - VT-DRIFTS schematic representation.

The sample compartment of this instrument is large enough to hold the diffuse reflection optics, a Harrick Scientific Inc. diffuse reflection accessory, and a modified Harrick Scientific Inc. sample holder environmental chamber.[84] A representation of the stainless steel sample holder is shown in Figure 2.4. Potassium bromide windows were placed over apertures connecting the front and rear FTIR compartments to limit heat transfer from the diffuse reflection accessory (DRA) to the interferometer and the detector, which are particularly sensitive to temperature changes. The detector was a liquid nitrogen-cooled InfraRed Associated, Inc. J-5385-2 Mercury-Cadmium-Telluride (MCT) detector with a spectral range of 666-4762 cm^{-1}.

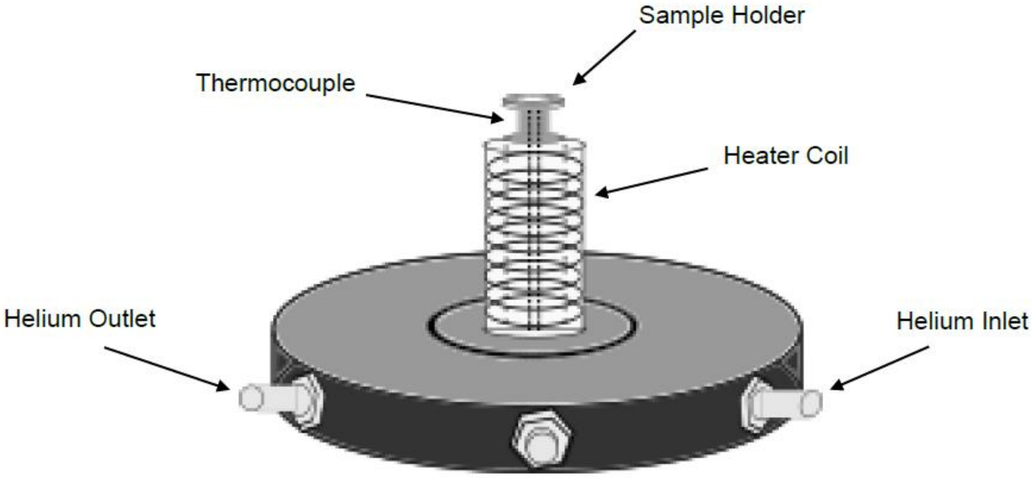

Figure 2.4 – Sample holder apparatus for VT-DRIFTS experiments.

A stainless steel cover is placed on top of the sample holder during experiments and forms a gas-tight seal with the O-ring in the sample holder base. Purging inside the cover with helium allows for an inert sample environment. The cover contains zinc selenide windows that allow IR radiation to pass through with minimal loss of intensity. An Omega CHAL-010 precision fine wire thermocouple extends up through a hole in the stainless steel base and touches the bottom of the sample holder, which is a thin platinum foil. The sample holder is supported by a stainless steel post, which is contained within two quartz tubes. Between the inner and outer quartz tube is a coil of nickel-chromium resistance wire which is used to heat the sample. The sample heater was controlled by a Eurotherm Controls, Inc. model 818p temperature controller. A software macro program was employed to measure sample temperatures that were later correlated with acquired spectra. A linear sample heating ramp and 10 mL/min helium purge were used for analysis. The sample was heated at 5 ^{o}C/min beginning from ambient temperature. Infrared spectra were measured at 1 min (5 ^{o}C) intervals.

2.4 Data Manipulation

2.4.1 Thermogravimetry-Mass Spectrometry Data

The TGA simultaneously measured temperature (°C) and sample mass (mg), and correlated those measurements with elapsed time (min). Percent mass was calculated by dividing each measured sample mass by the initial mass and multiplying the result by 100% (eq 2.1).

$$\% \text{ mass} = (m/m_i) \times 100\% \qquad (2.1)$$

The MS only correlated measured ion intensities with time (min), so the relationship between time and the temperature that was recorded by the TGA was needed to relate ion intensity values to sample temperatures. During experiments, the TGA and the MS were started as close to the same time as possible (within approximately 1 second) so that the data measured by the two systems could be correlated by recorded times. However, the two instruments did not record measurements at the same time intervals, so in order to achieve this, a temperature *vs*. time plot was first generated in Microsoft Excel from the data produced by the TGA. The heating curve was not quite linear (a linear equation produced temperature values with ± 20 °C error), so the data were instead fit to a fifth-order polynomial. In a different spreadsheet in Excel, the fifth-order polynomial was used to generate temperature data from the times recorded by the MS. The measured ion intensities were then plotted against the calculated temperatures to obtain the TG-MS data contained in the chapters that follow. The low temperatures calculated by this method still had a ± 5

°C error, so they were individually corrected to match the temperatures recorded by the TGA. This only needed to be done for data recorded during the first 7.5 minutes of the experiment, because temperatures calculated for time points after that were within 1 °C of those measured by the TGA. For this reason, individual corrections were only applied to m/z profiles which had a significant intensity during the first 7.5 minutes of the experiment (primarily m/z 18). The heating curves varied enough from one experiment to the next that a new fifth-order polynomial had to be generated for every experiment in order to ensure an accurate relationship between measured ion intensity values and calculated temperatures.

2.4.2 VT-DRIFTS Data

Infrared spectra were initially collected as interferograms, and were converted to single beam spectra by a Fourier transformation. Reflectance spectra were computed by dividing successively acquired infrared single beam spectra by diluent (i.e. silver powder) reference single beam spectra (eq 2.2) measured over the same temperature range.

$$R_\infty = R_\infty\text{ (sample)}/R_\infty\text{ (reference)} \qquad (2.2)$$

This practice reduces the loss of spectrum intensity due to detector saturation. Reflectance spectra were converted to “apparent absorbance” spectra (eq 2.3) in order to make use of baseline offset and slope correction facilities provided by the instrument software package.

$$\text{Apparent absorbance} = -\log(R_\infty) \qquad (2.3)$$

After baseline correction, “apparent absorbance” spectra were converted back to reflectance spectra, and then converted to Kubelka-Munk format (eq 2.4) for display and subtractions, because the Kubeka-Munk function is linearly proportional to concentration.[84-86]

$$f(R_\infty) = (1-R_\infty)^2 / 2R_\infty \tag{2.4}$$

Chapter 3 : Thermogravimetry – Mass Spectrometry Investigations of Montmorillonite Interlayer Water Molecule Environment Perturbations caused by Aromatic Acid Adsorbates

3.1 Introduction

Results described here were obtained by using TG-MS to characterize interactions between potassium, sodium, and calcium montmorillonite interlayer water molecules and benzoic acid, salicylic acid, and acetylsalicylic acid adsorbates. By comparing temperature-dependent mass loss and water desorption temperature profiles obtained for samples containing these adsorbates, differences in adsorbate-water interactions can be correlated with their functional group differences. Samples were heated to at least 650 °C, but results obtained below 200 °C, where most water loss occurs, are described here. Although mass spectral information for a wide range of m/z values were obtained during analyses, only m/z 18 (water) profiles are described here. TG-MS characterizations of processes for water loss from clay samples containing adsorbates provide insights into montmorillonite interlayer water perturbations by aromatic acid adsorbates.

3.2 Results

Mass loss curves for neat potassium, sodium, and calcium montmorillonites (KMMT, NaMMT, and CaMMT) are shown in Figure 3.1.

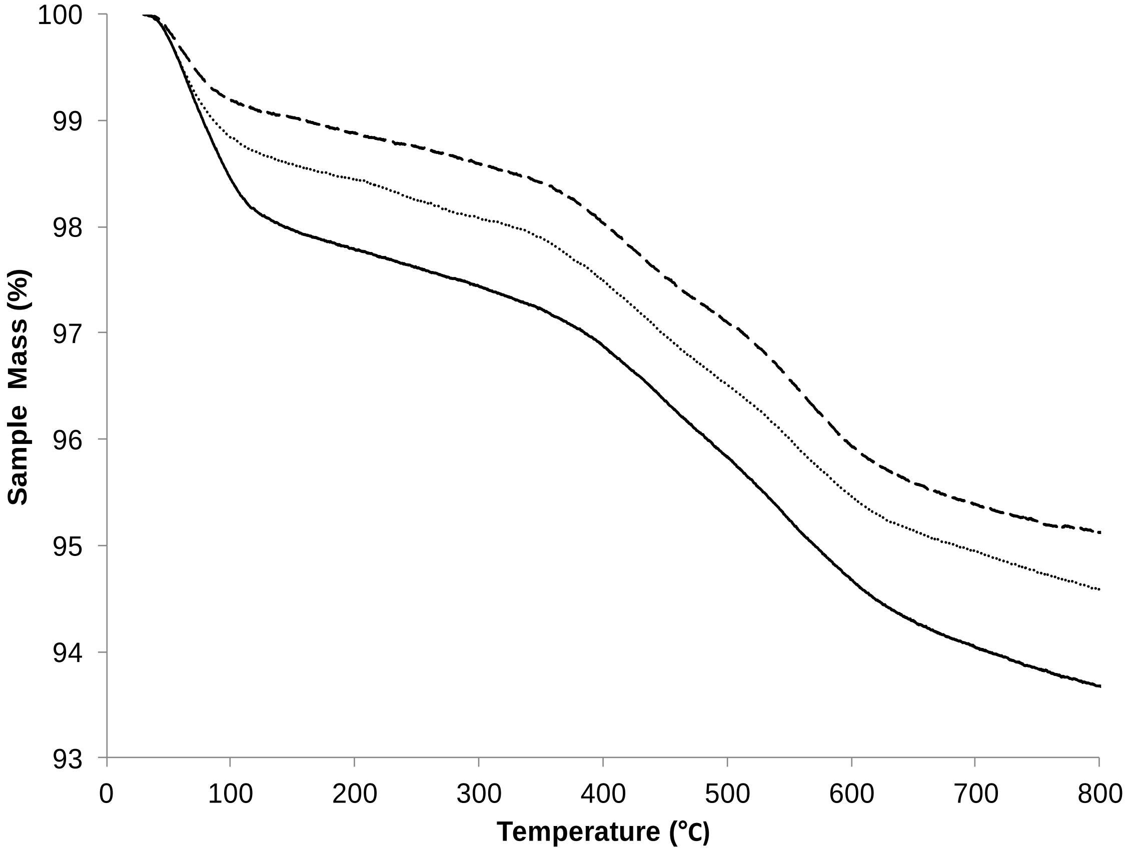

Figure 3.1 - Mass loss curves for neat KMMT (dashed line), NaMMT (dotted line), and CaMMT (solid line)

Mass spectrometric (MS) analysis of volatiles released from neat clay samples while heating them confirmed that water loss was primarily responsible for sample mass changes. Mass loss curves exhibit steep drops below 100 °C, caused by the loss of loosely bound water, including water not directly associated with interlayer cations.[61, 87-89] Above 100 ^{o}C, slopes of the curves decrease, and samples lose mass more gradually until about 400 °C. This temperature range most likely represents loss of interlayer water molecules more closely associated with cations.[88-91]. Near 400 °C, mass loss rates increase, likely due to dehydroxylation, which involves condensation reactions between neighboring hydroxyl groups on inorganic clay surfaces, resulting in the release of water.[73] Figure 3.1 shows that CaMMT had the highest interlayer water content. KMMT contained significantly less water than the other two samples. The dependence of water content on the identity of the interlayer cation shown in Figure 3.1 is in agreement with previous reports.[61, 63, 64, 66, 92] For example, Ferrage, et al. found that at 40% relative humidity (RH), KMMT, NaMMT, and CaMMT contained primarily zero, one, and two water layers, respectively.[63] The three mass loss curve shapes in Figure 3.1 are very similar after the initial loss of water (e.g. above 100 ^{o}C), confirming that the interlayer water content was the main structural difference between these clay samples.

By comparing mass loss results obtained for samples with adsorbates to corresponding neat clay results, information regarding interlayer water contents for the adsorbate containing clays can be derived. Effects of adsorbate on clay interlayer water content were found to be most dramatic for samples derived from KMMT because this clay contained the least amount of water (Figure 3.1). For example, Figure 3.2 shows mass loss temperature profiles obtained for KMMT samples containing (a) benzoic acid, (b) salicylic acid, and (c) acetylsalicylic acid adsorbates.

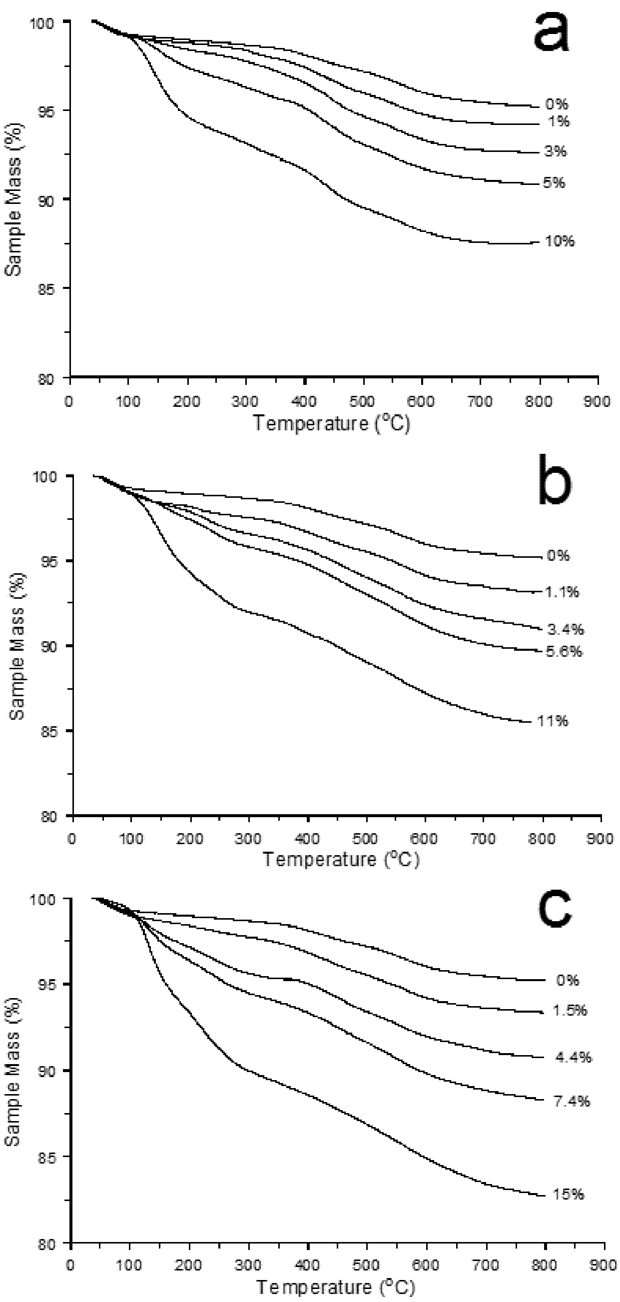

Figure 3.2 - Mass loss versus temperature curves for potassium montmorillonite samples containing (a) benzoic acid, (b) salicylic acid, and (c) acetylsalicylic acid adsorbates. Sample loading percentages are indicated for each curve.

Mass loss profiles for samples containing these adsorbates with NaMMT and CaMMT were similar to those shown in Figure 3.2, and are shown in Appendix B.

Interestingly, sample mass losses between ambient temperature and 100 °C were about the same for all samples. Because water is the primary constituent lost below 100 °C, this suggests that interlayer water contents were about the same for all samples. By assuming that clay water content remained unchanged after introduction of adsorbates, mass losses attributed to clay water evolution from samples containing adsorbates were estimated at each measurement temperature by scaling neat clay mass loss measurements by the clay mass fraction in samples with adsorbates. Mass loss curves for samples containing adsorbates were then "corrected" by removing estimated water loss masses from the adsorbate/clay sample mass loss curves. If the presence of adsorbate truly had no effect on clay moisture content or water desorption temperatures, corrected mass loss temperature profiles should reflect adsorbate losses only.

Figure 3.3 shows the results of subtracting scaled neat KMMT mass loss values from mass losses measured for each adsorbate/KMMT sample. Dashed lines in Figure 3.3 denote total adsorbate mass losses expected based on initial sample loadings. Corrected mass losses extended below maximum expected values (dashed lines) for the lowest loadings of each adsorbate. For salicylic acid (Figure 3.3b), mass losses for samples containing 3.4 and 5.6% adsorbate loadings also exceeded expected maxima. For samples containing acetylsalicylic acid (Figure 3.3c), the 4.4% sample exceeded the expected maximum and the mass loss for the 7.4% loading sample reached the predicted maximum by 800 °C. In contrast, mass losses were less than expected for samples containing the highest adsorbate loadings.

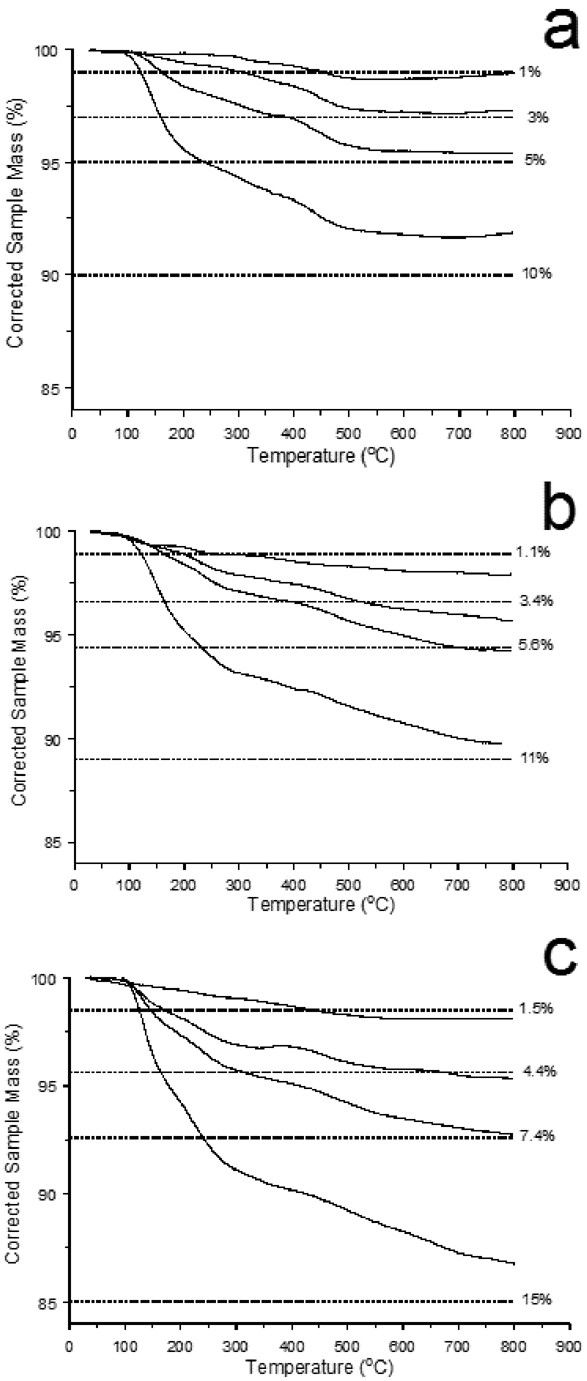

Figure 3.3 - Plots of mass loss differences calculated by subtracting corrected neat potassium montmorillonite mass losses from mass losses measured for (a) benzoic acid, (b) salicylic acid, and (c) acetylsalicylic acid containing samples plotted as a function of adsorbate loadings obtained at the selected temperatures.

Between ambient temperature and 100 ^oC, corrected mass losses did not change significantly and plotted values were near 100%, indicating that subtracting the scaled neat KMMT mass loss profile effectively removed clay water desorption contributions from adsorbate/clay sample mass loss profiles over this temperature range. Above 100 ^oC, corrected mass loss profile intensities decreased due to adsorbate loss. Corrected mass loss profiles for KMMT samples containing benzoic acid (Figure 3.3a) exhibited two successive steps. The initial mass loss rate maximized at about 150 ^oC and became relatively constant above 200 ^oC. A second mass loss rate increase began near 400 ^oC and continued to about 475 ^oC. The initial mass loss rates for samples containing salicylic acid (Figure 3.3b) maximized near 175 ^oC and then decreased above 200 ^oC. Mass loss rates for these samples increased again above 400^oC. Corrected mass loss profile shapes for samples containing acetylsalicylic acid (Figure 3.3c) were similar to those for salicylic acid.

Corrected mass loss profiles for samples containing high adsorbate loadings did not reflect expected sample mass losses, suggesting that these samples may have contained less than the specified amounts of adsorbates. Alternatively, the lower than expected mass losses may have resulted from incomplete removal of adsorbate, leaving high temperature residue in the form of char. In fact, some samples became darker after heating, indicating the presence of char. In order to determine if char formation was the primary source of the observed discrepancy, separate TG analyses of KMMT samples containing the highest loadings of each adsorbate were performed in air, using small sample sizes to maximize air access to clay surfaces, and the results are shown in Appendix C. The 10% benzoic acid/KMMT sample had a corrected mass loss of 9.8%

and the 11% salicylic acid/KMMT sample had a corrected mass loss of 11%, so it seems that char formation was primarily responsible for the discrepancies observed for those samples when helium was used as the carrier gas. The 15% acetylsalicylic acid/KMMT sample had a corrected mass loss of 13.8% in air, which is more than the corrected mass loss of 13.2% observed in helium, but is still somewhat less than the predicted 15%. However, several months had elapsed between sample preparation and analysis in air, so it is likely that some of the acetylsalicylic acid decomposed to form salicylic acid and acetic acid during that time, and some of the acetic acid may have evaporated.

Because mass spectrometer ion signal detection sensitivity greatly exceeds that for sample mass measurements, temperature dependent water evolution rate profiles for neat clays were represented by monitoring TG-MS m/z 18 (H_2O^+) ion signal intensity rather than by mass loss curve derivatives. The neat clay m/z 18 ion signal profiles shown in Figure 3.4 were baseline corrected to account for ambient water concentration variations and maximum intensities were normalized. Due to this scaling procedure, m/z 18 ion signal versus temperature plot areas are not proportional to the total amounts of water evolved from samples. Instead, this curve scaling method emphasizes differences in water evolution peak shapes. The peak shapes for neat NaMMT and CaMMT are consistent with those reported previously.[67] The m/z 18 ion signal temperature profile for KMMT was qualitatively similar to that for NaMMT, which is not surprising because potassium and sodium are both monovalent cations and would be expected to have similar properties. In contrast, the water evolution profile for CaMMT, which contains divalent Ca^{2+} interlayer ions, is much broader and extends to higher temperatures. This indicates that greater energy is required for removal of some water molecules from clay interlayer spaces when divalent Ca^{2+} is present compared to monovalent K^+ or Na^+. Because of plot normalizations, curves for NaMMT and KMMT appear to have similar magnitudes. However, mass loss results (Figure 3.1) clearly show that neat NaMMT lost more mass than neat KMMT over the displayed temperature range.

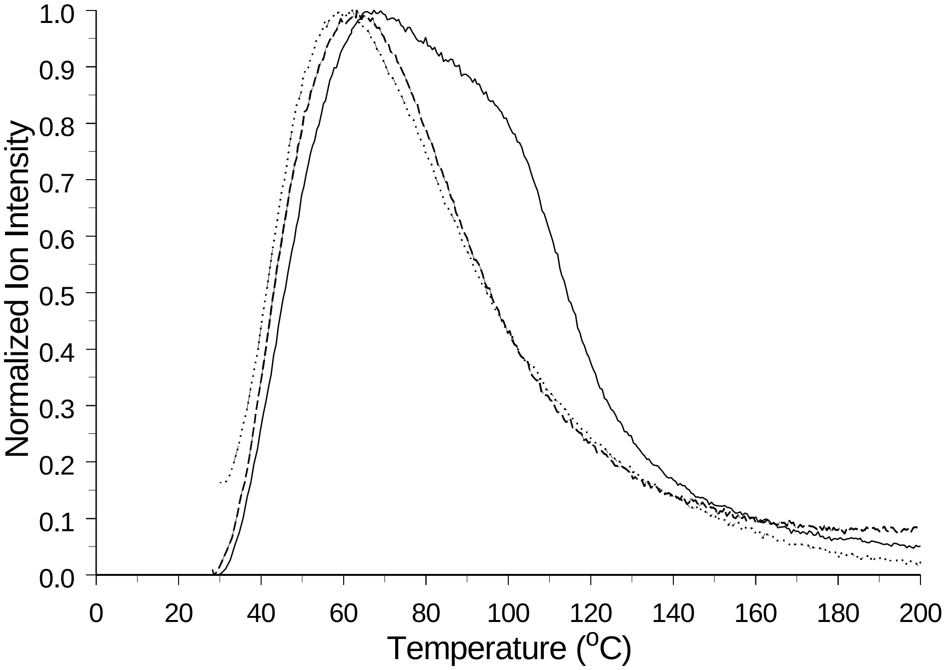

Figure 3.4 - Normalized m/z 18 profiles for neat KMMT (dashed line), NaMMT (dotted line), and CaMMT (solid line) samples.

Figure 3.5 shows m/z 18 ion signal temperature profiles for (a) KMMT, (b) NaMMT, and (c) CaMMT samples containing various loadings of benzoic acid. Plot baselines were offset for clarity. Figure 3.5a shows that the presence of benzoic acid perturbed the water evolution profile for samples containing KMMT in a systematic manner. With a 1% (w/w) benzoic acid loading, the water loss profile was very similar to that for the neat KMMT sample (0%), except that the peak maximum was shifted to slightly lower temperature and ion intensity was slightly greater above 150 °C. The peak maximum shift to lower temperature suggests that some water molecules were more easily removed by heating when benzoic acid was present. Conversely, the greater m/z 18 ion intensity above 150 °C indicates that some water molecules were stabilized by the presence of adsorbate.

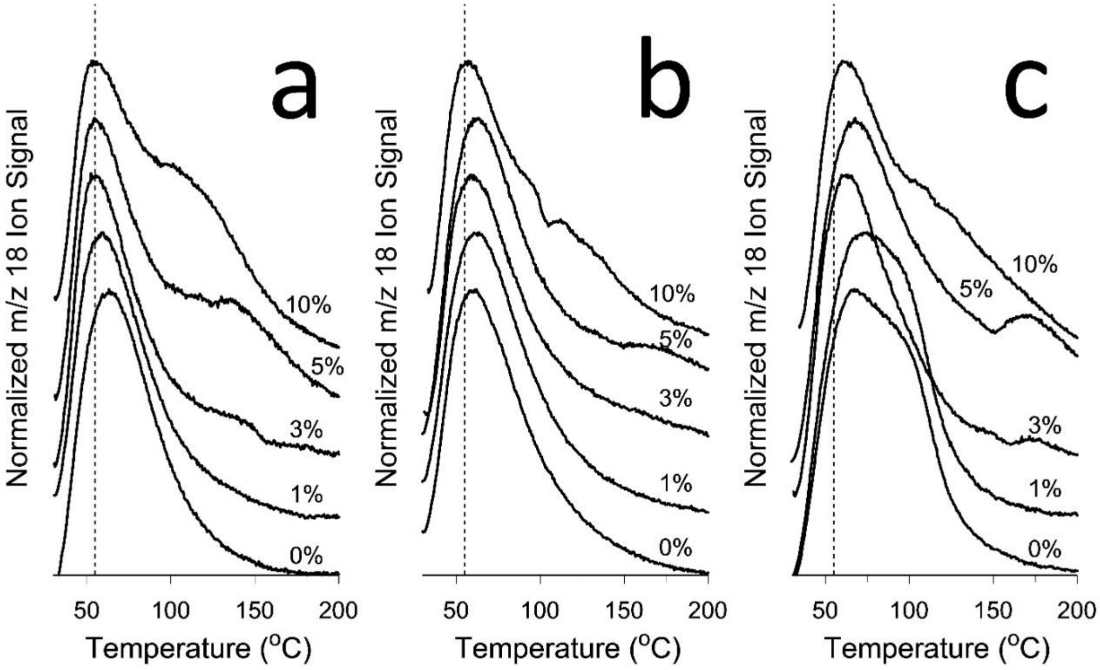

Figure 3.5 - M/z 18 ion signal temperature profiles for (a) KMMT, (b) NaMMT, and (c) CaMMT samples containing various loadings of benzoic acid.

With higher benzoic acid loadings, the peak maximum shifted to even lower temperatures (the dotted line denotes 55 °C) and additional overlapping peaks appear above 100 °C that were not observed when heating the neat KMMT sample. The lower profile maximum temperatures for samples containing benzoic acid compared to neat KMMT indicates destabilization of interlayer water molecules due to the presence of adsorbate. The relatively constant peak maxima temperatures for samples containing 3, 5, and 10% (w/w) benzoic acid suggest that this destabilizing effect is independent of adsorbate loading above 1% (w/w). Successive increases in m/z 18 ion intensity above 100 ^{o}C with increasing benzoic acid loading suggests that increasingly higher proportions of interlayer water molecules are stabilized by adsorbate. Maxima for overlapping water loss contributions detected above 100 ^{o}C shift to lower temperature with increasing benzoic acid loadings, which is consistent with a destabilizing water environment effect associated with higher adsorbate loadings. In Figure 3.5b and Figure 3.5c, it is apparent that benzoic acid also perturbs the water molecules in NaMMT and CaMMT interlayer spaces. Peak shapes for NaMMT m/z 18 ion signal temperature profiles (Figure 3.5b) exhibit trends similar to those for the samples containing KMMT. However, systematic peak shape changes were less obvious when benzoic acid was adsorbed on NaMMT compared to KMMT, possibly because NaMMT contains more interlayer water, so that the overlapping high temperature contributions represent smaller fractions of total peak areas. Peak maxima shifts for NaMMT are less dramatic than for KMMT and do not reach 55 ^{o}C (dotted line).

Water evolution temperature profiles for CaMMT samples containing varying benzoic acid loadings also exhibit trends. The curve for the sample containing a 1% (w/w) benzoic acid loading was similar to the neat CaMMT m/z 18 ion signal temperature profile. With higher benzoic acid loadings, the broad peak, characteristic of neat CaMMT and the CaMMT sample containing 1% (w/w) benzoic acid, was replaced by a narrower peak shape similar to those in Figure 3.5a and Figure 3.5b. Peak maxima for m/z 18 ion intensity versus temperature plots for the benzoic acid/CaMMT samples vary somewhat, but do not shift as much to lower temperatures as those obtained for samples containing KMMT and NaMMT.

Figure 3.6 shows m/z 18 ion signal temperature profiles for (a) KMMT, (b) NaMMT, and (c) CaMMT samples containing various loadings of salicylic acid. Molar loadings of salicylic acid on these clays were the same as those used to prepare samples containing benzoic acid, but salicylic acid has a higher molecular weight, so weight percentages were slightly higher.

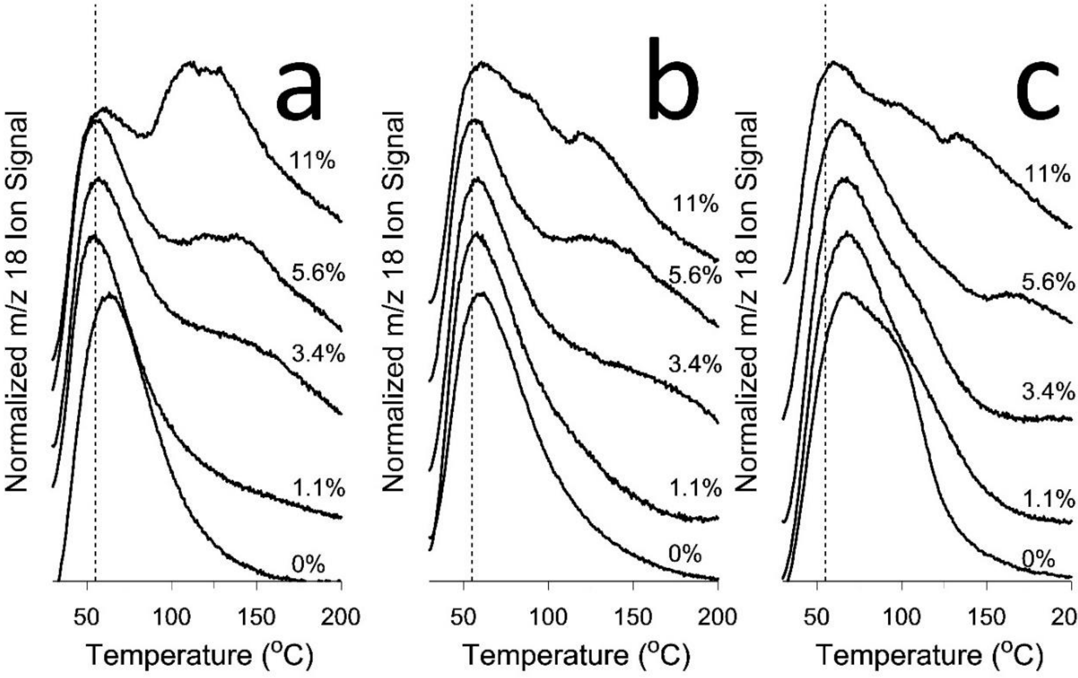

Figure 3.6 - M/z 18 ion signal temperature profiles for (a) KMMT, (b) NaMMT, and (c) CaMMT samples containing various loadings of salicylic acid.

Salicylic acid had an even more dramatic effect on clay interlayer water than benzoic acid. Ion signal versus temperature profile variations were most apparent for the sample containing KMMT (Figure 3.6a). Like samples comprised of KMMT and benzoic acid, low temperature peak maxima shifted to lower temperatures (dotted line represents 55 ^{o}C) with higher salicylic acid loadings, and maxima for overlapping higher temperature contributions to these profiles also shifted to lower temperatures with increasing loadings. Unlike the sample containing 10% (w/w) benzoic acid and KMMT, the higher temperature m/z 18 ion signal temperature profile component for the KMMT sample containing the highest salicylic acid loading (e.g. 11%) exceeded the low temperature component intensity. Like the KMMT/benzoic acid results, peak maxima shifts and overlapping higher temperature contributions to m/z 18 ion signal temperature profiles were less dramatic for samples containing NaMMT (Figure 3.6b). In contrast to results obtained for samples containing benzoic acid, the CaMMT sample containing the lowest loading of salicylic acid (1.1%) yielded an m/z 18 ion signal temperature profile that was significantly narrower than the neat CaMMT temperature profile (Figure 3.6c). Like the results obtained for CaMMT samples containing benzoic acid, low temperature peak maxima did not shift as much as those obtained for the KMMT and NaMMT samples and higher temperature profile contributions were less obvious than in the profiles obtained for those samples.

Figure 3.7 shows m/z 18 ion signal temperature profiles for (a) KMMT, (b) NaMMT, and (c) CaMMT samples containing various loadings of acetylsalicylic acid. Acetylsalicylic acid molar loadings were the same as the benzoic acid and salicylic acid molar loadings. The profile for the sample containing 15% (w/w) acetylsalicylic acid on KMMT (Figure 3.7a) has a shape that is similar to that for the 11% (w/w) salicylic acid/KMMT sample (Figure 3.6a), in which the overlapping higher temperature peak is more intense than the low temperature peak. Results obtained for the acetylsalicylic acid/NaMMT samples (Figure 3.7b) and acetylsalicylic acid/CaMMT samples (Figure

3.7c) exhibit trends similar to those observed for the corresponding samples containing salicylic acid (Figure 3.6b and Figure 3.6c), except that the profiles for the 15% acetylsalicylic acid loading include a depression above 100 °C for the NaMMT and CaMMT samples. The temperature corresponding to this ion signal decrease reasonably matches the maximum evolution temperature for acetic acid evolution detected by MS for these samples. Water evolution rates would be expected to decrease when acetic acid is produced because water that reacts with acetylsalicylic acid to form salicylic acid and acetic acid is not represented by m/z 18 ion signal temperature profiles.

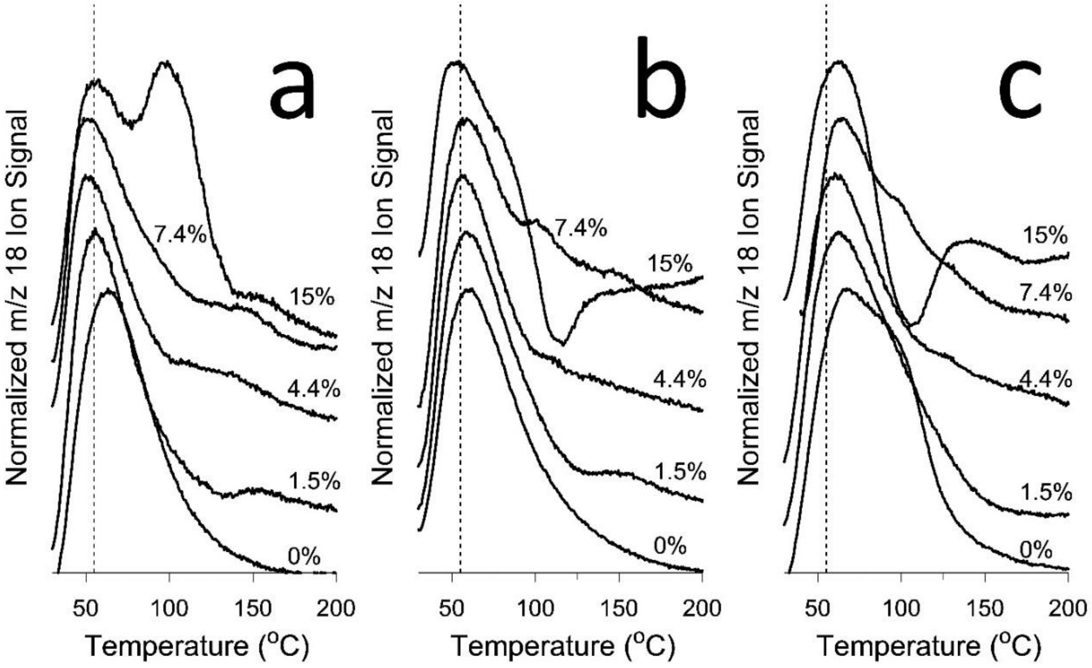

Figure 3.7 - M/z 18 ion signal temperature profiles for (a) K MMT, (b) Na MMT, and (c) Ca MMT samples containing various loadings of acetylsalicylic acid.

3.3 Discussion

The corrected mass loss curves for samples containing KMMT shown in Figure 3.3 exhibit interesting trends that were less obvious but still present in profiles obtained for the corresponding NaMMT and CaMMT samples. Below 100 ^{o}C, corrected mass values were near 100%, suggesting that the subtraction method used to correct for water loss by scaling and removing the mass loss curve for the neat clay (Figure 3.1) was effective between ambient temperature and 100 ^{o}C. By 800 ^{o}C, corrected mass losses for samples containing the lowest adsorbate loadings match or exceed expected values based on mixture compositions employed during sample preparation (dotted lines). Greater than expected mass losses for samples containing low adsorbate loadings may be due to these clays having higher water content than the neat clays. Additional water may be incorporated into samples because of interlayer expansion due to incorporation of adsorbate.[41, 93, 94]. Void spaces produced by this expansion may be filled by additional water molecules. Because corrected mass values remained near 100% at the start of sample heating, if the water content in these samples exceeded that for the corresponding neat clay, the excess water molecules must have been retained by samples below 100 ^{o}C. In contrast to samples containing low absorbate loadings, mass loss was less than expected for samples containing the highest adsorbate loadings. However, during TG analyses in air, KMMT samples containing the highest loadings of benzoic acid and salicylic did reach the predicted mass losses (within 0.2%), suggesting that char formation was the most likely cause of the discrepancy observed during analyses in helium. The acetylsalicylic acid/KMMT sample did not reach the predicted mass loss, but that was probably due to decomposition of the acetylsalicylic acid and subsequent evaporation of acetic acid.

Figure 3.3 shows that adsorbate mass loss begins near 100 ^{o}C for all samples. Above 500 ^{o}C, benzoic acid corrected sample masses remain relatively constant whereas mass continues to decrease for samples containing salicylic acid and acetylsalicylic acid. If adsorbate residues are responsible for mass losses above 500 ^{o}C, the profiles in Figure 3.3 suggest that residues derived from salicylic acid and acetylsalicylic acid are less stable than those derived from benzoic acid. Mass losses above 500 ^{o}C for samples containing salicylic acid and acetylsalicylic acid are greatest for samples containing the highest adsorbate loadings. This would be expected if high temperature residues were formed by reactions between adsorbate molecules, because these reactions would be better facilitated by increased adsorbate concentrations.

Mass spectrometric water evolution profiles (Figure 3.5, Figure 3.6, and Figure 3.7) show that the presence of adsorbates at 1% or greater loadings disrupt water molecule environments. For all adsorbates, increasing the loading resulted in greater water evolution profile changes compared to the corresponding neat clay. The presence of benzoic acid caused the smallest changes to evolution profiles. Profiles for benzoic acid adsorbed on KMMT and NaMMT were similar, and indicated that some water molecules required less thermal energy for desorption, whereas other water molecules required more energy for desorption, relative to water desorbing from neat clays. With a 1% benzoic acid loading, the CaMMT water desorption profile resembled that for neat CaMMT. For higher benzoic acid loadings, profiles more closely resembled those obtained for KMMT and NaMMT. Apparently, when small amounts (<3%) of benzoic acid were added to CaMMT, water molecule interactions with Ca^{2+} were only slightly perturbed. Larger benzoic acid loadings led to greater destabilization of water molecule interactions with Ca^{2+}, resulting in evolution profiles that more closely resembled those for samples containing KMMT and NaMMT.

Compared to results obtained for benzoic acid, salicylic acid loadings on KMMT, NaMMT, and CaMMT caused similar shifting of water evolution maxima, suggesting that the low temperature water environment destabilizing effects were similar to those observed for benzoic acid. Above 100 ^{o}C, salicylic acid/clay sample profiles contained higher m/z 18 ion relative intensities than corresponding benzoic acid/clay samples, suggesting that more water molecules were stabilized by salicylic acid than by benzoic acid. Like benzoic acid results, the m/z 18 ion signal intensity local maxima above 100 ^{o}C shifted to lower temperatures with higher salicylic acid loadings, indicating that the water stabilizing effects of salicylic acid decreased with increasing adsorbate loadings.

Water evolution profiles for acetylsalicylic acid (Figure 3.7) were more similar to those obtained for salicylic acid (Figure 3.6) than to benzoic acid (Figure 3.5). Mass spectrometric analyses of volatiles produced while heating acetylsalicylic acid/clay samples revealed that acetic acid formation began at about 60 ^{o}C and maximized slightly above 100 ^{o}C. Thus, above 60 ^{o}C, acetylsalicylic acid/clay samples were transformed into mixtures of acetylsalicylic acid and salicylic acid, with the fraction of salicylic acid steadily increasing with increasing temperature. Between ambient temperature and 60 ^{o}C, acetylsalicylic acid/clay water desorption temperature profile shapes were similar to those for salicylic acid, indicating that water environment destabilization effects were similar for these adsorbates. This similarity is likely due to the presence of additional functional groups (hydroxyl group for salicylic acid and ester group for acetylsalicylic acid) that can participate in hydrogen bonding interactions. Above 100 ^{o}C, m/z 18 ion signal intensities for acetylsalicylic acid/clay samples decreased because some water molecules reacted with acetylsalicylic acid to form acetic acid, which eliminated them from m/z 18 ion signal temperature evolution profiles.

Although mass loss versus temperature profile shapes for neat KMMT, NaMMT, and CaMMT samples were similar, TG-MS m/z 18 ion signal temperature profiles were significantly different between samples containing monovalent cations (e.g. KMMT and NaMMT) and CaMMT, which contains divalent Ca^{2+} (Figure 3.4). Greater thermal energy (i.e. higher temperature) was required for water desorption from CaMMT compared to KMMT and NaMMT. Because the clay structures differ only in the identities of interlayer cations and water content, higher water desorption temperatures may be attributed to stronger interactions between water molecules and Ca^{2+} compared to K^+ and Na^+. For samples containing KMMT and NaMMT, low adsorbate loadings caused water desorption rate maxima to shift to slightly lower temperatures, but the shapes of m/z 18 ion signal versus temperature profiles were not significantly altered. In contrast, the lowest CaMMT adsorbate loadings were sufficient to alter the shapes of water desorption temperature profiles for salicylic acid and acetylsalicylic acid. Previous work confirmed that benzoic acid interacts with Na^+ and Ca^{2+} through bridging water molecules. Thus, adsorbate effects on interlayer water environments likely arise from these interactions. The fact that adsorbate mediated water environment disruptions were greatest for clays containing Ca^{2+} indicates that the interlayer cation charge was important for determining water molecule environments and suggests that adsorbate molecules preferentially perturbed water molecules nearest the cations, most likely by forming bridging water molecule interactions. Compared to local environments in the absence of adsorbate, bridging water molecules would be more shielded from bulk water molecules, which would hinder hydrogen bonding with other water molecules. Thus, although formation of water molecule bridges between adsorbates and interlayer cations involves hydrogen bonding, the primary cause of interlayer water molecule environment disruption may derive from steric effects of adsorbate molecules blocking water-water hydrogen bonding interactions. This would result in thermal destabilization of water molecules that are in the vicinity of cations but are not directly interacting with them. The other possibility is that the ester and hydroxyl groups on acetylsalicylic acid and salicylic acid, respectively, form hydrogen bonds with interlayer water molecules, which would also block water-water hydrogen bonding interactions. Above 100 ^{o}C, water molecule loss included water molecules that were involved in interactions with interlayer cations.[88-91]. With increasing adsorbate loadings, the increased m/z 18 ion signal intensity shifted to lower temperatures (closer to 100 ^{o}C). This trend may be explained by increased intermolecular interactions between adsorbate molecules, which would be expected to occur at high adsorbate loadings and would lessen the impact of adsorbate disruption to water-water hydrogen bonding. Increased adsorbate-adsorbate interactions at higher loadings would also facilitate high temperature condensation reactions that would result in char formation.

Ferrage, et al.[89] proposed a calcium montmorillonite dehydration mechanism that included initial loss of interlayer water molecules that are not closely associated with cations followed by loss of water molecules from cation hydration spheres. Results described here are consistent with this model. Aromatic acid adsorbates are retained within clay interlayer spaces below 100 ^{o}C and interfere with the water loss processes described by Ferrage et al. by altering intermolecular hydrogen bonding interactions. Local water molecule environment changes result in some molecules becoming less thermally stable, whereas others become more stable, compared to their stabilities in the absence of adsorbates.

3.4 Summary

Potassium, sodium, and calcium montmorillonites were used as adsorbents to characterize the effects of cation charge and water content on adsorbate/clay properties. Benzoic acid, salicylic acid, and acetylsalicylic acid represent three PPCPs that all contain aromatic acid functionalities. Compared to benzoic acid, salicylic acid contains an additional hydroxyl group attached to the aromatic ring and acetylsalicylic acid has the same structure except that the hydroxyl group is replaced by an acetyl functionality. TG-MS results obtained for samples containing these adsorbates and montmorillonites with different interlayer cations and varying water contents were similar, but with subtle differences. Observed similarities were most likely due to the fact that the aromatic acid group, which was common to all three adsorbate structures, was largely responsible for adsorbate-clay interactions. The salicylic acid hydroxyl group and aspirin acetyl group provided additional hydrogen bonding effects compared to benzoic acid. Because primary interactions most likely consist of hydrogen bonding between adsorbate molecules and water molecules that bridge to interlayer cations, the use of detection methods that are capable of characterizing hydrogen bonding interactions should be well suited for future studies. In fact, additional studies of the adsorbate-clay interactions by using infrared spectroscopy have been conducted, and are discussed in Chapter 4.

Chapter 4 : Variable Temperature Infrared Spectroscopy Investigations of Montmorillonite Interlayer Water Molecule Environment Perturbations caused by Aromatic Acid Adsorbates

4.1 Introduction

Results described here were obtained by using VT-DRIFTS to characterize interactions between potassium, sodium, and calcium montmorillonite interlayer water molecules and benzoic acid, salicylic acid, and acetylsalicylic acid adsorbates. By comparing temperature-dependent infrared spectra obtained for samples containing these adsorbates, differences in adsorbate-water interactions can be correlated with their functional groups. Samples were heated to 400 °C, but results obtained below 60 °C, prior to acetylsalicylic acid decomposition and salicylic acid desorption, are described here. VT-DRIFTS characterizations of processes for water loss from clay samples containing adsorbates provide insights into montmorillonite interlayer water perturbations by aromatic acid adsorbates, and reveals details regarding the local environments of adsorbate molecules before and during dehydration processes.

4.2 Results and Discussion

Montmorillonite infrared spectra are dominated by strong features near 1050 cm^{-1} corresponding to inorganic oxide vibrations and over the 2500-3750 cm^{-1} range due to O-H stretching vibrations. The O-H stretching vibration band consists of overlapping contributions from inorganic oxide hydroxyl groups and interlayer water.[95] Vibrations of inorganic oxide Al-OH-Al functionalities are represented as a strong absorbance band spanning the 3750-3550 cm^{-1} range with maximum intensity near 3630 cm^{-1}.[95] Interlayer water molecule vibrations are affected by interactions with cations, inorganic oxide surfaces, and other water molecules, resulting in a broad absorbance band that extends from 3700 to about 2500 cm^{-1}. The stacked plots in Figure 4.1 and Figure 4.2 provide a comparison of neat montmorillonite infrared spectra with those obtained for samples containing adsorbates. The small band at 3740 cm^{-1} in Figure 4.1a denotes inorganic oxide hydroxyl groups, most likely Si-OH and Al-OH,[96, 97] that are not involved in hydrogen bonding. Addition of benzoic acid, salicylic acid, and acetylsalicylic acid (acetylsalicylic acid) adsorbates dramatically increases infrared absorbance below 3525 cm^{-1} (dotted line). The presence of these adsorbates disrupt the montmorillonite interlayer water hydrogen bonding network and provide additional hydroxyl functionalities, which also adsorb in this spectral region. Although all three adsorbates contain aromatic acid functionalities, which contribute to absorbance in this spectral range, salicylic acid also contains an aromatic hydroxyl group, providing additional infrared absorbance.

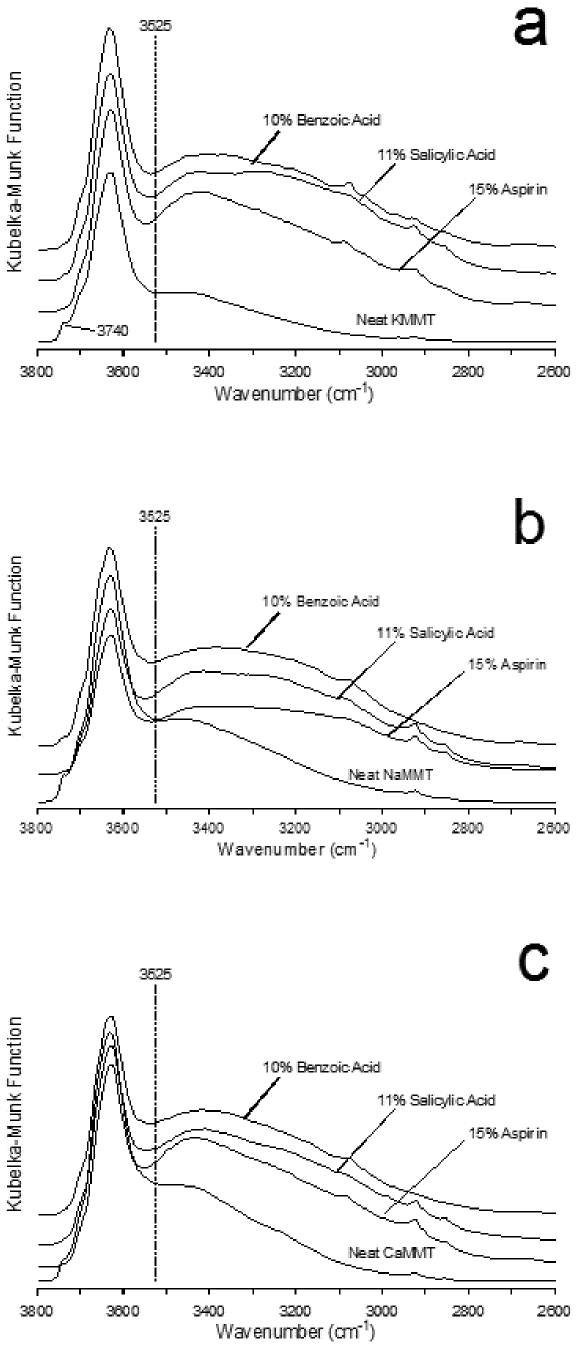

Figure 4.1 - VT-DRIFTS spectra representing the O-H stretching vibration region for samples containing (a) KMMT, (b) NaMMT, and (c) CaMMT.

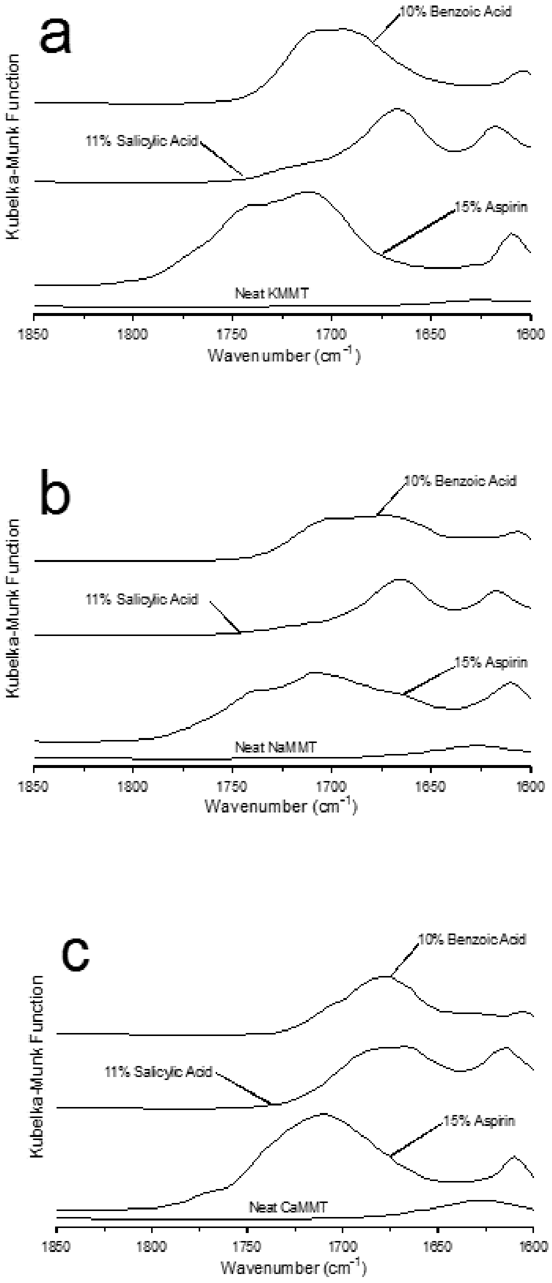

Figure 4.2 - VT-DRIFTS spectra representing the C=O stretching vibration region for samples containing (a) KMMT, (b) NaMMT, and (c) CaMMT.

The presence of adsorbate does not significantly affect the O-H stretching vibration band associated with inorganic oxide hydroxyl groups, suggesting that these functionalities primarily interact with water molecules, even when adsorbate is present.

Interestingly, the small 3740 cm^{-1} band is greatly reduced or absent in spectra obtained from samples containing adsorbate, suggesting that adsorbate molecules may interact with inorganic oxide hydroxyl groups that otherwise do not participate in hydrogen bonding. Spectra for neat clay samples exhibit increasing contributions from water O-H stretching vibration band intensity in the order KMMT<NaMMT<CaMMT, which is consistent with TG-MS analysis results confirming that the water content of these clays increased in the same order. The most significant differences in absorbance contributions from interlayer water for neat clay samples appear at high wavenumbers, suggesting that the water molecules added as a result of exchanging potassium cations for sodium and calcium cations were involved in minimal hydrogen bonding with their surroundings (i.e. more similar to bulk water).

Adsorbate interactions with montmorillonites involve hydrogen bonding to interlayer water molecules that bridge between cations and aromatic acid groups.[69] Hydrogen bonding perturbs the molecular vibrations of adsorbate and water molecules involved in the interactions. For water molecules, these perturbations cause changes to O-H stretching and bending vibrations. For adsorbates, vibrations involving the aromatic acid group are primarily affected. Consequently, adsorbate infrared spectra exhibit variations in C=O stretching vibration band shape and position that depend on the properties of the clay interlayer cation. This is illustrated by Figure 4.2, which shows ambient temperature C=O stretching vibration band regions of infrared spectra obtained for the neat clays and clays containing adsorbate. Neat clay spectra exhibit little absorbance in this spectral region, except for relatively low intensity broad bands with maxima near 1630 cm^{-1} that can be assigned to water molecule bending vibrations.

The intensities of the 1630 cm^{-1} bands vary in the order: KMMT<NaMMT<CaMMT, and can be correlated with clay water content. Small absorbance bands near 1606 cm^{-1} for benzoic acid, 1618 cm^{-1} for salicylic acid, and 1610 cm^{-1} for acetylsalicylic acid that overlap the 1630 cm^{-1} water bending vibration band show little band shape or intensity dependence on the nature of the interlayer cation and most likely represent aromatic ring vibrations. The more intense and broader absorbance bands above 1650 cm^{-1}can be assigned to C=O stretching vibrations. Figure 4.2 shows that the C=O stretching vibration band position and shape depend on both the adsorbate and the identity of the interlayer cation. For all adsorbates, C=O absorbance bands are most similar for samples containing KMMT and NaMMT clays, which suggests that cation charge largely dictates the frequency of this vibration. When adsorbed on KMMT, the benzoic acid C=O absorbance band appears as a broad feature with a maximum near 1700 cm^{-1}. When adsorbed on NaMMT, the benzoic acid C=O absorbance band becomes more broad and the maximum shifts to lower wavenumber (~1688 cm^{-1}) relative to the same band from the KMMT sample. On CaMMT, the benzoic acid C=O absorbance band is sharper and the band maximum is shifted to lower wavenumber (~1677 cm^{-1}) compared to results for samples containing KMMT and NaMMT. The salicylic acid C=O stretching vibration band for the sample containing KMMT is much sharper than the benzoic acid band and appears at lower wavenumber (~1667 cm^{-1}). When adsorbed on NaMMT, the salicylic acid C=O bandwidth and band maximum are comparable to those observed for the KMMT sample. On CaMMT, the salicylic acid band broadens and extends to higher wavenumber compared to results obtained for samples containing KMMT and NaMMT. The C=O stretching vibration absorbance band obtained for the

acetylsalicylic acid/KMMT sample was broad and consisted of overlapping contributions at about 1710 and 1740 cm^{-1}. A similar overlap of bands at these wavenumbers was obtained for the acetylsalicylic acid/NaMMT C=O stretching vibration absorbance band. In addition, a third overlapping absorbance contribution was apparent with maximum intensity near 1667 cm^{-1}. Compared to results obtained for samples containing KMMT and NaMMT, the acetylsalicylic acid/CaMMT sample C=O stretching vibration band was narrower, with the band maximum located near 1710 cm^{-1}.

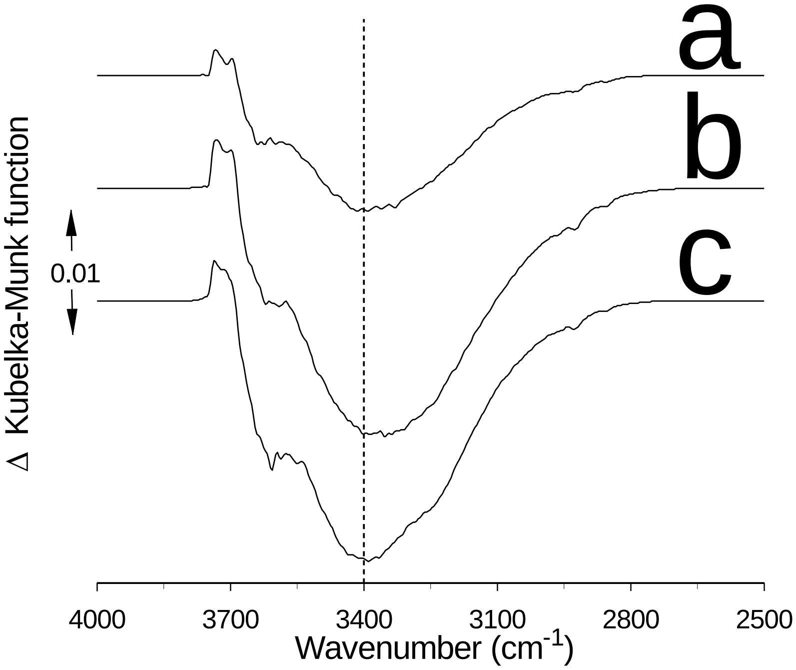

Figure 4.3 - Difference spectra obtained by subtracting the ambient temperature VT-DRIFTS spectrum from the spectrum obtained at 60 °C for (a) KMMT, (b) NaMMT, and (c) CaMMT neat clays. The dotted line denotes 3400 cm^{-1}.

TG-MS studies showed that all sample mass losses detected by heating from ambient temperature to 60 °C resulted exclusively from water loss. Therefore, infrared spectral changes detected over this temperature range can be attributed to sample dehydration effects. Figure 4.3 shows difference spectra obtained by subtracting the VT-DRIFTS ambient temperature spectrum from one obtained after the sample temperature reached 60 ^{o}C for each neat clay sample. Negative features represent absorbance that was lost by heating the sample and positive features denote absorbance spectrum gains. The broad negative spectral features for each clay are associated with water loss, which reduces the overall O-H stretching vibration band intensity. Each clay lost about 40% of the ambient temperature intensity at 3400 cm^{-1} after heating samples to 60 ^{o}C. The negative difference spectrum band was smallest for neat KMMT, which had the lowest initial water content. Two small overlapping positive bands were found at 3735 and 3696 cm^{-1}, which can be assigned to inorganic oxide hydroxyl groups (Si-OH and/or Al-OH) that lost hydrogen bonding partners as a result of sample heating. Negative bands for all three clay samples exhibit asymmetry near 3650 cm^{-1}, where inorganic oxide hydroxyl group vibrations overlap interlayer water molecule absorbance bands. The absorbance loss at 3650 cm^{-1} is most likely associated with the same inorganic oxide hydroxyl groups responsible for the 3735 and 3696 cm^{-1} positive bands. Neat clay difference spectra have similar shapes with intensity minima located near 3400 cm^{-1}, suggesting that water loss mechanisms were similar over this temperature range.

As described in Chapter 3, neat clay dehydration mechanisms were affected by the presence of adsorbates. VT-DRIFTS results suggest that this perturbation depended on the quantity of adsorbate added to clay samples. Figure 4.4-Figure 4.6 show VT-DRIFTS difference spectra representing infrared spectral changes that occurred between ambient temperature and 60 ^{o}C for samples containing various adsorbate loadings. Like the neat clay samples, TG-MS analyses of adsorbate containing samples confirmed that mass loss occurred exclusively by dehydration.

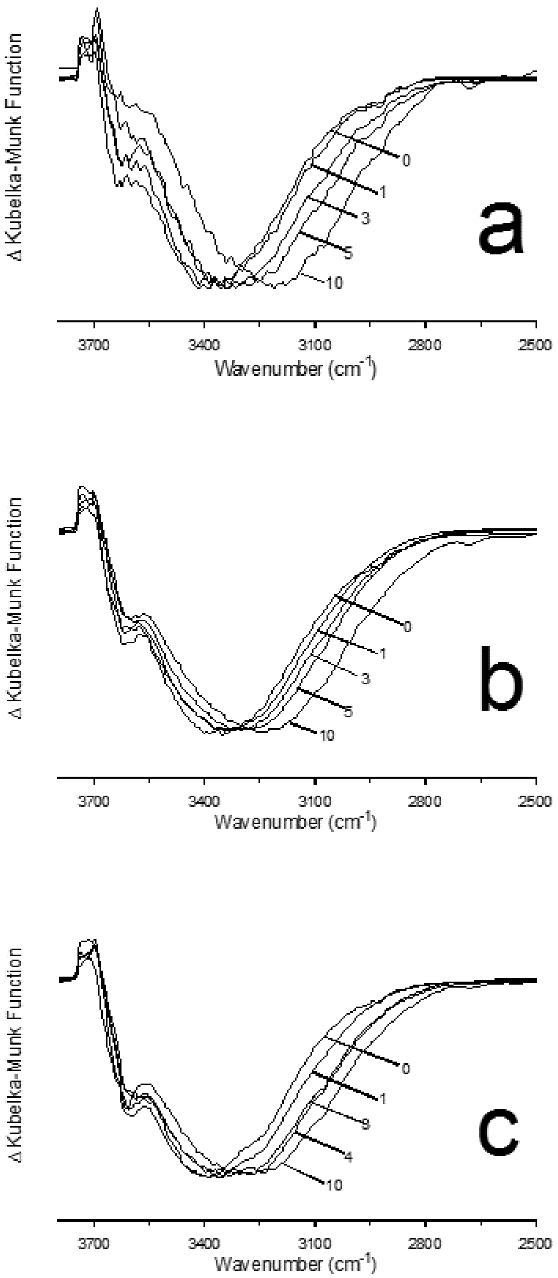

Figure 4.4 - Effects of benzoic acid loading on 60 °C – ambient temperature VT-DRIFTS difference spectra for samples containing: a) KMMT, b)NaMMT, and c) CaMMT. Numbers denote adsorbate percentages (w/w).

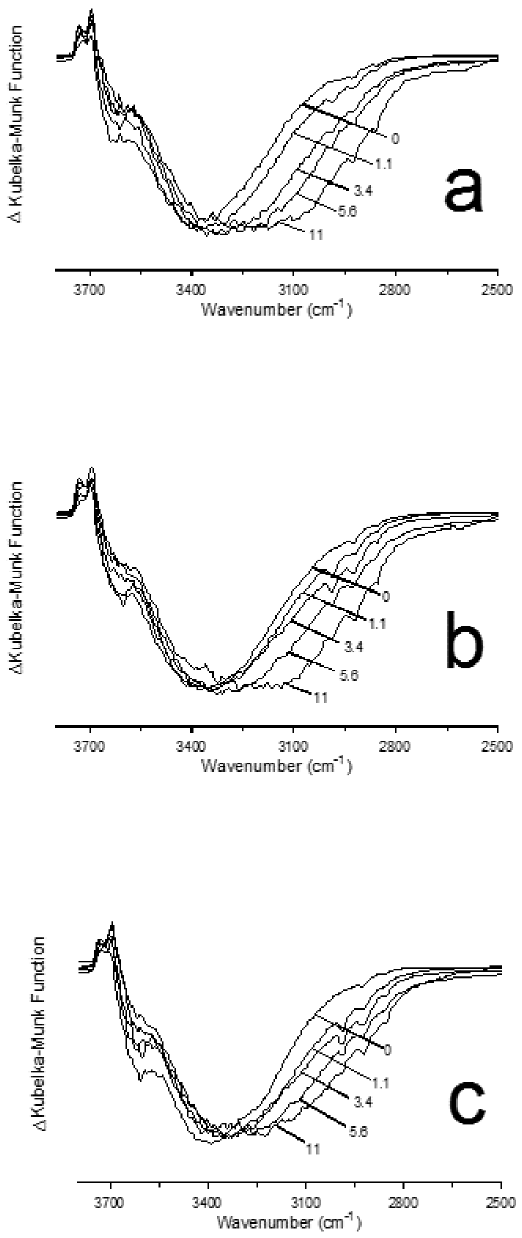

Figure 4.5 - Effects of salicylic acid loading on 60 ºC – ambient temperature VT-DRIFTS difference spectra for samples containing: a) KMMT, b) NaMMT, and c) CaMMT. Numbers denote adsorbate percentages (w/w).

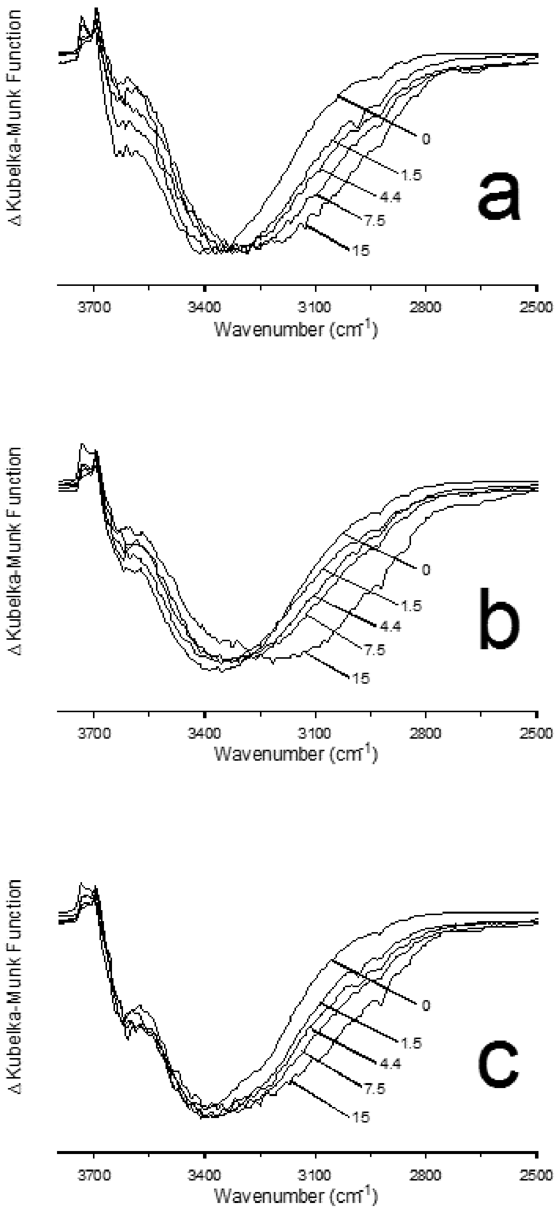

Figure 4.6 - Effects of acetylsalicylic acid loading on 60 ºC – ambient temperature VT-DRIFTS difference spectra for samples containing: a) KMMT, b) NaMMT, and c) CaMMT.Numbers denote adsorbate percentages (w/w).

Difference spectra shown in Figure 4.4-Figure 4.6 were normalized with respect to negative O-H stretching vibration band minima so that band shape differences were more apparent. For all samples, increased adsorbate loadings resulted in a greater shift of the negative O-H stretching vibration band to lower wavenumbers, indicating a correlation between enhanced water molecule hydrogen bonding and adsorbate content.

Figure 4.7-Figure 4.15 show plots of the same normalized VT-DRIFTS difference spectra shown in Figure 4.4-Figure 4.6, but for the C=O stretching vibration band region. Each Figure consists of two plots. The overlaid plots shown at the top of these Figures reflect the effect of adsorbate quantities on C=O band shape changes. Graphs at the bottom of each figure show how difference spectra change with temperature for samples containing the highest adsorbate loadings. Negative bands at 1630 cm^{-1}, corresponding to loss of water bending vibrations, were the only spectral features detected for neat clay samples (i.e. 0% loading results) in this wavenumber region. The 1630 cm^{-1} band remained relatively unchanged in spectra obtained for samples containing the lowest adsorbate loadings, but changed shape and shifted in spectra obtained for samples containing higher adsorbate loadings. For the benzoic acid/KMMT sample (Figure 4.7a), systematic changes to C=O stretching vibration bands were apparent for loadings of 3-10%. Negative features with minima located at 1678 cm^{-1} and positive features maximizing at 1722 cm^{-1} increased in magnitude with increasing adsorbate loadings. This “first derivative” peak shape is the result of a blue shift in the C=O stretching vibration band wavenumber caused by heating the sample. Although the magnitudes of negative and positive C=O stretching vibration band difference spectra features can be correlated with adsorbate loading, the band wavenumber shift was relatively constant. This suggests that the nature of molecular interactions responsible for these C=O bands did not change, and that the number of

adsorbate molecules involved in these interactions increased with higher benzoic acid loadings.

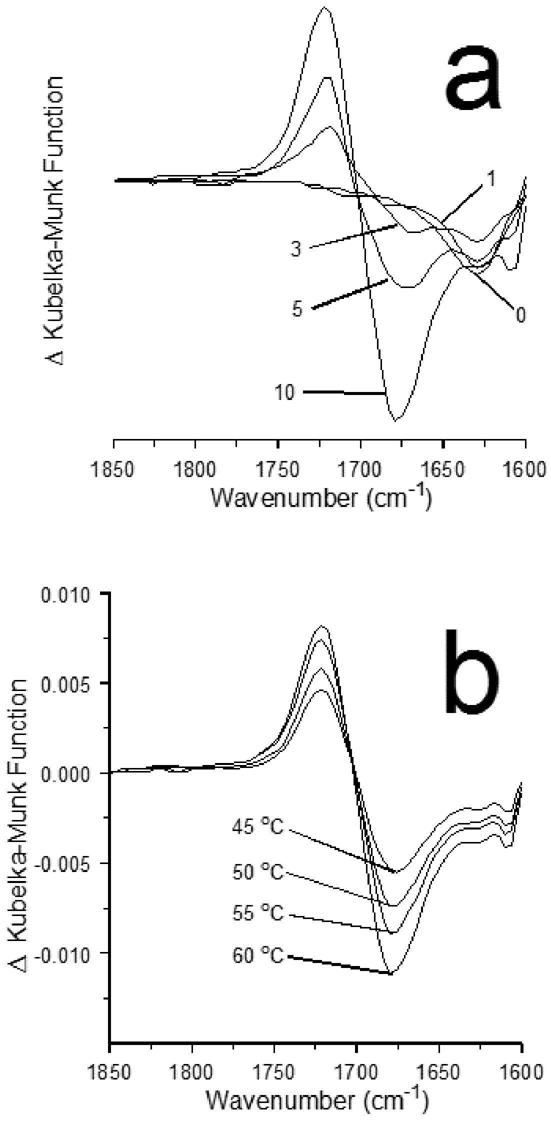

Figure 4.7 - Effects of a) benzoic acid loading (numbers denote w/w percentages) on normalized 60 °C – ambient temperature spectra and b) 60 °C water desorption temperature for the 10% benzoic acid/KMMT sample on VT-DRIFTS C=O stretching vibration band region difference spectra.

Figure 4.7b shows that these trends were also evident for the 10% benzoic acid/KMMT sample as a function of increasing temperature. Apparently, increasing water loss for this sample resulted in a consistent blue shift of the C=O stretching vibration wavenumber, most likely indicating a decrease in adsorbate hydrogen bonding interactions.

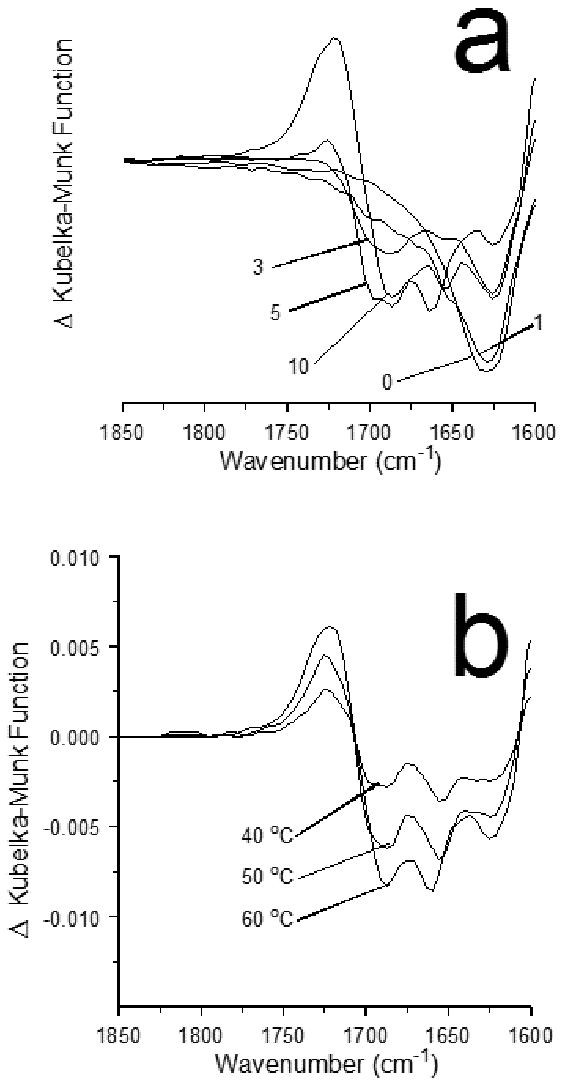

Figure 4.8 - Effects of a) benzoic acid loading (numbers denote w/w percentages) on normalized 60 ºC – ambient temperature spectra and b) 60 ºC water desorption temperature for the 10% benzoic acid/NaMMT sample on VT-DRIFTS C=O stretching vibration band region difference spectra.

Similar trends are evident in spectra obtained for the benzoic acid/NaMMT sample (Figure 4.8) except that the negative C=O stretching vibration band was less intense and its shape was more dependent on adsorbate loading. For the 3% benzoic acid loading on NaMMT, the negative C=O stretching vibration band occurs near 1690 cm^{-1} but no positive feature is discernible. With 5% benzoic acid loading, the negative C=O stretching vibration band consisted of overlapping contributions with minima near 1693 and 1653 cm^{-1} and a small positive band maximized at 1725 cm^{-1}. Negative bands at the same wavenumbers were detected for the sample containing 3% benzoic acid, but the relative intensity for the 1653 cm^{-1} band was much lower than the 1693 cm^{-1} band. Results obtained for the 10% benzoic acid/NaMMT sample (Figure 4.8b) at 60 ^{o}C included greater positive band intensity with a maximum near 1720 cm^{-1} and overlapping negative bands with minima at 1688 and 1662 cm^{-1}. Band locations in difference spectra obtained for the sample containing 10% benzoic acid at 40 and 50 ^{o}C were similar to those obtained for samples containing 3 and 5% loadings. Thus, C=O stretching vibration band shape changes suggest that benzoic acid occupied at least two different environments prior to dehydration but adopted similar hydrogen bonding environments after water loss. Furthermore, the two initial environments are affected by adsorbate loading, with the 10% loading exhibiting a slight temperature-dependent shift in C=O band wavenumber. Adsorbate environment differences for samples containing KMMT and NaMMT are likely due to the increased interlayer spacing for NaMMT, allowing for greater flexibility in adsorbate orientations.

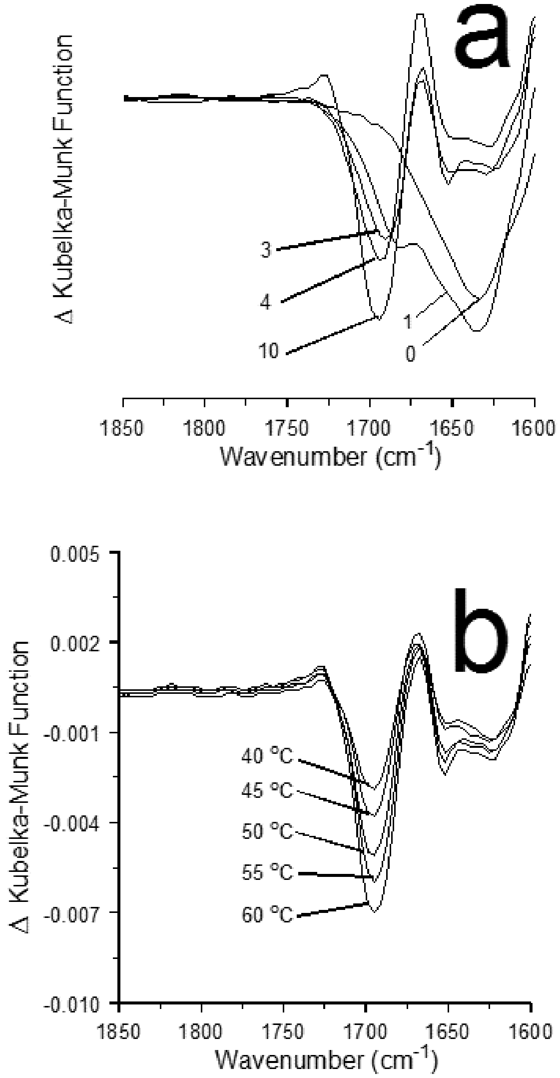

Figure 4.9 – Effects of a) benzoic acid loading (numbers denote w/w percentages) on normalized 60 °C – ambient temperature spectra and b) 60 °C water desorption temperature for the 10% benzoic acid/CaMMT sample on VT-DRIFTS C=O stretching vibration band region difference spectra.

Difference spectra shown in Figure 4.9a exhibit a single negative C=O stretching vibration band near 1694 cm^{-1} in spectra obtained for the 4 and 10% benzoic acid/CaMMT samples and positive features above and below the negative band location for the sample containing 10% adsorbate. This shape may be explained by the formation of a positive C=O stretching vibration band at 60 °C that was broader but had lower absorptivity than the corresponding ambient temperature band. The shapes exhibited in Figure 4.9 would be expected as a result of subtracting these overlapping features. Figure 4.9b shows that this shape is maintained while heating the 10% benzoic acid/CaMMT sample. Thus, for this sample, the main changes to the C=O stretching vibration caused by sample dehydration involve a decrease in absorptivity and a slight broadening of the absorbance band.

Difference spectra representing the dehydration of samples containing salicylic acid and KMMT (Figure 4.10) indicate that the C=O stretching vibration of affected acid functionalities shifted from about 1660 $cm^{-1}$to environments characterized by C=O band maxima at 1725 and 1695 cm^{-1}. The results obtained for salicylic acid/NaMMT samples (Figure 4.11) were very similar to those obtained for samples containing KMMT. Results for KMMT and NaMMT suggest that a single salicylic acid environment characterized by a relatively high degree of hydrogen bonding interactions is replaced by at least two new environments having much less hydrogen bonding interactions when water is driven off from these samples.

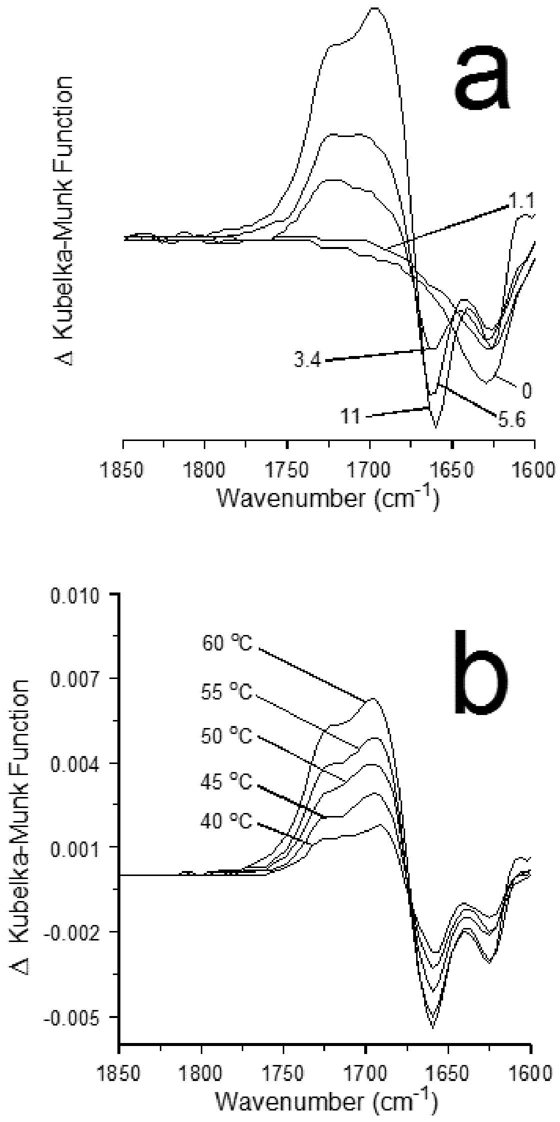

Figure 4.10 - Effects of a) salicylic acid loading (numbers denote w/w percentages) on normalized 60 °C – ambient temperature spectra and b) 60 °C water desorption temperature for the 11% salicylic acid/KMMT sample on VT-DRIFTS C=O stretching vibration band region difference spectra

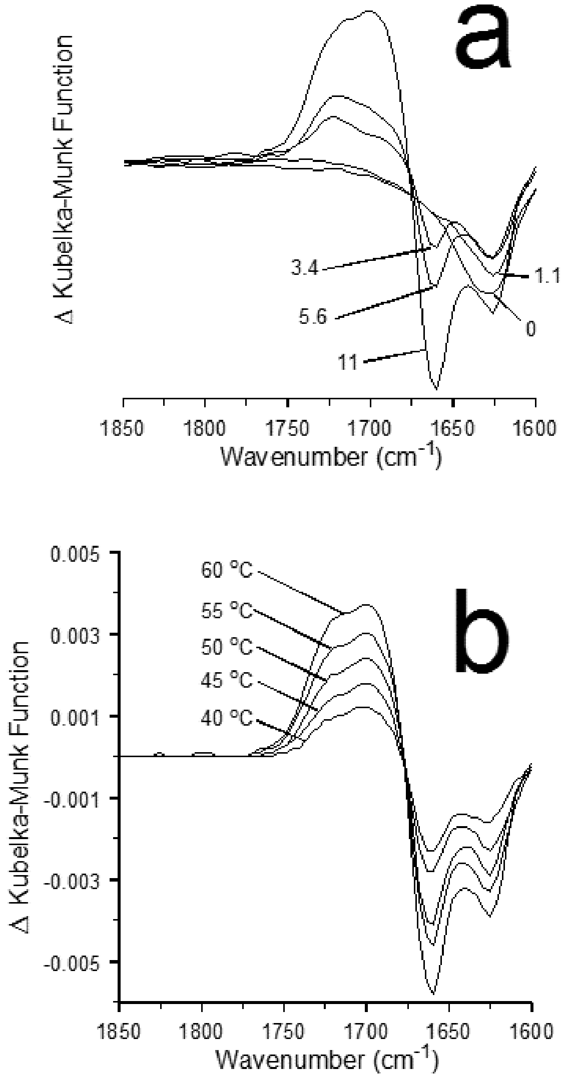

Figure 4.11 - Effects of a) salicylic acid loading (numbers denote w/w percentages) on normalized 60 ºC – ambient temperature spectra and b) 60 ºC water desorption temperature for the 11% salicylic acid/NaMMT sample on VT-DRIFTS C=O stretching vibration band region difference spectra.

Results obtained for salicylic acid/CaMMTsamples with loadings of 3.4 and 5.6% (Figure 4.12) were similar to those obtained for samples containing KMMT and NaMMT. However, for the sample containing 11% adsorbate, the positive C=O stretching vibration band contribution at 1687 cm^{-1} was much greater than the higher wavenumber contribution. Figure 4.12b shows that this effect was observed throughout sample dehydration. Apparently, compared to the samples with 3.4 and 5.6% salicylic acid loadings, the higher 11% loading caused a change in adsorbate environment after dehydration that was characterized by a dramatic increase in absorptivity at 1687 cm^{-1}.

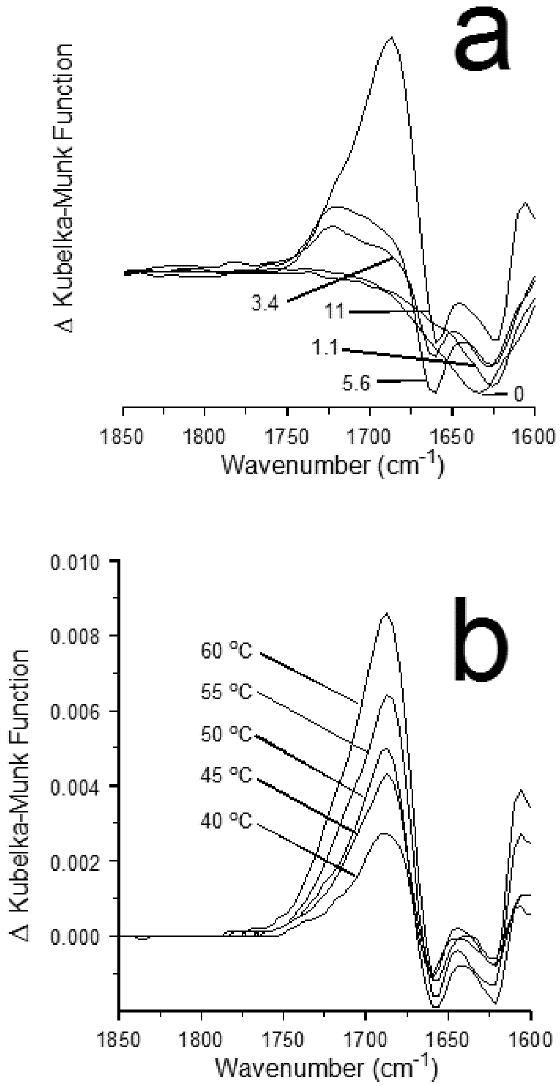

Figure 4.12 - Effects of a) salicylic acid loading (numbers denote w/w percentages) on normalized 60 ºC – ambient temperature spectra and b) 60 ºC water desorption temperature for the 11% salicylic acid/CaMMT sample on VT-DRIFTS C=O stretching vibration band region difference spectra.

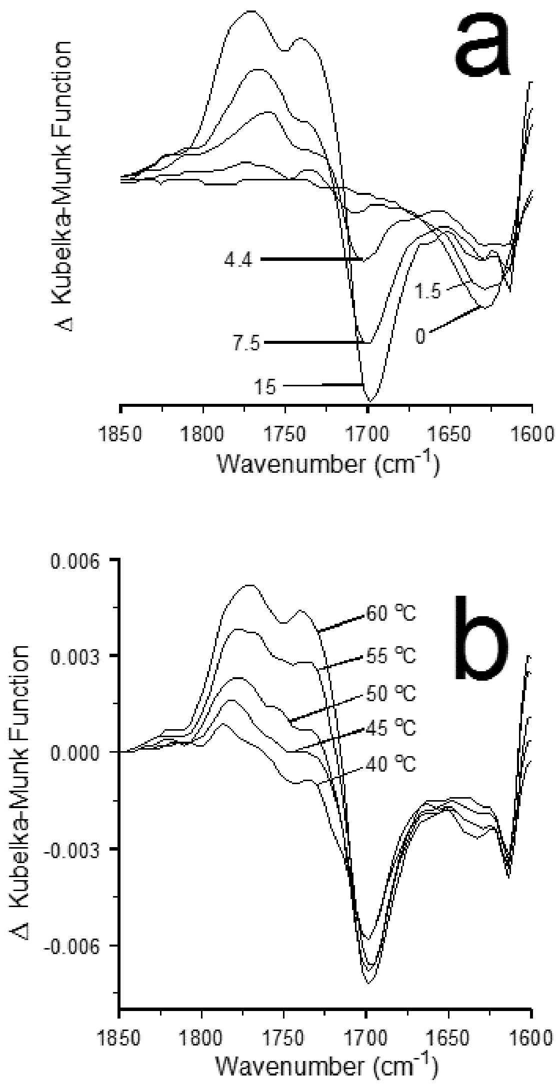

Figure 4.13 - Effects of a) acetylsalicylic acid loading (numbers denote w/w percentages) on normalized 60 ºC – ambient temperature spectra and b) 60 ºC water desorption temperature for the 15% acetylsalicylic acid/KMMT sample on VT-DRIFTS C=O stretching vibration band region difference spectra.

The shapes of difference spectra obtained for acetylsalicylic acid/KMMT samples (Figure 4.13) were similar to those obtained for salicylic acid/KMMT samples (Figure 4.10), exhibiting a single negative C=O band and two overlapping positive features at higher wavenumbers. However, the negative band (1698 cm^{-1}) and the overlapping positive features (1772 and 1738 cm^{-1}) were located at higher wavenumbers. This may be explained by the fact that acetylsalicylic acid molecules cannot form intramolecular hydrogen bonds like salicylic acid. The lack of this hydrogen bonding contribution would lead to higher C=O stretching vibration band wavenumbers for acetylsalicylic acid compared to salicylic acid. The intensity for the lower wavenumber contribution of the overlapping positive features became more intense with increasing adsorbate loading. Figure 4.13b shows that the intensity of the negative C=O stretching vibration band is less variable as a function of temperature compared to the positive features. This could result from a gradual shift in the 1738 cm^{-1} feature to lower wavenumber with increasing temperature, which would increasingly cancel more of the negative C=O band intensity. Results obtained for acetylsalicylic/NaMMT samples (Figure 4.14) were similar to those obtained for acetylsalicylic acid/KMMT samples, except that the positive features consisted of three overlapping contributions (1774, 1756, and 1734 cm^{-1}). Like the results obtained for samples containing KMMT, the relative intensity for the low wavenumber positive band component increased with increasing adsorbate loading and the negative feature intensity did not change with temperature as much as the overlapping positive features. In fact, increased intensity for the positive band canceled some of the negative band intensity for the 15% sample loading, causing it to be smaller and appear to shift to lower wavenumber relative to the 7.5% loading results (Figure 4.14a). Negative C=O stretching vibration bands in temperature-dependent spectra obtained for the 15% acetylsalicylic acid/NaMMT sample were much broader and less well defined than those obtained for the samples containing 4.4 and 7.5% adsorbate. Thus, for sample loadings below 15%, C=O stretching vibration band shape changes are consistent with a single initial adsorbate environment that becomes multiple environments after dehydration. In contrast, 15% sample loading results suggest that many adsorbate environments exist at ambient temperature, but that they change into environments with adsorbate interactions similar to those detected for the lower adsorbate loadings after dehydration.

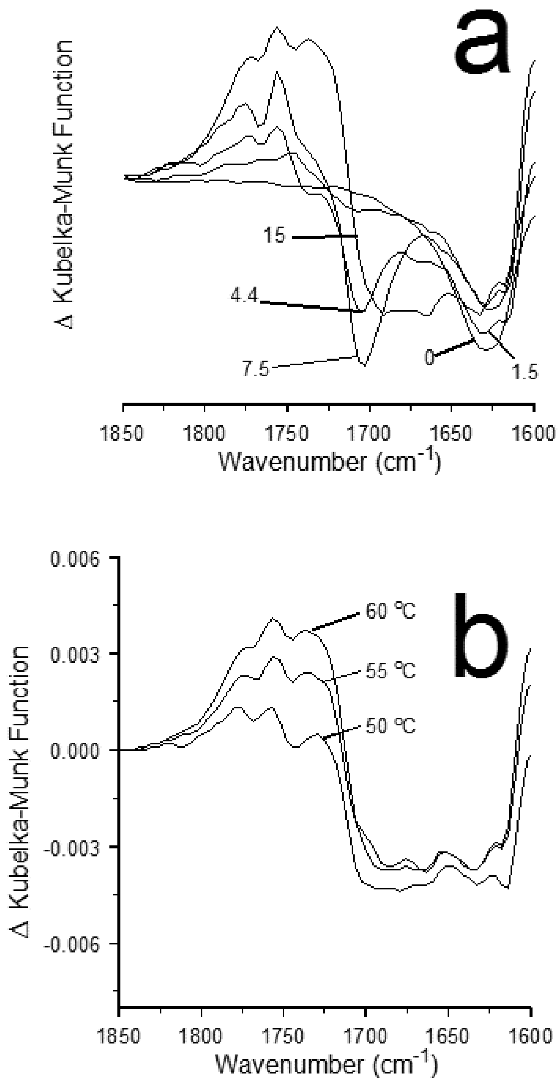

Figure 4.14 - Effects of a) acetylsalicylic acid loading (numbers denote w/w percentages) on normalized 60 °C – ambient temperature spectra and b) 60 °C water desorption temperature for the 15% acetylsalicylic acid/NaMMT sample on VT-DRIFTS C=O stretching vibration band region difference spectra.

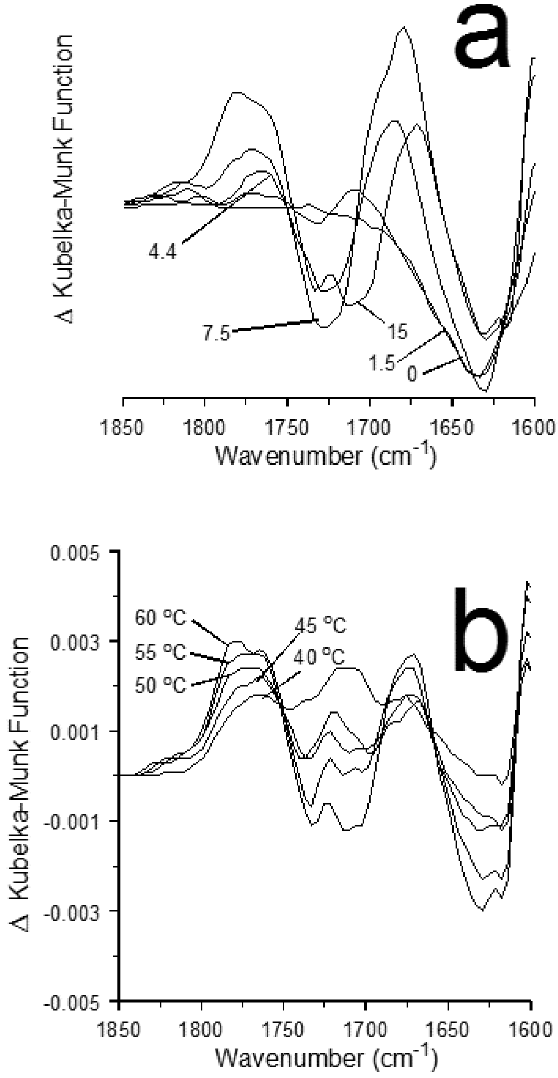

Figure 4.15 - Effects of a) acetylsalicylic acid loading (numbers denote w/w percentages) on normalized 60 °C – ambient temperature spectra and b) 60 °C water desorption temperature for the 15% acetylsalicylic acid/CaMMT sample on VT-DRIFTS C=O stretching vibration band region difference spectra.

Overall, trends in difference spectra found for acetylsalicylic acid/CaMMT samples (Figure 4.15) were similar to those observed for benzoic acid/CaMMT samples. Broad positive bands cancel much of the negative C=O stretching vibration band, leaving only residual positive intensity on either side of the negative band. However, this effect was more dramatic for the acetylsalicylic acid/CaMMT samples than for the benzoic acid/CaMMT samples. Figure 4.15b shows that a small positive band is superimposed on the negative C=O band near 1720 cm^{-1}. This may represent the band maximum of a positive feature that is not completely canceled by the negative band. Figure 4.15b shows that the maximum of this positive residual shifts to higher wavenumber with increasing temperature.

Figure 4.16 shows O-H stretching vibration region difference spectrum overlays for samples containing the highest adsorbate loadings on each clay. Whereas negative band minima were found near 3400 cm^{-1} for neat clay samples, minima for samples containing KMMT and NaMMT were found about 200 cm^{-1} lower. For samples containing CaMMT, minima occurred at higher wavenumbers, but were still below 3400 cm^{-1}. In addition, although the negative O-H stretching vibration band loss for the neat clays was detected above 2800 cm^{-1}, absorbance loss for samples containing adsorbate extended below 2800 cm^{-1}. With the exception of the benzoic acid/NaMMT sample, the 3740 cm^{-1} positive feature was absent in difference spectra. This suggests that the neat clay inorganic oxide hydroxyl groups that lost hydrogen bonding partners and shifted vibration wavenumbers to 3740 cm^{-1} remained hydrogen bonded at 60 ^{o}C when samples contained adsorbate. It is likely that these hydroxyl groups preferentially hydrogen bonded to adsorbate rather than water molecules. For each adsorbate, results obtained for samples containing KMMT and NaMMT were the most similar, and broad negative band minima occurred at higher wavenumbers in spectra obtained for samples containing CaMMT compared to the other clays. This trend may be associated with the fact that CaMMT contains a divalent cation whereas KMMT and NaMMT cations are monovalent. Alternatively, the shift to higher wavenumber for samples containing

CaMMT may be associated with the higher water content of CaMMT compared to KMMT and NaMMT. A larger fraction of the adsorbate/CaMMT sample interlayer water molecules may occupy environments that are more similar to those in neat CaMMT.

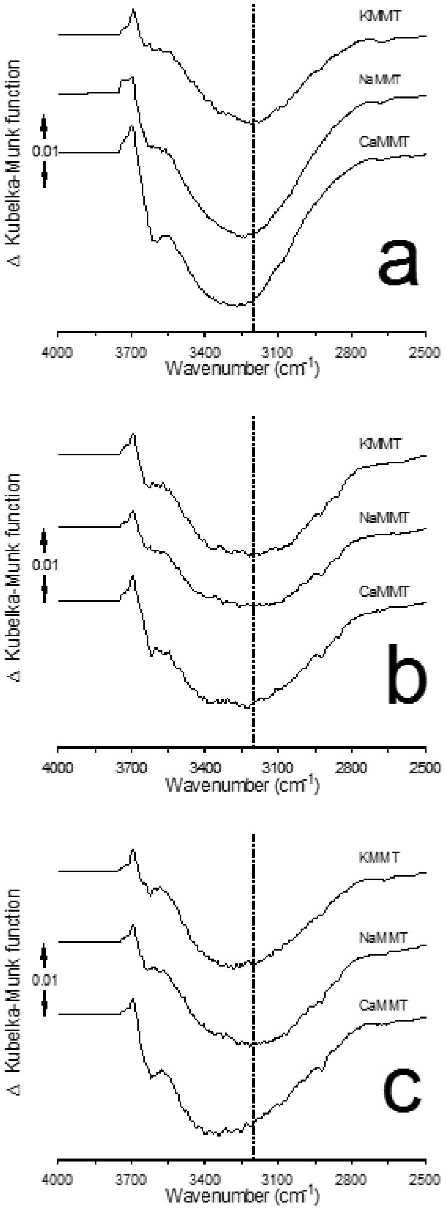

Figure 4.16 - Difference spectra obtained by subtracting the ambient temperature VT-DRIFTS spectrum from the spectrum obtained at 60 °C for samples consisting of (a) 10% benzoic acid, (b) 11% salicylic acid, and (c) 15% acetylsalicylic acid adsorbed on the designated clays. The dotted line denotes 3200 cm^{-1}.

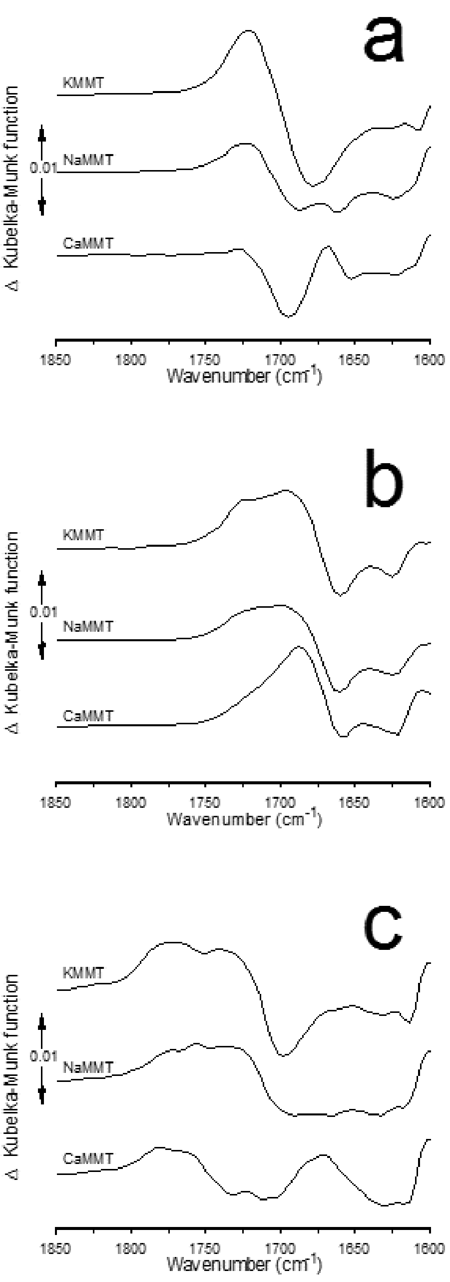

Figure 4.17 - Difference spectra obtained by subtracting the ambient temperature VT-DRIFTS spectrum from the spectrum obtained at 60 °C for samples consisting of (a) 10% benzoic acid, (b) 11% salicylic acid, and (c) 15% acetylsalicylic acid adsorbed on the designated clays.

TG-MS analyses of samples containing adsorbates showed that mass loss below 60 °C did not involve adsorbate desorption or decomposition processes (Chapter 3). Thus, infrared spectral changes detected between ambient temperature and 60 °C cannot be attributed to adsorbate loss. Instead, spectral variations must be attributed to changes in adsorbate local environments due to loss of water molecules. Figure 4.17 shows overlays of difference spectra spanning the C=O stretching vibration band range for samples containing the highest adsorbate loadings on each clay. Although the C=O stretching vibration band center locations before (i.e. at ambient temperature) and after (i.e. at 60 ^{o}C) sample dehydration for the benzoic acid/KMMT sample cannot be determined accurately, the minimum wavenumber for this band before water loss was 1678 cm^{-1} and the maximum band center wavenumber after the shift was 1720 cm^{-1}. The C=O stretching vibration band shift from ~1678 to ~1720 cm^{-1} resulted from a loss of hydrogen bonding for the aromatic acid functionality due to dehydration. For the sample containing benzoic acid adsorbed on NaMMT, the negative C=O stretching vibration difference spectrum component exhibits two overlapping minima at 1662 and 1687 cm^{-1}, but the positive feature occurs at 1720 cm^{-1}, which is the same as for the benzoic acid/KMMT sample. This suggests that there were initially two distinct benzoic acid hydrogen bonding environments which, after water desorption, adopted a hydrogen bonding environment that was similar to the dehydrated benzoic acid/KMMT sample. Compared to samples containing KMMT and NaMMT, the benzoic acid/CaMMT C=O functionality was involved in less intense hydrogen bonding. Therefore, the C=O stretching vibration band wavenumber did not shift as much after dehydration.

Figure 4.17b shows that the C=O stretching vibration band shifts for samples containing salicylic acid and clays with monovalent cations (KMMT and NaMMT) were similar, but differed significantly from spectra obtained for samples containing benzoic acid (Figure 4.17a). Negative bands representing C=O stretching vibrations prior to water loss exhibited minima at 1660 cm^{-1} for both samples. Positive spectral features were broad, extended to 1750 cm^{-1}, and consisted of overlapping contributions, suggesting that salicylic acid molecules adopted at least two different environments after water desorption. For the salicylic acid/CaMMT sample, the negative C=O stretching vibration band minimum also appeared at 1660 cm^{-1}. However, unlike the monovalent clays, the blue shift due to water loss resulted in a sharper feature with maximum intensity at 1687 cm^{-1}. Thus, salicylic acid samples exhibited the same general trend as the benzoic acid samples, in which the C=O stretching vibration band shift was less when divalent Ca^{2+} was present compared to K^+ and Na^+.

Difference spectra representing C=O stretching vibration band changes resulting from heating clay samples containing acetylsalicylic acid are shown in Figure 4.17c. The negative C=O stretching vibration band location for the sample containing KMMT was at 1698 cm^{-1}, which was much higher than in difference spectra obtained for benzoic acid and salicylic acid. This indicates that acetylsalicylic acid C=O functionalities affected by the water loss were involved in less intense hydrogen bonding than either benzoic acid or salicylic acid. Like the results obtained for salicylic acid, the positive difference spectrum feature representing adsorbate environments after dehydration consisted of at least two broad overlapping features. However, the positive band intensity extended to higher wavenumbers (1800 cm^{-1}) compared to the corresponding salicylic acid/KMMT spectrum (1750 cm^{-1}). Peak maxima for the two overlapping band components occurred at 1740 and 1770 cm^{-1}. Thus, compared to benzoic acid and salicylic acid, acetylsalicylic acid was involved in weaker hydrogen bonding interactions before water desorption and adopted orientations that also involved weaker hydrogen bonding interactions after dehydration. Results obtained for acetylsalicylic acid adsorbed on NaMMT were qualitatively similar to those for the KMMT sample, except that the negative C=O stretching vibration band was very broad. The difference spectrum obtained for the sample containing acetylsalicylic acid and CaMMT contained overlapping negative features with minima at 1710 and 1732 cm^{-1} corresponding to C=O stretching vibrations that were lost due to sample dehydration. The corresponding overlapping positive C=O stretching vibration bands were located at 1760 and 1780 cm^{-1}. Thus, the difference spectrum for the acetylsalicylic acid/CaMMT sample indicated that adsorbate hydrogen bonding interactions were weaker for this adsorbate/clay combination than any of the others.

Liquid water consists of a dynamic hydrogen bonding network in which typical water molecules participate in 2-4 hydrogen bonds.[98-101] However, the properties of confined water differ from the bulk liquid.[98] In particular, cation hydration sphere characteristics are significantly perturbed when water molecules are restricted to movement in two dimensions.[102, 103] Clay interlayer water molecules can be categorized into three types of local environments. Some molecules are found near inorganic oxide layers, some occupy cation hydration spheres, and others fill voids.[104] In addition to interactions between water molecules and inorganic oxide surfaces or cations, interlayer water molecules participate in hydrogen bonding with other water molecules. The broad negative O-H stretching vibration bands in VT-DRIFTS difference spectra (Figure 4.3) reflect the net results of changes to interlayer water molecules caused by heating samples from ambient temperature to 60 ^{o}C. Much of this negative band intensity can be attributed to water molecule desorption. However, O-H stretching vibration band properties may change for water molecules that remain with the clay if they experience local environment variations, such as: loss of hydrogen bonding, gain in hydrogen bonding, and variations in the strength of interactions with inorganic oxide layers and cations. In fact, the positive difference spectra features at 3696 and 3740 cm^{-1} are evidence of a disruption of interactions between water molecules and inorganic oxide hydroxyl groups. Thus, loss of water molecules during sample heating initiates a reorganization of the remaining interlayer water molecules. The similarity of difference spectra shapes in Figure 4.3 suggests that mechanisms for water desorption and subsequent interlayer water reorganization are similar for the three clays, even though they initially contain different quantities of interlayer water.

4.3 Summary

The structures of benzoic acid, salicylic acid, and acetylsalicylic acid all contain an aromatic acid functionality. All three adsorbates readily form dimers by hydrogen bonding through these groups.[105-108] These aromatic carboxylic acid functionalities also participate in hydrogen bonding with interlayer water molecules and inorganic oxide hydroxyl groups.[109] In addition, the hydroxyl and acetyl groups in salicylic acid and acetylsalicylic acid provide additional sites for hydrogen bonding.[105, 109] When placed within montmorillonite interlayer spaces, these adsorbates disrupt the hydrogen bonding network, which affects water molecule O-H stretching vibration band properties. In general, hydrogen bond formation alters O-H stretching vibration band characteristics by increasing absorptivity (i.e. intensity), increasing band width, and shifting absorbance maxima to lower wavenumber.[110-112] Comparing difference spectra shown in Figure 4.4-Figure 4.6 with those in Figure 4.3 reveals that the presence of adsorbate molecules caused a general shift in water molecule O-H stretching vibration to lower wavenumber, suggesting that hydrogen bonding interactions were enhanced.

Whereas variations in O-H stretching vibration wavenumbers provide information regarding trends in water molecule hydrogen bonding interaction strengths, shifts in C=O stretching vibration wavenumbers provide more specific information regarding changes in adsorbate local environments. Results shown in Figure 4.17 indicate that the salicylic acid C=O functionality is involved in greater hydrogen bonding interactions compared to the other two adsorbates. This is most likely due to intramolecular hydrogen bonding between the aromatic hydroxyl functionality and carboxylic acid group.[105] This intramolecular hydrogen bonding is also apparent after sample dehydration, resulting in positive C=O stretching vibration band features that occur at lower wavenumbers than the other adsorbates.

Chapter 5 : Thermogravimetry-Mass Spectrometry Investigations of Salicylic Acid and Acetylsalicylic Acid Desorption from Montmorillonite Clays

5.1 Introduction

Results described here detail TG-MS studies of salicylic acid and acetylsalicylic acid desorption from potassium, sodium, and calcium montmorillonite clays, as well as desorption of benzoic acid from potassium montmorillonite. TG-MS analyses are used to identify volatiles evolved during sample heating. This information can be used to characterize desorption and decomposition processes effected by sample heating. Comparisons are made between the behaviors of these three aromatic acid adsorbates, and the effect of the interlayer cation is explored as well.

5.2 Results and Discussion

Nickels, *et al*. [67] studied the interactions between benzoic acid adsorbate and montmorillonites containing sodium and calcium cations. To better understand the importance of cation charge and water content on adsorbate-clay interactions, those studies were extended by characterizing benzoic acid interactions with potassium montmorillonite. Potassium ions fit better than sodium ions into inorganic clay layer hexagonal voids, so that less of the ion surface area is available for adsorbate interactions.[65, 66] Although potassium and sodium cations are both monovalent, sodium ions are more polarizing.[64] Thus, water molecules in sodium ion hydration spheres should be more stable than those surrounding potassium ions. The introduction of potassium to clay interlayer spaces reduces basal spacing, so that less water can be accommodated by the clay. Thus, adsorbate-clay effects related to water content may be apparent after comparing analysis results obtained from samples containing sodium and potassium montmorillonites.

Results from TG-MS analysis of a sample consisting of potassium montmorillonite (KMMT) containing 10% (w/w) benzoic acid are shown in Figure 5.1. Mass spectrometric signals for molecular ions representing water (m/z 18), carbon dioxide (m/z 44), benzene (m/z 78), and benzoic acid (m/z 122) are plotted as a function of sample temperature. Below about 100 °C, water desorption was the only significant process responsible for mass loss. Intact benzoic acid (m/z 122) began to desorb near 100 °C and reached a maximum evolution rate at 151 °C. The m/z 122 ion signal temperature profile also exhibited a broad, less intense feature between 250 and 450 °C. Above 400 °C, some benzoic acid decomposed to form benzene and carbon dioxide. The m/z 78 (benzene) ion signal temperature profile maximized at 436 °C, and m/z 44 (CO_2) maximized at 471 °C. The m/z 78 ion signal temperature profile exhibits a local maximum at 151 °C, which coincides with the m/z 122 ion signal maximum. The m/z 78 ion signal responsible for this local maximum does not reflect the presence of benzene in TG effluent. Instead, this ion signal is derived from benzoic acid fragmentation.

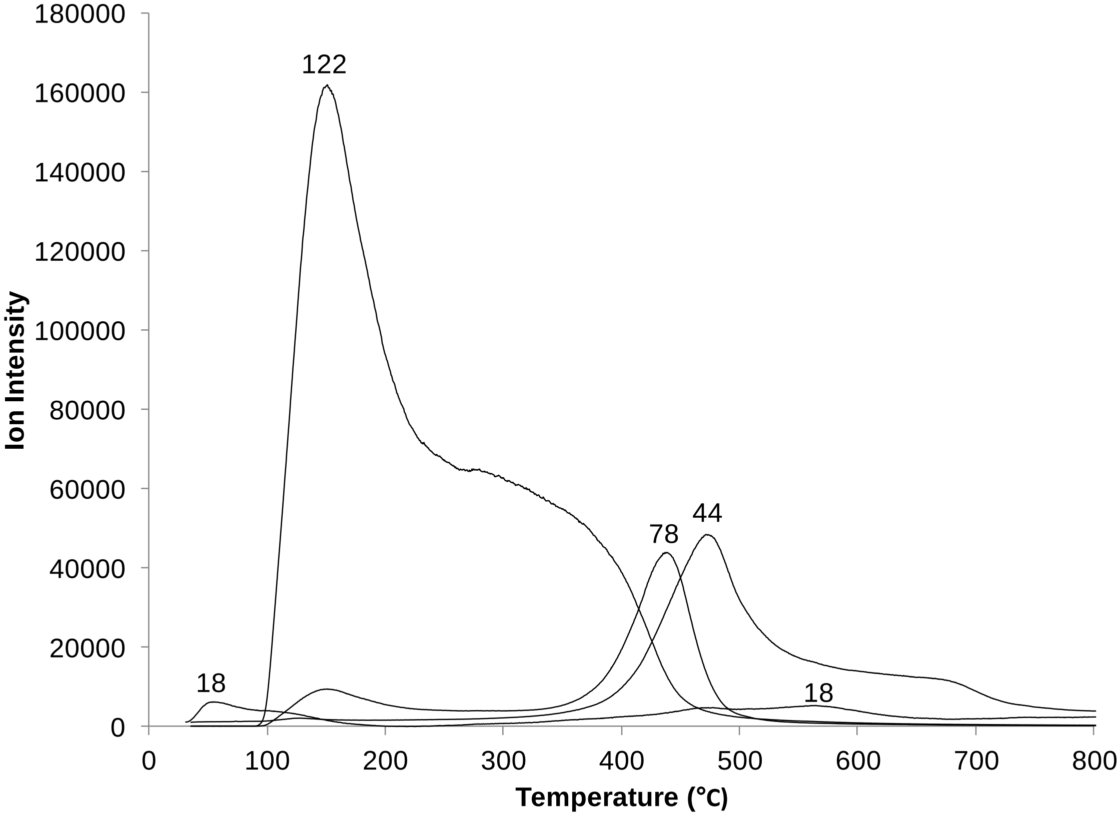

Figure 5.1 – Mass spectrometric ion signal intensity profiles representing water (m/z 18), benzoic acid (m/z 122), benzene (m/z 78), and carbon dioxide (m/z 44) measured during TG-MS analysis of a KMMT sample containing 10% benzoic acid.

The ion signal temperature profiles shown in Figure 5.1 have similar shapes to those previously reported for NaMMT samples containing 10% (w/w) benzoic acid.[67] This is not surprising, because sodium and potassium are both monovalent ions. Benzoic acid desorption began from both KMMT and NaMMT near 100 °C, but much higher temperatures were required for CaMMT, which contains divalent Ca^{2+}. These trends are in agreement with proposals from Nickels, *et al.*,[67] and others,[38, 41] who found that the charge on the interlayer cation is the determining factor for adsorrbate desorption temperatures. Figure 5.1 contains some interesting differences when compared to previous benzoic acid/NaMMT results. For example, the m/z 78 ion signal temperature profile above 300 ^{o}C is less intense relative to the other ion signal profiles than it was when a benzoic acid/NaMMT sample was analyzed under similar conditions.[67] In addition, the low temperature component of the m/z 122 profile in Figure 5.1 is more intense relative to the other ion signal profiles than it was for the benzoic acid/NaMMT sample.[67] It should be noted that the ion signal intensity values plotted in Figure 5.1 do not accurately reflect the concentrations of the corresponding species. In addition to vapor concentration, ion signal intensities depend on molecular ionization cross-sectional areas, ionization energies, and degree of fragmentation. Despite this limitation, significant changes to relative ion signal temperature profile intensities between samples reflect variations in the importance of competing desorption/decomposition pathways. More intense m/z 122 ion signals coupled with lower m/z 78 ion signals for the benzoic acid/KMMT sample compared to the benzoic acid/NaMMT sample indicate that more of the acid desorbed and less decomposed when the clay interlayer space contained potassium. Apparently, compared to NaMMT, a smaller amount of benzoic acid was retained on KMMT at temperatures high enough to facilitate decomposition. Mass loss results are in agreement with this assertion. Mass loss results for KMMT and NaMMT samples containing 10% benzoic acid are compared to those for the neat clays in Table 5.1. Mass losses are divided into three temperature intervals: room temperature (RT) – 100 °C, 100 – 400 °C, and 400 – 550 °C. The lowest temperature range corresponded primarily to water loss for all samples.

Table 5.1 - Comparison of mass loss data for KMMT containing 10% benzoic acid (this work) to mass loss data for NaMMT containing 10% benzoic acid from Nickels, *et al*.[67] Neat clay data are presented for comparison.

	Neat clays		**10% BA loaded clays**	
Temp Range	KMMT	NaMMT[67]	K MMT	NaMMT[67]
RT-100	0.8%	1.0%	0.9%	1.1%
100-400	1.2%	1.4%	7.5%	6.6%
400-550	1.4%	1.7%	2.7%	3.3%
Total	3.4%	4.1%	11.1%	11.0%

Consequently, mass losses for the neat clays were similar to those for samples containing benzoic acid adsorbate. Between 100 and 400 °C, which spans the temperature range corresponding to most benzoic acid desorption, the benzoic acid/KMMT sample lost 7.5% of its mass, whereas the benzoic acid/NaMMT sample lost only 6.6%. For reference, neat NaMMT lost 0.2% more mass than neat KMMT over this temperature range. As shown in Figure 5.1, benzene and carbon dioxide formed by benzoic acid decomposition dominated volatile products above 400 ^{o}C. The benzoic acid/KMMT sample lost only 2.7% of its mass above 400 ^{o}C, whereas the benzoic acid/NaMMT sample lost 3.3% (0.6% difference). For reference, neat NaMMT lost 0.3% more mass than neat KMMT over the same temperature range. Interestingly, neither benzoic acid/clay sample lost as much mass as would be predicted based on an initial 10% (w/w) loading. Assuming that benzoic acid/clay samples contained 90% of the water found in the corresponding neat clays (i.e. because 10% of the sample mass was due to adsorbate), the benzoic acid/KMMT sample lost about 8.0% and the benzoic acid/NaMMT sample lost about 7.3% of the sample mass that could be attributed to benzoic acid. Samples became darker after heating, possibly indicating char residue formation. In order to confirm that residual char was responsible for the darker sample color and the less than expected mass loss, a TG analysis of the 10% benzoic acid/KMMT sample was carried out in air instead of helium (Appendix C). Under these conditions, all benzoic acid should have been oxidized and therefore lost from the sample after heating it to 800 °C. A small sample size of ~2 mg was employed and solid material was evenly spread throughout the sample pan to maximize air exposure to clay surfaces. Under these experimental conditions and after compensating for water loss, the mass loss that could be attributed to benzoic acid was 9.8%, which was close to the expected 10%. This result confirms that the presence of thermally stable residue was the primary cause of the discrepancy between predicted and observed mass losses when samples were heated in helium.

The fact that the benzoic acid/KMMT sample lost more mass at lower temperatures as a result of benzoic acid desorption, whereas the benzoic acid/NaMMT sample lost more mass at higher temperatures through benzoic acid decomposition indicates that NaMMT facilitated greater retention of benzoic acid to high temperatures. This may be associated with a higher water content for NaMMT, and consequently a larger interlayer spacing.[63] The greater interlayer space may allow benzoic acid molecules to better align with interlayer cations, forming more thermally stable interactions.

For NaMMT and CaMMT, the temperature at which benzoic acid desorption begins was found to depend on adsorbate loading. [67] It was postulated that the most favorable adsorption environments were occupied first, and less favorable environments were populated only after favored adsorption sites were filled.[67] TG-MS results obtained for benzoic acid adsorbed on KMMT show a similar trend. Ion signal temperature profiles for benzoic acid (m/z 122; dashed line) and benzene (m/z 78; solid line) for KMMT samples containing various benzoic acid loadings are shown in Figure 5.2. The m/z 122 ion signal temperature profile consisted of at least two overlapping features. At the highest loading (10% (w/w) benzoic acid), the lower temperature component of the m/z 122 profile was the most significant feature. At a 5% loading of benzoic acid, the low temperature component of the m/z 122 ion signal temperature profile was significantly less intense, becoming comparable to the high temperature component. For the sample containing a 3% benzoic acid loading, the low temperature component of the m/z 122 ion signal temperature profile was less intense than the high temperature component. The m/z 122 ion signal temperature profile for the sample containing 1% benzoic acid was barely detected above the baseline, indicating that a small amount of intact benzoic acid desorbed from the clay. The m/z 78 ion signal temperature profile intensity above 300 ^{o}C decreased with decreasing benzoic acid loading, but changes were not as dramatic as they were for the m/z 122 profiles. Thus, for small benzoic acid loadings, most adsorbate occupies environments that are stable at higher temperatures, resulting in benzoic acid loss by decomposition rather than desorption. These findings suggest that there are at least three possible environments available to adsorbates, corresponding to: (1) benzoic acid that decomposes above 400 ^{o}C, (2) benzoic acid that desorbs between 200 and 425 ^{o}C, and (3) loosely held benzoic acid that desorbs between 100 and 200 ^{o}C. These findings are in agreement with the reported results of similar experiments for samples containing benzoic acid adsorbed on NaMMT and CaMMT.[67]

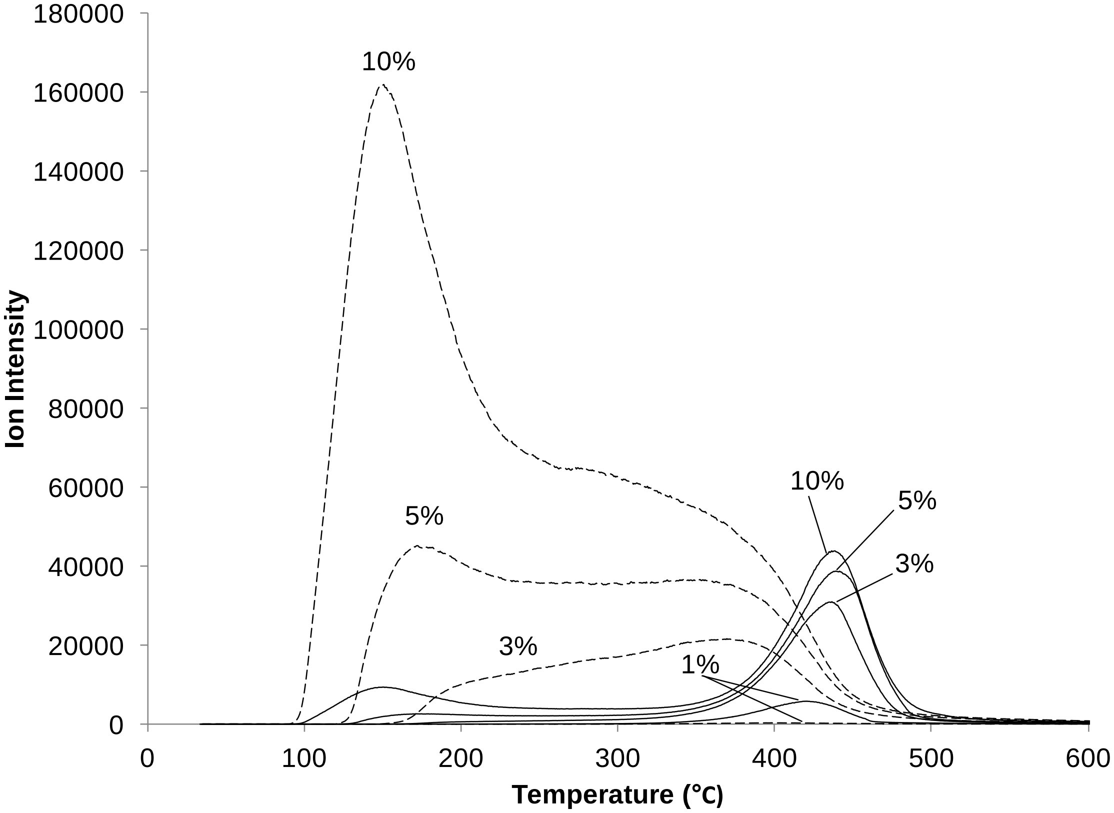

Figure 5.2 - MS profiles for benzoic acid (m/z 122; dashed line) and benzene (m/z 78; solid line) for KMMT samples containing various loadings of benzoic acid.

To determine if other aromatic acids interact with montmorillonites in a manner similar to benzoic acid, and to elucidate the effects of different functional groups on adsorption behavior, salicylic acid and acetylsalicylic acid were separately loaded onto potassium, sodium, and calcium montmorillonites and studied by using TG-MS. Ion signal temperature profiles for the most abundant volatiles evolved during TG-MS analyses of clay samples containing 11% (w/w) salicylic acid are shown in Figure 5.3. Salicylic acid loadings were selected to contain the same molar amounts of adsorbate as benzoic acid samples. Thus, an 11% (w/w) salicylic acid loading contains the same number of adsorbate molecules per gram of clay as a 10% (w/w) benzoic acid loading. Mass spectrometric ion signals representing water (m/z 18), carbon dioxide (m/z 44), phenol (m/z 94), and salicylic acid (m/z 120) are shown. With the exception of m/z 120, which corresponds to the salicylic acid mass spectrum base peak, ion signal temperature profiles were derived from molecular ions. The molecular ion for salicylic acid occurs at m/z 138, which was detected during TG-MS analyses of samples containing 5.6 and 11% (w/w) salicylic acid, but was below the detection limit for samples containing less salicylic acid. Figure 5.3a shows the results obtained for a KMMT sample containing 11% (w/w) salicylic acid. At temperatures below 80 °C, the only significant sample change could be attributed to loss of water, as evidenced by the fact that only the m/z 18 ion signal profile intensity exhibited non-zero values.

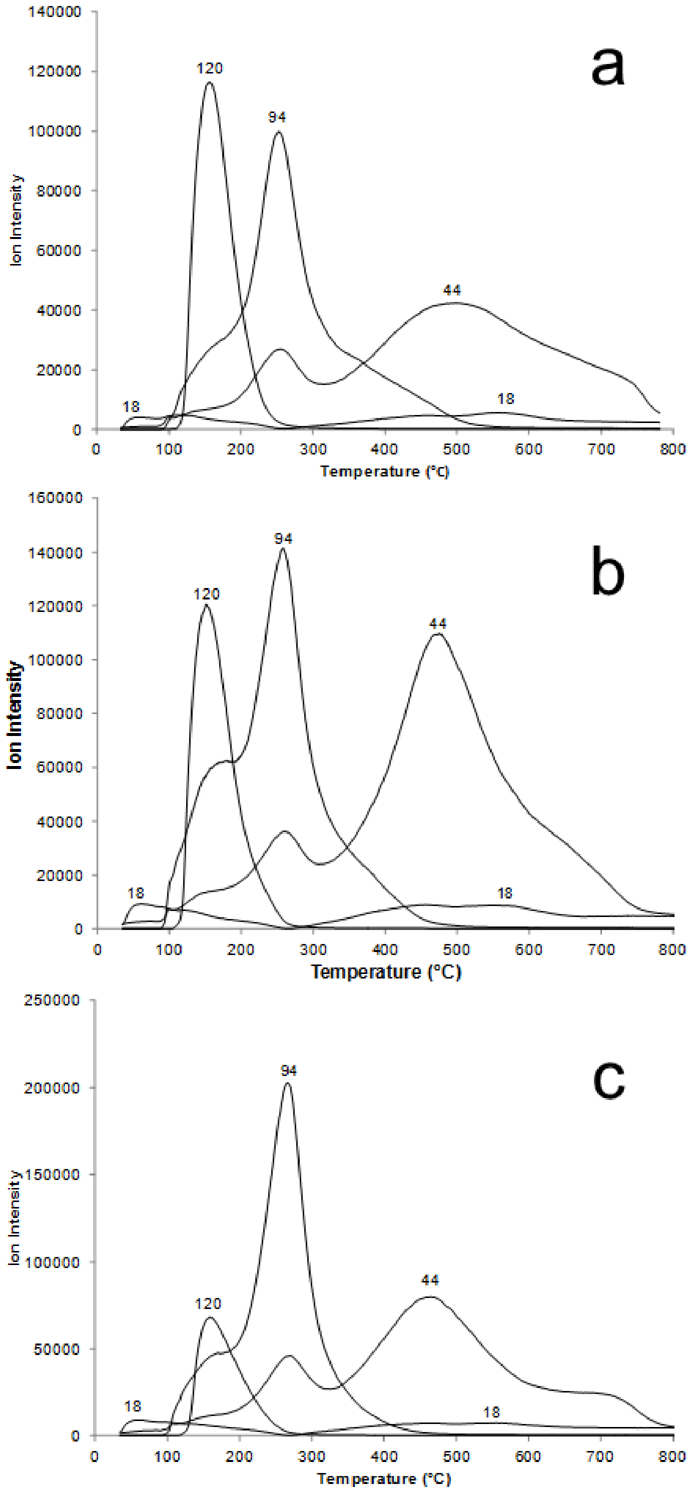

Figure 5.3 - MS ion signal intensity profiles representing water (m/z 18), salicylic acid (m/z 120), phenol (m/z 94), and carbon dioxide (m/z 44) measured during TG-MS analysis of a) KMMT, b) NaMMT, and c) CaMMT samples containing 11% salicylic acid.

Salicylic acid (m/z 120) began to desorb above 100 °C, and reached a maximum evolution rate at 153 °C. Interestingly, phenol (m/z 94) and carbon dioxide (m/z 44) were detected in TG effluent at temperatures below 100 ºC. These substances were likely formed by salicylic acid decomposition.[113, 114] TG-MS analyses of samples containing clays loaded with phenol revealed that it desorbed immediately after samples were heated, which was consistent with previous reports.[44, 115] Therefore, the appearance of m/z 94 in TG-MS mass spectra obtained while heating salicylic acid/clay samples can be used to track salicylic acid decomposition. Above 200 °C, salicylic acid decomposition competed with desorption, as evidenced by the increase in m/z 94 ion signal intensity, which maximized near 250 °C. Unlike the results obtained for benzoic acid, the overlap between the m/z 120 and m/z 94 ion signal temperature profiles shows that there was no temperature range over which adsorbate desorption occurred without some decomposition. Unlike phenol, carbon dioxide (m/z 44) desorption from clay surfaces was delayed. Although the m/z 44 ion signal temperature profile exhibited a local maximum near 250 °C, the profile shape consisted of a broad peak with global maximum just below 500 °C. According to Schaef, et al.,[116] carbon dioxide is not easily intercalated by clays that are excessively dehydrated or hydrated. Rather, a small amount of interlayer water is optimal for carbon dioxide retention. Apparently, carbon dioxide can be stabilized by interactions with interlayer cations, but if sufficient water is available, it can displace carbon dioxide from adsorption sites near cations. Thus, unlike phenol, carbon dioxide desorption temperatures depend on clay characteristics. This explains why m/z 44 ion signal maxima occur at similar temperatures for clay samples containing salicylic acid and benzoic acid (Figure 5.1).

Figure 5.3b shows results obtained for the NaMMT sample containing 11% (w/w) salicylic acid, which are similar to those for the KMMT sample containing the same salicylic acid loading. The most significant difference between results obtained for samples containing KMMT and NaMMT was in the m/z 120 ion signal profiles. Although the m/z 120 ion signal temperature profile maximum was greater than the m/z 94 profile for the KMMT sample, the opposite was observed for the NaMMT sample. This suggests that salicylic acid was more stable above 200 ^{o}C when adsorbed on NaMMT compared to KMMT. Greater thermal stabilization of salicylic acid by NaMMT is also supported by the mass loss results compiled in Table 5.2. Sample mass losses in three temperature intervals are provided: room temperature (RT) – 80 °C, 80 – 200 °C, and 200 – 650 °C.

Table 5.2 - Summary of mass loss data for salicylic acid loaded clay samples over selected temperature intervals (neat clay data are presented for comparison).

	Neat clays			**11% SA loaded clays**		
Temp range	KMMT	NaMMT	CaMMT	KMMT	NaMMT	CaMMT
RT-80	0.6%	0.9%	1.1%	0.7%	0.8%	1.0%
80-200	0.5%	0.7%	1.1%	5.1%	4.6%	4.4%
200-650	3.3%	3.3%	3.5%	7.7%	8.2%	9.6%
Total	4.4%	4.9%	5.7%	13.5%	13.6%	15.0%

Based on MS analysis of volatiles evolved while heating samples, water evolution was the only significant contribution to mass loss below 80 °C. Salicylic acid desorption occurred primarily between 80 and 200 °C, whereas, above 200 °C, mass loss could be attributed mostly to salicylic acid decomposition into phenol and carbon dioxide. The KMMT sample containing 11% (w/w) salicylic acid lost more mass in the 80 – 200 °C temperature range than the NaMMT sample (5.1 *vs*. 4.6 %). Conversely, the sample containing 11% (w/w) salicylic acid adsorbed on NaMMT lost more mass in the 200 – 650 °C range than the KMMT sample (8.2 *vs*. 7.7 %). Interestingly, the total mass losses (measured at 650 °C) for these two samples were about the same (13.5 % for KMMT *vs*. 13.6 % for NaMMT).

TG-MS results for the CaMMT sample containing 11% (w/w) salicylic acid are shown in Figure 5.3c. There are two significant differences between the ion signal temperature profiles for this sample and the KMMT and NaMMT samples containing the same amount of salicylic acid. First, salicylic acid began to desorb from CaMMT near 115 °C, which was 15 °C higher than for samples containing NaMMT and KMMT. This trend is consistent with results from a previous study of benzoic acid interactions with NaMMT and CaMMT, which found that benzoic acid began to desorb from CaMMT at 110 °C and from NaMMT at 100 °C.[67] This difference was attributed to stronger interactions between benzoic acid and Ca^{2+} ions because of the greater charge. It appears that salicylic acid desorption exhibits a similar effect. Secondly, the m/z 120 ion signal temperature profile intensity for the sample containing CaMMT is much smaller than the m/z 94 ion intensity. This suggests that the CaMMT interlayer environment inhibits salicylic acid desorption more than the other clays. This trend is corroborated by mass loss results (Table 5.2). The CaMMT sample containing 11% (w/w) salicylic acid lost 4.4 % mass in the 80 – 200 °C temperature range, which is less than the mass lost by the NaMMT sample containing the same amount of salicylic acid

(4.6 %). Although 0.2% is a small difference, Table 5.2 also shows that the neat CaMMT sample lost more mass in this temperature range than neat NaMMT (1.1 *vs*. 0.7 %) due to its higher water content. Additionally, the CaMMT sample containing 11% (w/w) salicylic acid lost 9.6 % of its mass between 200 and 650 °C, which is significantly more than the 8.2% lost by the NaMMT sample containing the same salicylic acid loading.

Figure 5.4 compares ion signal temperature profiles for salicylic acid (m/z 120; dotted line) and phenol (m/z 94; solid line) for various loadings of salicylic acid on (a) potassium, (b) sodium, and (c) calcium montmorillonites. For each clay, intact salicylic acid was only detected in purge gas effluent from samples containing high loadings. Rather than desorbing, salicylic acid initially present at lower loadings was thermally stable to temperatures high enough to facilitate decomposition, producing phenol and carbon dioxide. This suggests that adsorption sites that better stabilized salicylic acid molecules were the first to be occupied. After those sites were filled, additional salicylic acid occupied less stable environments. This behavior is similar to that observed for the benzoic acid/KMMT sample (Figure 5.1) and described by Nickels, *et al*.[67] Interestingly, the number of high stability sites available for each clay appears to be different. CaMMT has the largest decomposition to desorption ratio, whereas KMMT has the lowest, and NaMMT is intermediate. This order (KMMT<NaMMT<CaMMT) is the same as the order of increasing interlayer spacing for the neat clays. CaMMT has the largest interlayer spacing, which may allow greater steric flexibility for salicylic acid adsorption orientations. In contrast, because neat

KMMT has the smallest interlayer spacing, fewer salicylic acid orientations would be sterically permitted.

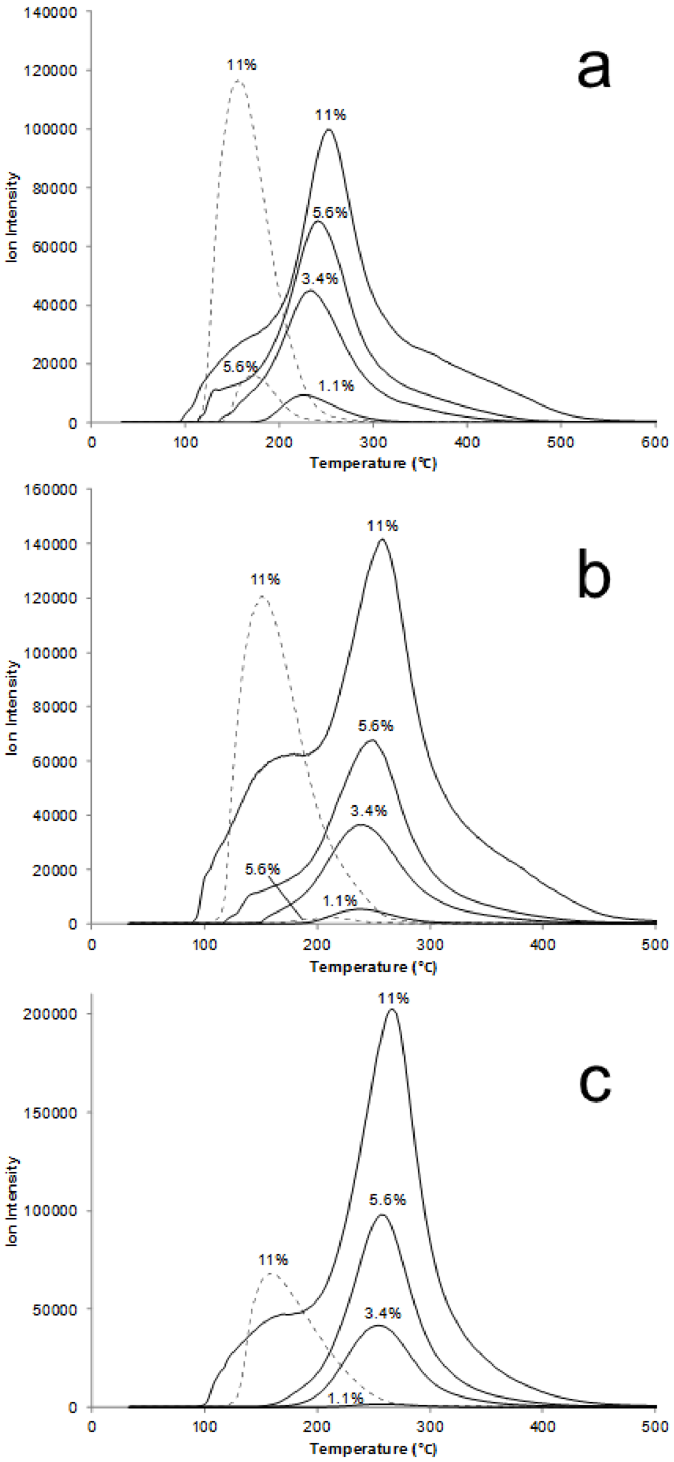

Figure 5.4 - MS profiles for salicylic acid (m/z 120; dashed line) and phenol (m/z 94; solid line) for (a) KMMT, (b) NaMMT, and (c) CaMMT samples containing various loadings of salicylic acid.

The clay samples containing 11% (w/w) salicylic acid did not lose as much mass as expected, which was also observed for samples containing benzoic acid. However, TG analysis in air confirmed that these samples contained 11% (w/w) salicylic acid (Appendix C). Like the benzoic acid samples, clay samples containing salicylic acid appeared darker after heating, suggesting that residual char had formed.

Another interesting trend apparent in Figure 5.4 is that m/z 94 (e.g. phenol) ion signal temperature profile maxima shifted to higher temperatures for samples containing higher salicylic acid loadings. It appears that higher salicylic acid concentrations provided a stabilizing effect, likely via hydrogen bonding. Also, interactions between phenol molecules resulting from decomposition with salicylic acid molecules and other phenol molecules may have delayed desorption of phenol from the interlayer, which would shift m/z 94 ion signal temperature profile maxima to higher temperatures.

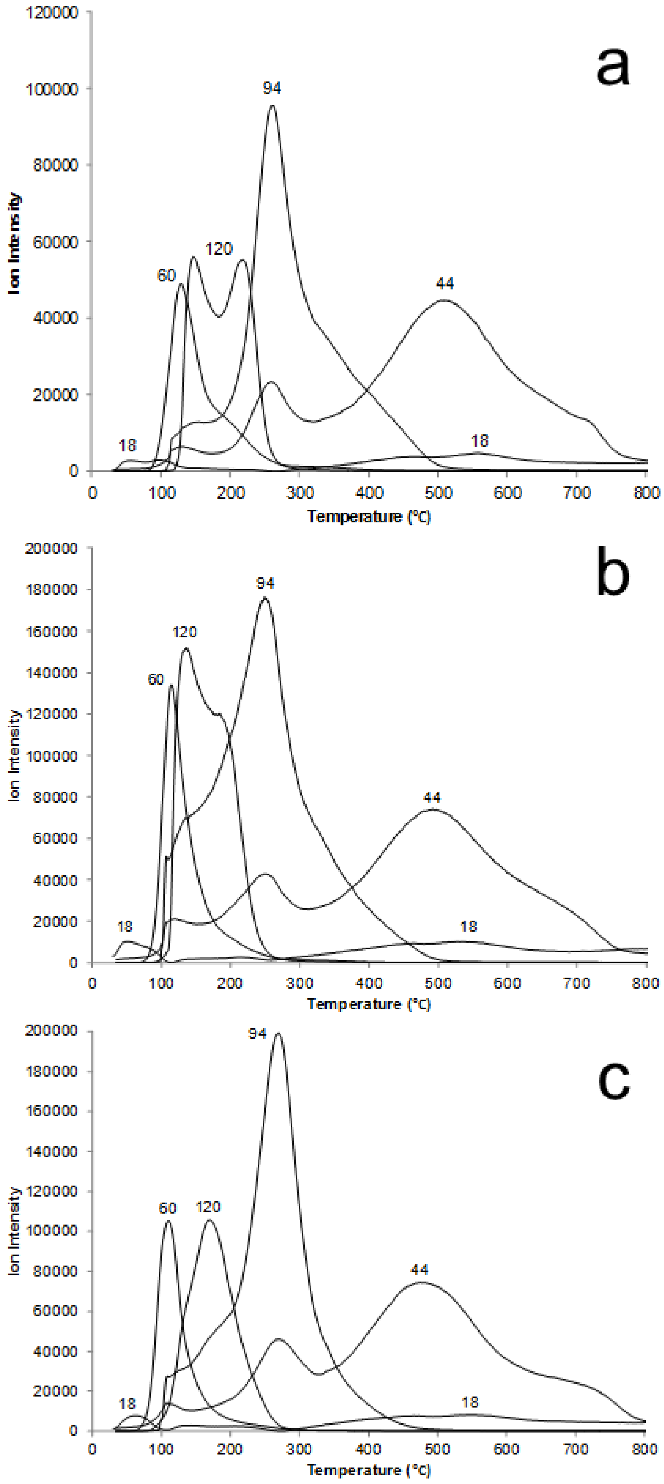

Figure 5.5 - MS ion signal intensity profiles representing water (m/z 18), acetic acid (m/z 60), salicylic acid (m/z 120), phenol (m/z 94), and carbon dioxide (m/z 44) measured during TG-MS analysis of a) KMMT, b) NaMMT, and c) CaMMT samples containing 15% acetylsalicylic acid.

Figure 5.5 shows TG-MS ion signal temperature profiles obtained for (a) KMMT, (b) NaMMT, and (c) CaMMT samples containing 15% (w/w) acetylsalicylic acid, which represents a molar content comparable to 11% (w/w) salicylic acid and 10% (w/w) benzoic acid. Profiles for water (m/z 18), carbon dioxide (m/z 44), acetic acid (m/z 60), phenol (m/z 94), and salicylic acid (m/z 120) are shown. Intact acetylsalicylic acid was not detected in TG effluent at any temperature. Acetic acid evolution began for KMMT, NaMMT, and CaMMT samples at 75, 67, and 55 °C, and maximized at 128, 112, and 108 °C, respectively. Acetic acid was a decomposition product formed by a reaction between acetylsalicylic acid and water. TG-MS analyses of samples containing acetic acid deposited on montmorillonites showed that it desorbs immediately upon heating. Thus, the appearance of acetic acid in TG effluent signifies the occurrence of acetylsalicylic acid decomposition in the solid sample. Salicylic acid is the other product of acetylsalicylic acid decomposition reactions. It is less volatile than acetic acid and has a stronger affinity for the clay, therefore it did not immediately desorb from solid samples. Acetic acid evolution maximized at about 90 °C for the KMMT and NaMMT samples, and at 94 °C for the CaMMT sample. The fact that acetylsalicylic acid decomposition began at the lowest temperature for the CaMMT sample and at the highest temperature for the KMMT sample is most likely related to relative clay water content. Water is a reactant in the decomposition reaction mechanism. Therefore the presence of more interlayer water in CaMMT would shift the reaction equilibrium towards greater deacetylation. KMMT contains less water, so greater energy is required for decomposition. The interlayer water content of NaMMT is intermediate between KMMT and CaMMT, therefore decomposition reactions require temperatures that are intermediate between those needed for KMMT and CaMMT. Another possible explanation for the difference in acetylsalicylic acid decomposition temperatures could be the difference in width of clay interlayer space. CaMMT has the greatest interlayer distance, which could allow more flexibility for the transition states to maneuver in the hydrolysis reaction. In contrast, KMMT has the smallest interlayer space, which could sterically hinder the hydrolysis reaction from going forward.

The shapes and maximum temperatures corresponding to m/z 94 and m/z 44 ion signal temperature profiles obtained for KMMT, NaMMT, and CaMMT samples were similar. In fact, these profiles were also similar to those obtained for 11% (w/w) salicylic acid adsorbed on the same clays. This suggests that phenol and carbon dioxide were formed at temperatures lower than those reflected by ion signal temperature profiles and that desorption maxima temperatures were determined by clay properties that were similar for the three montmorillonites. Unlike results obtained for salicylic acid (Figure 5.3), the m/z 120 ion signal temperature profiles for samples comprised of acetylsalicylic acid adsorbed on KMMT and NaMMT consisted of overlapping contributions, suggesting at least two decomposition events occurred during sample heating. The low temperature m/z 120 ion signal maxima occurred near 150 ^{o}C, which was about the same temperature as corresponding profiles obtained for samples containing salicylic acid (Figure 5.3). Maxima for the higher temperature contribution occurred closer to 200 ^{o}C. Results for the acetylsalicylic acid/KMMT sample (Figure 5.5a) show that the m/z 120 ion signal temperature profile was significantly different from that obtained for the salicylic acid/KMMT sample (Figure 5.3a). Salicylic acid began to evolve at 117 °C from the acetylsalicylic acid/KMMT sample compared to 100 °C from the salicylic acid/KMMT sample. Also, the salicylic acid/KMMT sample maximum evolution rate occurred at 153 °C, but the acetylsalicylic acid/KMMT sample profile contained two maxima, at 146 and 216 °C. The m/z 120 ion signal temperature profile obtained for the sample containing CaMMT appeared to be a single peak with a maximum near 180 ^{o}C, which lies between the maxima observed for samples containing KMMT and NaMMT. Apparently, although acetylsalicylic acid decomposition to form salicylic acid occurred by at least two steps for samples containing KMMT and NaMMT, this process occurred in a single step for the CaMMT sample. This suggests that there were at least two adsorption environments for acetylsalicylic acid on KMMT and NaMMT that had significant potential energy differences but only one environment for CaMMT. Results for the acetylsalicylic acid/CaMMT sample (Figure 5.5c) were the most similar to those for the salicylic acid/CaMMT sample (Figure 5.3c). The m/z 120 ion signal temperature profile maximized at 159 °C for salicylic acid and at 168 °C for acetylsalicylic acid, and desorption began at 80 °C from the acetylsalicylic acid loaded sample, compared to 115 ^{o}C for the sample containing salicylic acid. The lower desorption onset temperature for the sample containing acetylsalicylic acid indicates that some salicylic acid decomposition products were unable to adopt thermally stable orientations, possibly because those adsorption sites were already occupied.

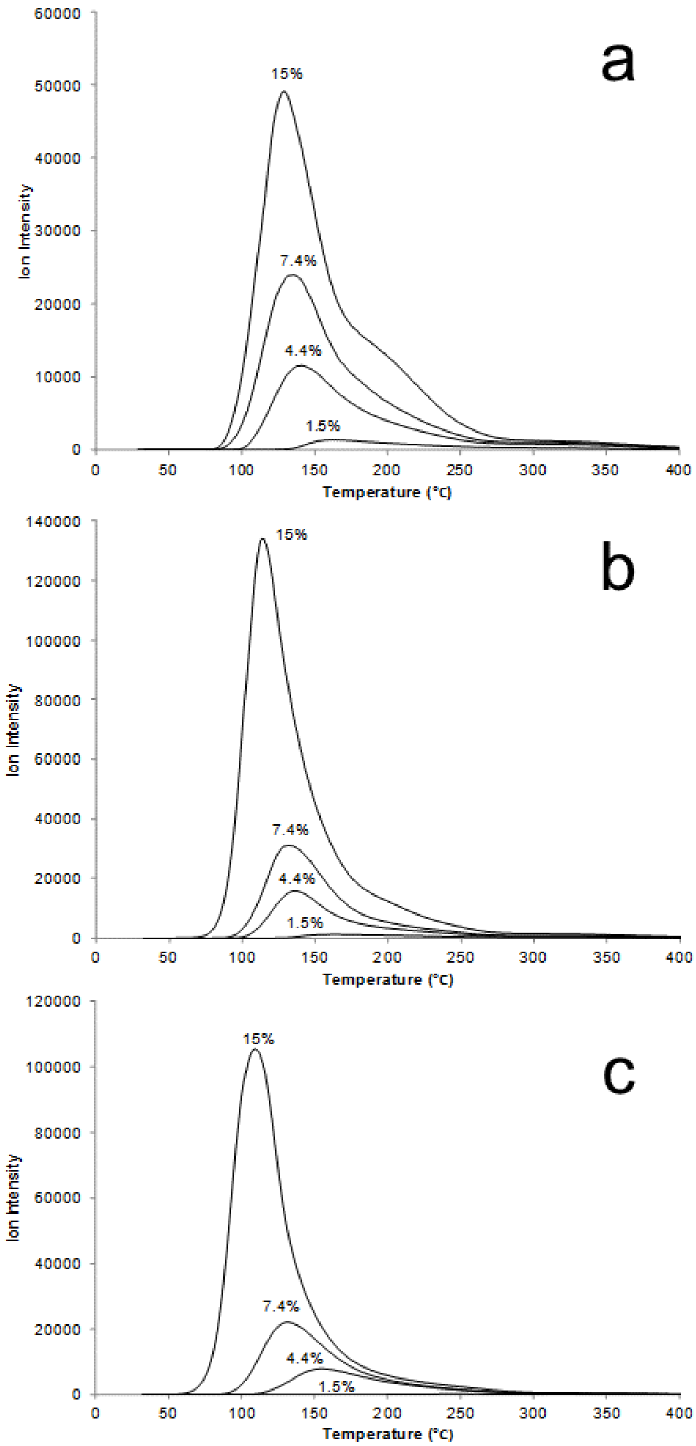

Figure 5.6 - M/z 60 (acetic acid) profiles for (a) KMMT, (b) NaMMT, and (c) CaMMT samples containing various loadings of acetylsalicylic acid.

Figure 5.6 shows m/z 60 (acetic acid) ion signal temperature profiles for (a) KMMT, (b) NaMMT, and (c) CaMMT samples containing varying acetylsalicylic acid loadings. For the KMMT samples (Figure 5.6a), ion signal profiles began at about 75 °C for the 15 and 7.4% (w/w) samples, and at about 95 and 130 °C for the 4.4 and 1.5% (w/w) samples, respectively. The maximum rates of acetic acid evolution occurred at 128, 133, 139, and 160 °C for the 15, 7.4, 4.4, and 1.5% (w/w) acetylsalicylic acid loaded samples, respectively. Profiles for the NaMMT samples (Figure 5.6b) were similar to those for KMMT, but the m/z 60 profile began at a slightly lower temperature for the highest acetylsalicylic acid loading. Acetic acid evolution was initially detected at 67, 88, 98, and 131 °C for samples containing 15, 7.4, 4.4, and 1.5% (w/w) acetylsalicylic acid, respectively. The maximum acetic acid evolution rates occurred at 112, 130, 134, and 160 °C for these samples. The m/z 60 ion signal temperature profile began at lower temperature for the CaMMT sample containing 15% (w/w) acetylsalicylic acid (Figure 5.6c). The m/z 60 ion signal temperature profiles for the 15, 7.4, and 4.4% (w/w) samples started at 55, 85, and 107 °C, and maximized at 108, 130, and 153 °C, respectively. The m/z 60 ion signal temperature profile for the 1.5% (w/w) acetylsalicylic acid/CaMMT sample was not detected above ambient noise.

The overlapping high temperature m/z 120 (salicylic acid) ion signal temperature profile component for the acetylsalicylic acid/KMMT sample (Figure 5.5a) coincides with a similar overlapping component in the m/z 60 (acetic acid) ion signal temperature profile, signifying that acetylsalicylic acid decomposition at these temperatures resulted in simultaneous production of salicylic acid and acetic acid. The delay in acetylsalicylic acid decomposition to higher temperatures may be ascribed to less water available for reaction in KMMT and NaMMT compared to CaMMT. For all three acetylsalicylic acid/clay samples, some of the salicylic acid formed after acetylsalicylic acid decomposition was retained by the clay at sufficiently high temperatures that it decomposed to produce phenol and carbon dioxide, which was the primary decomposition mechanism for clay samples loaded with salicylic acid.

Figure 5.7 shows ion intensity temperature profiles for salicylic acid (m/z 120; dotted line) and phenol (m/z 94; solid line) for various loadings of acetylsalicylic acid on (a) potassium, (b) sodium, and (c) calcium montmorillonites. The m/z 94 (phenol) evolution profiles were similar to those obtained for samples loaded with salicylic acid, suggesting that, at temperatures above 200 ^{o}C, there was little difference in adsorption behavior for salicylic acid directly adsorbed on clays compared to salicylic acid created in-situ by acetylsalicylic acid decomposition. However, the salicylic acid evolution profiles (m/z 120) were different for samples loaded with acetylsalicylic acid vs. salicylic acid, especially at the highest loadings. Interestingly, Figure 5.7 shows that salicylic acid desorbed from samples initially containing as little as 4.4% (w/w) acetylsalicylic acid. In contrast, salicylic acid was retained by the clays until temperatures at which it decomposed when it was directly adsorbed. For example, volatile salicylic acid was not detected for either the KMMT or NaMMT samples containing 3.4% (w/w) loadings (Figure 5.4a and Figure 5.4b), but the corresponding KMMT and NaMMT samples containing 4.4% (w/w) acetylsalicylic acid (Figure 5.7a and Figure 5.7b) exhibited m/z 120 ion signal intensity, although most of the salicylic acid remained on these samples to higher temperatures and subsequently decomposed to phenol and carbon dioxide.

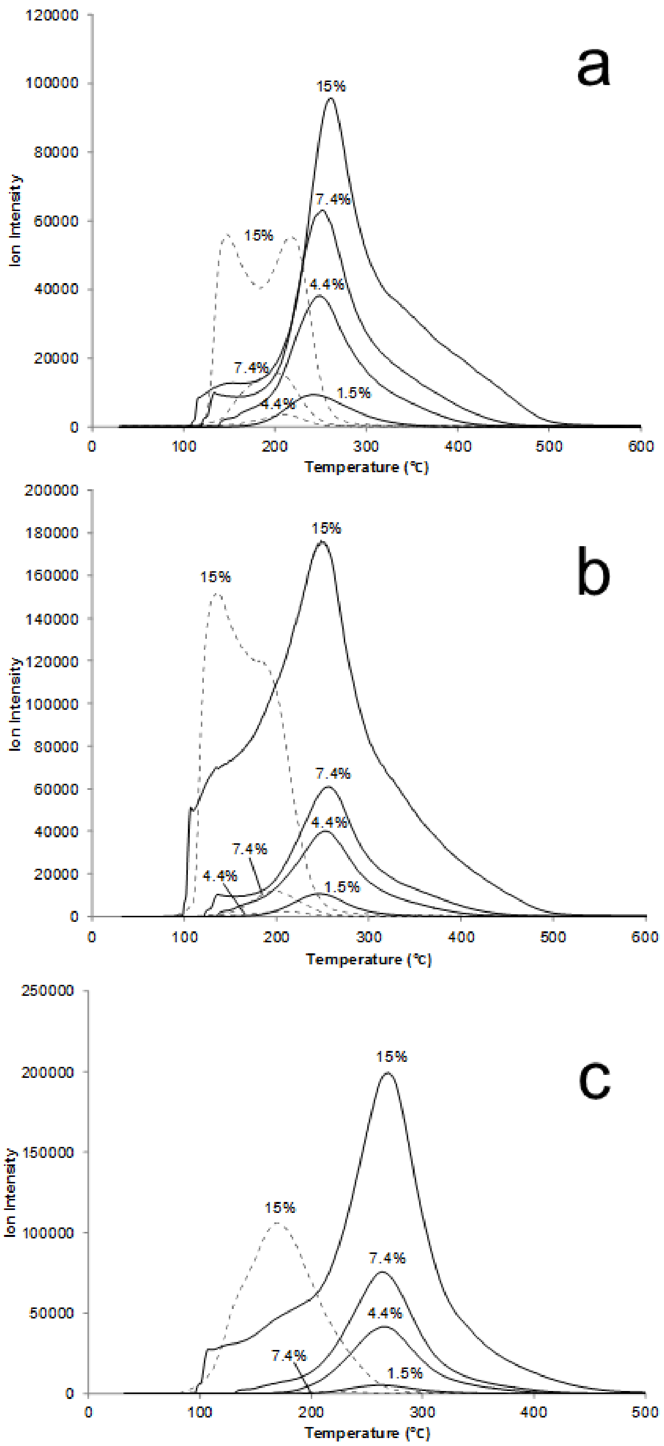

Figure 5.7 - MS profiles for salicylic acid (m/z 120; dashed line) and phenol (m/z 94; solid line) for (a) KMMT, (b) NaMMT, and (c) CaMMT samples containing various loadings of acetylsalicylic acid.

Additionally, salicylic acid evolution from the 5.6% (w/w) salicylic acid/CaMMT sample (Figure 5.4c) was not detected at any temperature. However, salicylic acid was detected for acetylsalicylic acid/CaMMT samples containing 4.4 and 7.4% (w/w) adsorbate (Figure 5.7c). This may indicate that newly formed salicylic acid molecules were incapable of making sufficiently strong hydrogen bonds in the environment previously occupied by the acetylsalicylic acid molecules from which they originated. Consequently, desorption was the more energetically favorable option.

5.3 Summary

Thermogravimetry-mass spectrometry was employed to characterize desorption of salicylic acid and acetylsalicylic acid from potassium, sodium, and calcium montmorillonites. Whereas salicylic acid exhibited behavior similar to benzoic acid in that the interlayer cation charge was the most significant factor affecting desorption temperature, acetylsalicylic acid behaviors were mostly dictated by clay water contents. In all cases, no intact adsorbate evolved from samples containing the lowest loadings, suggesting that without competition for adsorption sites, contaminants occupy the most energetically favored environments.

Chapter 6 : Variable Temperature Infrared Spectroscopy Investigations of Salicylic Acid and Acetylsalicylic Acid Desorption from Potassium, Sodium, and Calcium Montmorillonite Clays

6.1 Introduction

VT-DRIFTS was utilized to characterize salicylic acid and acetylsalicylic acid desorption from potassium, sodium, and calcium montmorillonite, as well as benzoic acid desorption from potassium montmorillonite. VT-DRIFTS provides information regarding solid-state sample changes during heating. It also allows characterization of local sample environment changes occurring throughout the heating process.

6.2 Benzoic Acid Desorption from Potassium Montmorillonite

Nickels, *et al.*,[70] utilized VT-DRIFTS to study desorption of benzoic acid from sodium and calcium montmorillonites. As a continuation of that study, desorption of benzoic acid from potassium montmorillonite was investigated by using VT-DRIFTS. The size of potassium ions are a better match than sodium ions for clay inorganic oxide hexagonal voids, so less of the cation surface area is exposed for adsorbate interactions.[65, 66] Although potassium and sodium cations are both monovalent, sodium ions are more polarizing. Thus, water molecules in sodium ion hydration spheres should be more stable than those surrounding potassium ions.[64] The exchange of potassium ions for sodium ions in clay interlayer spaces reduces basal spacing, therefore less water can be accommodated by the clay. Thus, adsorbate-clay effects related to water content may be apparent when comparing results obtained from

VT-DRIFTS analyses of adsorbate samples containing sodium and potassium montmorillonites.

VT-DRIFTS measurements were made by heating benzoic acid/KMMT samples from ambient temperature to 400 ^{o}C. Difference spectra employed for comparisons were calculated by subtracting a DRIFTS spectrum obtained at a specified temperature from a spectrum obtained at a higher temperature. VT-DRIFTS spectral changes were identified by overlaying successively acquired spectra and monitoring band shape differences. By using this method, several temperature ranges were identified over which band shape and location changes were minimal, but band intensity changes were apparent. Since VT-DRIFTS spectra reveal changes occurring in the solid sample while heating, whereas TG-MS results represent volatiles evolved during heating, the temperature ranges identified by examining VT-DRIFTS difference spectra do not exactly match temperature ranges identified in TG-MS results. Spectral changes detected below 60 ^{o}C could be attributed solely to water desorption. Those results are described in Chapter 4. VT-DRIFTS results obtained for the 10% benzoic acid/KMMT sample were similar between 60 and 137 ^{o}C, which constitutes the second temperature range investigated for this sample. In fact, four temperature ranges were identified for this sample (Table 6.1). The integrated Kubelka-Munk function over 1650 – 1800 cm^{-1} for spectra obtained for KMMT samples containing various loadings of benzoic acid is plotted *vs*. temperature in Figure 6.1. The temperature intervals shown in Table 6.1 are demarcated by dashed lines.

Table 6.1 – Temperature Intervals Identified in VT-DRIFTS Difference Spectra for 10% (w/w) Benzoic Acid/KMMT.

Temperature Interval Identifier	Temperature Interval (°C)
Interval I	RT – 60
Interval II	60 – 137
Interval III	137 – 198
Interval IV	198 – 284

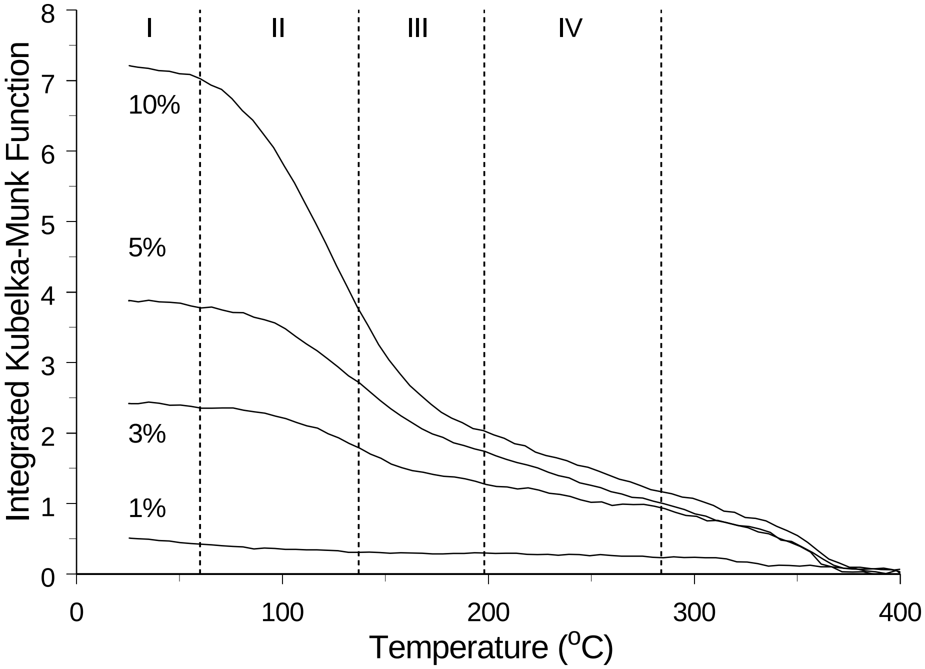

Figure 6.1 – Integrated Kubelka-Munk function over 1650 – 1800 cm^{-1} in spectra obtained for KMMT samples containing various loadings of benzoic acid, plotted *vs*. temperature. Dashed lines denote temperature limits used for difference spectra calculations (Table 6.1).

The integrated peak areas did not change significantly over Temperature Interval I, which makes sense because only water was lost from the sample over that temperature range. Based on this information, it would be expected that the total areas of positive and negative features over the 1650 – 1800 cm^{-1} range in the Temperature Interval I difference spectrum would be approximately equal. Figure 4.7 shows this to be correct. The 10% benzoic acid/KMMT sample showed a significant decrease in integrated peak area over Temperature Interval II. Spectra for samples containing lower loadings of benzoic acid also exhibited a decrease in peak area, but to a lesser extent. Thus, difference spectra over this temperature interval should primarily exhibit negative peaks due to loss of benzoic acid (Figure 6.2). Temperature Interval III is characterized by a continued loss of peak area, but less dramatic than Temperature Interval II. Temperature Interval IV also involves a net decline in peak area, but much less than for Temperature Intervals II and III.

Figure 6.2 (top) shows VT-DRIFTS spectra obtained for a potassium montmorillonite sample containing 10% (w/w) benzoic acid measured at 60 and 137 °C. Figure 6.2 (bottom) shows the result of subtracting the spectrum measured at 60 °C from the 137 °C spectrum. TG-MS analysis of this sample indicated that benzoic acid began to desorb from the clay near 117 °C, so the changes observed over the 60 to 137 °C temperature range are due in part to benzoic acid desorption, although water loss was still a significant factor. The positive feature near 1000 cm^{-1} is due to changes in spectral features of the clay with heating. Similar features were observed in neat clay sample difference spectra over comparable temperature ranges, and at higher temperature ranges, so features similar to this appear in all of the clay samples presented here.

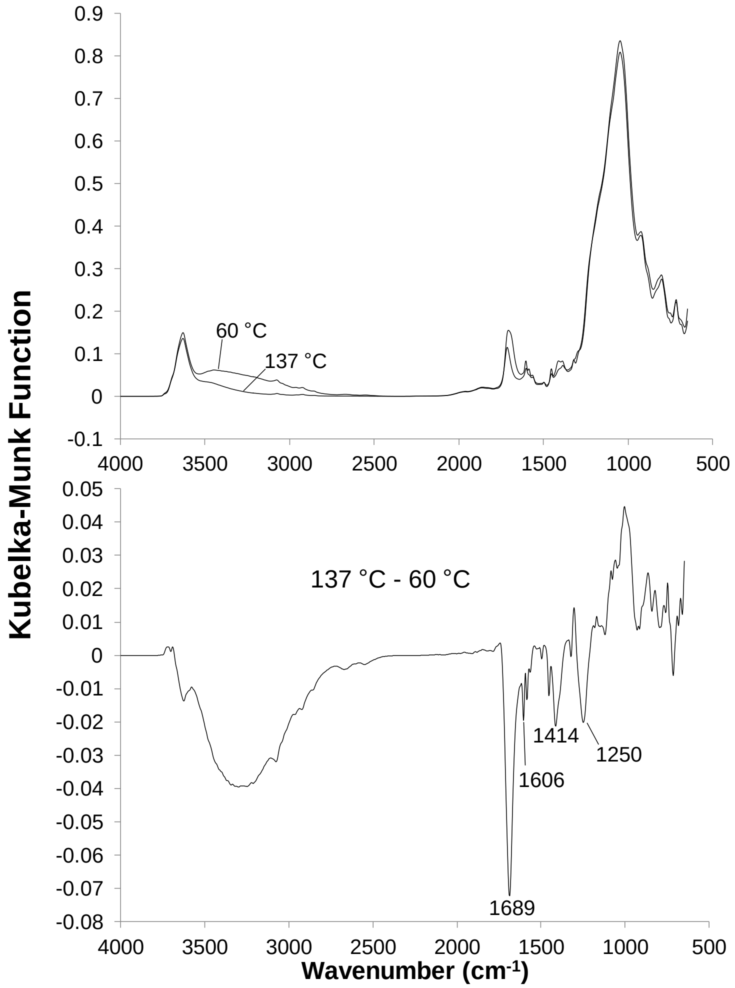

Figure 6.2 - VT-DRIFTS spectra for potassium montmorillonite containing 10% (w/w) benzoic acid over Temperature Interval II. The overlaid spectra shown at the top were subtracted to produce the difference spectrum at the bottom.

As shown in the difference spectrum, a loss of C=O stretching vibration band intensity occurred at 1689 cm^{-1}, which is higher than was obtained for samples containing NaMMT (1672 cm^{-1}) and CaMMT (1685 cm^{-1}) over comparable temperature ranges.[70] In contrast, other negative peaks in Figure 6.2 appeared at lower wavenumbers than they did in spectra obtained for NaMMT and CaMMT samples. The O-H in-plane bending vibrations appeared at 1414 and 1250 cm^{-1}, which are lower than values reported for the benzoic acid dimer[108, 117] but higher than values reported for the benzoic acid monomer.[117-119] The C=O stretching vibration at 1689 cm^{-1} is lower than that of the monomer, but higher than observed for the dimer.[108, 117-119] The fact that these band locations are more similar to values reported for the benzoic acid monomer than the benzoic acid/NaMMT and benzoic acid/CaMMT samples may be the result of the KMMT lower water content. More hydrogen bonding partners afforded by the higher water content in NaMMT and CaMMT would make the benzoic acid environment more like the dimer configuration. The negative aromatic ring C-C stretching vibration band at 1606 cm^{-1}, on the other hand, occurs at about the same location as was previously reported for benzoic acid/CaMMT and benzoic acid/NaMMT samples. This is consistent with the conclusion reached by Nickels, *et al*., that the aromatic ring was not significantly affected by the interlayer cation.[70]

Benzoic acid/KMMT VT-DRIFTS spectra obtained at 137 and 198 ^{o}C are shown in Figure 6.3 (top) along with the calculated difference spectrum (bottom). Relative to the Temperature Interval II difference spectrum, the negative C=O stretching vibration band blue shifted to 1714 cm^{-1}, whereas one of the O-H in-plane bending vibrations red shifted to 1405 cm^{-1}, and the other O-H in-plane bending vibration remained at 1239 cm^{-1}. The aromatic ring C-C stretching vibration band wavenumber shifted slightly to lower energy, appearing at 1602 cm^{-1}. These trends are consistent with those observed for NaMMT and CaMMT samples containing benzoic acid at these temperatures, although the O-H bending vibrations occur at lower wavenumber and the C=O stretching vibration band shifts to higher wavenumber for the benzoic acid/KMMT sample compared to the NaMMT and CaMMT samples.[70]

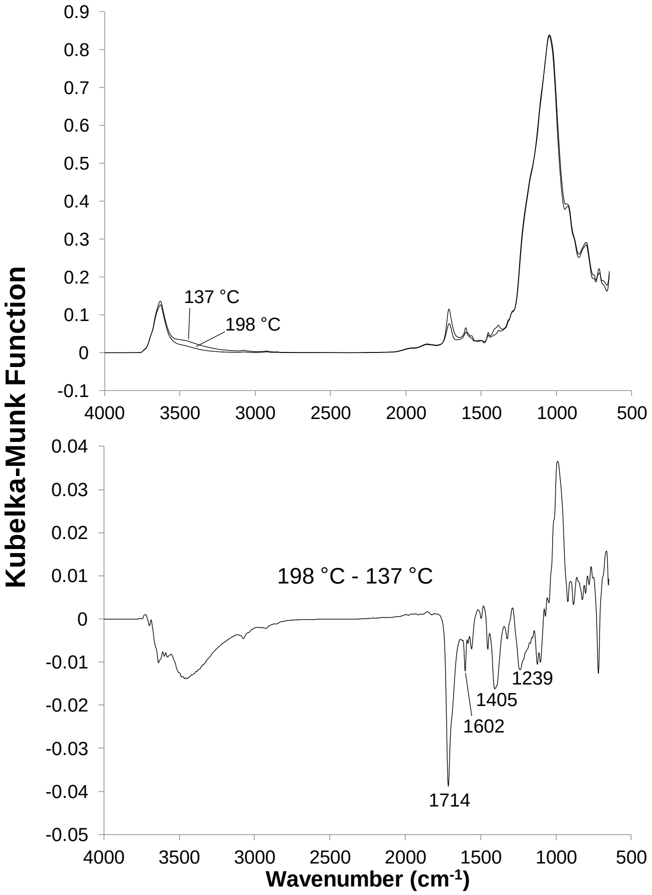

Figure 6.3 - VT-DRIFTS spectra for potassium montmorillonite containing 10% (w/w) benzoic acid over Temperature Interval III. The overlaid spectra shown at the top were subtracted to produce the difference spectrum at the bottom.

Between 198 and 284 ^{o}C, the C=O and O-H bands did not shift significantly (Figure 6.4), which is also consistent with previous results reported for benzoic acid/NaMMT and benzoic acid/CaMMT samples.

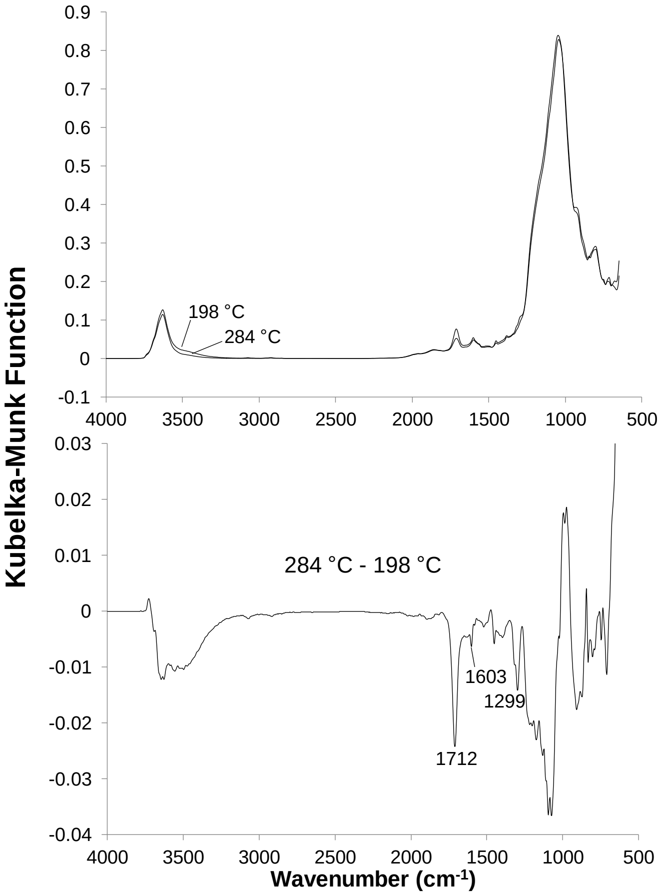

Figure 6.4 - VT-DRIFTS spectra for potassium montmorillonite containing 10% (w/w) benzoic acid over Temperature Interval IV. The overlaid spectra shown at the top were subtracted to produce the difference spectrum at the bottom.

6.3 Salicylic Acid Desorption from Potassium, Sodium, and Calcium Montmorillonite Clays

Figure 6.5 shows ambient temperature DRIFTS spectra for samples containing 11% (w/w) salicylic acid with (a) KMMT, (b) NaMMT, (c) CaMMT, and (d) silver powder. The inset shows an expansion of the salicylic acid C=O stretching and O-H in-plane bending vibration regions, where the bands associated with salicylic acid are most easily distinguished from clay absorbances. Salicylic acid absorbance band shapes and relative intensities varied due to strong interactions with the clays, but were less intense than bands in the salicylic acid/silver powder spectrum, due to dilution. The salicylic acid/silver powder sample contained 11% (w/w) adsorbate, whereas clay samples containing 11% (w/w) salicylic acid were further diluted 5:95 in silver powder, so they contained only 0.55% (w/w) salicylic acid. The salicylic acid band that is most easily discerned corresponds to the C=O stretching vibration, which appears near 1667 cm^{-1} for samples containing salicylic acid adsorbed on clays, and near 1659 cm^{-1} when salicylic acid was mixed with silver powder. The salicylic acid/silver powder sample spectrum contains an absorbance at 1673 cm^{-1}, which can also be attributed to the C=O stretching vibration. Denisov, *et al*.,[105] reported the appearance of a peak at 1697 cm^{-1}, which they assigned to the salicylic acid monomer in dilute carbon tetrachloride solutions. In more concentrated solutions, a peak associated with the dimer at 1660 cm^{-1} dominated. Similar results were reported by Murray, *et al*.[120] It is likely that dilution in silver powder caused a similar effect,[121] and that some of the salicylic acid was in the dimer form and some was in the monomer form, which would account for the presence of two C=O stretching vibration bands. Because the C=O stretching vibration for salicylic acid/clay samples appeared near 1667 cm^{-1}, it is likely that salicylic acid existed as a monomer in those samples, but that it formed hydrogen bonds with interlayer water molecules that reduced the C=O stretching vibration wavenumber. This effect is similar to that previously reported for a benzoic acid/clay sample.[70]

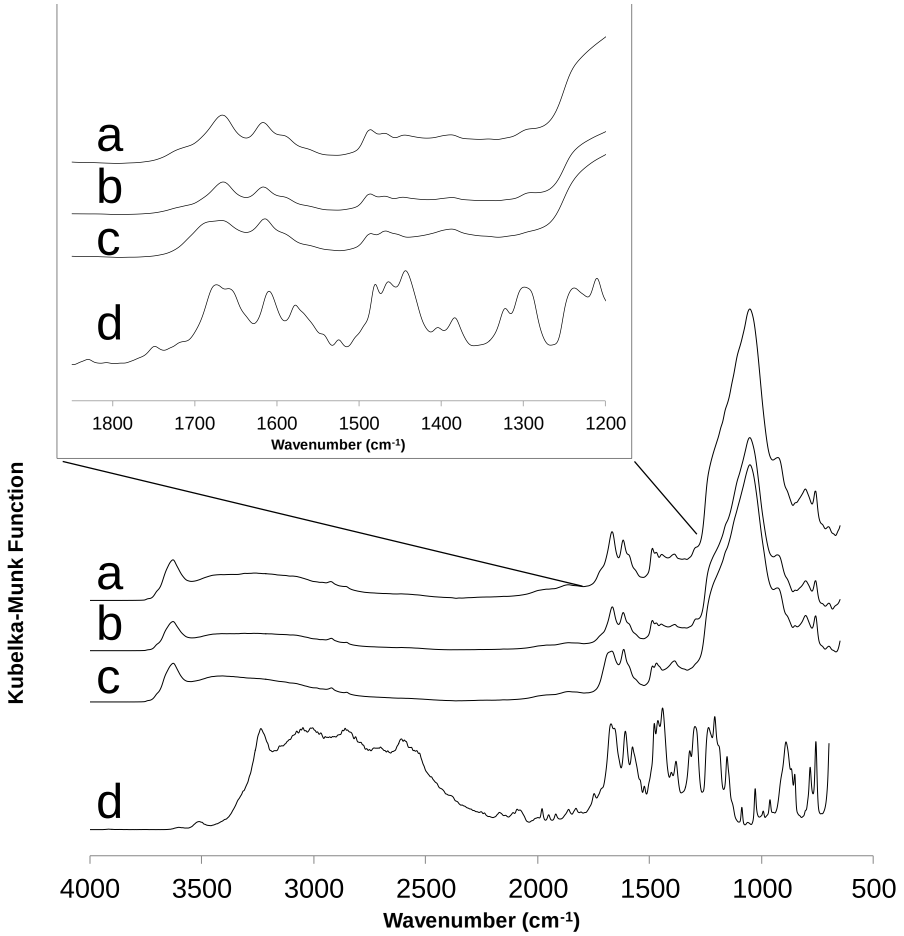

Figure 6.5 – Ambient temperature DRIFTS spectra of samples containing 11% (w/w) salicylic acid with (a) KMMT, (b) NaMMT, (c) CaMMT, and (d) silver powder. Inset shows expansion of the 1200 – 1850 cm^{-1} wavenumber range.

In addition to an absorbance at 1668 cm^{-1}, the salicylic acid/CaMMT sample spectrum exhibits a shoulder near 1683 cm^{-1}, which is not present in spectra obtained for salicylic acid samples containing KMMT and NaMMT. This shoulder may be due to some salicylic acid/CaMMT molecules adopting an orientation that restricted hydrogen bonding interactions. It is also possible that the higher charge of the Ca^{2+} ion reduced the electron density on the bridging water molecule oxygen, which in turn reduced the partial positive charge of the hydrogen donor to the carbonyl oxygen, so that the C=O stretching vibration was less affected by hydrogen bonding in the CaMMT environment compared to the KMMT and NaMMT environments.

Table 6.2 – Vibration band assignments for salicylic acid. Assignments and salicylic acid dimer values taken from reference [122]. ν = stretching vibration, δ = in-plane bending vibration

Vibration Assignment[122]	Dimer[122]	salicylic acid/silver powder	salicylic acid/ KMMT	salicylic acid/ NaMMT	salicylic acid/ CaMMT
ν(C=O) + ν(C=C) + δ(O-H)$_{carboxyl}$	1658	1659	1667	1666	1668 (shoulder near 1683)
ν(C=O) + ν(C=C) + δ(O-H)$_{carboxyl}$	1612	1609	1617	1617	1615
ν(C=C) + δ(O-H)$_{phen}$ + δ(C-H)	1579	1577	1590 (shoulder)	1590 (shoulder)	1590 (shoulder)
ν(C=C) + δ(O-H)$_{phen}$ + δ(C-H)	1484	1480	1486	1486	1486
δ(O-H)$_{carboxyl}$ + δ(O-H)$_{phen}$ + δ(C-H)	1466	1464	1471	1471	1467
ν(C=C) + δ(O-H)$_{carboxyl}$ + δ(C-H)	1444	1443	1444	1448	~1455 (shoulder)
ν(C=C) + δ(O-H)$_{phen}$ + δ(C-H)	1384	1383	1390	1386	1388
ν(C=C) + δ(O-H)$_{carboxyl}$ + δ(O-H)$_{phen}$	1325	1322	1343 (weak)	1344 (weak)	~1343 (shoulder)
ν(Ph-OH) + δ(O-H)$_{carboxyl}$ + δ(C-H)	1296	1298	1293 (shoulder)	1293 (shoulder)	~1295 (weak shoulder)
ν(C=C) + δ(O-H)$_{carboxy}$ + δ(C-H)	1249	1238	N/A	N/A	N/A
δ(O-H)$_{phen}$ + δ(C-H)	1211	1210	N/A	N/A	N/A

The location of the C=O stretching vibration band at 1659 cm^{-1}, as well as the other absobance bands found in the salicylic acid/silver powder spectrum, are consistent with those reported by Boczar, *et al.*, for the salicylic acid dimer.[122] They used theoretical modeling to aid in vibration assignments. Table 6.2 lists these assignments and their band location measurements, and provides a comparison to our results for salicylic acid diluted in silver powder, and also adsorbed on potassium, sodium, and calcium montmorillonites. Only the C=O stretching and O-H in-plane bending regions are included in the table, because they undergo the greatest changes when salicylic acid/clay samples are heated. It is interesting that in this region of the salicylic acid infrared spectrum, every absorbance is attributed to a combination of at least two, but usually three different motions of the molecule. It seems likely that intramolecular hydrogen bonding provides a more rigid structure, so that when one part of the molecule stretches or bends, other parts vibrate as well. This is not the case for benzoic acid or acetylsalicylic acid, which makes salicylic acid unique for studies described here.

Salicylic acid/clay samples were heated at 5 °C/minute from ambient temperature to 400 °C, and spectra were collected every minute. Successive spectra were compared in order to identify significant transitions which occurred during heating. The identified transitions were used to demarcate temperature ranges of interest. Since VT-DRIFTS spectra reveal changes occurring in the solid sample while heating, whereas TG-MS results represent volatiles evolved during heating, the temperature ranges identified by examining VT-DRIFTS difference spectra do not exactly match temperature ranges identified in TG-MS results. Spectra collected below

60 °C show effects of water loss only, and are discussed in Chapter 4. Above 60 °C, four temperature intervals were identified in VT-DRIFTS spectra for 11% salicylic acid/clay samples (Table 6.3). Figure 6.6 shows the integrated Kubelka-Munk function obtained from successive spectra over the 1650 – 1800 cm^{-1} range for (a) KMMT, (b) NaMMT, and (c) CaMMT samples containing various loadings of salicylic acid, plotted *vs*. temperature. Dashed lines denote interval temperature limits used for difference spectra calculations (Table 6.3).

Table 6.3 - Temperature Intervals Identified in VT-DRIFTS Difference Spectra for 11% (w/w) Salicylic Acid/Clay Samples.

Temperature Interval Identifier	Temperature Interval (°C)		
	KMMT	NaMMT	CaMMT
Interval I	RT – 60	RT – 60	RT – 61
Interval II	60 – 116	60 – 101	61 – 112
Interval III	116 – 137	101 – 132	112 – 163
Interval IV	137 – 178	132 – 178	163 – 194
Interval V	178 – 264	178 – 275	194 – 264

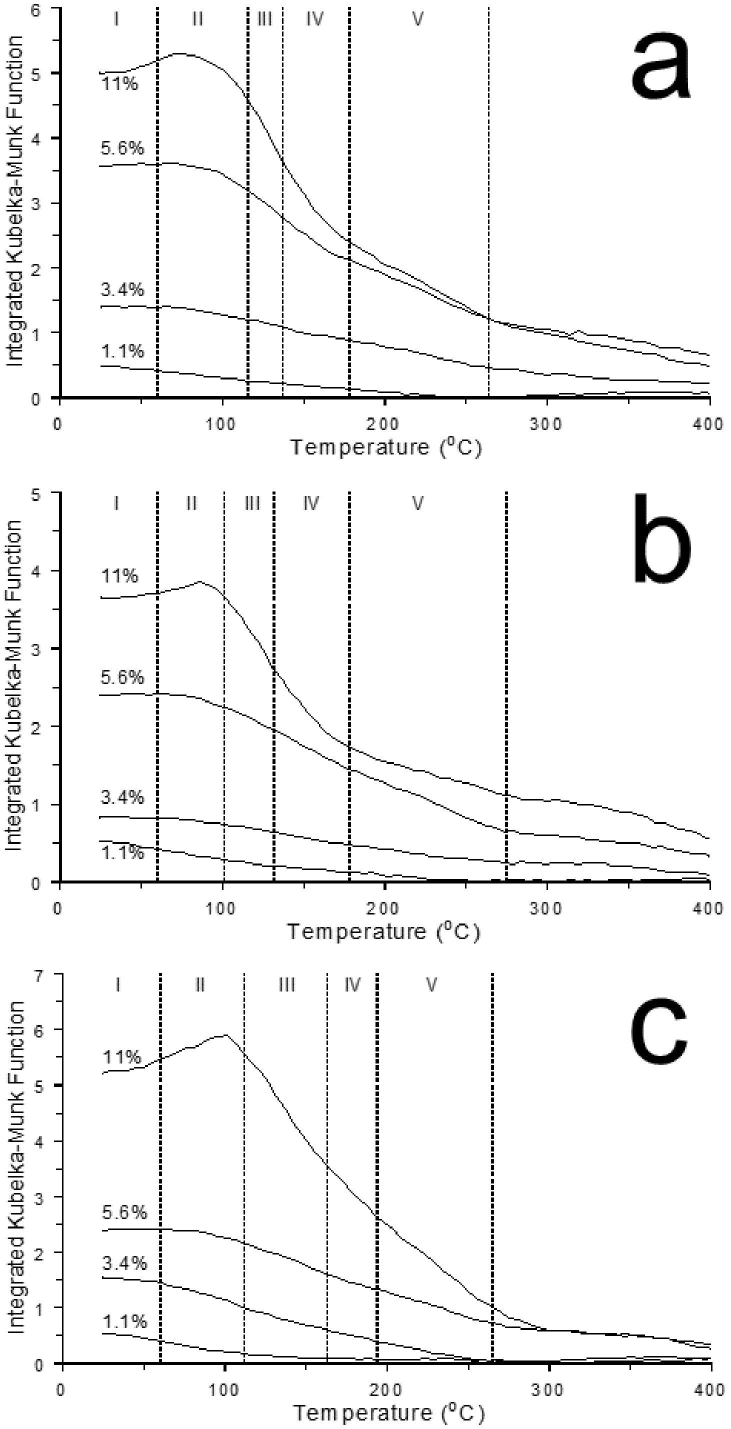

Figure 6.6 – Integrated Kubelka-Munk function obtained from spectra over the 1650 – 1800 cm^{-1} range for (a) KMMT, (b) NaMMT, and (c) CaMMT samples containing various loadings of salicylic acid, plotted *vs*. temperature. Dashed lines denote temperatures used for difference spectra calculations over selected temperature intervals (Table 6.3).

The integrated peak areas changed little over Temperature Interval I, although absorptivity increased slightly for the 11% samples. Figure 4.10, Figure 4.11, and Figure 4.12 show the difference spectra for salicylic acid/clay samples calculated over the 1650 – 1800 cm^{-1} range, and consistent with Figure 6.6, positive peak areas were slightly greater than negative peak areas. The integrated peak areas of the samples containing 11% salicylic acid show a steep increase over Temperature Interval II, indicating a marked increase in absorptivity due to local sample environment changes. Integrated areas decreased again below 100 °C for KMMT and NaMMT samples containing 11% salicylic acid, and at 100 °C for CaMMT containing 11% salicylic acid. TG-MS results for 11% salicylic acid/clay samples diluted in silver powder (5:95, w/w) are shown in Appendix D. Figures D.2 – D.4 show that salicylic acid began to desorb from KMMT and NaMMT near 100 °C, and from CaMMT above 100 °C. The decline in integrated peak area began at temperatures slightly lower than those required for salicylic acid desorption. However, temperature measurement differences for VT-DRIFTS and TG-MS could be the cause of these discrepancies. Temperature Intervals III, IV, and V all involve declines in peak area due to continued salicylic acid loss.

Figure 6.7 shows overlaid VT-DRIFTS spectra obtained for the 11% salicylic acid/KMMT sample collected at 60 and 116 °C (top). This temperature range is characterized by water loss and the beginning of salicylic acid desorption, which is reflected in the difference spectrum negative bands representing loss of water and salicylic acid. Figure 6.8 and Figure 6.9 show VT-DRIFTS results obtained over corresponding temperature ranges (Temperature Interval II) for 11% salicylic acid/NaMMT (Figure 6.8) and 11% salicylic acid/CaMMT (Figure 6.9) samples.

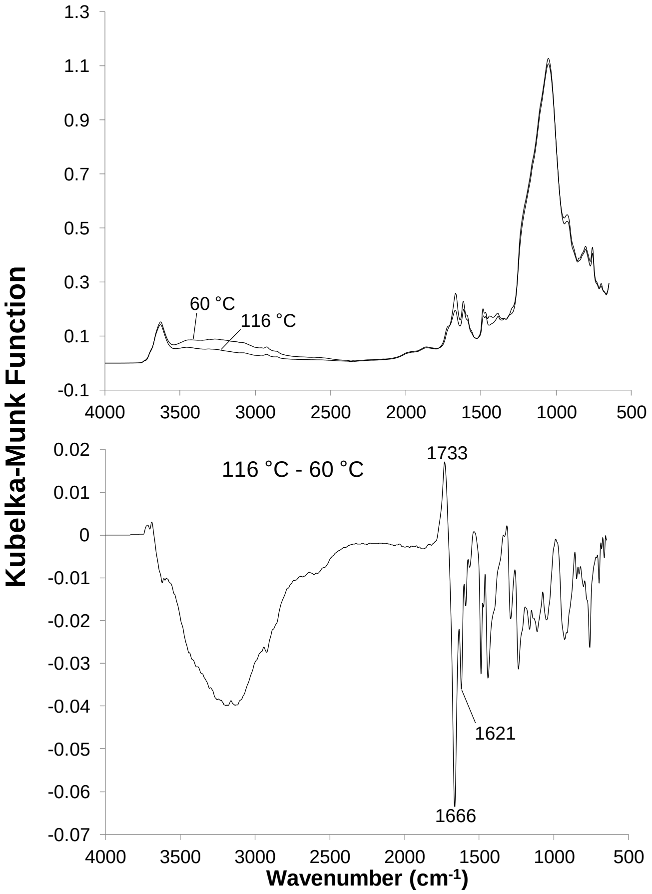

Figure 6.7 - VT-DRIFTS spectra for potassium montmorillonite containing 11% (w/w) salicylic acid obtained over Temperature Interval II. The overlaid spectra shown at the top were subtracted to produce the difference spectrum at the bottom.

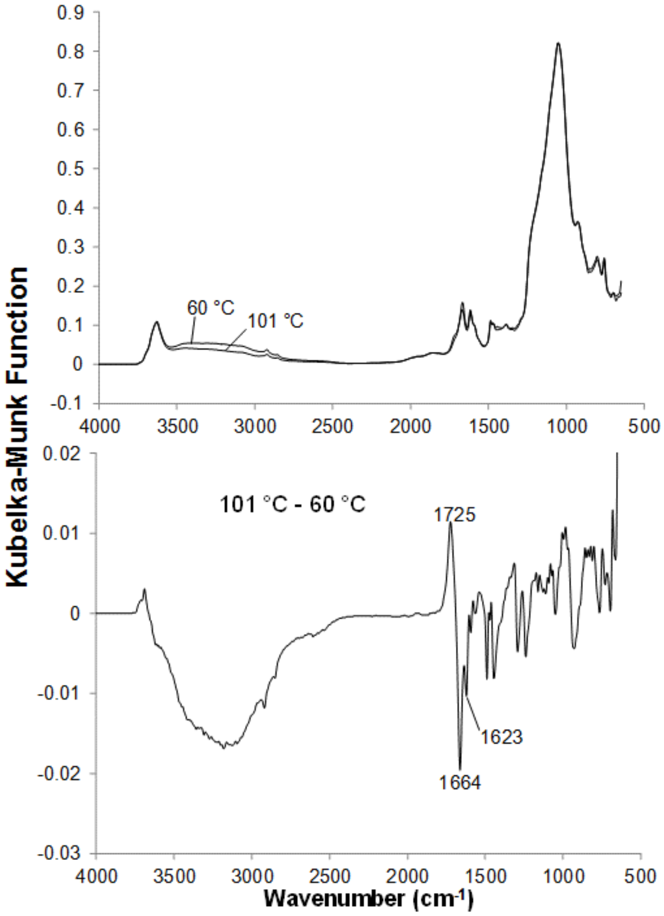

Figure 6.8 - VT-DRIFTS spectra for sodium montmorillonite containing 11% (w/w) salicylic acid obtained over Temperature Interval II. The overlaid spectra shown at the top were subtracted to produce the difference spectrum at the bottom.

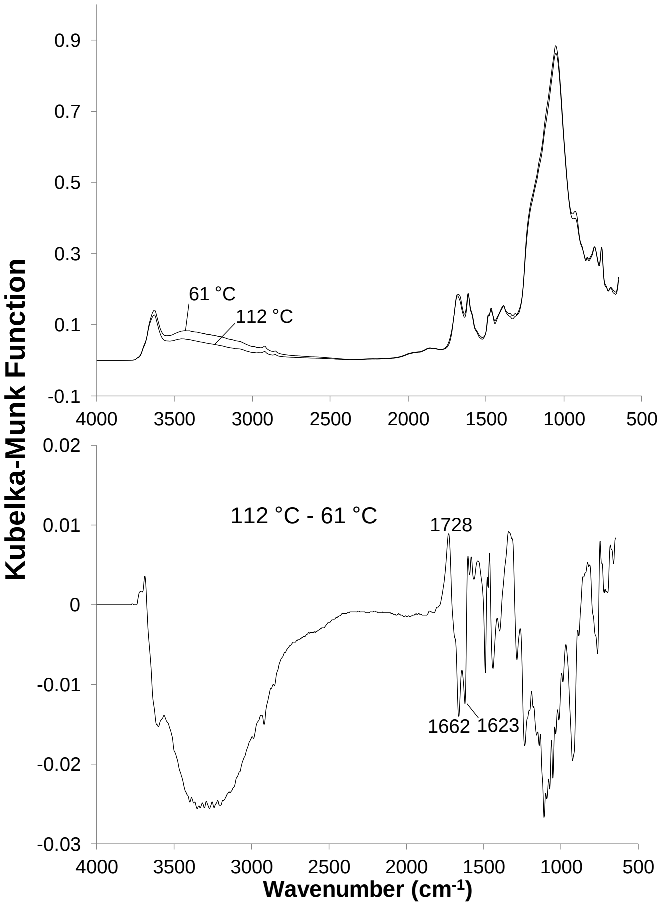

Figure 6.9 - VT-DRIFTS spectra for calcium montmorillonite containing 11% (w/w) salicylic acid obtained over Temperature Interval II. The overlaid spectra shown at the top were subtracted to produce the difference spectrum at the bottom.

Difference spectra are dominated by the loss of O-H stretching intensity, apparent from 2400 cm^{-1} to almost 3700 cm^{-1}. This wavenumber range is expanded in Figure 6.10 to facilitate a better comparison for the three clay samples. Figure 6.10 shows results for KMMT (left), NaMMT (center) and CaMMT (right) samples containing 11% salicylic acid obtained over Temperature Interval II (Table 6.3). All three of the spectra show small positive peaks near 3692 cm^{-1}. Spectra for the NaMMT and CaMMT samples also have a shoulder near 3715 cm^{-1}, whereas the spectrum for the

KMMT sample has a more distinct peak at 3722 cm^{-1}. These positive peaks represent the stretching vibrations of inorganic oxide hydroxyl groups that lost hydrogen bonding partners as a result of sample heating. The broad negative feature associated with loss of O-H stretching vibration band intensity due to water and salicylic acid loss has a minimum located near 3200 cm^{-1} for KMMT and NaMMT samples. The corresponding feature for the CaMMT sample is broader and the negative band minimum occurs at a higher wavenumber.

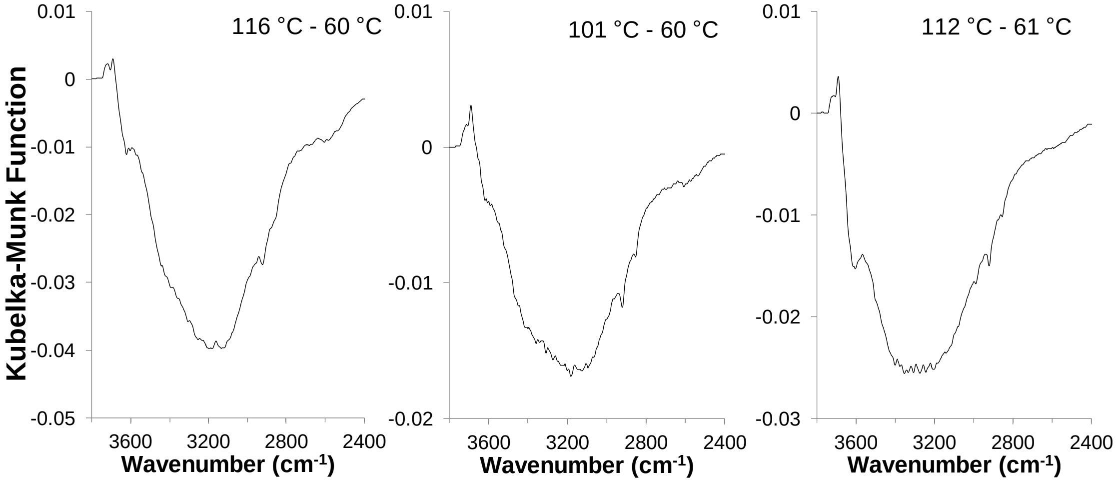

Figure 6.10 - Expansion of the O-H stretching region of difference spectra for 11% salicylic acid on KMMT (left), NaMMT (center), and CaMMT (right).

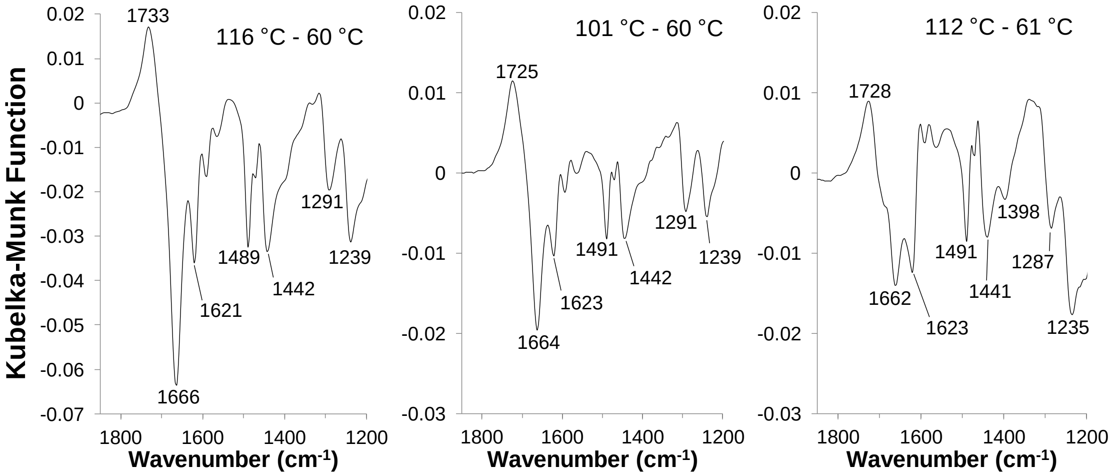

Figure 6.11 – Expansion of the C=O stretching and O-H in-plane bending region of difference spectra for 11% salicylic acid on KMMT (left), NaMMT (center), and CaMMT (right).

Specific information regarding the salicylic acid environment can be obtained by observing changes to the C=O stretching and O-H in-plane bending bands, which are found in spectra from 1200 to 1800 cm^{-1}. This difference spectrum region is expanded in Figure 6.11 for KMMT (left), NaMMT (center), and CaMMT (right) samples containing 11% salicylic acid for Temperature Interval II. In each case, the most significant features can be attributed to loss of C=O stretching vibration band intensity, which occurs at 1666, 1664, and 1662 cm^{-1} for KMMT, NaMMT, and CaMMT samples, respectively. Corresponding C=O stretching vibration band intensity gains were detected at 1733, 1725, and 1728 cm^{-1}. This shift of the C=O stretching vibration band to higher wavenumbers when water was lost from the sample was also observed below 60 °C for salicylic acid and benzoic acid (Figure 4.11). However, over a comparable temperature range, spectra obtained for samples containing benzoic acid adsorbed on NaMMT and CaMMT did not contain positive features that could be attributed to a gain in C=O stretching .[70] The wavenumbers associated with the gain in C=O intensity for salicylic acid and for benzoic acid below 60 °C are below the values reported for the benzoic acid monomer, but above those reported for the salicylic acid monomer[105] and observed for salicylic acid diluted in silver powder (Figure 6.5). Perhaps in this environment, salicylic acid intramolecular hydrogen bonding has less of an effect on the C=O stretching vibration frequency, causing it to be closer to that observed for benzoic acid in a similar environment. However, as shown in Figure 1.5, difference spectra maxima may appear at significantly higher wavenumbers than the band maximum that produces them, which may explain why the positive peaks in Figure 6.11 are higher than expected. One interesting trend is that the location of the salicylic acid C=O stretching vibration band loss was less dependent on the cation than the benzoic acid C=O stretching vibration band intensity loss. It may be that in the C=O group local environment before water loss, salicylic acid intramolecular hydrogen bonding reduced the effect of the cation on the C=O stretching vibration. Alternatively, salicylic acid molecules may not be oriented with the C=O group pointed directly at the cation, as predicted for benzoic acid.

Figure 6.12 shows O-H stretching region difference spectra for KMMT (left), NaMMT (center), and CaMMT (right) containing 11% salicylic acid obtained over Temperature Interval III. The low temperature limits in Figure 6.12 coincided with the high temperature limits of Temperature Interval II (Figure 6.7-Figure 6.11). Difference spectra shown in Figure 6.12 are similar to those in Figure 6.10, likely because the two primary mechanisms responsible for O-H stretching vibration band intensity loss in this temperature range were water desorption and salicylic acid desorption, as in the previous temperature range. The bandwidths are somewhat narrower, and shifted to slightly higher wavenumbers in Figure 6.12 than in Figure 6.10, especially for the CaMMT sample spectrum, which is due to reduced water content in the clay interlayer over this temperature range.

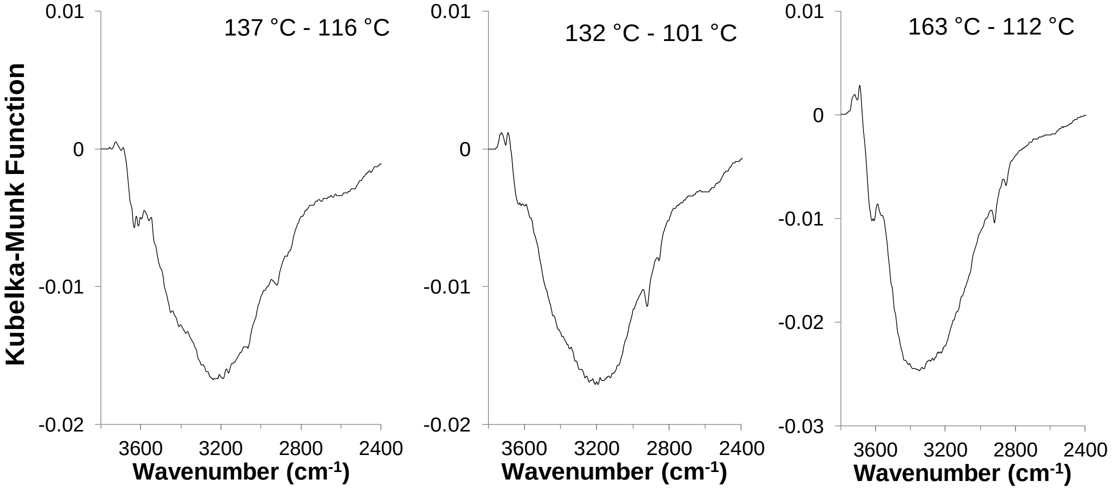

Figure 6.12 – Expansion of the O-H stretching region of difference spectra for 11% salicylic acid on KMMT (left), NaMMT (center), and CaMMT (right).

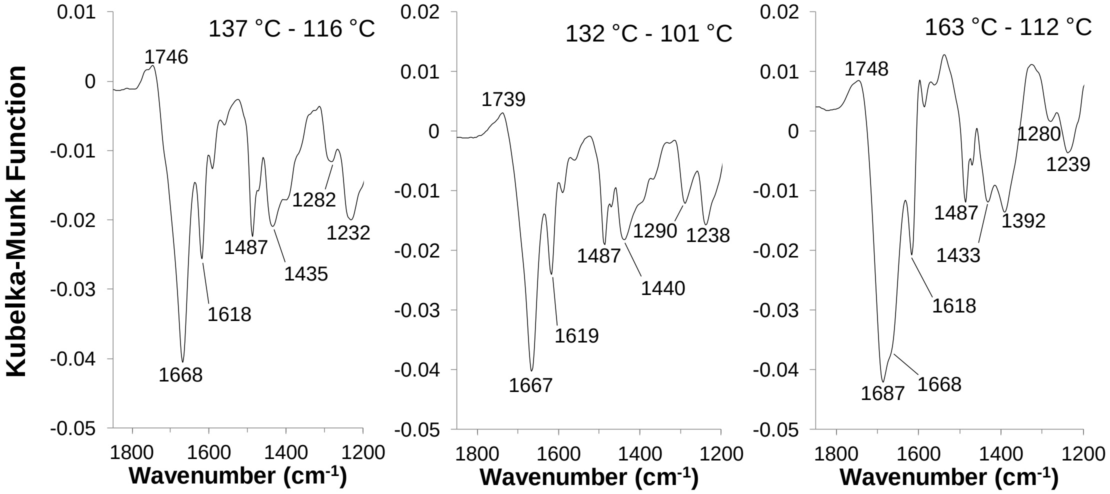

Figure 6.13 – Expansion of C=O stretching and O-H in-plane bending region of difference spectra for 11% salicylic acid on KMMT (left), NaMMT (center), and CaMMT (right).

Figure 6.13 compares the C=O stretching and O-H in-plane bending vibration band regions for KMMT (left), NaMMT (center), and CaMMT (right) samples containing 11% salicylic acid obtained over Temperature Interval III. Difference spectra in Figure 6.13 for samples containing KMMT and NaMMT are similar, and are also similar to difference spectra shown for Temperature Interval II. The primary difference relative to the previous temperature range is that the loss of C=O stretching vibration band intensities appeared at slightly higher wavenumbers. Also, the C=O stretching vibration band intensity gains were not as prominent as they were in the previous temperature range, and they appeared at significantly higher wavenumbers. Results obtained for the salicylic acid/CaMMT sample were significantly different from the other two clays. Interestingly, the upper temperature of this interval was higher for CaMMT (163 °C) than for the other two samples (132 and 137 °C). TG-MS results indicated that the maximum rates of salicylic acid evolution occurred near 150 °C for CaMMT and near 140 °C for KMMT and NaMMT, which are included within the temperature range for CaMMT, but not for the other two samples. Temperature intervals for difference spectra were selected based on transitions observed in VT-DRIFTS spectra, without regard to TG-MS results, so the intervals selected are based on changes in the solid sample that do not necessarily result in the evolution of a gaseous product. However, the CaMMT sample lost significantly less salicylic acid by desorption than the other two samples, because a greater fraction of salicylic acid remained on CaMMT until it decomposed. The negative band associated with C=O stretching vibration band intensity loss for the CaMMT sample shifted to slightly higher wavenumbers (1668 vs. 1662 cm^{-1} in Figure 6.13 and Figure 6.11), but the loss at 1668

cm^{-1} appeared as a shoulder on the more intense loss at 1687 cm^{-1}, suggesting that the majority of salicylic acid molecules lost during this temperature range were less strongly hydrogen bonded. The gain in C=O stretching vibration band intensity maximized at 1748 cm^{-1}, which was 20 cm^{-1} higher than in the 61-112 ^{o}C temperature range. The remaining features of the CaMMT difference spectrum for this temperature range are similar to those obtained for Temperature Interval II, although some bands appear at slightly lower wavenumbers. This is consistent with previous observations that bending vibrations lose energy when hydrogen bonding partners are lost, whereas stretching vibrations gain energy.[41]

Figure 6.14 shows VT-DRIFTS difference spectra O-H stretching regions for KMMT (left), NaMMT (center), and CaMMT (right) samples containing 11% salicylic acid corresponding to Temperature Interval IV. Negative features attributed to the loss of O-H stretching vibration band intensity were shifted to higher wavenumbers in this temperature range compared to lower temperature ranges, indicating that the lost O-H groups were involved in weaker hydrogen-bonding than those lost at lower temperatures, most likely because less water was present for hydrogen bonding. TG-MS results indicated that water evolution did not reach a minimum rate until 253 °C for the KMMT and NaMMT samples, and 260 °C for the CaMMT sample, so water loss was still occurring during this temperature interval.

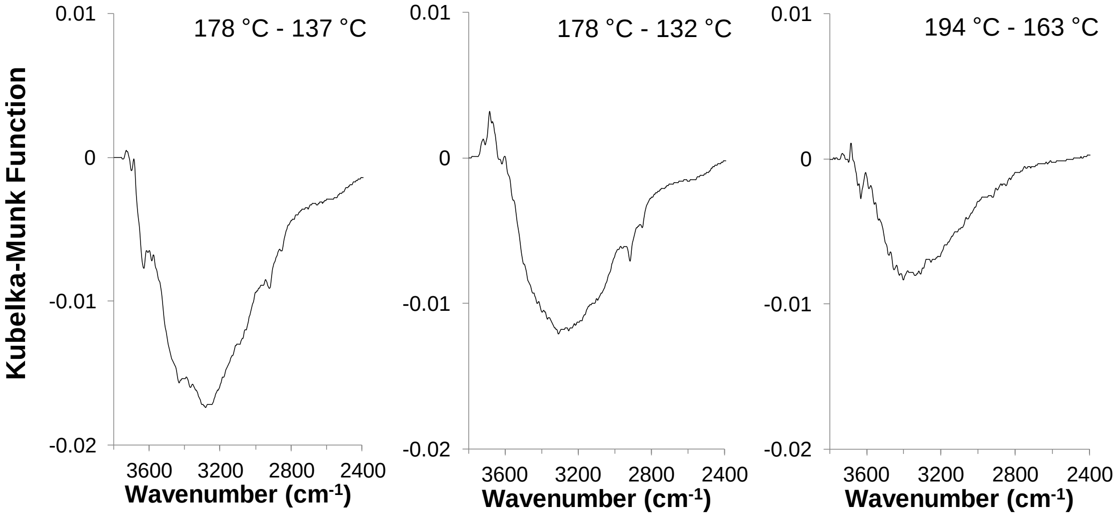

Figure 6.14 – Expansion of O-H stretching region of difference spectra for 11% salicylic acid on KMMT (left), NaMMT (center), and CaMMT (right).

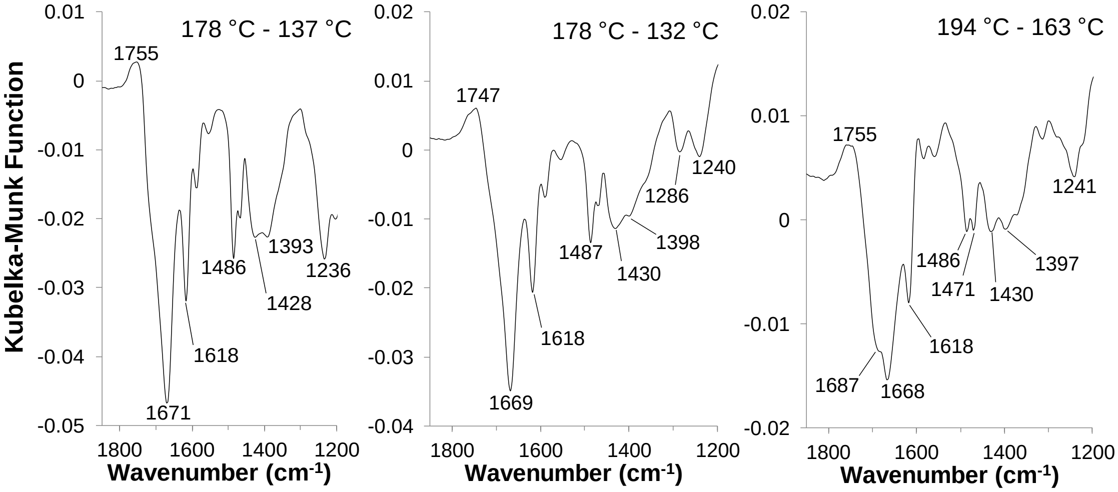

Figure 6.15 – Expansion of C=O stretching and O-H in-plane bending region of diference spectra for 11% salicylic acid on KMMT (left), NaMMT (center), and CaMMT (right).

The C=O stretching and O-H in-plane bending spectral regions for difference spectra calculated for Temperature Interval IV for KMMT (left), NaMMT (center), and CaMMT (right) samples containing 11% salicylic acid are shown in Figure 6.15. Most of the spectral features for the KMMT and NaMMT samples are similar to those detected at lower temperature ranges, although minima for C=O stretching vibration band intensity losses continued to shift to higher wavenumbers, and most of the O-H bending vibrations shifted to lower wavenumbers. Difference spectra negative bands at 1393 cm^{-1} for the KMMT sample and at 1398 cm^{-1} for the NaMMT sample were more prominent than they were in lower temperature difference spectra, where they were only visible as shoulders. The CaMMT sample spectrum contained the same two overlapping contributions for C=O stretching vibration band intensity loss as were found in the 112-163 ^{o}C range (1668 and 1687 cm^{-1}), but in this temperature range, 1668 cm^{-1} corresponded to the band minimum, and 1687 cm^{-1} was a shoulder, indicating that more of the salicylic acid molecules lost were more strongly hydrogen bonded than in the 112-163 ^{o}C temperature range. In fact, less strongly hydrogen bonded salicylic acid molecules would be expected to desorb at lower temperatures.

Figure 6.16 shows VT-DRIFTS difference spectra O-H stretching vibration band regions for KMMT (left), NaMMT (center), and CaMMT (right) samples containing 11% salicylic acid over the highest temperature range that yielded significant infrared band changes (Temperature Interval V). Although samples were heated to 400 °C, salicylic acid absorptions in spectra collected above the cutoff temperatures listed in Figure 6.16 were very broad and weak, and changes were very difficult to assign. Figure 6.16 shows that the O-H stretching vibration band intensity loss was shifted to higher wavenumbers in this temperature range compared to lower temperatures, likely due to the lack of hydrogen bonding partners. TG-MS results revealed that the evolution rate of intact salicylic acid steadily decreased over this temperature range, whereas the evolution rate of phenol, a decomposition product of salicylic acid, increased rapidly, maximizing near 245 °C for KMMT and NaMMT samples and at 259 °C for the sample containing CaMMT.

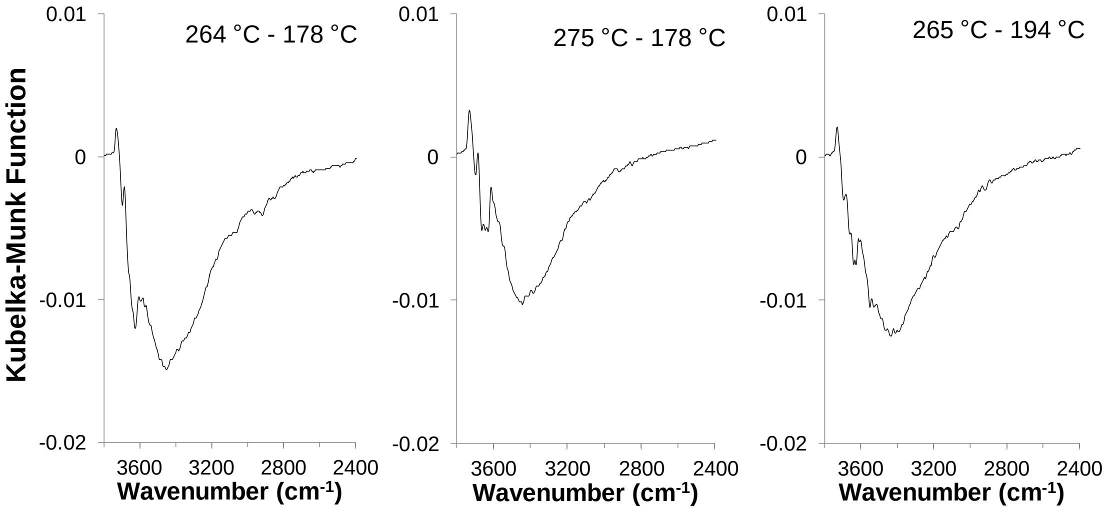

Figure 6.16 – Expansion of O-H stretching region of difference spectra region for 11% salicylic acid on KMMT (left), NaMMT (center), and CaMMT (right).

The C=O stretching vibration and O-H in-plane bending regions of difference spectra obtained for Temperature Interval V are shown in Figure 6.17. The C=O stretching vibration band intensity loss occurred at higher wavenumbers for the KMMT and NaMMT samples than in difference spectra obtained at lower temperatures, but still not as high as for the CaMMT sample, which no longer exhibited two different C=O stretching loss contributions, but instead only one at a higher energy (1684 cm^{-1}). It is likely that this feature derives from a shift of the 1668 cm^{-1} band detected for the lower temperature interval, because the C=O stretching vibration band locations for the other two samples also exhibited blue shifts. The progression of each of these vibrations with increasing temperature are summarized for KMMT, NaMMT, and CaMMT samples in Table 6.4, Table 6.5, and Table 6.6, respectively.

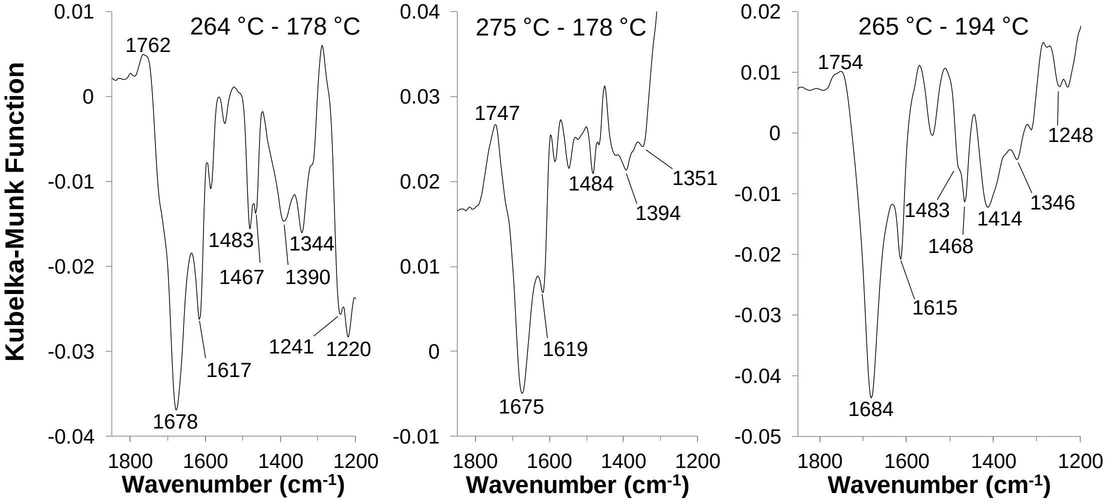

Figure 6.17 – Expansion of C=O stretching and O-H in-plane bending region of difference spectra for 11% salicylic acid on KMMT (left), NaMMT (center), and CaMMT (right).

Table 6.4 - Comparison of salicylic acid absorbance band locations over selected temperature intervals for 11% salicylic acid/KMMT. For temperature ranges, the wavenumbers shown represent the position of a negative peak in the difference spectrum. Vibration assignments taken from reference [122].

Vibration Assignment[122]	Ambient Temperature	116 – 60 °C	137 – 116 °C	178 – 137 °C	264 – 178 °C
ν(C=O) + ν(C=C) + δ(O-H)$_{carboxyl}$	1667	1666	1668	1671	1678
ν(C=O) + ν(C=C) + δ(O-H)$_{carboxyl}$	1617	1621	1618	1618	1617
ν(C=C) + δ(O-H)$_{phen}$ + δ(C-H)	1590 (shoulder)	1593	1591	1589	1587
ν(C=C) + δ(O-H)$_{phen}$ + δ(C-H)	1486	1489	1487	1486	1483
δ(O-H)$_{carboxyl}$ + δ(O-H)$_{phen}$ + δ(C-H)	1471	1471	1471	1468	1467
ν(C=C) + δ(O-H)$_{carboxyl}$ + δ(C-H)	1444	1442	1435	1428	N/A
ν(C=C) + δ(O-H)$_{phen}$ + δ(C-H)	1390	N/A	1397	1393	1390
ν(C=C) + δ(O-H)$_{carboxyl}$ + δ(O-H)$_{phen}$	1343 (weak)	1333	N/A	N/A	1344
ν(Ph-OH) + δ(O-H)$_{carboxyl}$ + δ(C-H)	1293 (shoulder)	1291	1282	N/A	N/A
ν(C=C) + δ(O-H)$_{carboxyl}$ + δ(C-H)	N/A	1239	1232	1236	1240

Table 6.5 - Comparison of salicylic acid absorbance band locations over selected temperature intervals for 11% salicylic acid/NaMMT. For temperature ranges, the wavenumbers shown represent the position of a negative peak in the difference spectrum. Vibration assignments taken from reference [122].

Vibration Assignment[122]	Ambient Temperature	101 – 60 °C	132 – 101 °C	178 – 132 °C	275 – 178 °C
$\nu(C=O)$ + $\nu(C=C)$ + $\delta(O\text{-}H)_{carboxyl}$	1666	1664	1667	1669	1675
$\nu(C=O)$ + $\nu(C=C)$ + $\delta(O\text{-}H)_{carboxyl}$	1617	1623	1619	1618	1619
$\nu(C=C)$ + $\delta(O\text{-}H)_{phen}$ + $\delta(C\text{-}H)$	1590 (shoulder)	1594	1591	1590	1586
$\nu(C=C)$ + $\delta(O\text{-}H)_{phen}$ + $\delta(C\text{-}H)$	1486	1491	1487	1487	1484
$\delta(O\text{-}H)_{carboxyl}$ + $\delta(O\text{-}H)_{phen}$ + $\delta(C\text{-}H)$	1471	1472	1471	1470	1467
$\nu(C=C)$ + $\delta(O\text{-}H)_{carboxyl}$ + $\delta(C\text{-}H)$	1448	1445	1440	1430	1423
$\nu(C=C)$ + $\delta(O\text{-}H)_{phen}$ + $\delta(C\text{-}H)$	1386	N/A	N/A	N/A	1394
$\nu(C=C)$ + $\delta(O\text{-}H)_{carboxyl}$ + $\delta(O\text{-}H)_{phen}$	1344 (weak)	N/A	N/A	N/A	1351
$\nu(Ph\text{-}OH)$ + $\delta(O\text{-}H)_{carboxyl}$ + $\delta(C\text{-}H)$	1293 (shoulder)	1293	1290	1286	1279
$\nu(C=C)$ + $\delta(O\text{-}H)_{carboxyl}$ + $\delta(C\text{-}H)$	N/A	1241	1238	1240	1238

Table 6.6 - Comparison of salicylic acid absorbance band locations over selected temperature intervals for 11% salicylic acid/CaMMT. For temperature ranges, the wavenumbers shown represent the position of a negative peak in the difference spectrum. Vibration assignments are taken from reference [122].

Vibration Assignment[122]	Ambient Temperature	112 – 61 °C	163 – 112 °C	194 – 163 °C	264 – 178 °C
$\nu(C{=}O) + \nu(C{=}C) + \delta(O\text{-}H)_{carboxyl}$	1668 (shoulder near 1683)	1662	1687 (shoulder at 1668)	1668 (shoulder at 1687)	1684
$\nu(C{=}O) + \nu(C{=}C) + \delta(O\text{-}H)_{carboxyl}$	1615	1623	1618	1618	1615
$\nu(C{=}C) + \delta(O\text{-}H)_{phen} + \delta(C\text{-}H)$	1590 (shoulder)	1592	1587	1583	N/A
$\nu(C{=}C) + \delta(O\text{-}H)_{phen} + \delta(C\text{-}H)$	1486	1491	1487	1486	1483
$\delta(O\text{-}H)_{carboxyl} + \delta(O\text{-}H)_{phen} + \delta(C\text{-}H)$	1467	1473	1471	1471	1468
$\nu(C{=}C) + \delta(O\text{-}H)_{carboxyl} + \delta(C\text{-}H)$	~1455 (shoulder)	1441	1433	1430	1414
$\nu(C{=}C) + \delta(O\text{-}H)_{phen} + \delta(C\text{-}H)$	1388	1398	1392	1397	N/A
$\nu(C{=}C) + \delta(O\text{-}H)_{carboxyl} + \delta(O\text{-}H)_{phen}$	~1343 (shoulder)	N/A	N/A	N/A	1346
$\nu(Ph\text{-}OH) + \delta(O\text{-}H)_{carboxyl} + \delta(C\text{-}H)$	~1295 (weak shoulder)	1287	1280	1281	1277
$\nu(C{=}C) + \delta(O\text{-}H)_{carboxyl} + \delta(C\text{-}H)$	N/A	1235	1239	1241	1248

In general, C=O stretching vibrations shifted to higher wavenumbers, and O-H in-plane bending vibrations shifted to slightly lower wavenumbers as continued sample heating resulted in more and more extensive sample dehydration, consistent with observations for benzoic acid samples.[70] For benzoic acid, this indicated that at low temperatures, prior to water desorption, adsorbate vibrations were more similar to those for the benzoic acid dimer, whereas the loss of hydrogen-bonding partners resulted in vibrations more similar to the monomer. To determine if this trend also occurred for salicylic acid, density-functional theory calculations were performed at the B3LYP/cc-pVTZ level and were compared to computational results reported by Boczar, *et al*.[122] (Table 6.7). Calculated vibrational frequencies were scaled by 0.9764. Although the results for the salicylic acid monomer were more similar to those for the dimer than the corresponding values for benzoic acid, the trends were similar. The C=O stretching vibration of the monomer appeared at a higher wavenumber, whereas several of the O-H in-plane bending vibrations appeared at lower wavenumbers for the monomer (Table 6.7). Some of the vibrations, especially ring stretching vibrations, were not significantly different between the monomer and dimer. These results confirm that salicylic acid/clay sample dehydration has a similar effect on the salicylic acid environment to that of benzoic acid adsorbate.

Table 6.7 - Vibration band assignments for salicylic acid. Assignments and calculated salicylic acid dimer values were taken from reference [122]. Vibrational frequencies for the salicylic acid dimer and monomer were calculated at the B3LYP/cc-pVTZ level and scaled by 0.9764. ν = stretching vibration, δ = in-plane bending vibration

Vibration Assignment[122]	Dimer[122]	Dimer	Monomer
ν(C=O) + ν(C=C) + δ(O-H)$_{\text{carboxyl}}$	1655	1655	1691
ν(C=O) + ν(C=C) + δ(O-H)$_{\text{carboxyl}}$	1614	1614	1618
ν(C=C) + δ(O-H)$_{\text{phen}}$ + δ(C-H)	1580	1580	1584
ν(C=C) + δ(O-H)$_{\text{phen}}$ + δ(C-H)	1486	1487	1489
δ(O-H)$_{\text{carboxyl}}$ + δ(O-H)$_{\text{phen}}$ + δ(C-H)	1459	1458	1461
ν(C=C) + δ(O-H)$_{\text{carboxyl}}$ + δ(C-H)	1449	1448	1404
ν(C=C) + δ(O-H)$_{\text{phen}}$ + δ(C-H)	1380	1381	1365
ν(C=C) + δ(O-H)$_{\text{carboxyl}}$ + δ(O-H)$_{\text{phen}}$	1330	1330	1323
ν(Ph-OH) + δ(O-H)$_{\text{carboxyl}}$ + δ(C-H)	1315	1315	1274
ν(C=C) + δ(O-H)$_{\text{carboxyl}}$ + δ(C-H)	1247	1247	N/A
δ(O-H)$_{\text{phen}}$ + δ(C-H)	1224	1227	1229

6.4 Acetylsalicylic Acid Desorption from Potassium, Sodium, and Calcium Montmorillonite Clays

In a similar manner described for analysis of salicylic acid/clay samples, VT-DRIFTS studies were employed to characterize temperature-dependent changes that occurred in KMMT, NaMMT, and CaMMT samples containing 15% (w/w) acetylsalicylic acid. Figure 6.18 shows ambient temperature DRIFTS spectra of 15% acetylsalicylic acid adsorbed on (a) KMMT, (b) NaMMT, (c) CaMMT, and (d) silver powder. The inset shows an expansion of the acetylsalicylic acid C=O stretching and O-H in-plane bending regions, where the peaks associated with acetylsalicylic acid are most easily distinguished from the clay absorbances. Like salicylic acid, infrared absorptions corresponding to acetylsalicylic acid were significantly muted when adsorbed on the clays. The most prominent acetylsalicylic acid/clay spectral features corresponded to the C=O stretching vibrations of the ester and carboxylic acid groups, which appeared at 1753 and 1688 cm^{-1}, respectively, for the silver-diluted sample. When adsorbed on clays, the carboxylic acid C=O stretching vibration band is located at 1710 cm^{-1}. The ester C=O stretching vibration band was not clearly visible in the CaMMT sample spectrum, but may be red shifted due to hydrogen bonding, so that it overlaps the broad 1710 cm^{-1} feature. Shoulders at 1740 and 1737 cm^{-1} represent the ester C=O stretching vibration bands in spectra obtained for KMMT and NaMMT samples, respectively.

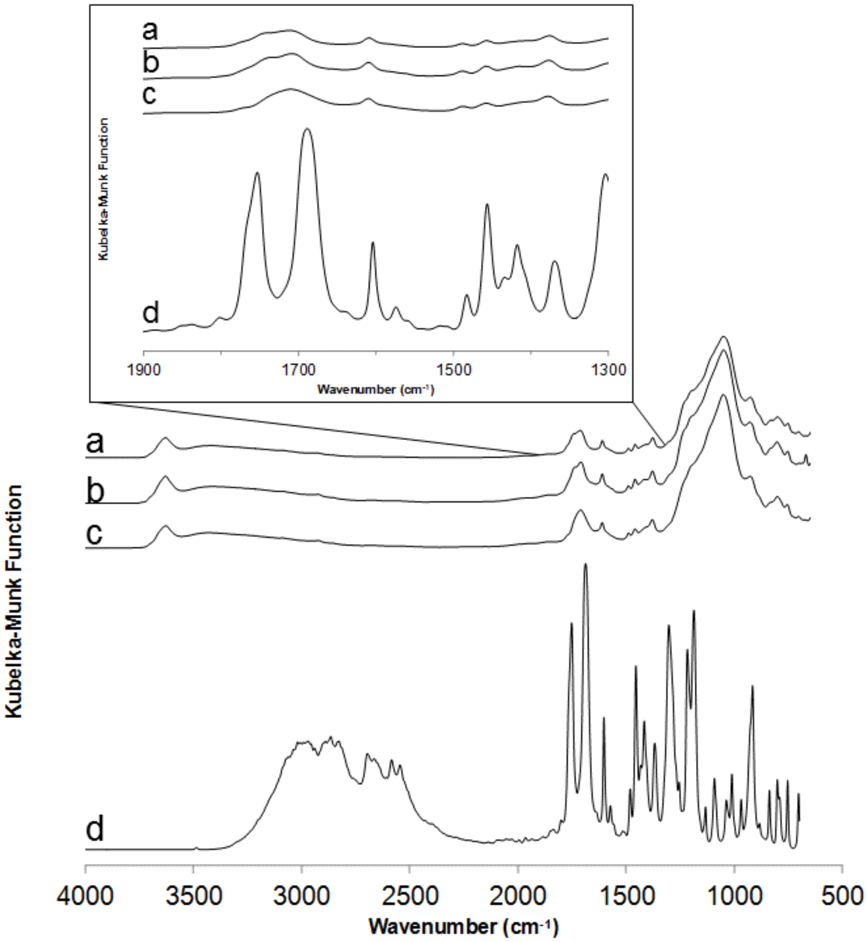

Figure 6.18 - DRIFTS spectra of samples containing 15% (w/w) acetylsalicylic acid with (a) KMMT, (b) NaMMT, (c) CaMMT, and (d) silver powder. Inset shows expansion of the 1300 – 1900 cm^{-1} wavenumber range.

Absorbance band locations in acetylsalicylic acid/silver powder spectral features are consistent with values reported by Boczar, *et al*., for the acetylsalicylic acid dimer.[123] They used theoretical modeling to assign these acetylsalicylic acid vibrations. Table 6.8 shows their band assignments and measured values, and provides a comparison to results obtained for samples of acetylsalicylic acid diluted in silver powder, and adsorbed on potassium, sodium, and calcium montmorillonites. Only the C=O stretching and O-H in-plane bending regions are included in the table, because those bands changed the most when samples were heated.

Table 6.8 – Vibration band assignments for acetylsalicylic acid (aspirin). Assignments and aspirin dimer absorbance values taken from reference [123]. ν = stretching vibration, δ = in-plane bending vibration

Vibration Assignment[123]	Aspirin Dimer[123]	Aspirin/ Silver Powder	Aspirin/ KMMT	Aspirin/ NaMMT	Aspirin/ CaMMT
$\nu(C=O)_{ester}$	1754	1753	1740	1737	N/A
$\nu(C=O)_{carboxyl}$ + δ(O-H)	1691	1688	1710	1710	1710
ν(C=C)	1606	1604	1610	1610	1610
ν(C=C)	1575	1574	~1582 (weak)	~1581 (weak)	~1582 (weak)
ν(C=C) + δ(C-H) + δ(O-H)	1483	1482	1488	1490	1488
ν(C=C) + δ(C-H) + $\delta(CH_3)$	1457	1456	1457	1458	1459
$\delta(CH_3)$	1435	1434	~1431 (very weak)	N/A	N/A
δ(O-H)	1420	1417	~1412 (shoulder)	1413	~1411 (shoulder)
$\delta(CH_3)$	1370	1369	1376	1378	1378
δ(O-H) + ν(C=C)	1306	1304	~1305 (shoulder)	~1301 (shoulder)	~1305 (shoulder)

Like salicylic acid/clay samples, samples containing acetylsalicylic acid were heated at 5 °C/minute from ambient temperature up to 400 °C, and spectra were collected every minute. Successive spectra were compared in order to identify significant transitions that occurred during heating. The identified transitions were used to demarcate temperature ranges of interest. Spectra collected below 60 °C show effects of water loss only, and are discussed in Chapter 4. Above 60 °C, five more temperature intervals were identified in VT-DRIFTS spectra for 15% acetylsalicylic acid/clay samples (Table 6.9).

Table 6.9 - Temperature Intervals Identified in VT-DRIFTS Difference Spectra for 15% (w/w) Acetylsalicylic Acid/Clay Samples.

Temperature Interval Identifier	Temperature Interval (°C)		
	KMMT	NaMMT	CaMMT
Interval I	RT – 60	RT – 60	RT – 61
Interval II	60 – 91	60 – 96	61 – 71
Interval III	91 – 137	96 – 142	71 – 107
Interval IV	137 – 157	142 – 168	107 – 173
Interval V	157 – 218	168 – 198	173 – 193
Interval VI	218 – 264	198 – 254	193 – 280

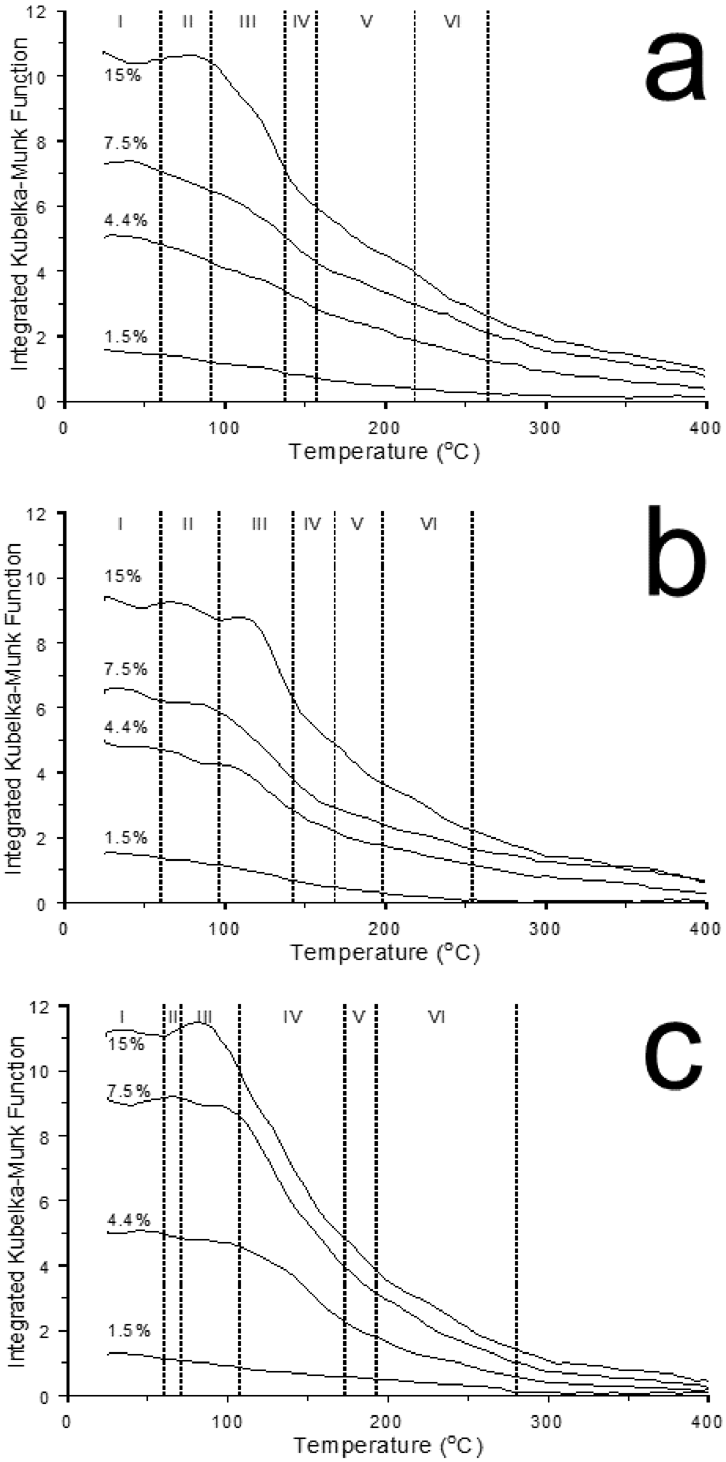

Figure 6.19 – Integrated Kubelka-Munk function obtained from spectra over the 1650 – 1800 cm^{-1} range for (a) KMMT, (b) NaMMT, and (c) CaMMT samples containing various loadings of acetylsalicylic acid, plotted *vs*. temperature. Dashed lines denote cutoff temperatures used for difference spectra calculations (Table 6.9).

Figure 6.19 shows the integrated Kubelka-Munk function over the 1650 – 1800 cm^{-1} range in spectra obtained for (a) KMMT, (b) NaMMT, and (c) CaMMT samples containing various loadings of acetylsalicylic acid, plotted *vs*. temperature. Dashed lines denote temperatures used for difference spectra calculations over the temperature intervals indicated in Table 6.9. Integrated peak areas do not change significantly over Temperature Interval I. Figure 4.13, Figure 4.14, and Figure 4.15 show significant positive and negative peaks, indicating significant changes to the local sample environment due to dehydration. TG-MS results (Figures D.5-D.7) indicated that acetylsalicylic acid did not decompose below 60 °C. Above 60 °C, integrated peak areas initially increased, but subsequently decreased for all three samples starting at temperatures below 100 °C. For the KMMT and NaMMT samples, Temperature Interval II included both increasing and decreasing portions of the integrated area plot, but Temperature Interval II was very narrow for the CaMMT sample, and did not include peak area decreases. The fact that the integrated peak area continued to increase even after acetylsalicylic acid began to decompose near 60 °C likely indicates that the changing environment for the remaining aspirin and salicylic acid molecules resulted in an absorptivity increase sufficient to counter absorbance losses caused by adsorbate loss. However, with the onset of salicylic acid desorption near 100 °C, adsorbate losses increased and the integrated peak area decreased over Temperature Intervals III – VI, although results for the NaMMT sample exhibited a local maximum in Temperature Interval III.

Figure 6.20 shows overlaid VT-DRIFTS spectra obtained for the KMMT sample containing 15% acetylsalicylic acid collected at 60 and 91 °C (top). The 60 °C spectrum was subtracted from the 91 °C spectrum to produce the difference spectrum (bottom). Temperature Interval II is characterized by water loss and the start of acetylsalicylic acid decomposition to form salicylic acid and acetic acid. VT-DRIFTS spectra and difference spectra obtained over Temperature Interval II are shown for the acetylsalicylic acid/NaMMT sample in Figure 6.21 and for the acetylsalicylic acid/CaMMT sample in Figure 6.22.

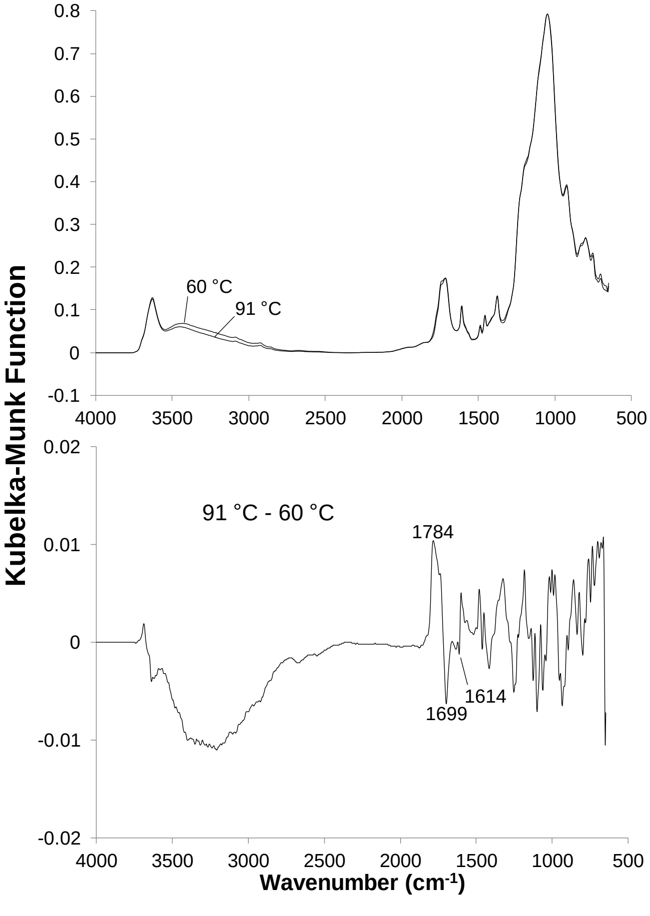

Figure 6.20 - VT-DRIFTS spectra for potassium montmorillonite containing 15% (w/w) acetylsalicylic acid. The overlaid spectra shown at the top were subtracted to produce the difference spectrum at the bottom.

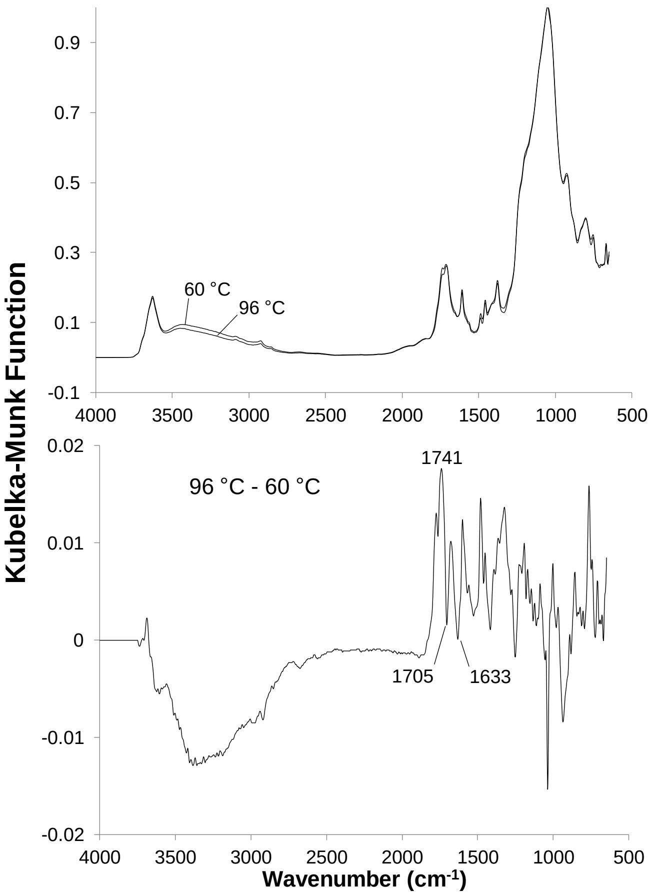

Figure 6.21 - VT-DRIFTS spectra for sodium montmorillonite containing 15% (w/w) acetylsalicylic acid. The overlaid spectra shown at the top were subtracted to produce the difference spectrum at the bottom.

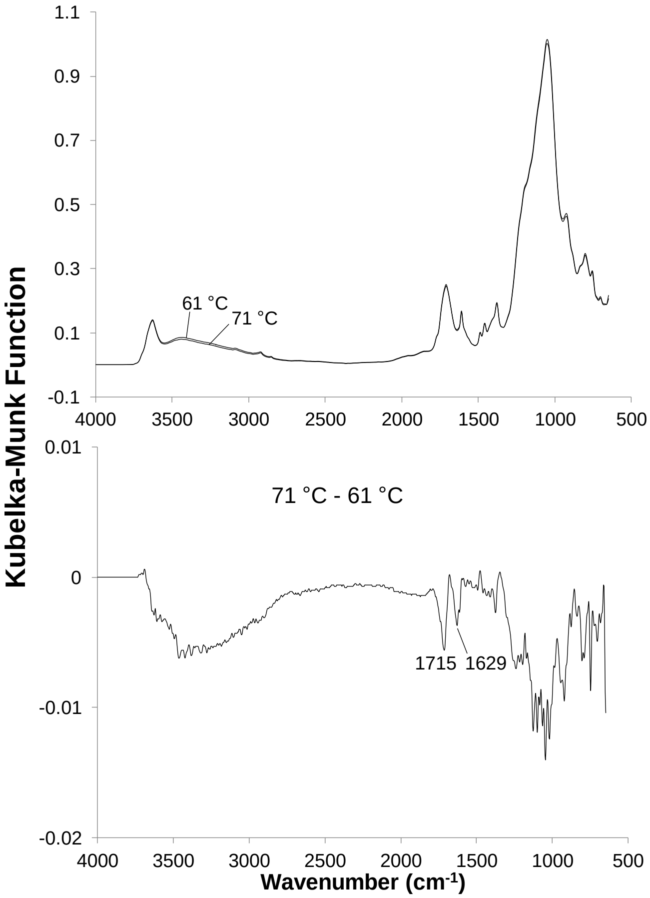

Figure 6.22 - VT-DRIFTS spectra for calcium montmorillonite containing 15% (w/w) acetylsalicylic acid. The overlaid spectra shown at the top were subtracted to produce the difference spectrum at the bottom.

Expanded plots from 2400 to 3700 cm^{-1} of difference spectra contained in Figure 6.20-Figure 6.22 are shown in Figure 6.23. Like the corresponding results obtained for the salicylic acid/clay samples, these difference spectra show small, positive peaks near 3691, with shoulders near 3720, which represent inorganic oxide hydroxyl groups that lost hydrogen bonding partners due to sample heating. Also like the salicylic acid sample results, the acetylsalicylic acid/KMMT sample difference spectrum exhibits a minimum near 3200 cm^{-1}. In contrast, minima for the NaMMT and CaMMT samples occur at higher wavenumbers.

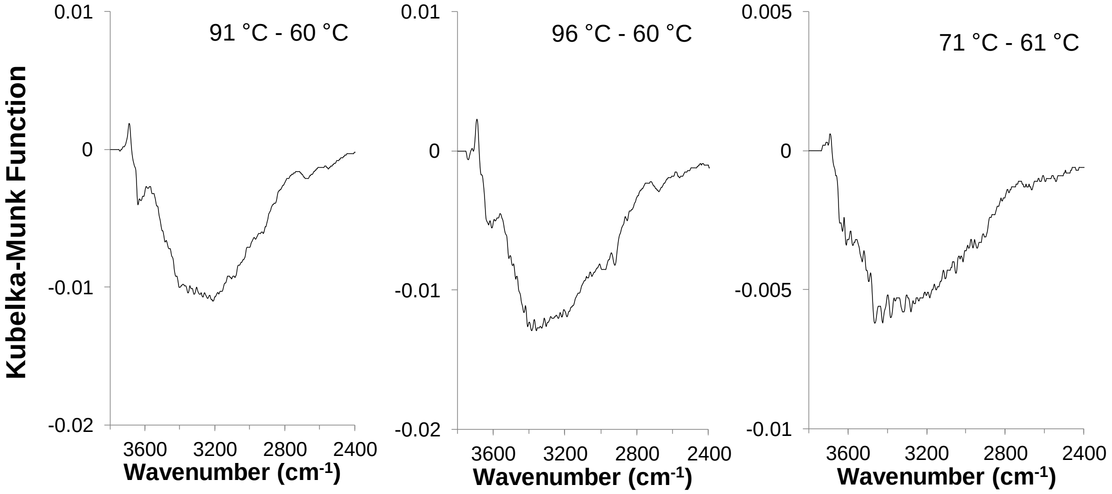

Figure 6.23 – Expansion of O-H stretching region of difference spectra for 15% acetylsalicylic acid on KMMT (left), NaMMT (center), and CaMMT (right).

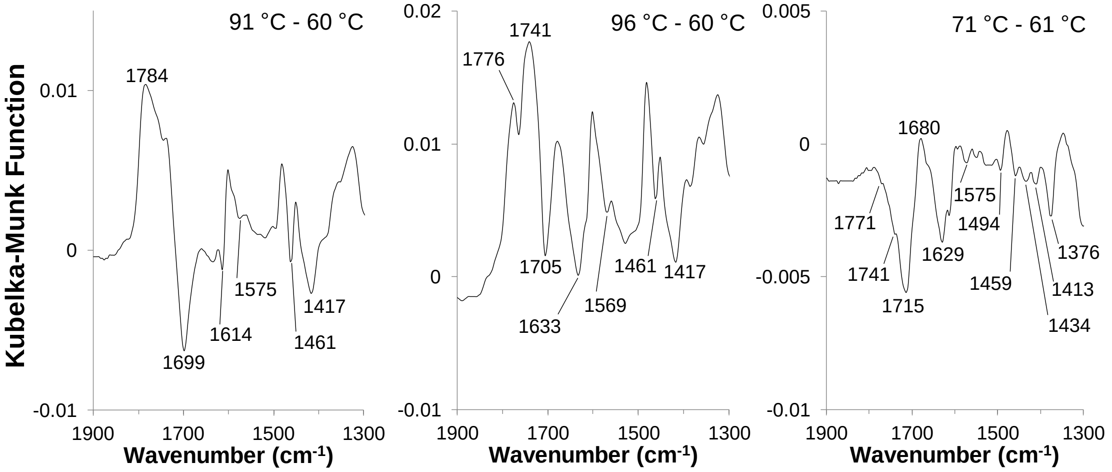

Figure 6.24 – Expansion of C=O stretching and O-H in-plane bending region of difference spectra for 15% acetylsalicylic acid on KMMT (left), NaMMT (center), and CaMMT (right).

The C=O and O-H in-plane bending spectral regions for Temperature Interval II are shown for (left to right) KMMT, NaMMT, and CaMMT samples containing 15% acetylsalicylic acid in Figure 6.24. The loss of carboxylic acid C=O stretching vibration band intensity exhibits a significant dependence on interlayer cation, appearing at 1699

cm^{-1} for KMMT, 1705 cm^{-1} for NaMMT, and 1715 cm^{-1} for CaMMT samples. The trend that the negative C=O stretching vibration band reflected higher energy when acetylsalicylic acid was adsorbed on CaMMT compared to the other clays is consistent with previous findings for benzoic acid, and is consistent with a model in which acetylsalicylic acid carboxylic acid C=O groups interact with interlayer cations through water bridges.[41, 69, 70] Another similarity to results obtained for benzoic acid is that the KMMT and NaMMT samples show increases in C=O stretching intensity at higher wavenumbers, but the CaMMT sample does not. The CaMMT sample has negative shoulders near 1741 and 1771 cm^{-1}, which is consistent with the behavior of all three samples at higher temperatures (*vide infra*). The acetylsalicylic acid/KMMT sample spectrum contains a negative peak at 1614 cm^{-1}, likely due to loss of ring stretching intensity, and a negative peak at 1633 cm^{-1} which can be assigned to the loss of water bending vibration intensity. The NaMMT and CaMMT samples also lost water bending vibration band intensity, at 1633 cm^{-1} and 1629 cm^{-1}, respectively. These features had shoulders near 1614 cm^{-1}, likely representing loss of ring stretching band intensity. Because the ring stretching vibration band wavenumbers do not show a dependence on the cation, it is apparent that acetylsalicylic acid, like benzoic acid and salicylic acid, interacts with interlayer cations primarily through its polar carboxylic acid group, rather than the aromatic ring.

Figure 6.25 shows difference spectra O-H stretching vibration band regions for (left to right) KMMT, NaMMT, and CaMMT samples containing 15% acetylsalicylic acid over Temperature Interval III. Most features are similar to those identified in Temperature Interval II (Figure 6.23), with the exception that the minimum for all three samples appeared near 3400 cm^{-1}. Although water still evolved from samples during this temperature range, there were fewer hydrogen bonding partners available compared to lower temperatures, accounting for slightly higher vibration energies associated with lost O-H groups.

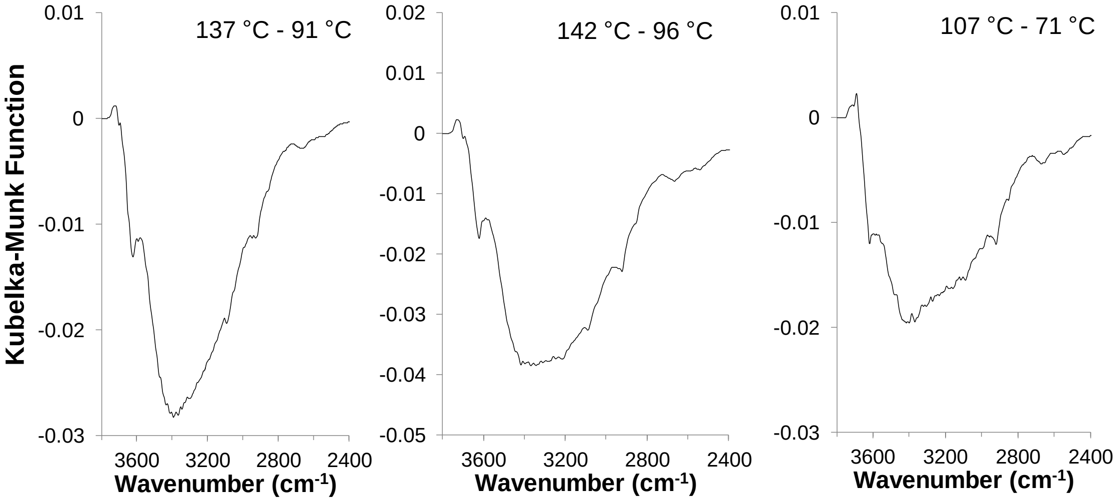

Figure 6.25 - Expansion of O-H stretching region of difference spectra for 15% acetylsalicylic acid on KMMT (left), NaMMT (center), and CaMMT (right).

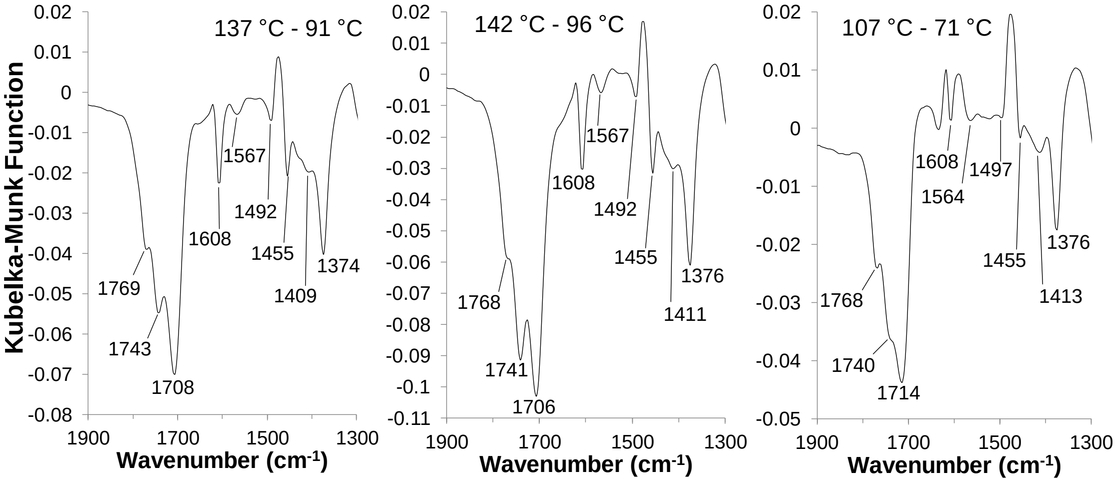

Figure 6.26 – Expansion of C=O stretching and O-H in-plane bending region of difference spectra for 15% acetylsalicylic acid on KMMT (left), NaMMT (center), and CaMMT (right).

The C=O stretching and O-H in-plane bending difference spectra regions corresponding to Temperature Interval III are shown in Figure 6.26. The loss of carboxylic acid C=O stretching vibration band intensity occurred at a higher wavenumber for CaMMT (1714 cm^{-1}) than for KMMT (1708 cm^{-1}) and NaMMT (1706 cm^{-1}) samples. The shoulders near 1768 cm^{-1} apparent in each spectrum may be assigned to the loss of ester C=O stretching vibration bands that had blue shifted to these wavenumbers at lower temperatures. The negative peaks near 1740 cm^{-1} for each sample can be attributed to loss of stretching vibration intensity of ester C=O groups that were still involved in hydrogen bonding. Acetylsalicylic acid decomposition occurred over this temperature range, which resulted in formation of salicylic and acetic acids. TG-MS results showed that acetic acid immediately evolved after it was formed, but that salicylic acid remained on the clay, beginning to desorb near 115, 100, and 81 °C for KMMT, NaMMT, and CaMMT samples, respectively.

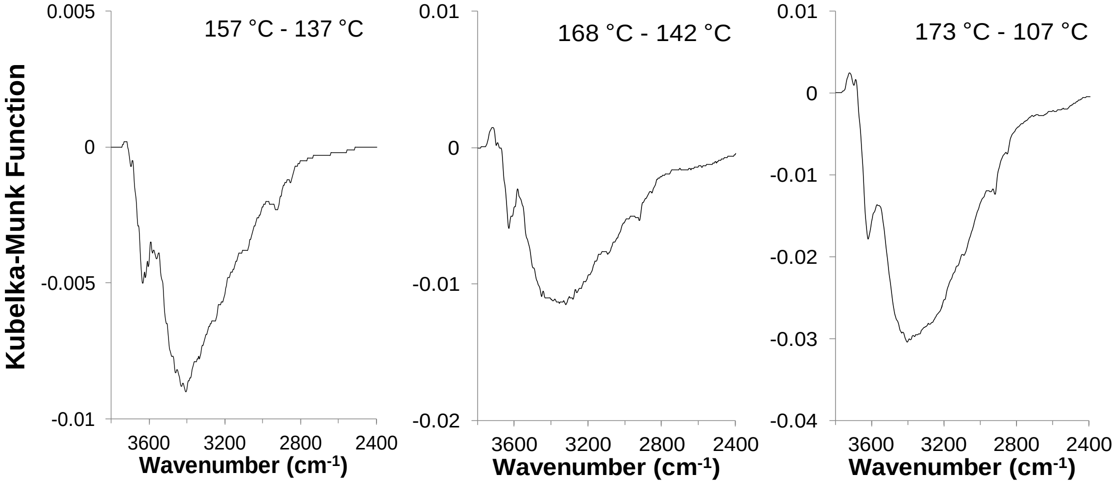

Figure 6.27 – Expansion of O-H stretching region of difference spectra for 15% acetylsalicylic acid on KMMT (left), NaMMT (center), and CaMMT (right).

Figure 6.27 shows O-H stretching vibration band regions from difference spectra obtained for Temperature Interval IV. Although band minima still appear near 3400 cm^{-1}, bands are narrower compared to those obtained at lower temperatures, suggesting that fewer hydrogen-bonded O-H groups were lost over this temperature range. TG-MS results indicated that the maximum rates of salicylic acid evolution occurred near 140 °C for KMMT and NaMMT samples, and at 167 °C for CaMMT.

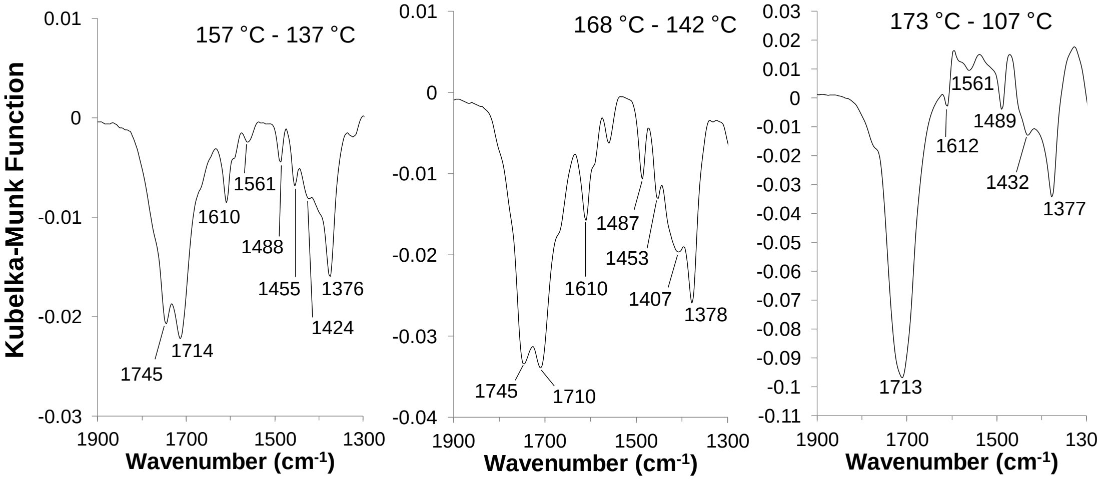

Figure 6.28 – Expansion of C=O stretching and O-H in-plane bending region of difference spectra for 15% acetylsalicylic acid on KMMT (left), NaMMT (center), and CaMMT (right).

Figure 6.28 shows C=O stretching and O-H in-plane bending vibration band regions from difference spectra obtained over Temperature Interval IV. In comparison to lower temperatures, the carboxylic acid C=O stretching vibration band intensity loss continued to shift to higher wavenumbers for KMMT (1714 cm^{-1}) and NaMMT (1710 cm^{-1}). In contrast, the negative C=O stretching vibration band location remained relatively unchanged (1713 cm^{-1}) for the CaMMT sample. Spectra for the KMMT and NaMMT samples still exhibited a loss of ester C=O stretching vibration band intensity at 1745 cm^{-1}, but this band was not apparent in the difference spectrum for the CaMMT sample, except for a slight shoulder. This may indicate that most of the acetylsalicylic acid had been converted to salicylic acid at 173 °C for the sample containing CaMMT. Additionally, the fact that no C=O stretching vibrations were visible at higher wavenumbers (*e.g.*, 1768 cm^{-1} in Temperature Interval III, Figure 6.26) suggests that the acetylsalicylic acid molecules with ester groups that lost hydrogen bonding had decomposed at lower temperatures, and only hydrogen bonded ester groups remained during Temperature Interval IV.

The O-H stretching vibration band region difference spectra obtained for Temperature Interval V are shown in Figure 6.29. Spectral features were less broad and less intense than those obtained at lower temperatures, and minima for the KMMT and NaMMT samples were blue shifted to wavenumbers above 3400 cm^{-1} relative to spectra obtained at lower temperatures.

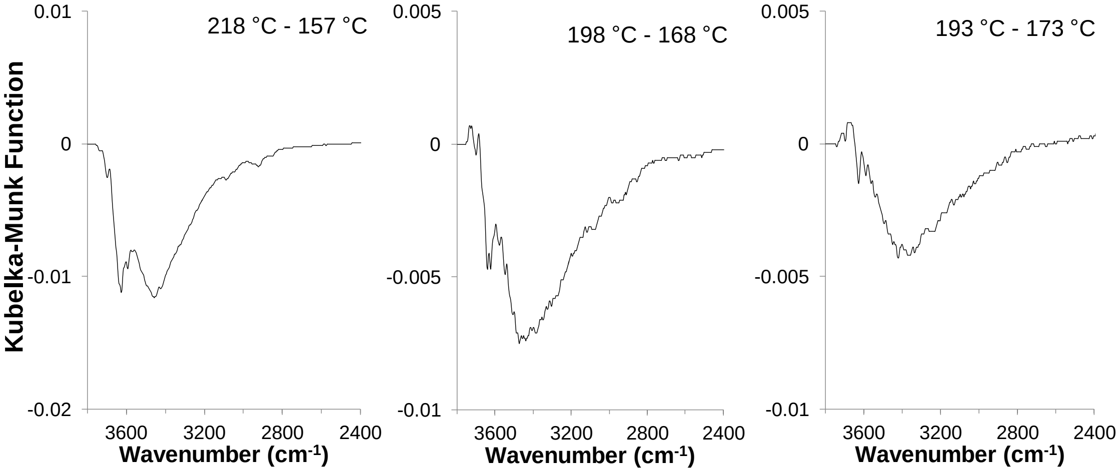

Figure 6.29 – Expansion of O-H stretching region of difference spectra for 15% acetylsalicylic acid on KMMT (left), NaMMT (center), and CaMMT (right).

Figure 6.30 shows the C=O stretching and O-H in-plane bending vibration band regions of difference spectra obtained for Temperature Interval V. These three spectra are quite different over this temperature range. The KMMT sample exhibits a negative shoulder near 1745 cm^{-1}, indicating loss of ester C=O stretching band intensity. This band is not apparent in difference spectra for the other two samples, likely because the conversion of acetylsalicylic acid to salicylic and acetic acids had completed for samples containing NaMMT and CaMMT. This hypothesis is supported by TG-MS results for these samples. The carboxylic acid C=O stretching band loss was observed at 1724 cm^{-1} for the KMMT sample, 1718 cm^{-1} for the NaMMT sample, and at 1699 cm^{-1} for the CaMMT sample. The CaMMT sample spectrum also exhibits a distinct shoulder near 1684 cm^{-1}, and a less obvious shoulder near 1670 cm^{-1}. Over a similar temperature range, the salicylic acid/CaMMT sample difference spectrum contained a large negative band at 1668 cm^{-1} with a shoulder near 1687 cm^{-1} (Figure 6.15). The acetylsalicylic acid/CaMMT sample spectrum also contains a negative band at 1617 cm^{-1}, which is significantly higher wavenumber than previously detected ring-stretching vibrations, but quite close to the negative band at 1618 cm^{-1} in Figure 6.15 obtained for the salicylic acid/CaMMT sample over a similar temperature range. Apparently, sufficient acetylsalicylic acid had been converted to salicylic acid over this temperature range that salicylic acid desorption was primarily occurring. The same effect may explain results obtained for the NaMMT sample, but the shoulder at 1682 cm^{-1} is located at a significantly higher wavenumber than the C=O stretching vibration band intensity loss detected for the salicylic acid/NaMMT sample over a comparable temperature range.

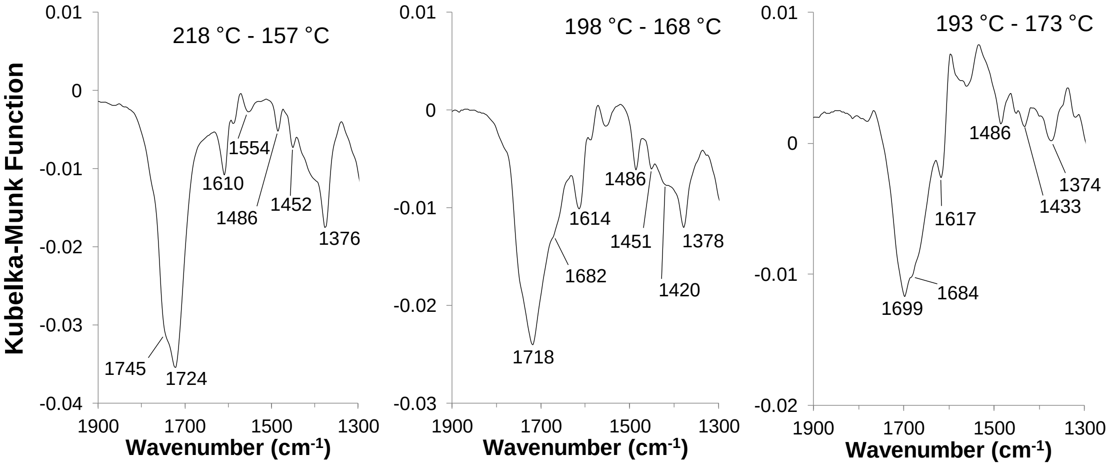

Figure 6.30 – Expansion of C=O stretching and O-H in-plane bending region of difference spectra for 15% acetylsalicylic acid on KMMT (left), NaMMT (center), and CaMMT (right).

The difference spectra O-H stretching vibration band regions obtained from VT-DRIFTS measurements over the highest temperature ranges (i.e. Temperature Interval VI) are shown in Figure 6.31. Band minima in spectra for all three samples occurred at wavenumbers above 3400 cm^{-1}, which is consistent with a continuing trend of reduced hydrogen bonding with increased sample temperature.

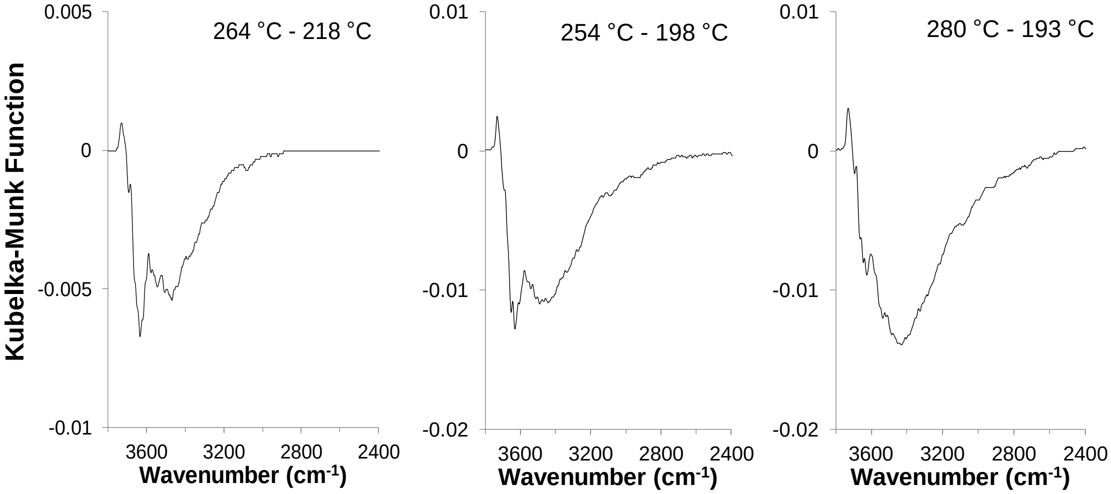

Figure 6.31 – Expansion of O-H stretching region of difference spectra for 15% acetylsalicylic acid on KMMT (left), NaMMT (center), and CaMMT (right).

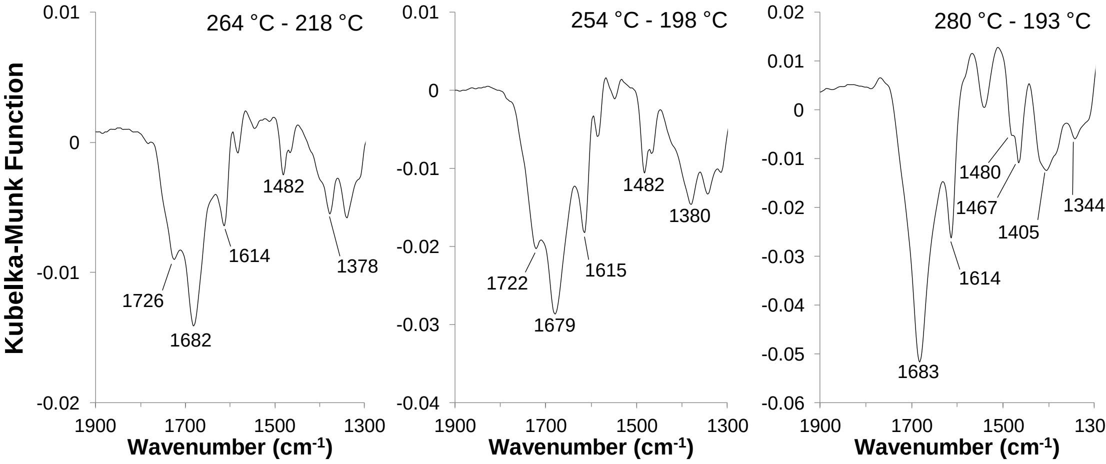

Figure 6.32 – Expansion of C=O stretching and O-H in-plane bending region of difference spectra for 15% acetylsalicylic acid on KMMT (left), NaMMT (center), and CaMMT (right).

Figure 6.32 shows the C=O stretching and O-H in-plane bending vibration band regions from difference spectra obtained for Temperature Interval VI. The difference spectrum for the CaMMT sample (right) is very similar to the difference spectrum for the salicylic acid/CaMMT sample obtained over a comparable temperature range (Figure 6.17). Apparently, little acetylsalicylic acid remained at this temperature, so mainly salicylic acid loss features were detected in the difference spectrum. This is consistent with TG-MS results for this sample, which indicated that the m/z 60 profile (acetic acid, which maximized at 103 °C) was returning to baseline at 200 °C, and that salicylic acid desorption and decomposition processes dominated, as shown by the m/z 120 profile, which exhibited a maximum evolution rate at 167 °C, and the m/z 94 profile, which maximized at 263 °C. The KMMT and NaMMT samples spectra in Figure 6.32 contain bands similar to those obtained for salicylic acid/clay samples over comparable temperature ranges (Figure 6.17), but also exhibited acetylsalicylic acid carboxylic acid C=O stretching vibration band intensity losses at 1726 cm^{-1} and 1722

cm^{-1} (KMMT and NaMMT samples, respectively). TG-MS results indicated that the m/z 60 profile extended to higher temperatures for samples containing KMMT and NaMMT than for CaMMT samples, which would explain why spectra would reflect loss of acetylsalicylic acid along with salicylic acid desorption, even though salicylic acid was decomposing during this temperature range. The salicylic acid evolution rate steadily decreased during this temperature range, and the phenol evolution rate increased, maximizing at 238 °C for the NaMMT sample and at 254 °C for the KMMT sample. Changes in selected acetylsalicylic acid vibration band locations as a function of temperature are summarized in Table 6.10, Table 6.11, and Table 6.12.

Table 6.10 - Comparison of acetylsalicylic acid absorbance band locations over selected temperature intervals for 15% acetylsalicylic acid/KMMT. For temperature ranges, the wavenumbers shown represent the position of a negative peak in the difference spectrum. Vibration assignments are taken from reference [123].

Vibration Assignment[123]	Ambient Temperature	91 – 60 °C	137 – 91 °C	157 – 137 °C	218 – 157 °C	264 – 218 °C
$\nu(C=O)_{ester}$	1740	N/A	1743	1745	1745	N/A
$\nu(C=O)_{carboxyl} + \delta(O\text{-}H)$	1710	1699	1708	1714	1724	1726/ 1682
$\nu(C=C)$	1610	1614	1608	1610	1610	1614
$\nu(C=C)$	~1582 (weak)	1575	1567	1561	1554	1546
$\nu(C=C) + \delta(C\text{-}H) + \delta(O\text{-}H)$	1488	1496	1492	1488	1486	1482
$\nu(C=C) + \delta(C\text{-}H) + \delta(CH_3)$	1457	1461	1455	1455	1452	N/A
$\delta(CH_3)$	~1431 (very weak)	N/A	N/A	1424	N/A	N/A
$\delta(O\text{-}H)$	~1412 (shoulder)	1417	1409	N/A	N/A	N/A
$\delta(CH_3)$	1376	1384	1374	1376	1376	1378

Table 6.11 - Comparison of acetylsalicylic acid absorbance band locations over selected temperature intervals for 15% acetylsalicylic acid/NaMMT. For temperature ranges, the wavenumbers shown represent the position of a negative peak in the difference spectrum. Vibration assignments are taken from reference [123].

Vibration Assignment[123]	Ambient Temperature	96 – 60 °C	142 – 96 °C	168 – 142 °C	198 – 168 °C	254 – 198 °C
$\nu(C=O)_{ester}$	1737	N/A	1741	1745	1745	N/A
$\nu(C=O)_{carboxyl} + \delta(O\text{-}H)$	1710	1705	1706	1710	1718	1722/ 1679
$\nu(C=C)$	1610	~1615	1608	1610	1614	1615
$\nu(C=C)$	~1581 (weak)	1569	1567	1560	1553	1548
$\nu(C=C) + \delta(C\text{-}H) + \delta(O\text{-}H)$	1490	N/A	1492	1487	1486	1482
$\nu(C=C) + \delta(C\text{-}H) + \delta(CH_3)$	1458	1462	1455	1453	1451	N/A
$\delta(CH_3)$	N/A	~1438	N/A	N/A	~1420	N/A
$\delta(O\text{-}H)$	1413	1417	1411	1407	N/A	N/A
$\delta(CH_3)$	1378	1386	1376	1378	1378	~1380

Table 6.12 - Comparison of acetylsalicylic acid absorbance band locations over selected temperature intervals for 15% acetylsalicylic acid/CaMMT. For temperature ranges, the wavenumbers shown represent the position of a negative peak in the difference spectrum. Vibration assignments are taken from reference [123].

Vibration Assignment[123]	Ambient Temperature	71 – 61 °C	107 – 71 °C	173 – 107 °C	198 – 173 °C	280 – 193 °C
$\nu(C{=}O)_{ester}$	N/A	N/A	N/A	N/A	N/A	N/A
$\nu(C{=}O)_{carboxyl} + \delta(O\text{-}H)$	1710	1715	1714	1713	1699/ ~1684	1683
$\nu(C{=}C)$	1610	1614	1608	1612	1617	1614
$\nu(C{=}C)$	~1582 (weak)	1594	N/A	~1584	~1580	N/A
$\nu(C{=}C) + \delta(C\text{-}H) + \delta(O\text{-}H)$	1488	1494	1497	1489	1486	~1480
$\nu(C{=}C) + \delta(C\text{-}H) + \delta(CH_3)$	1459	1459	1455	N/A	1451	N/A
$\delta(CH_3)$	N/A	1434	N/A	1432	1433	N/A
$\delta(O\text{-}H)$	~1411 (shoulder)	1413	1413	N/A	N/A	1405
$\delta(CH_3)$	1378	1376	1376	1378	1374	N/A

The C=O stretching vibrations of the carboxylic acid and ester functionalities shifted to higher wavenumbers while samples were heated and loss of water resulted in the loss of hydrogen bonding partners. Although the stretching vibrations associated with the aromatic ring were not significantly affected by sample dehydration, the O-H in-plane bending vibrations shifted to slightly lower wavenumbers when samples were heated. This is consistent with the behavior observed for samples containing benzoic and salicylic acids, which exhibited spectra similar to their respective dimers at lower temperatures but shifted towards monomer characteristics at higher temperatures. Vibrational frequencies for the acetylsalicylic acid monomer were calculated at the B3LYP/cc-pVTZ level and scaled by 0.9764, like the calculations for the salicylic acid monomer described in section 6.3. These calculated frequencies are compared to experimental results for the acetylsalicylic acid dimer diluted in silver powder in Table 6.13. These results show that the acetylsalicylic acid monomer exhibits higher energy C=O stretching vibrations than the dimer, but lower energy O-H in-plane bending vibrations, indicating that acetylsalicylic acid/clay sample spectra also shifted from more dimer character to more monomer character when samples were heated.

Table 6.13 - Vibration band assignments and experimental values for the acetylsalicylic acid (aspirin) dimer, and calculated values for the aspirin monomer. Assignments taken from reference [123]. ν = stretching vibration, δ = in-plane bending vibration

Vibration Assignment[123]	Aspirin/ Silver Powder	Aspirin Monomer
$\nu(C{=}O)_{ester}$	1753	1794
$\nu(C{=}O)_{carboxyl}$ + δ(O-H)	1688	1745
ν(C=C)	1604	1609
ν(C=C)	1574	1579
ν(C=C) + δ(C-H) + δ(O-H)	1482	1484
ν(C=C) + δ(C-H) + $\delta(CH_3)$	1456	1443
$\delta(CH_3)$	1434	1439
δ(O-H)	1417	1337
$\delta(CH_3)$	1369	1364
δ(O-H) + ν(C=C)	1304	1302

6.5 Summary

Desorption of salicylic and acetylsalicylic acids from potassium, sodium, and calcium montmorillonite clays were characterized by using VT-DRIFTS. Difference spectra provide information about adsorbate environment changes on a molecular level. Adsorbate aromatic ring vibrations exhibited little to no dependence on the identity of clay interlayer cations, indicating that aromatic acids interacted with cations through polar carboxylic acid functional groups rather than aromatic rings. Stretching vibrations of carboxylic acid C=O functionalities were most affected by interlayer cations, showing that the acid group plays a key role in adsorption interactions with clays. Whereas benzoic acid and acetylsalicylic acid likely adopt orientations with carboxylic acid C=O groups hydrogen bonded to water molecule bridges and oriented directly towards cations, salicylic acid may not be oriented with its C=O group aligned with a cation. Alternatively, it may orient in a similar configuration, but intramolecular hydrogen bonding may reduce the sensitivity of the C=O group to the local environment.

Chapter 7 : Conclusion

When adsorbate/clay samples were initially heated, temperature-dependent changes involved loss of water and subsequent reorganization of the hydrogen bonding network. Affected hydrogen bonds may involve interlayer water, inorganic oxide hydroxyl groups, and adsorbate functionalities. Each of these sample constituents may participate in multiple hydrogen bond interactions. Bonding interactions from multiple hydrogen bonds are not additive. For example, when X-H is involved in two hydrogen bonds, each interaction makes the X-H bond more polar, which strengthens both hydrogen bonds.[124] This property explains the tendency for bulk water to form hydrogen bonded chains and rings.[98] These structures are transient, with constituent hydrogen bonds continually breaking and reforming. The confines of montmorillonite interlayer spaces restrict hydrogen bonding networks to mainly two-dimensional structures.[98] In addition to water-water interactions, water molecules fill cation hydration spheres and form hydrogen bonds with inorganic oxide hydroxyl groups, further restricting the hydrogen bonding network flexibility. When adsorbates with hydrogen bonding capabilities are introduced, additional restrictions are placed on the hydrogen bonding network. Sample dehydration continues at higher temperatures and is accompanied by adsorbate desorption and decomposition reactions. Water loss due to dehydration causes interlayer distances to contract, which further confines adsorbate molecules. Thus, interlayer dimensions and therefore adsorbate local environments continuously change with increasing sample temperature. In fact, temperature-dependent sample changes resulted in a continuously varying solid-state structure. Consequently, different types of interactions were observed at different temperatures.

Many of the interactions characterized at high temperatures could not have occurred at lower temperature because a change in sample structure was required before these interactions were possible.

Information regarding interactions of small aromatic acid adsorbates with montmorillonite clays was collected via three different techniques: sample mass loss measurements, mass spectral analysis of volatiles evolved during heating, and FTIR analyses of clay surfaces. Mass loss data provided information regarding the temperatures at which sample losses occurred. Comparison of mass loss results for clay samples containing adsorbates with results obtained for neat clays made it possible to distinguish losses due to adsorbates from losses due to water, but did not provide information regarding what substances or processes were responsible for mass losses. Mass spectral analysis was the most sensitive analysis technique employed in these studies, and provided specific detail regarding which substances desorbed, and by inference, which substances decomposed at various sample temperatures. The temperatures at which desorption and decomposition occurred reflected the thermal stabilities of various adsorbate environments. Typically, loosely bound adsorbates desorbed at lower temperatures than more tightly bound molecules. Thus, mass selective ion signal temperature profiles associated with adsorbate desorption and decomposition for samples containing various interlayer cations and adsorbate loadings were compared to assess relative adsorption site thermal stabilities. Multiple TG-MS peaks indicated the presence of multiple adsorbate environments. Although mass spectrometric analyses did not directly provide information regarding solid state sample changes, clay analyses by FTIR provided structure-specific information regarding temperature-dependent changes to solid sample constituents, which was complementary to the information derived from thermogravimetry and mass spectrometry. Infrared spectroscopy provided a sensitive method for characterizing changes to hydrogen bonding environments. In general, increased hydrogen bond interactions resulted in O-H stretching vibration band absorptivity increases[110, 125] and O-H and C=O stretching vibration band maxima red shifts.[112, 126, 127] By combining the information provided by these three analysis techniques, a better assessment of temperature-dependent sample changes was possible than could have been accomplished by any of the three techniques separately.

At ambient temperature, the fact that infrared spectral features associated with adsorbates were significantly distorted compared to spectra for the neat acids indicated the presence of strong interactions with clays. Below 60 ^{o}C, heating adsorbate/clay samples resulted in changes to both the adsorbate and water molecule local environments. Results described here show that TG-MS m/z 18 ion signal temperature profiles can be employed to selectively monitor water molecule desorption, which can provide information regarding thermal stabilities of interlayer water molecule environments. These profiles exhibit systematic changes that can be correlated with the quantities of adsorbate added to clay samples. Maximum water evolution rates shifted to slightly lower temperatures for samples containing adsorbates, indicating that some water molecules lost during heating were destabilized, relative to the neat clay environment, by the presence of adsorbates. In addition, enhanced m/z 18 intensity was detected at higher temperatures in the m/z 18 profiles for samples containing adsorbates, which suggested that some water molecules were stabilized when adsorbates were present. These seemingly contradictory findings are consistent with molecular reorganization of the hydrogen bonding network during sample dehydration. VT-DRIFTS measurements below 60 ^{o}C also provided selective tracking of sample changes associated with water loss. Absorbance band changes that occur in the O-H stretching vibration regions of infrared spectra reflected local environment changes to adsorbate, inorganic oxide hydroxyl groups, and interlayer water molecules. Rather than revealing changes to specific hydroxyl functionalities types (i.e. inorganic oxide hydroxyls, cation hydration sphere water molecules, etc.), all VT-DRIFTS difference spectra contained broad O-H stretching vibration band features. In fact, even when differences were calculated by subtracting spectra acquired over small (i.e. 5 ^{o}C) temperature increments, broad negative O-H stretching vibration bands were obtained. This suggests that water molecule desorption does not occur in a stepwise fashion based on initial environment. Instead, as soon as the most loosely bound water molecules are removed, the remaining water molecules rearrange to form an assembly with lowest potential energy. This dynamic rearrangement affects adsorbate molecules because some water molecules that were involved in adsorbate hydrogen bonding may adopt more stable orientations that no longer involve this hydrogen bonding. Consequently, adsorbate molecule vibrations that are affected by hydrogen bonding can be altered, resulting in a frequency change, absorptivity change, or both. These changes are detected as band shape variations in difference spectra. For adsorbates employed in these studies, hydrogen bonding interactions between aromatic acid functional groups and the clay local environment stabilize these molecules. Thus, changes to carboxylic acid C=O stretching and C-O-H bending vibration band shapes reflect changes in local environment caused by sample dehydration. Although TG-MS m/z 18 ion signal temperature profile shape changes associated with sample water loss were subtle, VT-DRIFTS C=O stretching and O-H bending vibration band changes were more dramatic and provided greater selectivity with respect to the nature of adsorbate molecule environment changes. Results described and interpreted in Chapter 4 demonstrate the sensitivity of this perturbation sample analysis technique. Dehydration by heating samples from ambient temperature to 60 ^{o}C resulted in complex changes to adsorbate acid group environments that depended on the structure of the adsorbate and the clay interlayer cation. Samples containing KMMT yielded the least complexity. This can be attributed to the small ambient temperature basal spacing of KMMT, which restricts the range of orientations that adsorbate molecules can adopt. When adsorbed on KMMT, benzoic acid difference spectra features were consistent with a blue shift in C=O stretching vibration band location and minimal change in absorptivity with increasing sample temperature. Blue shifts were also observed for salicylic acid and acetylsalicylic acid adsorbed on KMMT. VT-DRIFTS difference spectra obtained for all three adsorbates on KMMT confirmed that the local environments formed as a result of sample dehydration involved higher C=O stretching vibration frequencies, which would be consistent with a reduction in hydrogen bonding interactions. However, unlike benzoic acid, salicylic acid and acetylsalicylic acid results suggested that water desorption resulted in the formation of at least two distinct new local environments. The NaMMT and CaMMT clays have larger ambient temperature basal spacings and support higher water contents, allowing more steric flexibility for adsorbate molecule orientations. This results in more complicated adsorbate spectral changes, which sometimes involve significant C=O stretching vibration band absorptivity changes along with temperature-dependent band shifts. VT-DRIFTS results tended to be most similar for the salicylic and acetylsalicylic acid samples, both of which show evidence for the creation of multiple new local environments after dehydration. Unlike acetylsalicylic acid, salicylic acid contains an aromatic hydroxyl group that can form intramolecular hydrogen bonds with the aromatic acid functionality or intermolecular hydrogen bonds with inorganic oxide hydroxyls, interlayer water, or other adsorbate molecules. Difference spectra contained features consistent with salicylic acid intramolecular hydrogen bonding. The fact that results obtained for salicylic acid were most similar to those obtained for acetylsalicylic acid suggests that additional hydrogen bond interactions associated with hydroxyl (salicylic acid) and ester (acetylsalicylic acid) functionalities not available with benzoic acid were responsible.

Above 60 °C, TG-MS results for samples containing acetylsalicylic acid indicated that it decomposed by reaction with water to form salicylic acid and acetic acid. Acetic acid was not retained by the clays, so the m/z 60 (i.e. acetic acid molecular ion) ion signal temperature profile reflected the temperature range over which acetylsalicylic acid decomposition occurred. When adsorbed on the clays, salicylic acid also decomposed, but at higher temperatures than acetylsalicylic acid. VT-DRIFTS results obtained for samples initially containing salicylic acid indicated that between 60 and 100 °C, the loss of clay interlayer water resulted in new changes to salicylic acid local environments. The acid group C=O stretching vibration band shifted to higher wavenumbers with increased temperature, whereas the O-H in-plane bending vibrations shifted to lower wavenumbers. VT-DRIFTS difference spectra obtained for acetylsalicylic acid/clay samples, on the other hand, contained negative spectral features that could be attributed to loss of acetylsalicylic acid and to changes in the environments of remaining adsorbate molecules.

Above 100 °C, TG-MS results indicated that salicylic acid desorbed from samples containing relatively high loadings of salicylic acid or acetylsalicylic acid, whereas samples containing lower adsorbate loadings tended to retain the salicylic acid to higher temperatures. VT-DRIFTS difference spectra for these samples contained intense negative features associated with salicylic acid, along with positive C=O stretching vibration band intensity above 1700 cm^{-1}, indicating that the local environment of these more thermally stable molecules was changing due to continued dehydration and the related contraction of the clay interlayer.

Above 200 °C, salicylic acid desorption processes gave way to decomposition, which produced phenol and carbon dioxide. Acetylsalicylic acid/CaMMT VT-DRIFTS difference spectra were nearly identical to those obtained for salicylic acid/CaMMT samples over a similar temperature range, because almost all of the acetylsalicylic acid had been converted to salicylic acid. Difference spectra for the KMMT and NaMMT samples containing acetylsalicylic acid also strongly resembled the difference spectra for the KMMT and NaMMT samples containing salicylic acid, but small negative bands associated with acetylsalicylic acid C=O stretching vibration bands were also apparent.

The level of detail achieved by TG-MS and VT-DRIFTS for adsorbate-clay interaction studies far exceeded that possible by using other analysis methods and conventional batch experiments or soil column studies, which are the most common methods used to characterize soil contaminant adsorption processes. Those studies provide empirical results, such as that polar contaminants adsorb preferentially to the clay component of soils, but do not provide information regarding adsorbate-clay interactions at the molecular level. TG-MS and VT-DRIFTS have proven to be sensitive and powerful tools for analysis of adsorbate-clay interactions. Results from studies at the lowest temperature range (i.e. below 60 ^{o}C) are most relevant to interactions of pharmaceuticals and personal care products with soils in the environment. They provide information regarding variations in adsorbate molecule local environments caused by clay water content changes. Soil contaminant transport processes are primarily related to increased water solvation due to rainfall, which would involve changes to adsorbate hydrogen bonding within clay interlayer spaces. Results obtained at higher sample temperatures provide information regarding adsorbate interactions with dehydrated environments as well as measures of relative adsorbate stabilities. Studies described here provide a unique and detailed characterization of adsorbate environments within clay substrates and how these environments change as a result of dehydration. Results are consistent with a hypothesis originally proposed by Yariv, *et al*.,[41] that polar molecules interact with montmorillonite interlayer cations through water bridges, and that benzoic acid molecules align with the acid C=O group oriented toward the cation. VT-DRIFTS results suggest that salicylic acid and acetylsalicylic acid likely adopt similar orientations, but the effect of the cation on salicylic acid C=O stretching vibration frequency is mitigated by intramolecular hydrogen bonding.[105] On the other hand, salicylic acid may adopt a slightly different orientation, in which the C=O group still interacts with the cation through a water molecule bridge, but is not oriented directly toward the cation.

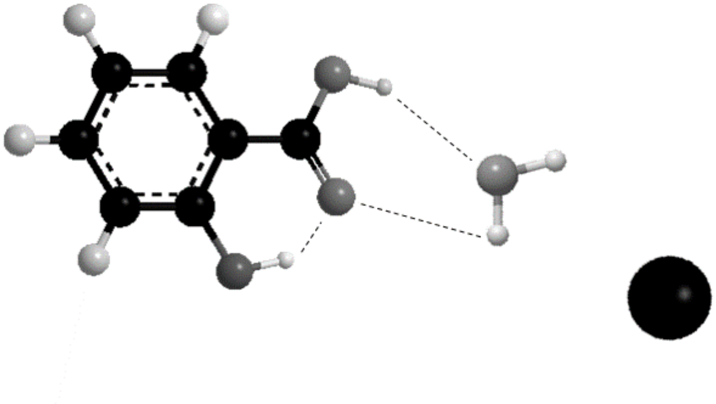

Figure 7.1 – Depiction of a salicylic acid molecule interacting with a cation through a water bridge. Dashed lines denote hydrogen bonds.

Figure 7.1 shows a depiction of a salicylic acid molecule interacting with a cation through a water bridge, with an orientation similar to that proposed for benzoic acid. Dashed lines denote hydrogen bonds. Hydrogen bonding between the O-H and C=O group would likely decrease the sensitivity of the C=O stretching vibration to its local environment.

The acetylsalicylic acid ester group was extremely sensitive to its local environment, with C=O stretching vibrations appearing at wavenumbers low enough to overlap with the carboxylic acid C=O stretching vibration near 1712 cm^{-1} for the CaMMT sample containing 15% (w/w) acetylsalicylic acid, and shifting to wavenumbers above 1770 cm^{-1} as sample heating resulted in the loss of hydrogen bonding partners. Acetylsalicylic acid molecules may orient themselves within the interlayer in such a way that both the acid and ester C=O groups may be oriented toward a cation. Unfortunately, VT-DRIFTS studies do not provide information regarding the structures of adsorption sites. Infrared spectra merely provide information regarding molecular vibrations. However, molecular modeling can be employed to calculate molecular vibration frequencies for selected molecular orientations. Thus, specific adsorption site conformations can be tested by calculating molecular vibration frequencies absorptivities and comparing them with VT-DRIFTS measured values. By combining the perturbation VT-DRIFTS technique described here with molecular modeling calculations, it should be possible to determine the relative positions and characterize interactions between adsorption site constituents.

Chapter 8 : Acid/Base Properties of Non-heme, (Hydr)oxo-bridged Diiron Coordination Complexes

8.1 Introduction

8.1.1 Acid/Base Properties of (Hydr)oxo-bridged Metalloenzymes and Metalloproteins

The chemistry of metalloenzymes is truly remarkable. Some of them are capable of catalyzing reactions much more efficiently than modern technology.[128] These enzymes contain within their active sites one or more “biological” metals; that is, a metal which may naturally occur in such an active site or be substituted therein, including calcium, magnesium, vanadium, manganese, iron, cobalt, nickel, copper, zinc, molybdenum, tungsten, cadmium, and mercury.[129] Which metal or metals are present affects the chemistry of the active site, since different metals have different properties. However, even the behavior of the same metal may vary depending on its coordination environment. Iron is commonly found in the active sites of enzymes and proteins because it is so abundant in nature.[130-133] Within an active site, iron may be coordinated by a porphyrin group, and the iron-porphyrin system is referred to as a heme unit. When iron is coordinated by other types of ligands, it is known as non-heme iron. Iron in a heme unit may have very different properties than it would in a non-heme setting.[129] Even the chemistry of non-heme coordinated iron units is dependent on the individual ligands, or combinations thereof.

Many enzymes and proteins contain more than one metal within their active sites, sometimes multiple ions of the same metal and sometimes more than one type of metal. In sites where there are two or more metal ions present, they are often bridged by simple ligands such as oxo, hydroxo, or carboxylato groups.[134, 135] In order to perform their functions, these active sites generally pass through transition states, in which the oxidation states of the metals may be different, and they may temporarily bind different ligands. In some cases, a transition may involve the transformation of the oxo group to a hydroxo group, or vice versa, so the acidity of the hydroxo proton is an important factor affecting active site function.[136-139]

8.1.2 Non-heme (Hydr)oxo-bridged Diiron Enzymes and Proteins: Structure and Function

There are several important examples of enzymes and proteins containing non-heme, (hydr)oxo-bridged diiron active sites which have diverse functions, from oxygen transport and DNA replication and repair to C-H bond activation for conversion of methane to methanol. One such protein is hemerythrin, which is used by marine invertebrates to transport oxygen instead of hemoglobin or myoglobin.[135, 140] The active site of hemerythrin consists of two iron (III) ions which are bridged by two carboxylate amino acid residues and one oxo group.[136, 141] In its fully reduced state, known as deoxyhemerythrin, both irons exist in the +2 oxidation state. One is coordinated by three histidine residues in addition to the bridging groups, making it hexacoordinate, and the other is coordinated by two histidine residues, making it pentacoordinate. They are bridged by a hydroxo group, rather than an oxo group (Figure 8.1).[136, 137, 141, 142] Deoxyhemerythrin binds dioxygen to form oxyhemerythrin. In that process, dioxygen removes the proton from the bridging hydroxo group and binds to the pentacoordinate iron center, so that in oxyhemerythrin, both iron centers are hexacoordinate iron (III), and the bridging ligand is again an oxo group.[136, 137, 141, 142]

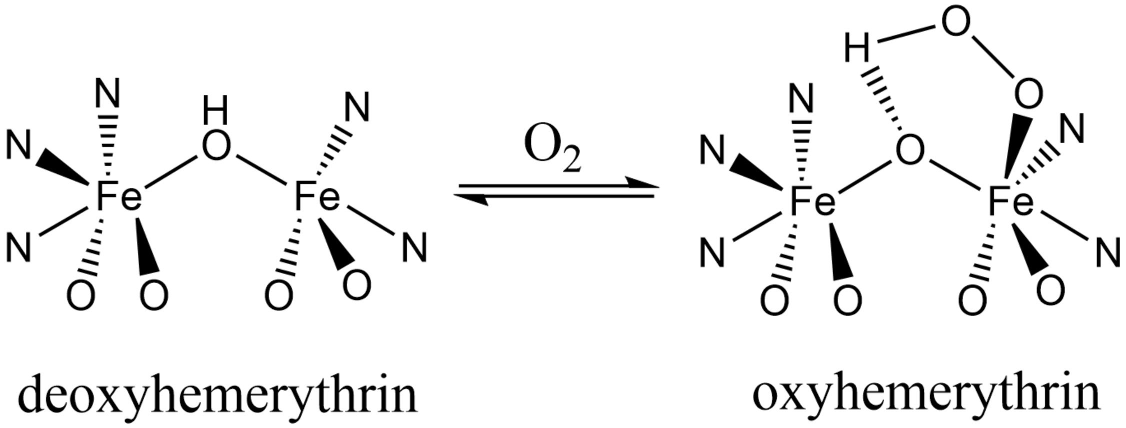

Figure 8.1 – Schematic showing the iron coordination environments within deoxyhemerythrin and oxyhemerythrin. Figure adapted from reference [143].

Another example of an enzyme containing a non-heme, (hydr)oxo-bridged diiron active site is ribonucleotide reductase (RNR), which is found in *Escherechia coli*, mammals, and viruses, where it catalyzes the conversion of ribonucleotides to deoxyribonucleotides.[144, 145] In its reduced state, the active site of RNR contains two iron (II) centers bridged by two glutamate residues.[135, 146] When this site reacts with molecular oxygen, both iron centers are oxidized to the +3 state, and an oxo bridge is formed between them (Figure 8.2).[135, 146]

The exact details of the reaction pathways of the RNR active site are still not fully known, but it has been established that one intermediate structure contains a diiron (III, IV) active site, still bridged by one glutamate and one oxo ligand, and also bridged by a third group.[146, 147] Some evidence has suggested that the third ligand is another oxo group, but most evidence points to a hydroxo ligand.[146, 147]

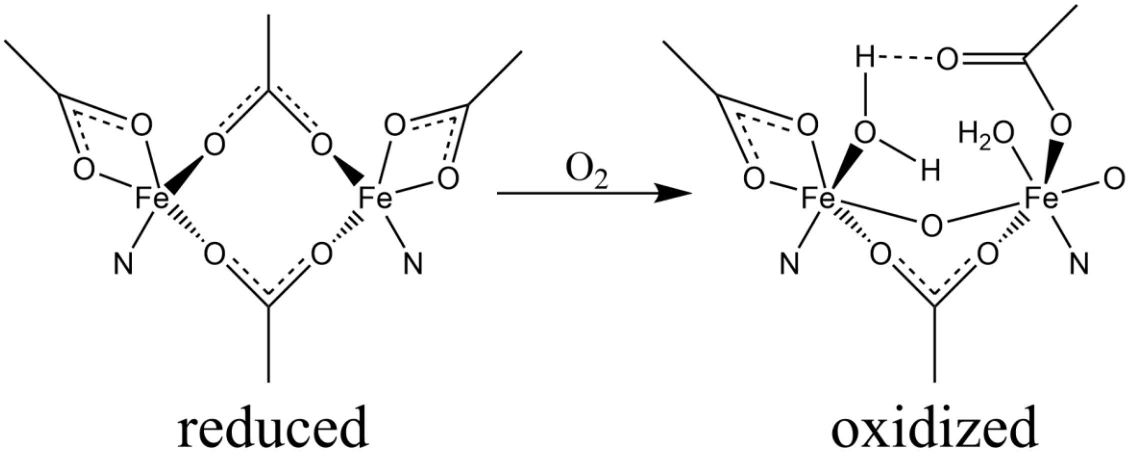

Figure 8.2 – Representation of the active site of RNR. Figure adapted from reference [143].

Another very interesting enzyme containing a non-heme, (hydr)oxo-bridged diiron active site is soluble methane monooxygenase (sMMO), which is found in methanotrophic bacteria and catalyzes the conversion of methane into methanol.[148, 149] sMMO has mainly been studied in the methanotrophs *Methylococcus capsulatus* (Bath), called *Mc* for short, and *Methylosinus trichosporium* OB3b, called *Mt* for short.[149] The resting state of sMMO is known as $MMOH_{ox}$. $MMOH_{ox}$ contains a diiron (III) core bridged by two hydroxo ligands. Each iron center is also coordinated by one histidine and two glutamate residues. One iron is also coordinated by a water molecule, so it is hexacoordinate, whereas the other iron center is only pentacoordinate. In the reduced form, $MMOH_{red}$, both iron centers are reduced to the +2 oxidation state. Both hydroxo bridges leave, so that the iron centers are bridged by two of the glutamate ligands instead. A representation of the $MMOH_{ox}$ and $MMOH_{red}$ states of sMMO are shown in Figure 8.3.

The catalytic cycle of sMMO begins with O_2 binding to $MMOH_{red}$. The first transition state after that step may be a mixed-valence diiron (II, III) superoxide species, but as of 2011 this was still unconfirmed.[149] The next intermediate, which has been directly observed, is a peroxodiiron(III) species; however, its exact structure still has not been confirmed. The sMMO intermediate which is capable of activating the C-H bonds of methane is known as intermediate Q. It contains a diiron(IV) core with two oxo groups, but it is unclear whether the oxo groups both bridge the iron centers, or if one is a terminal oxo ligand.

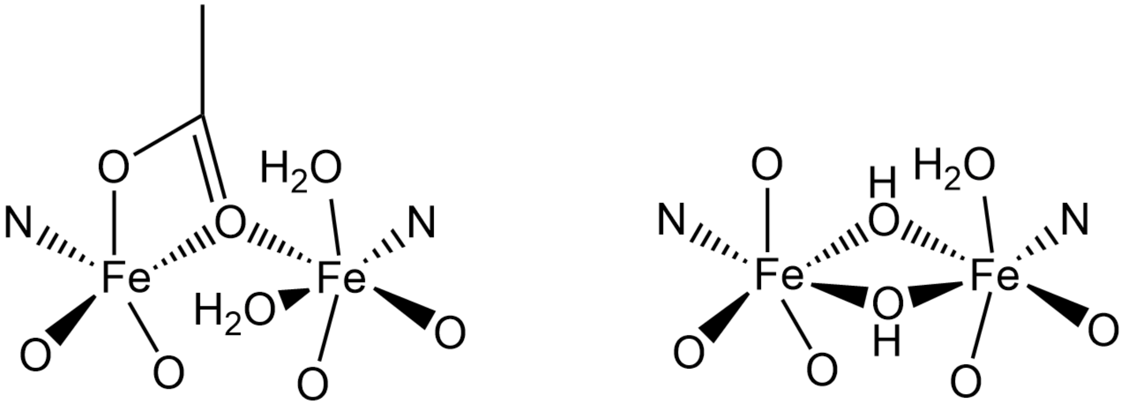

$MMOH_{red}$ $MMOH_{ox}$

Figure 8.3 – Representation of the diiron active sites within the resting ($MMOH_{ox}$) and reduced ($MMOH_{red}$) states of sMMO. Figure adapted from reference [143].

Though the catalytic cycle of sMMO does not involve a direct conversion between a bridging hydroxo and oxo ligand, reaction rates for the formation of the peroxodiiron(III) species and its conversion to intermediate Q were found to be pH dependent, indicating that proton transfer is a rate determining step for these processes.[149] Though the exact mechanisms are still uncertain, there is likely a proton transfer from the terminal water molecule to the bridging carboxylate oxygen, followed by a second proton transfer from the resulting terminal hydroxo ligand to the bridging peroxo group. This information makes it clear that the acid-base properties of this enzyme are essential to its function.

Yet another interesting enzyme is purple acid phosphatase (PAP), which is found in plants, animals, fungi, and bacteria. PAP has an Fe(III)-M(II) active site, where M can be Fe, Zn, or Mn.[150] Its name stems from its characteristic purple color (λ_{max} = 510-560 nm; ε = ~ 3000-4000 M^{-1} cm^{-1}) which is the result of a charge transfer transition from a tyrosine ligand to the iron(III) center.[138] An example of a PAP active site is shown in Figure 8.4.

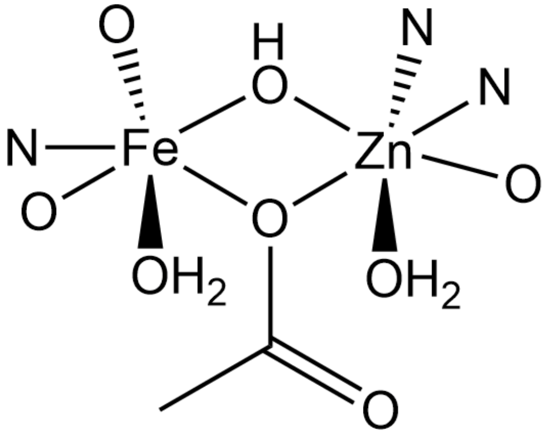

Figure 8.4 – Representation of the active site of red kidney bean PAP. Figure adapted from reference [150].

The diiron form of PAP is found in mammals, where it plays a variety of roles, including iron transport, formation of reactive oxygen species, and increased bone resorption.[138, 150] Its involvement in bone metabolism is perhaps its most interesting function, as it makes it a target for anti-osteoporotic drugs.[150] Within the active site of PAP, the iron(III) center is always coordinated by an aspartate, a tyrosine, and a histidine residue. The divalent metal ion is coordinated by two histidines and an asparagine, and the two metal centers are always bridged by an aspartate ligand.[138] Based on spectroscopic and crystallographic evidence, the active site is also thought to contain a hydroxo bridge between the two metals, but many of the crystal structures obtained did not have sufficient resolution to rule out the possibility of an oxo bridge.[138, 139, 150-155] The μ-hydroxo group is thought to be the hydrolysis-initiating nucleophile, suggesting that its pK_a is an important factor affecting the function of the enzyme.[138, 139]

8.1.3 Acid-Base Studies of Non-heme (Hydr)oxo-bridged Diiron Model Complexes: Motivation and Progress

One motivation for developing synthetic models for the active sites of metalloenzymes is simply to better understand their chemistry and function. A better understanding of PAP, for example, could lead to better treatment of osteoporosis.[150] Comparing the observed properties of intermediates in the catalytic cycles of enzymes to properties of well-characterized model complexes can help to elucidate the structures of transient states which would be otherwise difficult to pin down. A further motivation for producing model complexes which mimic the chemistry of enzymes is to eventually achieve the function of the enzyme synthetically. For example, methane is an important fuel, but it is inefficient and expensive to transport methane over long distances because of its low energy density.[156] Methanol is much more efficient to transport, and is used for many industrial purposes in its own right, so if methane could be cheaply and efficiently converted to methanol, it would be a significant improvement.[156]

Unfortunately, the current industrial methods of converting methane into methanol either require high inputs of energy or use costly materials.[128]

Since the acid/base properties of many of these enzymes are essential to their functions, it is important to gain a full understanding of these properties. Studies of the acid/base behavior of synthetic model complexes will help to gain better insight into the function of the enzymes that they model. There have been a number of studies on the acid/base properties of (hydr)oxo-bridged dimanganese complexes, with reported pK_a values ranging from -2.0 to 8.35 in water and from 6.8 to 16.2 in CH_3CN.[157-163] The pK_a value was estimated to be between 14 and 17 for one heme iron(III)-Cu(II) complex bridged by a hydroxo ligand,[164] and between 16.7 and 17.6 for another.[165] The first instance in the literature of a transformation between the oxo- and hydroxo-bridged form of a diiron complex was reported by Armstrong and Lippard.[166] Several acid/base studies have been performed on hydroxo-bridged diiron complexes since then,[167-171] but only two studies reported pK_a values for the μ-hydroxo ligand.[172, 173] Zheng, et al., synthesized and characterized a series of diiron(III) complexes with $[\mu\text{-O(H)}]_2$ cores and found that the protons on the bridging groups had pK_a values ranging from 15.9 to 17.6 in CH_3CN.[172] Cui, et al., reported the reversible protonation of the oxo-bridge in the diiron(III) complex $[(LFeCl)_2(\mu\text{-O})][PF_6]_2$ (L = 4-((1-methyl-1*H*-imidazol- 2-yl)methyl)-1-thia-4,7-diazacyclononane). They found the resulting hydroxo bridge to have a pK_a of 6.1 in aqueous solution. They also reported a mixed-valence diiron(II,III) version of the complex, and reported the pK_a of its hydroxo bridge to be 10.3.[173]

8.1.4 Progress in the Houser Research Group

Our group previously reported the synthesis and coordination chemistry of the ligand 2,2'-(2-methyl-2-(pyridine-2-yl)propane-1,3-diyl)bis(azanediyl)bis(methylene)diphenol (H_2L).[174] This ligand has an N_3O_2 donor set; the N donors originate from two amine groups and a pyridyl group, and the O donors are both phenolate groups, which, when deprotonated, cause the ligand to be dianionic (Figure 8.5).

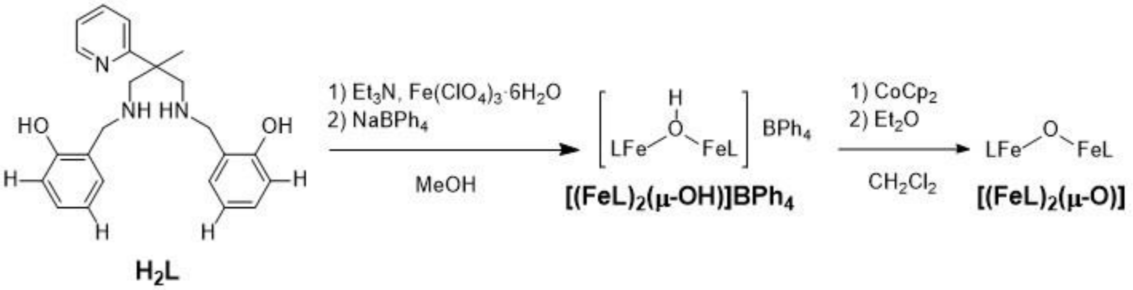

Figure 8.5 – Scheme depicting structure of H_2L and synthesis methods for $[(FeL)_2(\mu\text{-}OH)]BPh_4$ and $[(FeL)_2(\mu\text{-}O)]$.

Our group also reported the synthesis and initial characterization of the asymmetric, unsupported hydroxo-bridged diiron(III) complex $[(FeL)_2(\mu\text{-}OH)]BPh_4$ (Figure 8.6) and its related monomeric complex, [FeLCl].[175] Additional characterization and an alternative synthesis for $[(FeL)_2(\mu\text{-}OH)]BPh_4$, as well as the synthesis and characterization of $[(FeL)_2(\mu\text{-}O)]$, have also been presented by our group (Figure 8.5 and Figure 8.7).[176] $[(FeL)_2(\mu\text{-}OH)]BPh_4$ and $[(FeL)_2(\mu\text{-}O)]$ are asymmetric because the amine hydrogens of the ligand coordinated to one of the iron centers in each complex donate hydrogen bonds to the phenolate oxygens of the ligand coordinated to the other iron center. In a sense, these hydrogen bonds add extra support for the "unsupported" (hydr)oxo bridges. On the other hand, they force the complex into an arrangement in which the Fe-O-Fe bond angle is strained. This hydrogen bonding is unique to our ligand system, and its effect on the behavior of our complexes is quite interesting. Usually there is a significant difference in Fe-O-Fe bond angle between unsupported oxo-bridged diiron complexes and hydroxo-bridged diiron complexes. Oxo-bridged complexes usually fall between 160 – 180°,[134] with a few exceptions in the 139 – 145° range,[169, 177-179] whereas there are only a few instances of non-heme, unsupported hydroxo-bridged diiron complexes, with reported Fe-O-Fe bond angles including 147° for a hydroxo-bridged diiron(II) complex,[180] and 159° for a hydroxo-bridged diiron(III) complex.[181] The Fe-O-Fe bond angle for our hydroxo-bridged diiron complex fell at the low end of the expected range (139°), but the corresponding angle for the oxo-bridged diiron complex was only slightly larger (144°), suggesting that the hydrogen-bonding of the ligands forces the complex into a strained configuration.

The spectroscopic properties of $[(FeL)_2(\mu\text{-OH})]BPh_4$, $[(FeL)_2(\mu\text{-O})]$, and [FeLCl] were characterized in CH_2Cl_2.[175, 176] The monomer [FeLCl] exhibited a LMCT feature with λ_{max} = 519 nm (ε = 2,590 M^{-1} cm^{-1}), so it appeared purple. To the naked eye, $[(FeL)_2(\mu\text{-OH})]BPh_4$ appeared to be identical in color, though more intense, because its LMCT had λ_{max} = 516 nm (ε = 6,580 M^{-1} cm^{-1}; Figure 8.8). In contrast, λ_{max} for $[(FeL)_2(\mu\text{-O})]$ appeared at 420 nm (ε = 7900 M^{-1} cm^{-1}), so it appeared bright orange (Figure 8.8).

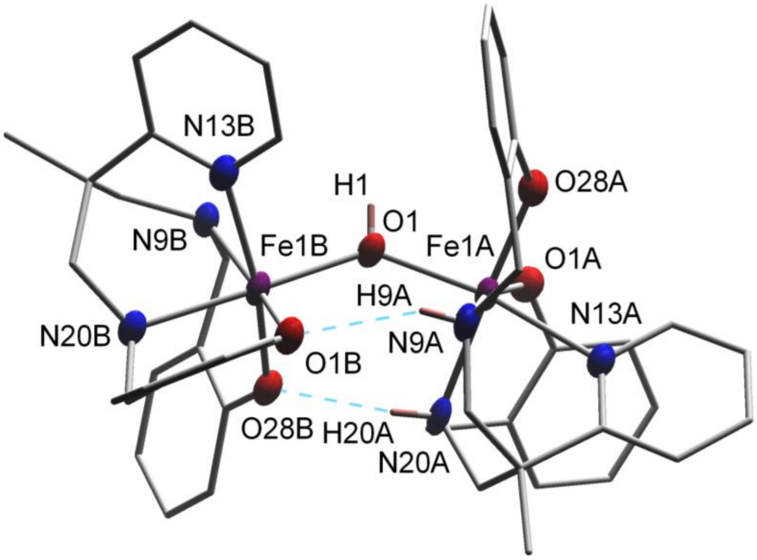

Figure 8.6 – Crystal structure of [(FeL)$_2$(μ-OH)]BPh$_4$. The counter ion, trapped solvent molecules, and H atoms are omitted for clarity, except for N9A and N20A amine and μ-hydroxo H atoms. H-bonding interactions are represented by dashed lines. (Figure adapted from reference [175]).

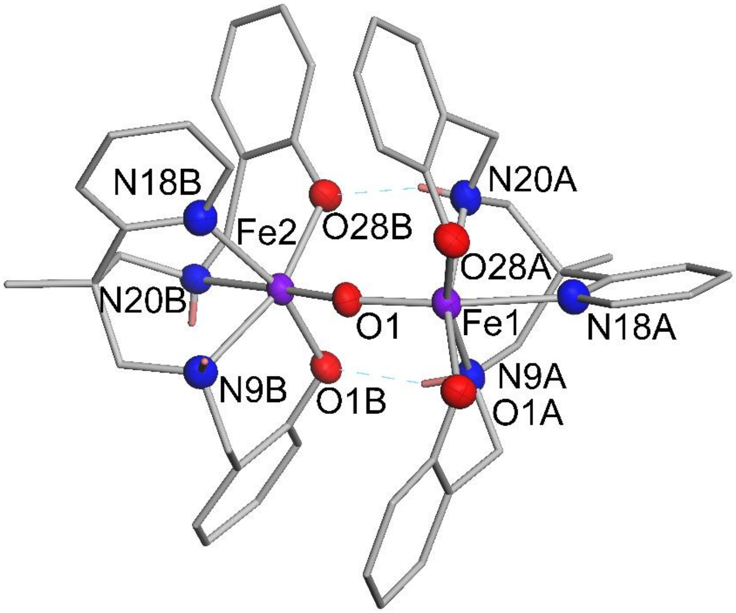

Figure 8.7 – Crystal structure of [(FeL)$_2$(μ-O)]. H atoms are removed for clarity, except those involved in H-bonding interactions, which are represented by dashed lines. (Figure adapted from reference [176]).

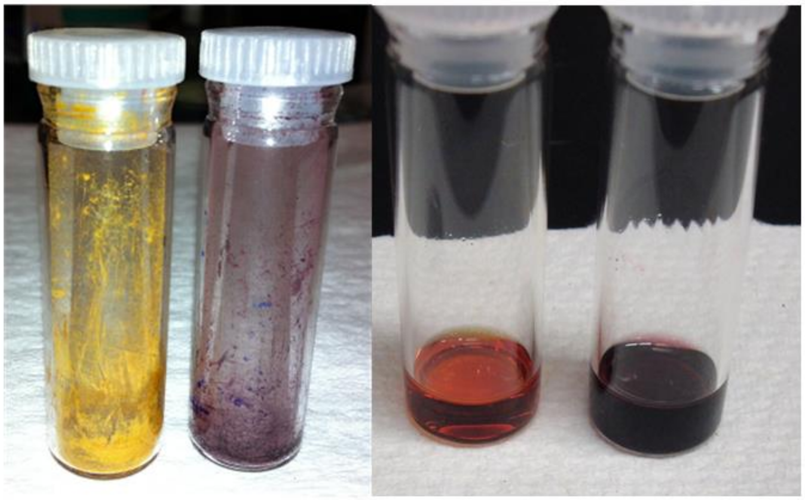

Figure 8.8 – Left: photograph of $[(FeL)_2(\mu\text{-}O)]$ (orange powder) and $[(FeL)_2(\mu\text{-}OH)]BPh_4$ (purple powder). Right: photograph of solutions of $[(FeL)_2(\mu\text{-}O)]$ and $[(FeL)_2(\mu\text{-}OH)]BPh_4$.

8.1.5 Research Goals

The goal of this research project was to thoroughly characterize the acid/base properties of $[(FeL)_2(\mu\text{-}OH)]BPh_4$ and to determine the pK_a of its hydroxo ligand. Because of the distinct difference in the visible absorbance spectra between the hydroxo- and oxo-bridged forms, UV-visible spectroscopy was extremely useful for this purpose. Titrations with various acids and bases under different conditions were performed and monitored by UV-vis, and the results are described in the following section.

8.2 Stability of $[(FeL)_2(\mu\text{-}OH)]BPh_4$ in Dichloromethane and Acetonitrile

Initially there was some concern that the hydroxo-bridged dimer might not stay intact in solution, and that it might break apart into monomers, or have some sort of equilibrium between a dimer and two monomers. However, the mass spectrum (MS) shows a peak which can only be attributed to a hydroxo-bridged dimer, and the cyclic voltammetry (CV) data show two reduction waves, attributed to the reduction of first one iron center, then the other, to Fe(II).[175] If the dimer were to completely split into two identical monomers, one would expect to see only one reduction wave, and if the dimer existed in equilibrium with a monomeric species, one would expect to see three waves, one for each type of iron center present in solution. Finally, the diffuse-reflectance UV-visible (DR-UV/vis) spectrum of the solid complex was obtained by Anna Jozwiuk, and found to be almost identical to its UV-vis spectrum in dichloromethane. This confirms that, while a hydroxo bridge may not be as resistant to dissociation as on oxo bridge, there is still enough preference for that configuration to keep this complex together in solution. The hydrogen bonds between the phenolate oxygens of one ligand and the amine hydrogens of the other ligand in the complex may provide the extra stability needed.

Dichloromethane (CH_2Cl_2) is a good solvent for the hydroxo-bridged complex, and it had been the solvent of choice for most characterization (MS, CV, UV-vis), but there is very little pK_a data for CH_2Cl_2 available. Consequently, acetonitrile (CH_3CN) was chosen for titrations. The MS and CV data in CH_3CN were very similar to that in CH_2Cl_2. The visible spectrum displayed a peak at 496 nm instead of 516 nm as in CH_2Cl_2, but this could be attributed to a solvent effect. The spectrum did not change after days or even weeks, implying that the complex is stable in CH_3CN.

8.3 Titrations of $[(FeL)_2(\mu\text{-}OH)]BPh_4$ with Various Bases

Preliminary exploration of the acidity of $[(FeL)_2(\mu\text{-}OH)]BPh_4$[175] suggested that it has a very high pK_a because it did not appear to be completely deprotonated by either triethylamine or proton sponge (pK_a values in CH_3CN = 18.82 and 18.62, respectively).[182] Our investigations corroborated those initial results. Under atmospheric conditions, addition of 100 μL aliquots, each containing approximately 2700 equivalents of Et_3N to $[(FeL)_2(\mu\text{-}OH)]BPh_4$, shifted the peak maximum from 496 nm to 480 nm (dashed line, Figure 8.9). Any further addition of Et_3N (dotted line, Figure 8.9) did not shift the peak significantly closer to 412 nm, which is the λ_{max} observed for $[(FeL)_2(\mu\text{-}O)]$ in CH_3CN.

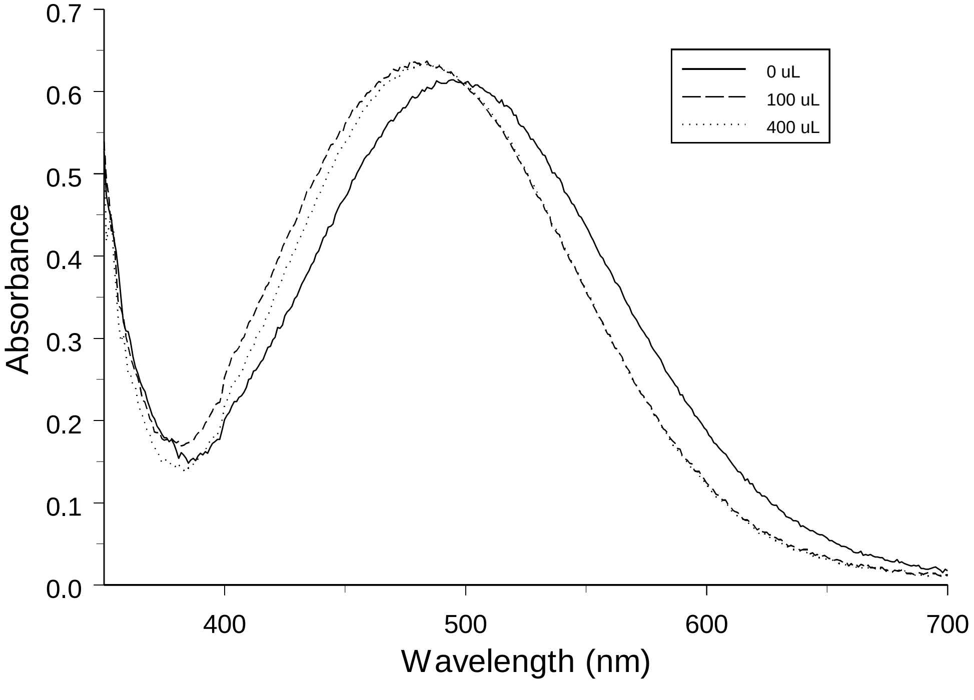

Figure 8.9 - Titration of a 7.5 x 10^{-5} M solution of $[(FeL)_2(\mu\text{-}OH)]BPh_4$ (solid line) with 100 μL aliquots (2700 equivalents each) of triethylamine.

Titrations with proton sponge yielded similar results; addition of 1000 equivalents of proton sponge only shifted the peak to 485 nm (Figure 8.10), so we concluded that the p*K*a of the hydroxo bridge must be significantly higher than 18.

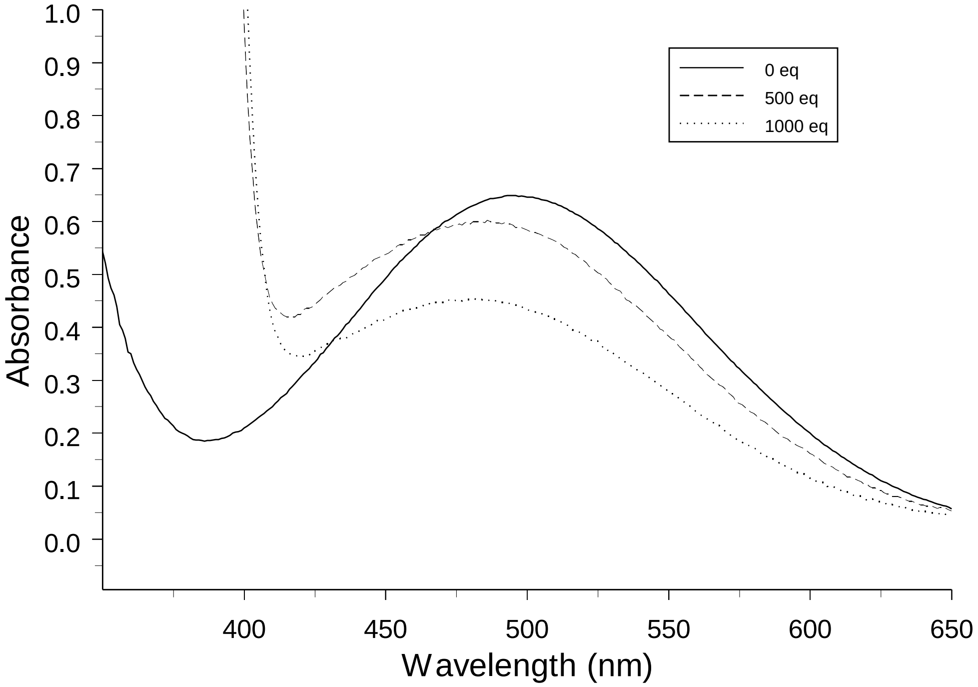

Figure 8.10 - Titration of an 8.55 x 10^{-5} M solution of [(FeL)$_2$(μ-OH)]BPh$_4$ (solid line) with proton sponge.

1,8-Diazabicyclo[5.4.0]undec-7-ene (DBU) was selected as a base because of its relatively high pKa in CH_3CN (24.34),[182] and its bulky size, which makes it unlikely to compete for coordination to the iron sites. Initial titrations with DBU, in which aliquots containing 0.1 equivalent were added, showed that just 1.5 equivalents could shift the peak to 440 nm, with an isosbestic point at 460 nm (Figure 8.11). Further addition of base had no discernible effect; 1.7 equivalents of DBU were added in the titration pictured in Figure 8.11, but the spectra for the 1.6 and 1.7 total equivalent aliquots overlay with the 1.5 total equivalent spectrum.

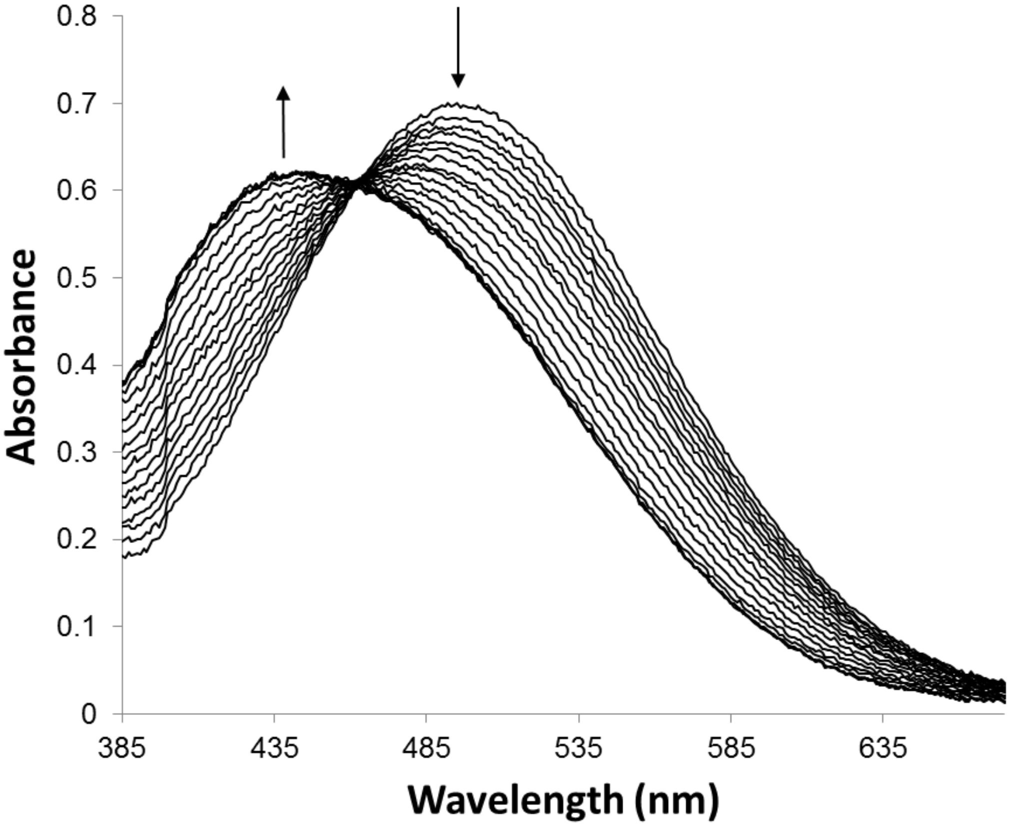

Figure 8.11 – Titration of 8.55 x 10^{-5} M solution of $[(FeL)_2(\mu\text{-}OH)]BPh_4$ with 0.1 equivalent aliquots of DBU.

In order to investigate this strange behavior, we added 2 equivalents of DBU all at once, and observed the spectrum change over time. Initially the peak shifted all the way to 420 nm, but after four minutes the peak already appeared to be shifting back towards its original position, and it continued to shift over the next day. Water from the air may have been re-protonating the complex, but the lack of an isosbestic point suggests that some other process may also have been occurring. (Figure 8.12). We hypothesized that some sort of decomposition was occurring after the initial deprotonation of the hydroxo bridge. In order to further support this idea, we again added 2 equivalents of DBU at one time to a solution of the hydroxo-bridged dimer, then immediately added 2 equivalents of trifluoromethanesulfonic acid (commonly known as triflic acid, or HOTf). The resulting spectrum, when corrected for dilution, was virtually identical to the original spectrum of the complex, suggesting that the deprotonation is reversible.

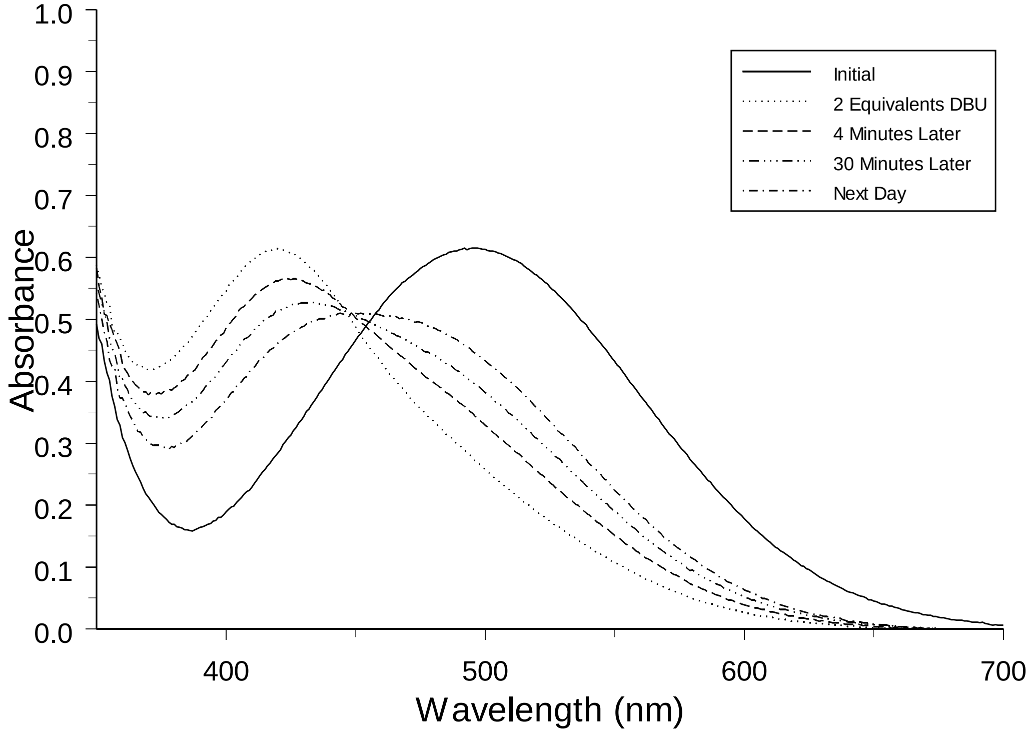

Figure 8.12 - Addition of 2 equivalents of DBU to an 8.55 x 10^{-5} M solution of $[(FeL)_2(\mu\text{-}OH)]BPh_4$ (solid line) and the subsequent peak shift over time.

The reversibility of the deprotonation was also tested using the solution from Figure 8.12 that sat until the next day. After measuring the initial spectrum, triflic acid (HOTf), was added to see if the original spectrum of the complex could be reproduced. Addition of one equivalent of HOTf only shifted the peak slightly, but addition of 2 equivalents caused a shift to about 500 nm, which is slightly higher than the usual peak maximum for the complex of 496 nm (Figure 8.13). Addition of a 3rd equivalent of HOTf shifted the peak only slightly further, and though a 4th equivalent was added, the resulting spectrum is not shown because it overlaps almost exactly with that for the 3rd equivalent.

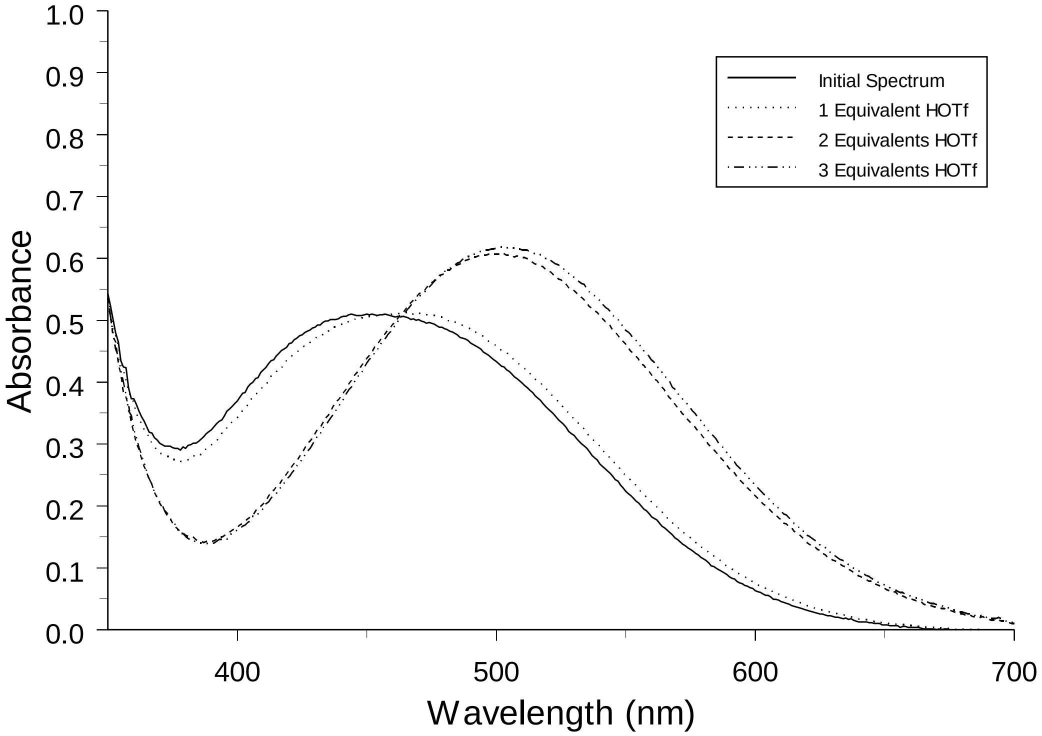

Figure 8.13 – Titration of the "Next Day" solution from Figure 8.12 with HOTf.

8.4 Acid-base Chemistry of the Monomer

Because we suspected that the monomer could exist in an acid-base equilibrium with the hydroxo-bridged dimer, an attempt was made to synthesize the monomer [FeLCl] according to the procedure from ref. [175], with slight modifications (see 8.8 Experimental). A CH_2Cl_2 solution of the product gave a visible spectrum with a peak at 533 nm, rather than the 519 nm previously reported.[175] Addition of approximately one equivalent of DBU shifted the peak to about 516 nm, suggesting conversion to the hydroxo-bridged dimer (Figure 8.14). This would be possible because when the synthesis is performed under atmospheric conditions, the extremely hygroscopic $FeCl_3$

would be able to absorb some water, which could then be present in the crystal lattice of the product and would not be easily removed, even by drying under high vacuum. Addition of DBU could cause the formation of hydroxide ions, which could replace the chloride ligands, and successively cause formation of the hydroxo-bridged dimer.

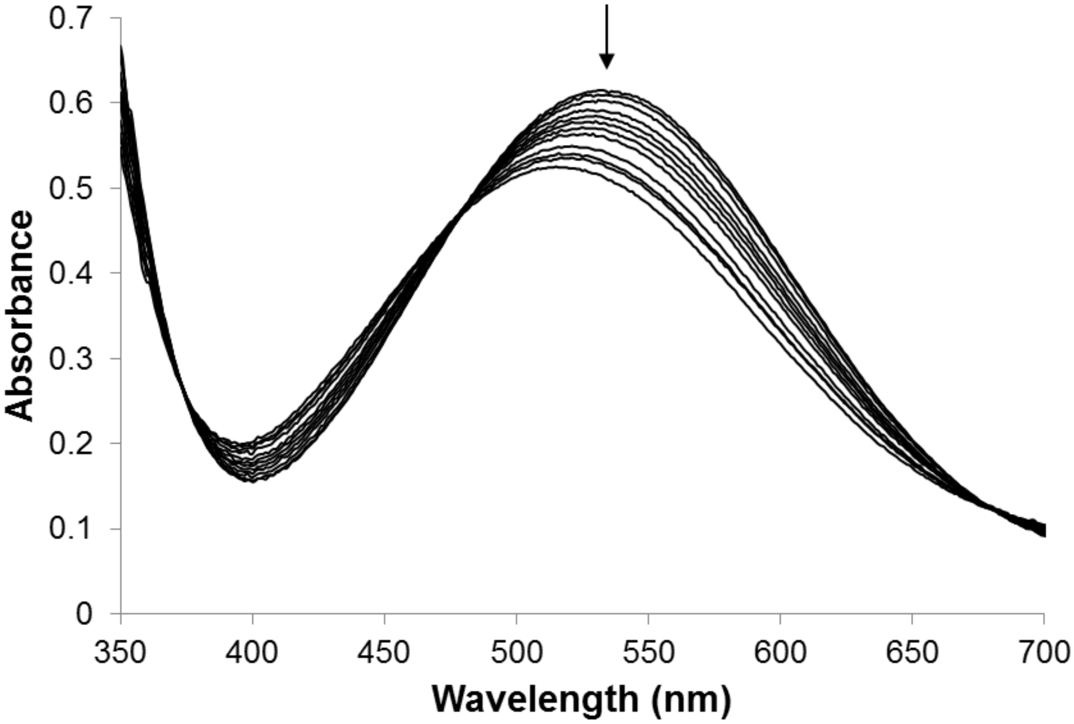

Figure 8.14 – Titration of a 1.46 x 10^{-4} M solution of [FeLCl] with one equivalent of DBU in 0.1 eq aliquots.

Addition of approximately 2 more equivalents of DBU (3 total), shifted the peak to around 420 nm, suggesting deprotonation of the hydroxo-bridge (Figure 8.15).

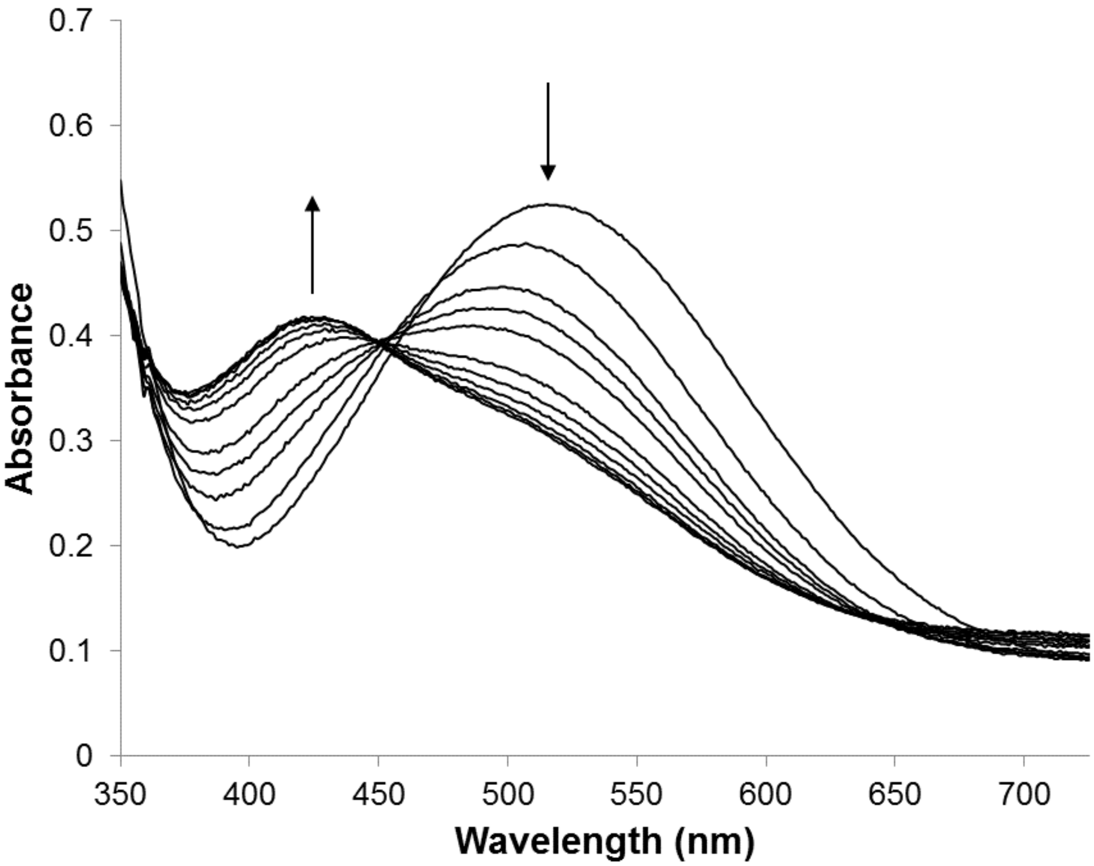

Figure 8.15 – Continuation of titration from Figure 8.14, beginning after one equivalent of DBU was added, continuing with aliquots containing 0.2 equivalents of DBU up to 3 equivalents total.

8.5 Behavior of [(FeL)$_2$(μ-O)] in Acetonitrile

The UV-vis spectrum of [(FeL)$_2$(μ-O)] in CH_2Cl_2 exhibited λ_{max} = 419 nm. Its behavior in CH_3CN was less straightforward, however. A relatively concentrated solution (4.3 x 10^{-4} M) initially had a spectrum identical to the spectrum in CH_2Cl_2, and did not change for the first hour, but after three hours the peak had shifted from 420 to 435 nm, with a shoulder appearing around 490 nm (Figure 8.16).

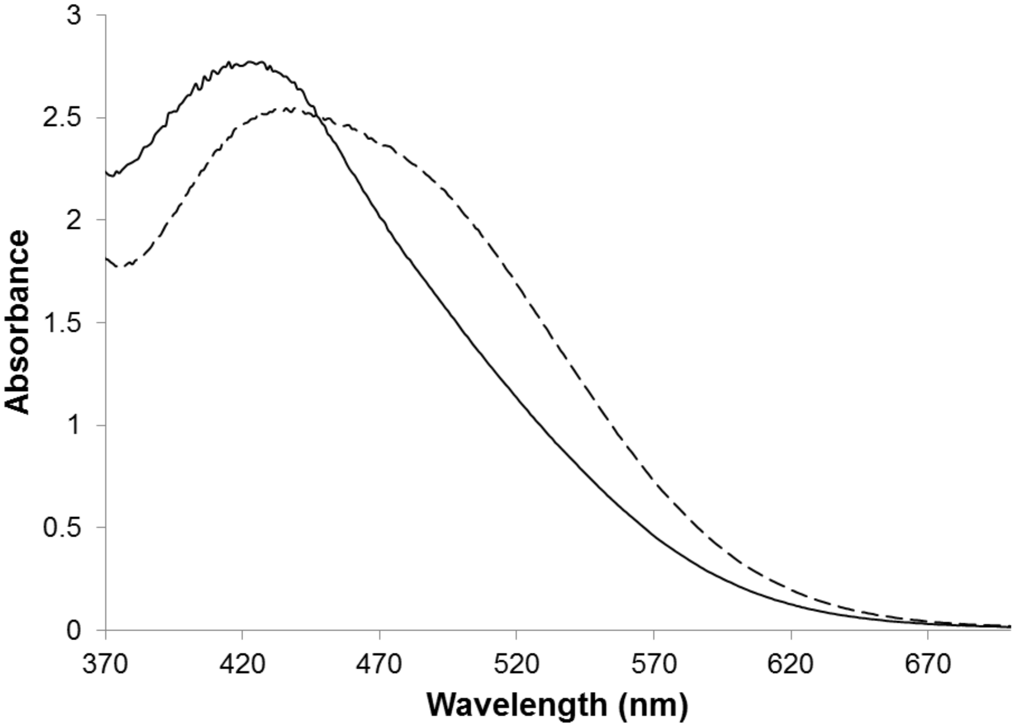

Figure 8.16 – Initial spectrum of a 4.3×10^{-4} M solution of $[(FeL)_2(\mu\text{-}O)]$ in acetonitrile (solid line) and after 3 hours (dashed line).

The initial spectrum of a more dilute solution (6.5×10^{-5} M) matched the appearance of the dashed line in Figure 8.16, suggesting that whatever process was occurring was able to happen more quickly at lower concentration. The dilute solution was titrated with HOTf, and after 0.6 equivalents were added, the peak shifted from 435 to 490 nm, with an isosbestic point around 454 nm (Figure 8.17).

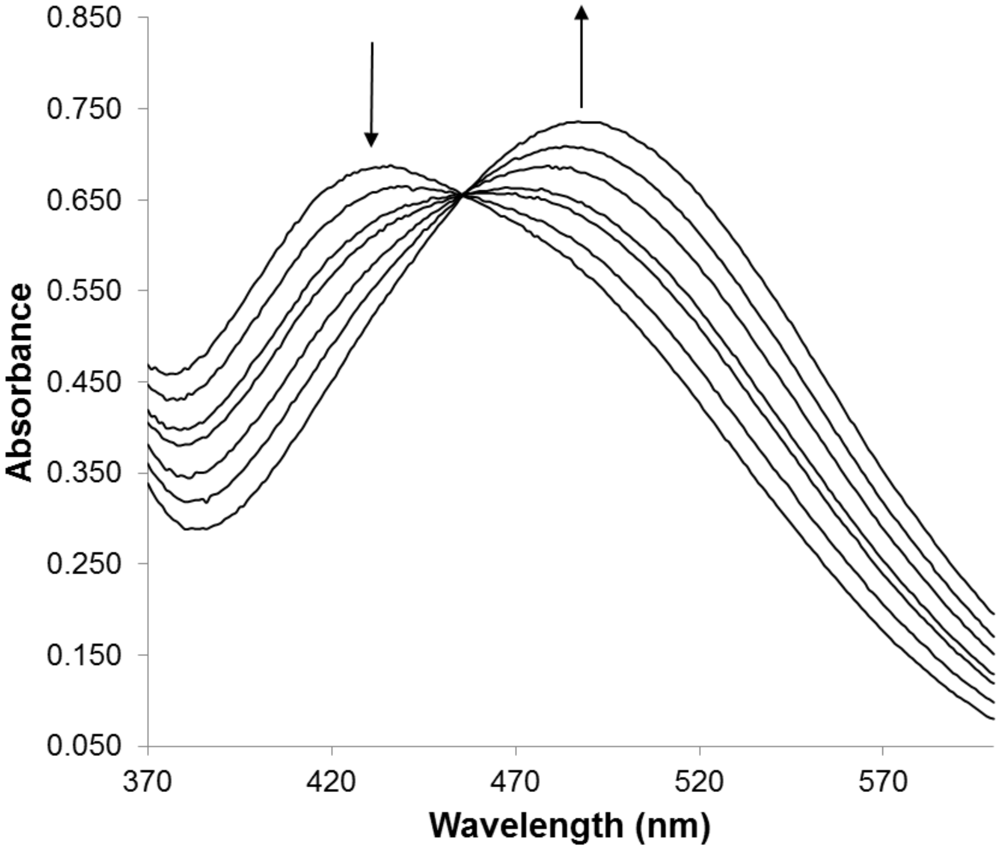

Figure 8.17 – Titration of a 6.5×10^{-5} M solution of $[(FeL)_2(\mu\text{-}O)]$ with HOTf.

Addition of another 0.1 equivalent of HOTf (1.1 equivalents total) shifted the peak to 500 nm, but it did not continue to pass through the isosbestic point. Further addition of HOTf shifted the peak a little farther to the red, suggesting dissociation of the complex into monomers. Addition of excess HOTf shifted the peak ever farther towards the red, and resulted in eventual bleaching of the solution. This is probably an indication that the protonation of the amine and phenolate groups of the ligand cause it to become unbound from the iron ions.

8.6 Air-free Titrations of $[(FeL)_2(\mu\text{-}O)]$ with Benzoic Acid

In order to avoid further complications, solid benzoic acid (HOBz), which is easier to dry, was selected and solutions were prepared in a glove box under nitrogen. An air-free titration of $[(FeL)_2(\mu\text{-}O)]$ with benzoic acid shifted the peak from 412 nm to 489 nm, with an isosbestic point at 442 nm (Figure 8.18). Though 489 nm is slightly different than 496 nm, as is usually observed for $[(FeL)_2(\mu\text{-}OH)]BPh_4$ in acetonitrile, in this case the counter ion is benzoate (OBz^-) rather than tetraphenylborate, which would accept a hydrogen bond from the bridging O–H, thus slightly weakening its bond strength and thereby slightly changing the coordination environment of the iron ions. The precise isosbestic point at 442 nm is evidence that no other side reactions were occurring, such as the coordination of benzoic acid to the iron centers.

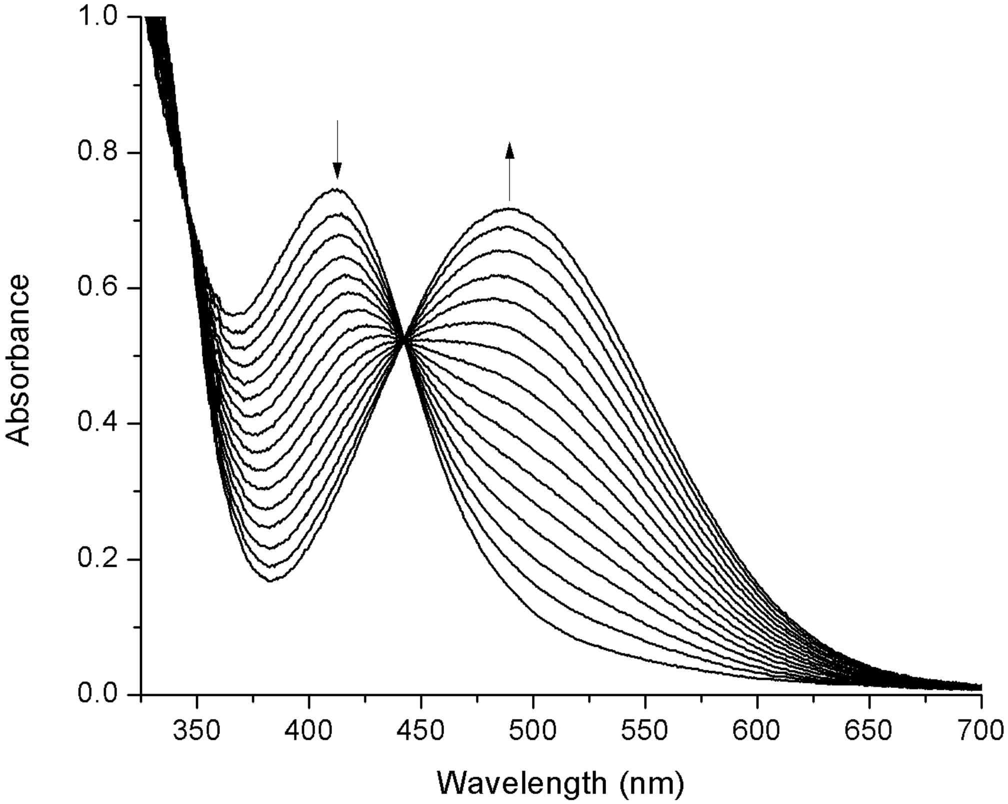

Figure 8.18 – Titration of [(FeL)$_2$(μ-O)] (9.1 x 10^{-5} M) with up to 2.5 equivalents of benzoic acid in CH$_3$CN to generate [(FeL)$_2$(μ-OH)]$^+$ monitored by UV-visible spectroscopy.

The equilibrium constant, K_{eq}, was calculated at several points throughout the titration, based on the change in absorbance at 505 nm, because that region of the spectrum showed the greatest change. K_{eq} is defined as:

$$K_{eq} = \frac{[[(\mathrm{FeL})_2(\mu\text{-OH})]^+][\mathrm{OBz}^-]}{[[(\mathrm{FeL})_2(\mu\text{-O})]][\mathrm{HOBz}]}$$

The change in absorbance makes it possible to determine the fraction of the complex that still exists as [(FeL)$_2$(μ-O)] and how much has been converted to [(FeL)$_2$(μ-OH)]$^+$ at any given point in the titration, because the complex is assumed to exist entirely as [(FeL)$_2$(μ-O)] at the beginning of the titration and [(FeL)$_2$(μ-OH)]$^+$ at the end. [OBz$^-$] is then assumed to be equal to [[(FeL)$_2$(μ-OH)]$^+$], and [HOBz] is assumed to be equal to the amount of benzoic acid added at that point, minus [OBz$^-$].Then, the K_a of the complex was calculated from Eq. 2:[157, 172]

$$K_a(\text{complex}) = K_a(\text{acid})/K_{eq} \qquad (2)$$

where K_a (acid) = 3.09×10^{-22} (pK_a = 21.51) in acetonitrile.[183] The titration was performed in triplicate (Figure 8.19), and K_a(complex) was calculated at several different points between the start and endpoint of each titration, and the average value for each titration was determined. The average of those values is $5.3 \pm 1 \times 10^{-22}$ (pK_a = 21.3 ±0.1).

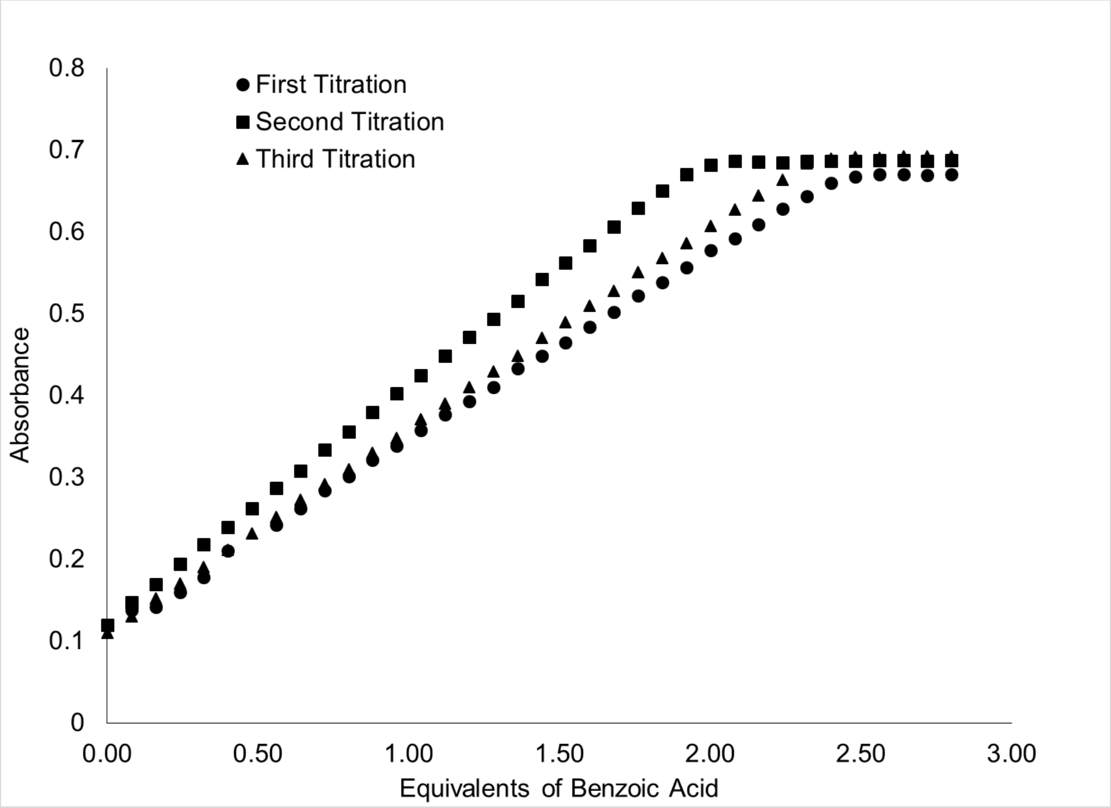

Figure 8.19 - Change in absorbance at 505 nm of 9.1×10^{-5} M [$(FeL)_2(\mu\text{-}O)$] with addition of benzoic acid (9.1×10^{-4} M) in acetonitrile.

However, the values calculated from different points within the same titration, rather than showing random variability due to error, showed a trend. The value calculated for the pK_a increased as the titration progressed. This makes sense, because as more benzoic acid is added, more benzoate is available to hydrogen bond to the bridging hydroxo proton and to the amine proton. This has the effect of making the protonated form even more stable, thus raising the apparent pK_a. The actual pK_a can be estimated by plotting the observed pK_a vs. the quantity of benzoic acid added to the system (Figure 8.20).

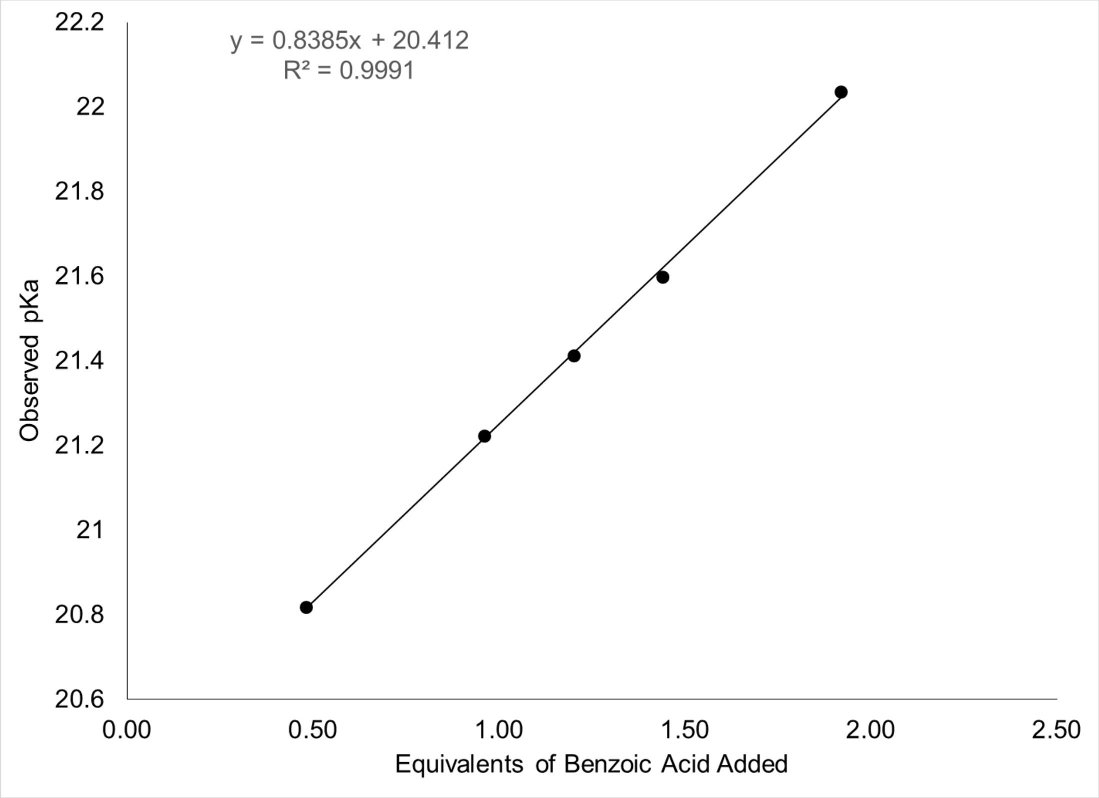

Figure 8.20 - Change in calculated pK_a value for [$(FeL)_2(\mu\text{-}O)$] as more equivalents of benzoic acid were added. The theoretical value if no benzoic acid were present was estimated from the y-intercept; 20.4 in this case.

The y-intercept represents the theoretical pK_a if no benzoic acid had been added; in this case, 20.4. A similar analysis of the other two titrations gave values of 20.3 and 20.6, respectively. Even though these estimates are lower than the values calculated by averaging all of the various determinations of K_a(complex), they are still unusually high values, even for a diiron complex. The closest values we have observed in the literature were published by Zheng, *et al.*, for their series of complexes with (μ-oxo)(μ-hydroxo)diiron(III) cores, having pK_a values in acetonitrile ranging from 15.9 to 17.6.[172] It has been observed that phenolates are more strongly electron donating than pyridine and other N-donor ligands, which would result in more electron density on the iron centers.[158] This may be an important factor contributing to the high pK_a that we observed.

8.7 Conclusion

In conclusion, the acid-base properties of $[(FeL)_2(\mu\text{-OH})]BPh_4$, $[(FeL)_2(\mu\text{-O})]$, and [FeLCl] were characterized in CH_3CN. $[(FeL)_2(\mu\text{-OH})]BPh_4$ was reversibly deprotonated by strong bases such as DBU. Addition of acid to $[(FeL)_2(\mu\text{-OH})]BPh_4$ caused protonation of the hydroxo bridge to form a labile water molecule, which likely led to the dissociation of the complex into monomers, $2[FeL]^+$. Spectroscopic evidence suggested that in the presence of OH^-, [FeLCl] spontaneously formed $[(FeL)_2(\mu\text{-OH})]^+$, and further addition of base removed the hydroxo proton to form $[(FeL)_2(\mu\text{-O})]$. The oxo bridge of $[(FeL)_2(\mu\text{-O})]$ seems to be so basic that in CH_3CN, it can be protonated by atmospheric H_2O. Finally, $[(FeL)_2(\mu\text{-O})]$ was titrated with benzoic acid under inert conditions and the pK_a of the hydroxo bridge in $[(FeL)_2(\mu\text{-OH})]^+$ was estimated to be

20.4. This is remarkably high compared to literature reports for other hydroxo-bridged diiron complexes. There are several possible factors that may contribute to the high pK_a observed for this complex. First of all, the hydrogen bonding between the two ligands forces the Fe-O-Fe bond into a bent configuration (<145°), which likely favors the protonated form over the deprotonated form. Second, phenolate ligands are known to be strongly electron donating, which decreases the Lewis acidity of the ions to which they are coordinated. A decrease in the Lewis acidity of the iron ions in an oxo-bridged diiron complex would increase the basicity of the oxo-bridge. Finally, in the deprotonation reaction of benzoic acid by $[(FeL)_2(\mu\text{-}O)]$, the benzoate anion is likely stabilized by hydrogen bonding to the ligand's amine proton, facilitating proton transfer from benzoic acid to the oxo-bridging ligand.

8.8 Experimental

8.8.1 General Procedures

Unless otherwise stated, all reagents were used as received from commercial sources. 2-methyl-2-(pyridine-2-yl)propane-1,3-diamine (ppda) was synthesized according to the published procedure.[184] 2,2'-(2-Methyl-2-(pyridin-2-yl)-propane-1,3-diyl)bis(azanediyl)-bis(methylene)diphenol (H_2L) was synthesized according to the published procedure.[175] Solvents were doubly purified using alumina columns in an MBraun solvent purification system (MB-SPS). UV-visible spectra were recorded using a Shimadzu UV2401PC spectrophotometer.

8.8.2 Complex Syntheses

$[(FeL)_2(\mu\text{-}OH)]BPh_4$ and $[(FeL)_2(\mu\text{-}O)]$ were synthesized according to the published procedures.[176] To synthesize $[(FeL)_2(\mu\text{-}OH)]BPh_4$, 0.143 g $Fe(ClO_4)_3 \cdot 6H_2O$ in 1 mL methanol was mixed with a 10 mL methanol solution containing 0.117 g of ligand (L) and 0.075 g Et_3N. The solution, which turned dark wine-red, was stirred for one hour at room temperature (RT), then 0.160 g $NaBPh_4$ was added and a purple precipitate (ppt) immediately formed. The slurry was refluxed overnight and the ppt collected by filtration, washed with methanol and diethyl ether, and dried. The powder was collected (0.180 g), dissolved in CH_2Cl_2, and a small amount of insoluble residue was removed by filtration through celite. The product was crystallized by pentane diffusion into the CH_2Cl_2 solution. Only the crystalline product was used for characterization and titrations.

To synthesize $[(FeL)_2(\mu\text{-}O)]$, 0.1495 g of $[(FeL)_2(\mu\text{-}OH)]BPh_4$ were dissolved in 14 mL CH_2Cl_2 under an inert atmosphere. A 1 mL solution containing 0.0236 g cobaltocene ($CoCp_2$) was added with stirring. The color of the solution changed immediately from dark purple to orange, with the simultaneous formation of a yellow ppt. The solution was stirred for an additional 15 minutes, then 30 mL of diethyl ether (Et_2O) was added to complete the precipitation. The remaining steps were performed in air. The ppt was removed by filtration, and the filtrate was concentrated under high vacuum, then dissolved in acetone. Crystals were produced by pentane diffusion into the acetone solution. Only the crystalline product was used for characterization and titrations.

[FeLCl] was synthesized by the previously published method, but using a different crystallization technique.[175] Anhydrous $FeCl_3$ (0.0324 g) was added to a 5 mL CH_2Cl_2 solution containing 0.076 g ligand and 0.08 g Et_3N, and the solution turned dark red. After stirring for two hours at RT, the solution was filtered to remove any unreacted solids. The filtrate was placed in a small vial inside a larger vial containing hexane, and a cap was placed on the larger vial. The crystalline product was obtained by very slow evaporation of the CH_2Cl_2 into the hexane.

8.8.3 Titrations of Complexes

Titrations of $[(FeL)_2(\mu\text{-OH})]BPh_4$ with various bases were carried out as follows: Et_3N was added in 100 µL aliquots (2700 equivalents each) to an acetonitrile solution of $[(FeL)_2(\mu\text{-OH})]BPh_4$ (7.5×10^{-5} M). Solution of proton sponge in acetonitrile (3.3×10^{-2} M) was added in increments of 500 equivalents to an acetonitrile solution of $[(FeL)_2(\mu\text{-OH})]BPh_4$ (8.6×10^{-5} M). Acetonitrile solutions of DBU or TMG (8.6×10^{-3} M) were added to an acetonitrile solution of $[(FeL)_2(\mu\text{-OH})]BPh_4$ (8.6×10^{-5} M) in increments of 0.1 equivalent of base up to 1.2 equivalents, then in increments of 1 equivalent up to 4 equivalents. In all cases, a UV-visible spectrum was recorded after each addition of base to the sample.

Air-free titrations of $[(FeL)_2(\mu\text{-O})]$ with benzoic acid (BZA) were monitored by UV-visible spectroscopy. Acetonitrile solutions of $[(FeL)_2(\mu\text{-O})]$ (9.1×10^{-5} M) and of benzoic acid (9.1×10^{-4} M) were prepared under nitrogen atmosphere. The solution of $[(FeL)_2(\mu\text{-O})]$ was placed in a cuvette fitted with a septum, and the benzoic acid solution was introduced in increments of 0.08 equivalents of benzoic acid to $[(FeL)_2(\mu\text{-O})]$ using an airtight syringe. The temperature was held constant at 25° C.

References

1. Bendz, D., Paxéus, N.A., Ginn, T.R., and Loge, F.J., Occurrence and fate of pharmaceutically active compounds in the environment, a case study: Höje River in Sweden. *Journal of Hazardous Materials,* 2005. **122**(3): p. 195-204.

2. Ternes, T.A., Joss, A., and Siegrist, H., Peer Reviewed: Scrutinizing Pharmaceuticals and Personal Care Products in Wastewater Treatment. *Environmental Science & Technology,* 2004. **38**(20): p. 392A-399A.

3. Zhou, J.L., Zhang, Z.L., Banks, E., Grover, D., and Jiang, J.Q., Pharmaceutical residues in wastewater treatment works effluents and their impact on receiving river water. *Journal of Hazardous Materials,* 2009. **166**(2-3): p. 655-661.

4. Maeng, S.K., Sharma, S.K., Lekkerkerker-Teunissen, K., and Amy, G.L., Occurrence and fate of bulk organic matter and pharmaceutically active compounds in managed aquifer recharge: A review. *Water Research,* 2011. **45**(10): p. 3015-3033.

5. Cooper, E.R., Siewicki, T.C., and Phillips, K., Preliminary risk assessment database and risk ranking of pharmaceuticals in the environment. *Science of The Total Environment,* 2008. **398**: p. 26-33.

6. Phillips, P.J., Schubert, C., Argue, D., Fisher, I., Furlong, E.T., Foreman, W., Gray, J., and Chalmers, A., Concentrations of hormones, pharmaceuticals and other micropollutants in groundwater affected by septic systems in New England and New York. *Science of The Total Environment,* 2015. **512–513**(0): p. 43-54.

7. Ternes, T.A., Occurence of Drugs in German Sewage Treatment Plants and Rivers. *Water Research,* 1998. **32**(11): p. 3245-3260.

8. Snyder, S.A., Keith, T.L., Verbrugge, D.A., Snyder, E.M., Gross, T.S., Kannan, K., and Giesy, J.P., Analytical Methods for Detection of Selected Estrogenic Compounds in Aqueous Mixtures. *Environmental Science & Technology,* 1999. **33**(16): p. 2814-2820.

9. Pedersen, J.A., Soliman, M., and Suffet, I.H., Human Pharmaceuticals, Hormones, and Personal Care Product Ingredients in Runoff from Agricultural Fields Irrigated with Treated Wastewater. *Journal of Agricultural and Food Chemistry,* 2005. **53**(5): p. 1625-1632.

10. Kümmerer, K., The presence of pharmaceuticals in the environment due to human use – present knowledge and future challenges. *Journal of Environmental Management,* 2009. **90**(8): p. 2354-2366.

11. Holm, J.V., Ruegge, K., Bjerg, P.L., and Christensen, T.H., Occurrence and Distribution of Pharmaceutical Organic Compounds in the Groundwater Downgradient of a Landfill (Grindsted, Denmark). *Environmental Science & Technology,* 1995. **29**(5): p. 1415-1420.

12. Eckel, W.P., Ross, B., and Isensee, R.K., Pentobarbital Found in Ground Water. *Ground Water,* 1993. **31**(5): p. 801-804.

13. Stumm-Zollinger, E. and Gordon, M.F., Biodegradation of Steroid Hormones. *Journal (Water Pollution Control Federation),* 1965. **37**(11): p. 1506-1510.

14. Díaz-Cruz, M.S. and Barceló, D., Recent advances in LC-MS residue analysis of veterinary medicines in the terrestrial environment. *TrAC Trends in Analytical Chemistry,* 2007. **26**(6): p. 637-646.

15. *Pharmaceutical in Drinking-Water*. 2012, World Health Organization: France.

16. Celiz, M.D., Tso, J., and Aga, D.S., Pharmaceutical Metabolites in the Environment: Analytical Challenges and Ecological Risks. *Environmental Toxicology and Chemistry,* 2009. **28**(12): p. 2473-84.

17. Smil, V., Detonator of the population explosion. *Nature,* 1999. **400**(6743): p. 415-415.

18. Speidel, J.J., Weiss, D.C., Ethelston, S.A., and Gilbert, S.M., Population policies, programmes and the environment. *Philosophical Transactions of the Royal Society of London B: Biological Sciences,* 2009. **364**(1532): p. 3049-3065.

19. Heeb, F., Singer, H., Pernet-Coudrier, B., Qi, W., Liu, H., Longrée, P., Müller, B., and Berg, M., Organic Micropollutants in Rivers Downstream of the Megacity Beijing: Sources and Mass Fluxes in a Large-Scale Wastewater Irrigation System. *Environmental Science & Technology,* 2012. **46**(16): p. 8680-8688.

20. Díaz-Cruz, M.S. and Barceló, D., LC-MS^2 trace analysis of antimicrobials in water, sediment and soil. *TrAC Trends in Analytical Chemistry,* 2005. **24**(7): p. 645-657.

21. Kun, Y. and Baoshan, X., *Soil Physicochemical and Biological Interfacial Processes Governing the Fate of Anthropogenic Organic Pollutants,* in *Handbook of Soil Sciences*. 2011, CRC Press. p. 1-44.

22. Kinney, C.A., Furlong, E.T., Werner, S.L., and Cahill, J.D., Presence and Distribution of Wastewater-derived Pharmaceuticals in Soil Irrigated with

Reclaimed Water. *Environmental Toxicology and Chemistry,* 2006. **25**(2): p. 317-26.

23. Calderón-Preciado, D., Jiménez-Cartagena, C., Matamoros, V., and Bayona, J.M., Screening of 47 organic microcontaminants in agricultural irrigation waters and their soil loading. *Water Research,* 2011. **45**(1): p. 221-231.

24. Baran, W., Adamek, E., Ziemiańska, J., and Sobczak, A., Effects of the presence of sulfonamides in the environment and their influence on human health. *Journal of Hazardous Materials,* 2011. **196**: p. 1-15.

25. Rabølle, M. and Spliid, N.H., Sorption and mobility of metronidazole, olaquindox, oxytetracycline and tylosin in soil. *Chemosphere,* 2000. **40**(7): p. 715-722.

26. Xu, J., Wu, L., and Chang, A.C., Degradation and adsorption of selected pharmaceuticals and personal care products (PPCPs) in agricultural soils. *Chemosphere,* 2009. **77**(10): p. 1299-1305.

27. Monteiro, S.C. and Boxall, A.B.A., Factors affecting the degradation of pharmaceuticals in agricultural soils. *Environmental Toxicology and Chemistry,* 2009. **28**(12): p. 2546-2554.

28. Doucette, W.J., Quantitative structure-activity relationships for predicting soil-sediment sorption coefficients for organic chemicals. *Environmental Toxicology and Chemistry,* 2003. **22**(8): p. 1771-1788.

29. Guo, R., Liang, X., Chen, J., Wu, W., Zhang, Q., Martens, D., and Kettrup, A., Prediction of soil organic carbon partition coefficients by soil column liquid chromatography. *Journal of Chromatography A,* 2004. **1035**(1): p. 31-36.

30. Bi, E. and Schmidt, T., Determination of Soil-Water Distribution Coefficients of Organic Compounds. *Earth Science Frontiers,* 2005. **12 (Suppl)**: p. 199-208.

31. Haderlein, S.B., Weissmahr, K.W., and Schwarzenbach, R.P., Specific Adsorption of Nitroaromatic Explosives and Pesticides to Clay Minerals. *Environmental Science & Technology,* 1996. **30**(2): p. 612-622.

32. Sparks, D.L., Milestones in Soil Chemistry. *Soil Science,* 2006. **171**(6, Suppl. 1): p. S47-S50.

33. MacEwan, D.M.C., Identification of the Montmorillonite Group of Minerals by X-Rays. *Nature,* 1944. **154**(3914): p. 577-578.

34. Bradley, W.F., Molecular Associations between Montmorillonite and Some Polyfunctional Organic Liquids1. *Journal of the American Chemical Society,* 1945. **67**(6): p. 975-981.

35. Simpson, A.J., McNally, D.J., and Simpson, M.J., NMR spectroscopy in environmental research: From molecular interactions to global processes. *Progress in Nuclear Magnetic Resonance Spectroscopy,* 2011. **58**(3–4): p. 97-175.

36. Chen, J.-S. and Chiu, C.-Y., Characterization of soil organic matter in different particle-size fractions in humid subalpine soils by CP/MAS 13C NMR. *Geoderma,* 2003. **117**(1–2): p. 129-141.

37. Hatcher, P.G., Dria, K.J., Kim, S., and Frazier, S.W., Modern Analytical Studies of Humic Substances. *Soil Science,* 2001. **166**(11): p. 770-794.

38. Lu, L., Frost, R., and Cai, J., Desorption of benzoic and stearic acid adsorbed upon montmorillonites: a thermogravimetric study. *Journal of Thermal Analysis and Calorimetry,* 2010. **99**(2): p. 377-384.

39. Yariv, S., Study of the adsorption of organic molecules on clay minerals by differential thermal analysis. *Thermochimica Acta,* 1985. **88**(1): p. 49-68.

40. Plante, A.F., Fernández, J.M., and Leifeld, J., Application of thermal analysis techniques in soil science. *Geoderma,* 2009. **153**(1–2): p. 1-10.

41. Yariv, S., Russell, J.D., and Farmer, V.C., Infrared Study of the Adsorption of Benzoic Acid and Nitrobenzene in Montmorillonite. *Israel Journal of Chemistry,* 1966. **4**(5-6): p. 201-213.

42. Yariv, S. and Lapides, I., Thermo-infrared-spectroscopy analysis of dimethylsulfoxide-kaolinite intercalation complexes. *Journal of Thermal Analysis & Calorimetry,* 2008. **94**: p. 433-440.

43. Yariv, S., Thermo-IR-spectroscopy analysis of the interactions between organic pollutants and clay minerals. *Thermochimica Acta,* 1996. **274**(0): p. 1-35.

44. Saltzman, S. and Yariv, S., Infrared Study of the Sorption of Phenol and p-Nitrophenol by Montmorillonite. *Soil Science Society of America Journal,* 1975. **39**: p. 474 - 479.

45. Ovadyahu, D., Shoval, S., Lapides, I., and Yariv, S., Thermo-IR-spectroscopy study of the mechanochemical adsorption of 3,5-dichlorophenol by TOT swelling clay minerals. *Thermochimica Acta,* 1996. **282–283**(0): p. 369-383.

46. Evanko, C.R. and Dzombak, D.A., Influence of Structural Features on Sorption of NOM-Analogue Organic Acids to Goethite. *Environmental Science & Technology*, 1998. **32**(19): p. 2846-2855.

47. Evanko, C.R. and Dzombak, D.A., Surface Complexation Modeling of Organic Acid Sorption to Goethite. *Journal of Colloid and Interface Science*, 1999. **214**(2): p. 189-206.

48. *CRC Handbook of Chemistry and Physics*, D.R. Lide, Editor. 2013, CRC Press: Boca Raton, FL.

49. Rainsford, K.D., *Aspirin and the Salicylates*. 1984, London: Butterworth & Co. (Publishers) Ltd.

50. Hayat, S. and Ahmad, A., eds. *Salicylic Acid: A Plant Hormone*. 2007, Springer: Dordrecht, The Netherlands.

51. Heberer, T., Occurrence, fate, and removal of pharmaceutical residues in the aquatic environment: a review of recent research data. *Toxicology Letters*, 2002. **131**(1–2): p. 5-17.

52. Fuster, V. and Sweeny, J.M., Aspirin: A Historical and Contemporary Therapeutic Overview. *Circulation*, 2011. **123**(7): p. 768-778.

53. *The Aspirin Foundation*. 2015 [cited 2015 October 8th, 2015]; Available from: http://www.aspirin-foundation.com/.

54. Smith, T., Elwood, P., Keating, C., Rothwell, P., Detering, E., Freedman, A., Langley, R., Logan, R., Phillips, C., and DeCensi, A., The Aspirin Foundation Scientific Conference: the history, the present state and the future of aspirin prophylaxis. *ecancermedicalscience*, 2014. **8**: p. 388.

55. Arif, T., Salicylic acid as a peeling agent: a comprehensive review. *Clinical, Cosmetic and Investigational Dermatology*, 2015. **8**: p. 455-461.

56. *National Center for Biotechnology Information. PubChem Compound Database; CID=338, http://pubchem.ncbi.nlm.nih.gov/compound/338 (accessed May 15, 2015).*

57. Celis, R., Real, M., Hermosín, M.C., and Cornejo, J., Sorption and leaching behaviour of polar aromatic acids in agricultural soils by batch and column leaching tests. *European Journal of Soil Science*, 2005. **56**(3): p. 287-297.

58. Kubicki, J.D., Schroeter, L.M., Itoh, M.J., Nguyen, B.N., and Apitz, S.E., Attenuated total reflectance Fourier-transform infrared spectroscopy of

carboxylic acids adsorbed onto mineral surfaces. *Geochimica et Cosmochimica Acta,* 1999. **63**(18): p. 2709-2725.

59. Gieseking, J.E., ed. *Soil Components*. Vol. 2. 1975, Springer-Verlag: New York.

60. Mering, J., *Smectites*, in *Soil Components*, J.E. Gieseking, Editor. 1975, Springer-Verlag: New York. p. 97-119.

61. Gates, W.P., Bordallo, H.N., Aldridge, L.P., Seydel, T., Jacobsen, H., Marry, V., and Churchman, G.J., Neutron Time-of-Flight Quantification of Water Desorption Isotherms of Montmorillonite. *The Journal of Physical Chemistry C,* 2012. **116**(9): p. 5558-5570.

62. Emmerich, K., Koeniger, F., Kaden, H., and Thissen, P., Microscopic structure and properties of discrete water layer in Na-exchanged montmorillonite. *Journal of Colloid and Interface Science,* 2015. **448**(0): p. 24-31.

63. Ferrage, E., Lanson, B., Sakharov, B.A., and Drits, V.A., Investigation of smectite hydration properties by modeling experimental X-ray diffraction patterns: Part I. Montmorillonite hydration properties. *American Minerologist,* 2005. **90**: p. 1358-1374.

64. Zhang, L., Lu, X., Liu, X., Zhou, J., and Zhou, H., Hydration and Mobility of Interlayer Ions of (Nax, Cay)-Montmorillonite: A Molecular Dynamics Study. *The Journal of Physical Chemistry C,* 2014. **118**(51): p. 29811-29821.

65. Foth, H.D., *Fundamentals of Soil Science*. 7th ed. 1984, New York: John Wiley & Sons.

66. Liu, X.-D. and Lu, X.-C., A Thermodynamic Understanding of Clay-Swelling Inhibition by Potassium Ions. *Angewandte Chemie,* 2006. **118**(38): p. 6448-6451.

67. Nickels, T.M., Ingram, A.L., Maraoulaite, D.K., and White, R.L., Thermogravimetry - Mass Spectrometry Investigations of Benzoic Acid Interactions with Sodium and Calcium Montmorillonite Clay. *Thermochimica Acta,* 2015. **614**: p. 157-162.

68. Yariv, S. and Cross, H., eds. *Organo-Clay Complexes and Interactions*. 2002, Marcel Dekker, Inc.: New York, NY.

69. Nickels, T.M., Ingram, A.L., Maraoulaite, D.K., and White, R.L., Variable Temperature Infrared Spectroscopy Investigation of Benzoic Acid Interactions with Montmorillonite Clay Interlayer Water. *Applied Spectroscopy,* 2015. **69**(7): p. 850-856.

70. Nickels, T.M., Ingram, A.L., Maraoulaite, D.K., and White, R.L., Variable Temperature Infrared Spectroscopy Investigations of Benzoic Acid Desorption from Sodium and Calcium Montmorillonite Clays. *Applied Spectroscopy,* 2015. **69**(12): p. 1381-1389.

71. Bonina, F.P., Giannossi, M.L., Medici, L., Puglia, C., Summa, V., and Tateo, F., Adsorption of salicylic acid on bentonite and kaolin and release experiments. *Applied Clay Science,* 2007. **36**(1–3): p. 77-85.

72. Nakai, Y., Yamamoto, K., Terada, K., Oguchi, T., and Izumikawa, S., Interactions between Crystalline Medicinals and Porous Clay. *Chemical & Pharmaceutical Bulletin,* 1986. **34**(11): p. 4760-4766.

73. Mackenzie, R.C. and Caillère, S., *The Thermal Characteristics of Soil Minerals and the Use of These Characteristics in the Qualitative and Quantitative Determination of Clay Minerals in Soils*, in *Soil Components*, J.E. Gieseking, Editor. 1975, Springer-Verlag: New York.

74. Yariv, S., Borisover, M., and Lapides, I., Few introducing comments on the thermal analysis of organoclays. *Journal of Thermal Analysis and Calorimetry,* 2011. **105**(3): p. 897-906.

75. Thomas, J.E. and Kelley, M.J., Interaction of mineral surfaces with simple organic molecules by diffuse reflectance IR spectroscopy (DRIFT). *Journal of Colloid and Interface Science,* 2008. **322**(2): p. 516-526.

76. Maraoulaite, D.K., Nickels, T.M., Ingram, A.L., and White, R.L., *VT-DRIFTS Investigations of Interactions between Benzoic Acid and Montmorillonite Clay*, in *Spectroscopy*. 2015, Advanstar Communications. p. 32-42.

77. Stanley, D.A. and Scheiner, B.J., *Flocculation and Dewatering of Montmorillonite Modified by Ion Exchange*. 1986, U.S. Dept. of Interior, Bureau of Mines, Avondale, MD.

78. Stanley, D.A., Webb, S.W., and Scheiner, B.J., *Rheology of ion-exchanged montmorillonite clays*. 1984, U.S. Dept. of Interior, Bureau of Mines: Avondale, MD

79. Lahav, N., Chean, Y., and Bar-Yosef, B., CLAY SUSPENSIONS IN A DRYING-OUT PROCESS. *Soil Science,* 1968. **106**(4): p. 297-302.

80. Fitzsimmons, R.F., Posner, A.M., and Quirk, J.P., Electron Microscopic and Kinetic Study of Flocculation of Calcium Montmorillonite. *Israel Journal of Chemistry,* 1970. **8**: p. 301-314.

81. El Younssi, I., Rhadfi, T., Atlamsani, A., Quisefit, J.-P., Herbst, F., and Draoui, K., K-10 montmorillonite: An efficient and reusable catalyst for the aerobic CC bond cleavage of α-substituted ketones. *Journal of Molecular Catalysis A: Chemical*, 2012. **363–364**: p. 437-445.

82. Hapke, B., *Specular reflection*, in *Theory of Reflectance and Emittance Spectroscopy*. 2012, Cambridge University Press.

83. Griffiths, P.R. and de Haseth, J.A., *Specular Reflection*, in *Fourier Transform Infrared Spectrometry*. 2006, John Wiley & Sons, Inc. p. 277-301.

84. White, D.R. and White, R.L., Isoconversion Effective Activation Energy Profiles by Variable Temperature Diffuse Reflection Infrared Spectroscopy. *Applied Spectroscopy,* 2008. **62**(1): p. 116-120.

85. Lin, R. and White, R.L., Effect of Diffuse Reflectance Fourier Transform Infrared Spectroscopy Sample Temperature on Photoconducting Semiconductor and Pyroelectric Infrared Detectors. *Analytical Chemistry*, 1994. **66**(18): p. 2976-2980.

86. Griffiths, P.R. and de Haseth, J.A., *Diffuse Reflection*, in *Fourier Transform Infrared Spectrometry*. 2006, John Wiley & Sons, Inc. p. 349-362.

87. Morodome, S. and Kawamura, K., Swelling behavior of Na- and Ca-montmorillonite up to 150°C by in situ X-ray diffraction experiments. *Clays and Clay Minerals,* 2009. **57**(2): p. 150-160.

88. Ferrage, E., Kirk, C.A., Cressey, G., and Cuadros, J., Dehydration of Ca-montmorillonite at the crystal scale. Part I: Structure evolution. *American Mineralogist,* 2007. **92**(7): p. 994-1006.

89. Ferrage, E., Kirk, C.A., Cressey, G., and Cuadros, J., Dehydration of Ca-montmorillonite at the crystal scale. Part 2. Mechanisms and kinetics. *American Mineralogist,* 2007. **92**(7): p. 1007-1017.

90. Hendricks, S.B., Nelson, R.A., and Alexander, L.T., Hydration Mechanism of the Clay Mineral Montmorillonite Saturated with Various Cations. *Journal of the American Chemical Society,* 1940. **62**(6): p. 1457-1464.

91. Michot, L.J., Ferrage, E., Jiménez-Ruiz, M., Boehm, M., and Delville, A., Anisotropic Features of Water and Ion Dynamics in Synthetic Na- and Ca-Smectites with Tetrahedral Layer Charge. A Combined Quasi-elastic Neutron-Scattering and Molecular Dynamics Simulations Study. *The Journal of Physical Chemistry C,* 2012. **116**(31): p. 16619-16633.

92. Sayegh, A.H., Harward, M.E., and Knox, E.G., Humidity and Temperature Interaction with Respect to K-saturated Expanding Clay Minerals. *The American Minerologist*, 1965. **50**(3-4): p. 490-495.

93. Morillo, E., Perezrodriguez, J.L., and Maqueda, C., Mechanisms of Interaction Between Montmorillonite and 3-aminotriazole. *Clay Minerals,* 1991. **26**(2): p. 269-279.

94. Akyuz, T. and Akyuz, S., Investigation of adsorption of 5-bromouracil from aqueous solutions to montmorillonite and its interaction with clay framework: a FT-IR spectroscopic study. *Asian Journal of Chemistry,* 2011. **23**(7): p. 3211-3213.

95. Zviagina, B.B., McCarty, D.K., Srodon, J., and Drits, V.A., Interpretation of Infrared Spectra of Dioctahedral Smectites in the Region of OH-Stretching Vibrations. *Clays and Clay Minerals,* 2004. **52**(4): p. 399-410.

96. Morterra, C. and Magnacca, G., A Case Study: Surface Chemistry and Surface Structure of Catalytic Aluminas, as Studied by Vibrational Spectroscopy of Adsorbed Species. *Catalysis Today,* 1996. **27**: p. 497-532.

97. Radtsig, V.A., Baskie, E.G., and Korolev, V.A., Geminal Silanol Groups at the Surface of Silica. *Kinetics and Catalysis,* 1995. **36**(4): p. 568-574.

98. Meng, S., Greenlee, L.F., Shen, Y.R., and Wang, E., Basic Science of Water: Challenges and Current Status towards a Molecular Picture. *Nano Research,* 2015. **8**(10): p. 3085-3110.

99. Wernet, P., Nordlund, D., Bergmann, U., Cavalleri, M., Odelius, M., Ogasawara, H., Naslund, L.A., Hirsch, T.K., Ojamae, L., Glatzel, P., Pettersson, L.G.M., and Nilsson, A., The Structure of the First Coordination Shell in Liquid Water. *Science,* 2004. **304**: p. 995-999.

100. Smith, J.D., Cappa, C.D., Wilson, K.R., Messer, B.M., Cohen, R.C., and Saykally, R.J., Energetics of Hydrogen Bond Network Rearrangements in Liquid Water. *Science,* 2004. **306**: p. 851-853.

101. Hyeon-Deuk, K. and Ando, K., Quantum Effects of Hydrogen Atoms on the Dynamical Rearrangement of Hydrogen-Bond Networks in Liquid Water. *Journal of Chemical Physics,* 2010. **132**: p. 164507.

102. Meng, S., Chakarov, D.V., Kasemo, B., and Gao, S.W., Two Dimensional Hydration Shells of Alkali Metal Ions at a Hydrophobic Surface. *Journal of Chemical Physics,* 2004. **121**: p. 12572.

103. Meng, S. and Gao, S.W., Formation and Interaction of Hydrated Alkali Metal Ions at the Graphite-Water Interface. *Journal of Chemical Physics,* 2006. **125**: p. 014708.

104. Dazas, B., Ferrage, E., Delville, A., and Lanson, B., Interlayer Structure Model of Tri-Hydrated Low-Charge Smectite by X-Ray Diffraction and Monte Carlo Modeling in the Grand Canonical Ensemble. *American Minerologist,* 2014. **99**: p. 1724-1735.

105. Denisov, G.S., Golubev, N.S., Schreiber, V.M., Shajakhmedov, S.S., and Shurukhina, A.V., Effect of intermolecular hydrogen bonding and proton transfer on fluorescence of salicylic acid. *Journal of Molecular Structure,* 1997. **436–437**: p. 153-160.

106. Glaser, R., Aspirin. An Ab Initio Quantum-Mechanical Study of Conformational Preferences and of Neighboring Group Interactions. *Journal of Organic Chemistry,* 2001. **66**: p. 771-779.

107. Yurtsever, Z., Erman, B., and Yurtsever, E., Competitive Hydrogen Bonding in Aspirin-Aspirin and Aspirin-Leucine Interactions. *Turkish Journal of Chemistry,* 2012. **36**: p. 383-395.

108. Boczar, M., Szczeponek, K., Wójcik, M.J., and Paluszkiewicz, C., Theoretical modeling of infrared spectra of benzoic acid and its deuterated derivative. *Journal of Molecular Structure,* 2004. **700**(1–3): p. 39-48.

109. Karthika, M., Senthilkumar, K., and Kanakaraju, R., Hydrogen Bond Interactions in Hydrated Acetylsalicylic Acid. *Computational and Theoretical Chemistry,* 2011. **966**: p. 167-179.

110. Gorbaty, Y.E. and Bondarenko, G.V., Comparison of the Sensitivities of IR Absorption and Raman Scattering Spectra to Hydrogen Bonding in Methanol. *Russian Journal of Physical Chemistry B,* 2012. **6**(8): p. 873-877.

111. Rozenberg, M., The Hydrogen Bond - Practice and QTAIM Theory. *RSC Advances,* 2014. **4**: p. 26928-26931.

112. Rozenberg, M., Loewenchuss, A., and Marcus, Y., An Empirical Correlation between Stretching Vibation Redshift and Hydrogen Bond Length. *Physical Chemistry Chemical Physics,* 2000. **2**: p. 2699-2702.

113. Li, J. and Brill, T.B., Spectroscopy of Hydrothermal Reactions 23: The Effect of OH Substitution on the Rates and Mechanisms of Decarboxylation of Benzoic Acid. *The Journal of Physical Chemistry A,* 2003. **107**(15): p. 2667-2673.

114. Lindquist, E. and Yang, Y., Degradation of benzoic acid and its derivatives in subcritical water. *Journal of Chromatography A,* 2011. **1218**(15): p. 2146-2152.

115. Lock, P.A. and Skipper, N.T., Computer simulation of the structure and dynamics of phenol in sodium montmorillonite hydrates. *European Journal of Soil Science,* 2007. **58**(4): p. 958-966.

116. Schaef, H.T., Loring, J.S., Glezakou, V.-A., S. Miller, Q.R., Chen, J., Owen, A.T., Lee, M.-S., Ilton, E.S., Felmy, A.R., Pete McGrail, B., and Thompson, C.J., Competitive Sorption of CO2 and H2O in 2:1 Layer Phyllosilicates. *Geochimica et Cosmochimica Acta,* (0).

117. Stepanian, S.G., Reva, I.D., Radchenko, E.D., and Sheina, G.G., Infrared spectra of benzoic acid monomers and dimers in argon matrix. *Vibrational Spectroscopy,* 1996. **11**(2): p. 123-133.

118. Bakker, J.M., Mac Aleese, L., von Helden, G., and Meijer, G., The infrared absorption spectrum of the gas phase neutral benzoic acid monomer and dimer. *The Journal of Chemical Physics,* 2003. **119**(21): p. 11180-11185.

119. Antony, J., von Helden, G., Meijer, G., and Schmidt, B., Anharmonic midinfrared vibrational spectra of benzoic acid monomer and dimer. *The Journal of Chemical Physics,* 2005. **123**(1): p. 014305.

120. Murray, F.E. and Sundaram, S., Molecular Interactions: I. Infrared Spectra of Some Carboxylic Acids in Carbon Tetrachloride and Benzene Solutions. *Canadian Journal of Chemistry,* 1961. **39**(8): p. 1625-1632.

121. Philip, D., John, A., Panicker, C.Y., and Varghese, H.T., FT-Raman, FT-IR and surface enhanced Raman scattering spectra of sodium salicylate. *Spectrochimica Acta Part A: Molecular and Biomolecular Spectroscopy,* 2001. **57**(8): p. 1561-1566.

122. Boczar, M., Boda, Ł., and Wójcik, M.J., Theoretical model for a tetrad of hydrogen bonds and its application to interpretation of infrared spectra of salicylic acid. *Journal of Chemical Physics,* 2006. **124**(8): p. 084306.

123. Boczar, M., Wójcik, M.J., Szczeponek, K., Jamróz, D., Zięba, A., and Kawałek, B., Theoretical modeling of infrared spectra of aspirin and its deuterated derivative. *Chemical Physics,* 2003. **286**(1): p. 63-79.

124. Steiner, T., The Hydrogen Bond in the Solid State. *Angewandte Chemie International Edition,* 2002. **41**: p. 48-76.

125. Iogansen, A.V., Direct Proportionality of the Hydrogen Bonding Energy and the Intensification of the Stretching v(XH) Vibration in Infrared Spectra.

Spectrochimica Acta A: Molecular and Biomolecular Spectroscopy, 1999. **55**(7-8): p. 1585-1612.

126. Del Bene, J.E., Molecular Orbital Theory of the Hydrogen Bond. X Monosubstituted Carbonyls as Proton Acceptors. *Journal of Chemical Physics,* 1975. **62**(4): p. 1314-1322.

127. Rozenberg, M., Shoham, G., Reva, I., and Fausto, R., A Correlation between the Proton Stretching Vibration Red Shift and the Hydrogen Bond Lengths in Polycrystalline Amino Acids and Peptides. *Physical Chemistry Chemical Physics,* 2005. **7**: p. 2376-2383.

128. Bergman, R.G., Organometallic chemistry: C-H activation. *Nature,* 2007. **446**(7134): p. 391-393.

129. Holm, R.H., Kennepohl, P., and Solomon, E.I., Structural and Functional Aspects of Metal Sites in Biology. *Chemical Reviews,* 1996. **96**(7): p. 2239-2314.

130. Wilkins, R.G., Binuclear iron centres in proteins. *Chemical Society Reviews,* 1992. **21**(3): p. 171-178.

131. Wallar, B.J. and Lipscomb, J.D., Dioxygen Activation by Enzymes Containing Binuclear Non-Heme Iron Clusters. *Chemical Reviews,* 1996. **96**(7): p. 2625-2658.

132. Que, L. and Ho, R.Y.N., Dioxygen Activation by Enzymes with Mononuclear Non-Heme Iron Active Sites. *Chemical Reviews,* 1996. **96**(7): p. 2607-2624.

133. Bullock, R.M. and Helm, M.L., Molecular Electrocatalysts for Oxidation of Hydrogen Using Earth-Abundant Metals: Shoving Protons Around with Proton Relays. *Accounts of Chemical Research,* 2015. **48**(7): p. 2017-2026.

134. Kurtz, D.M., Oxo- and hydroxo-bridged diiron complexes: a chemical perspective on a biological unit. *Chemical Reviews,* 1990. **90**(4): p. 585-606.

135. Tshuva, E.Y. and Lippard, S.J., Synthetic Models for Non-Heme Carboxylate-Bridged Diiron Metalloproteins: Strategies and Tactics. *Chemical Reviews,* 2004. **104**(2): p. 987-1012.

136. Stenkamp, R.E., Dioxygen and Hemerythrin. *Chemical Reviews,* 1994. **94**(3): p. 715-726.

137. Gray, H.B., *Structural Models for Iron and Copper Proteins Based on Spectroscopic and Magnetic Properties,* in *Bioinorganic Chemistry*. 1971, American Chemical Society. p. 365-389.

138. Schenk, G., Mitić, N., Hanson, G.R., and Comba, P., Purple acid phosphatase: A journey into the function and mechanism of a colorful enzyme. *Coordination Chemistry Reviews,* 2013. **257**(2): p. 473-482.

139. Smoukov, S.K., Quaroni, L., Wang, X., Doan, P.E., Hoffman, B.M., and Que, L., Electron−Nuclear Double Resonance Spectroscopic Evidence for a Hydroxo-Bridge Nucleophile Involved in Catalysis by a Dinuclear Hydrolase. *Journal of the American Chemical Society,* 2002. **124**(11): p. 2595-2603.

140. Du Bois, J., Mizoguchi, T.J., and Lippard, S.J., Understanding the dioxygen reaction chemistry of diiron proteins through synthetic modeling studies. *Coordination Chemistry Reviews,* 2000. **200-202**: p. 443-485.

141. Wilkins, P.C. and Wilkins, R.G., The coordination chemistry of the binuclear iron site in hemerythrin. *Coordination Chemistry Reviews,* 1987. **79**(3): p. 195-214.

142. Holmes, M.A., Le Trong, I., Turley, S., Sieker, L.C., and Stenkamp, R.E., Structures of deoxy and oxy hemerythrin at 2.0 Å resolution. *Journal of Molecular Biology,* 1991. **218**(3): p. 583-593.

143. Gray, H.B. and Ellis, W.R.J., *Electron Transfer*, in *Bioinorganic Chemistry*. 1994, University Science Books: Mill Valley, CA.

144. Lee, D., Lippard, S.J., McCleverty, J.A., and Meyer, T.J., *Nonheme Di-iron Enzymes*, in *Comprehensive Coordination Chemistry II*. 2003, Pergamon: Oxford. p. 309-342.

145. Que, L. and True, A.E., *Dinuclear Iron- and Manganese-Oxo Sites in Biology*, in *Progress in Inorganic Chemistry*. 1990, John Wiley & Sons, Inc. p. 97-200.

146. Tomter, A.B., Zoppellaro, G., Andersen, N.H., Hersleth, H.-P., Hammerstad, M., Røhr, Å.K., Sandvik, G.K., Strand, K.R., Nilsson, G.E., Bell Iii, C.B., Barra, A.-L., Blasco, E., Le Pape, L., Solomon, E.I., and Andersson, K.K., Ribonucleotide reductase class I with different radical generating clusters. *Coordination Chemistry Reviews,* 2013. **257**(1): p. 3-26.

147. Han, W.-G. and Noodleman, L., DFT calculations of comparative energetics and ENDOR/Moessbauer properties for two protonation states of the iron dimer cluster of ribonucleotide reductase intermediate X. *Dalton Transactions,* 2009(30): p. 6045-6057.

148. Hermans, I., Spier, E., Neuenschwander, U., Turrà, N., and Baiker, A., Selective Oxidation Catalysis: Opportunities and Challenges. *Topics in Catalysis,* 2009. **52**(9): p. 1162-1174.

149. Tinberg, C.E. and Lippard, S.J., Dioxygen Activation in Soluble Methane Monooxygenase. *Accounts of Chemical Research,* 2011. **44**(4): p. 280-288.

150. Mitić, N., Smith, S.J., Neves, A., Guddat, L.W., Gahan, L.R., and Schenk, G., The Catalytic Mechanisms of Binuclear Metallohydrolases. *Chemical Reviews,* 2006. **106**(8): p. 3338-3363.

151. Guddat, L.W., McAlpine, A.S., Hume, D., Hamilton, S., de Jersey, J., and Martin, J.L., Crystal structure of mammalian purple acid phosphatase. *Structure,* 1999. **7**(7): p. 757-767.

152. Klabunde, T., Sträter, N., Fröhlich, R., Witzel, H., and Krebs, B., Mechanism of Fe(III) – Zn(II) Purple Acid Phosphatase Based on Crystal Structures. *Journal of Molecular Biology,* 1996. **259**(4): p. 737-748.

153. Lindqvist, Y., Johansson, E., Kaija, H., Vihko, P., and Schneider, G., Three-dimensional structure of a mammalian purple acid phosphatase at 2.2 Å resolution with a μ-(hydr)oxo bridged di-iron center1. *Journal of Molecular Biology,* 1999. **291**(1): p. 135-147.

154. Sträter, N., Jasper, B., Scholte, M., Krebs, B., Duff, A.P., Langley, D.B., Han, R., Averill, B.A., Freeman, H.C., and Guss, J.M., Crystal Structures of Recombinant Human Purple Acid Phosphatase With and Without an Inhibitory Conformation of the Repression Loop. *Journal of Molecular Biology,* 2005. **351**(1): p. 233-246.

155. Yang, Y.-S., McCormick, J.M., and Solomon, E.I., Circular Dichroism and Magnetic Circular Dichroism Studies of the Mixed-Valence Binuclear Non-Heme Iron Active Site in Uteroferrin and Its Anion Complexes. *Journal of the American Chemical Society,* 1997. **119**(49): p. 11832-11842.

156. Park, D. and Lee, J., Biological conversion of methane to methanol. *Korean Journal of Chemical Engineering,* 2013. **30**(5): p. 977-987.

157. Baldwin, M., Gelasco, A., and Pecoraro, V., The effect of protonation on $[Mn(IV)(\mu_2\text{-}O)]_2$ complexes. *Photosynthesis Research,* 1993. **38**(3): p. 303-308.

158. Larson, E.J., Riggs, P.J., Penner-Hahn, J.E., and Pecoraro, V.L., Protonation of $[\{Mn^{IV}(saltn)(\mu\text{-}O)\}_2]$ results in significant modification of structure and catalase-like reactivity. *Journal of the Chemical Society, Chemical Communications,* 1992(2): p. 102-103.

159. Baldwin, M.J., Law, N.A., Stemmler, T.L., Kampf, J.W., Penner-Hahn, J.E., and Pecoraro, V.L., Reactivity of $[\{Mn^{IV}(salpn)\}_2(\mu\text{-}O,\mu\text{-}OCH_3)]^+$ and

$[\{Mn^{IV}(salpn)\}_2(\mu\text{-}O,\mu\text{-}OH)]^+$: Effects of Proton Lability and Hydrogen Bonding. *Inorganic Chemistry,* 1999. **38**(21): p. 4801-4809.

160. Dubé, C.E., Wright, D.W., and Armstrong, W.H., Multiple Reversible Protonations of the Adamantane-Shaped $\{Mn_4O_6\}^{4+}$ Core: Detection of Protonation Stereoisomers at the $\{Mn_4O_4(OH)_2\}^{6+}$ Level. *Journal of the American Chemical Society,* 1996. **118**(44): p. 10910-10911.

161. Hage, R., Krijnen, B., Warnaar, J.B., Hartl, F., Stufkens, D.J., and Snoeck, T.L., Proton-Coupled Electron-Transfer Reactions in $[MnIV_2(\mu\text{-}O)_3L'_2]^{2+}$ (L' = 1,4,7-Trimethyl- 1,4,7-triazacyclononane). *Inorganic Chemistry,* 1995. **34**(20): p. 4973-4978.

162. Manchanda, R., Thorp, H.H., Brudvig, G.W., and Crabtree, R.H., Proton-coupled electron transfer in high-valent oxomanganese dimers: role of the ancillary ligands. *Inorganic Chemistry,* 1991. **30**(3): p. 494-497.

163. Carroll, J.M. and Norton, J.R., Protonation of a bridging oxo ligand is slow. *Journal of the American Chemical Society,* 1992. **114**(22): p. 8744-8745.

164. Fox, S., Nanthakumar, A., Wikström, M., Karlin, K.D., and Blackburn, N.J., XAS Structural Comparisons of Reversibly Interconvertible Oxo- and Hydroxo-Bridged Heme-Copper Oxidase Model Compounds. *Journal of the American Chemical Society,* 1996. **118**(1): p. 24-34.

165. Kopf, M.-A., Neuhold, Y.-M., Zuberbuhler, A.D., and Karlin, K.D., Oxo- and Hydroxo-Bridged Heme-Copper Assemblies Formed from Acid-Base or Metal-Dioxygen Chemistry. *Inorganic Chemistry,* 1999. **38**(13): p. 3093-3102.

166. Armstrong, W.H. and Lippard, S.J., Reversible protonation of the oxo bridge in a hemerythrin model compound. Synthesis, structure, and properties of (.mu.-hydroxo)bis(.mu.-acetato)bis[hydrotris(1-pyrazolyl)borato]diiron(III) [(HB(pz)3)Fe(OH)(O2CCH3)2Fe(HB(pz)3)2]+. *Journal of the American Chemical Society,* 1984. **106**(16): p. 4632-4633.

167. Ghosh, S.K., Bhowmik, S., Sil, D., and Rath, S.P., Effect of Heme–Heme Interactions and Modulation of Metal Spins by Counter Anions in a Series of Diiron(III)-μ-hydroxo Bisporphyrins: Unusual Stabilization of Two Different Spins in a Single Molecular Framework. *Chemistry – A European Journal,* 2013. **19**(52): p. 17846-17859.

168. Ghosh, S.K. and Rath, S.P., A Remarkably Bent Diiron(III)-μ-Hydroxo Bisporphyrin: Unusual Stabilization of Two Spin States of Iron in a Single Molecular Framework. *Journal of the American Chemical Society,* 2010. **132**(51): p. 17983-17985.

169. Biswas, R., Drew, M.G.B., Estarellas, C., Frontera, A., and Ghosh, A., Synthesis and Crystal Structures of μ-Oxido- and μ-Hydroxido-Bridged Dinuclear Iron(III) Complexes with an N2O Donor Ligand – A Theoretical Study on the Influence of Weak Forces on the Fe–O–Fe Bridging Angle. *European Journal of Inorganic Chemistry,* 2011. **2011**(16): p. 2558-2566.

170. Evans, D.R., Mathur, R.S., Heerwegh, K., Reed, C.A., and Xie, Z., Protonation of a Linear Oxo-Bridged Diiron Unit without Rehybridization of the Bridging Oxygen: Structure of the (μ-Hydroxo)bis-(tetraphenylporphyrinato)iron (III) Cation. *Angewandte Chemie International Edition in English,* 1997. **36**(12): p. 1335-1337.

171. Kurosaki, H., Synthesis and characterization of Bis(m-hydroxo)diiron(III) complex of N-(4-Nitro-2-hydroxy)phenylmethyl-N-(2-pyridylethyl)-N-(2-pyridylmethyl)amine and hydroxylation reaction of alkane. *Bioinorganic and Medicinal Chemistry Letters,* 2001. **11**(6): p. 785-788.

172. Zheng, H., Zang, Y., Dong, Y., Young, V.G., and Que, L., Complexes with $\mathrm{FeIII_2(\mu\text{-}O)(\mu\text{-}OH)}$, $\mathrm{FeIII_2(\mu\text{-}O)_2}$, and $\mathrm{[FeIII_3(\mu_2\text{-}O)_3]}$ Cores: Structures, Spectroscopy, and Core Interconversions *Journal of the American Chemical Society,* 1999. **121**(10): p. 2226-2235.

173. Cui, J., Mashuta, M.S., Buchanan, R.M., and Grapperhaus, C.A., Synthesis, Structure, and Solution Properties of $\mathrm{[(mim\text{-}TASN)FeCl2]^+}$ and Its μ-Oxo Derivative. *Inorganic Chemistry,* 2010. **49**(22): p. 10427-10435.

174. Shakya, R., Jozwiuk, A., Powell, D.R., and Houser, R.P., Synthesis and Characterization of Polynuclear Copper(II) Complexes with Pyridylbis(phenol) Ligands. *Inorganic Chemistry,* 2009. **48**(9): p. 4083-4088.

175. Shakya, R., Powell, D.R., and Houser, R.P., Unsupported μ-Oxo- and μ-Hydroxo-Iron(III) Dimers and Mononuclear Iron(III) Complexes with Pyridylbis(aminophenol) Ligands. *European Journal of Inorganic Chemistry,* 2009. **2009**: p. 5319-5327.

176. Jozwiuk, A., Ingram, A.L., Powell, D.R., Moubaraki, B., Chilton, N.F., Murray, K.S., and Houser, R.P., Redox and acid-base properties of asymmetric non-heme (hydr)oxo-bridged diiron complexes. *Dalton Transactions,* 2014. **43**(25): p. 9740-9753.

177. Davies, J.E. and Gatehouse, B.M., The crystal and molecular structure of unsolvated [mu]-oxo-bis[N,N'-ethylenebis(salicylaldiminato)iron(III)]. *Acta Crystallographica Section B,* 1973. **29**(9): p. 1934-1942.

178. Weiss, M.C. and Goedken, V.L., Synthesis and crystal and molecular structure of the oxo-bridged, iron(III) macrocyclic dimer [Fe(C22H22N4)]2O.CH3CN:

.mu.-oxo-bis[7,16-dihydro-6,8,16,17-tetramethyldibenzo[b,i][1,4,8,11]tetraazacyclotetradecinato]iron(III)-acetonitrile. *Inorganic Chemistry,* 1979. **18**(3): p. 819-826.

179. Gerloch, M., McKenzie, E.D., and Towl, A.D.C., Crystal and molecular structure of [small micro]-oxo-bis-[NN[prime or minute]-ethylenebis(salicylideneiminato)iron(III)]-bispyridine. *Journal of the Chemical Society A: Inorganic, Physical, Theoretical,* 1969(0): p. 2850-2858.

180. Lopez, J.P., Kampf, H., Grunert, M., Gutlich, P., Heinemann, F.W., Prakash, R., and Grohmann, A., A non-heme dinuclear iron(ii) complex containing a single, unsupported hydroxo bridge. *Chemical Communications,* 2006(16): p. 1718-1720.

181. Jullien, J., Juhász, G., Mialane, P., Dumas, E., Mayer, C.R., Marrot, J., Rivière, E., Bominaar, E.L., Münck, E., and Sécheresse, F., Structure and Magnetic Properties of a Non-Heme Diiron Complex Singly Bridged by a Hydroxo Group. *Inorganic Chemistry,* 2006. **45**(17): p. 6922-6927.

182. Kaljurand, I., Kütt, A., Sooväli, L., Rodima, T., Mäemets, V., Leito, I., and Koppel, I.A., Extension of the Self-Consistent Spectrophotometric Basicity Scale in Acetonitrile to a Full Span of 28 pK_a Units: Unification of Different Basicity Scales. *The Journal of Organic Chemistry,* 2005. **70**(3): p. 1019-1028.

183. Kütt, A., Leito, I., Kaljurand, I., Sooväli, L., Vlasov, V.M., Yagupolskii, L.M., and Koppel, I.A., A Comprehensive Self-Consistent Spectrophotometric Acidity Scale of Neutral Brønsted Acids in Acetonitrile. *The Journal of Organic Chemistry,* 2006. **71**(7): p. 2829-2838.

184. Friedrich, S., Schubart, M., Gade, L.H., Scowen, I.J., Edwards, A.J., and McPartlin, M., Titanium and Zirconium Complexes Containing a Novel Dianionic Trifunctional Amido Ligand. *Chemische Berichte,* 1997. **130**(12): p. 1751-1759.

Appendix A: List of Abbreviations

CEC	cation exchange capacity
CH_2Cl_2	dichloromethane
CH_3CN	acetonitrile
$CoCp_2$	cobaltocene
CV	cyclic voltammetry
DBU	1,8-Diazabicyclo[5.4.0]undec-7-ene
DRIFTS	diffuse reflection infrared Fourier transform spectroscopy
Et_3N	triethylamine
Et_2O	diethyl ethere
FTIR	Fourier transform infrared spectroscopy
H_2L	2,2'-(2-Methyl-2-(pyridin-2-yl)-propane-1,3-diyl)bis(azanediyl)-bis(methylene)diphenol
HOBz	benzoic acid
HOTf	trifluoromethanesulfonic acid (triflic acid)
IR	infrared
M	molarity, or moles/liter
MMO	methane monooxygenase
MMT	montmorillonite
MS	mass spectrometry
OBz^-	benzoate
OTC	over-the-counter

PAP	purple acid phosphatase
PPCPs	pharmaceuticals and personal care products
ppda	2-methyl-2-(pyridine-2-yl)propane-1,3-diamine
RH	relative humidity
RNR	ribonucleotide reductase
RT	room temperature
sMMO	soluble methane monooxygenase
TG	thermogravimetry
TG-MS	thermogravimetry-mass spectrometry
UV-vis	ultraviolet-visible spectroscopy
VT-DRIFTS	variable temperature diffuse reflection infrared Fourier transform spectroscopy
WWTPs	waste water treatment plants
XRD	X-ray diffraction

Appendix B : NaMMT and CaMMT Mass Loss Curves

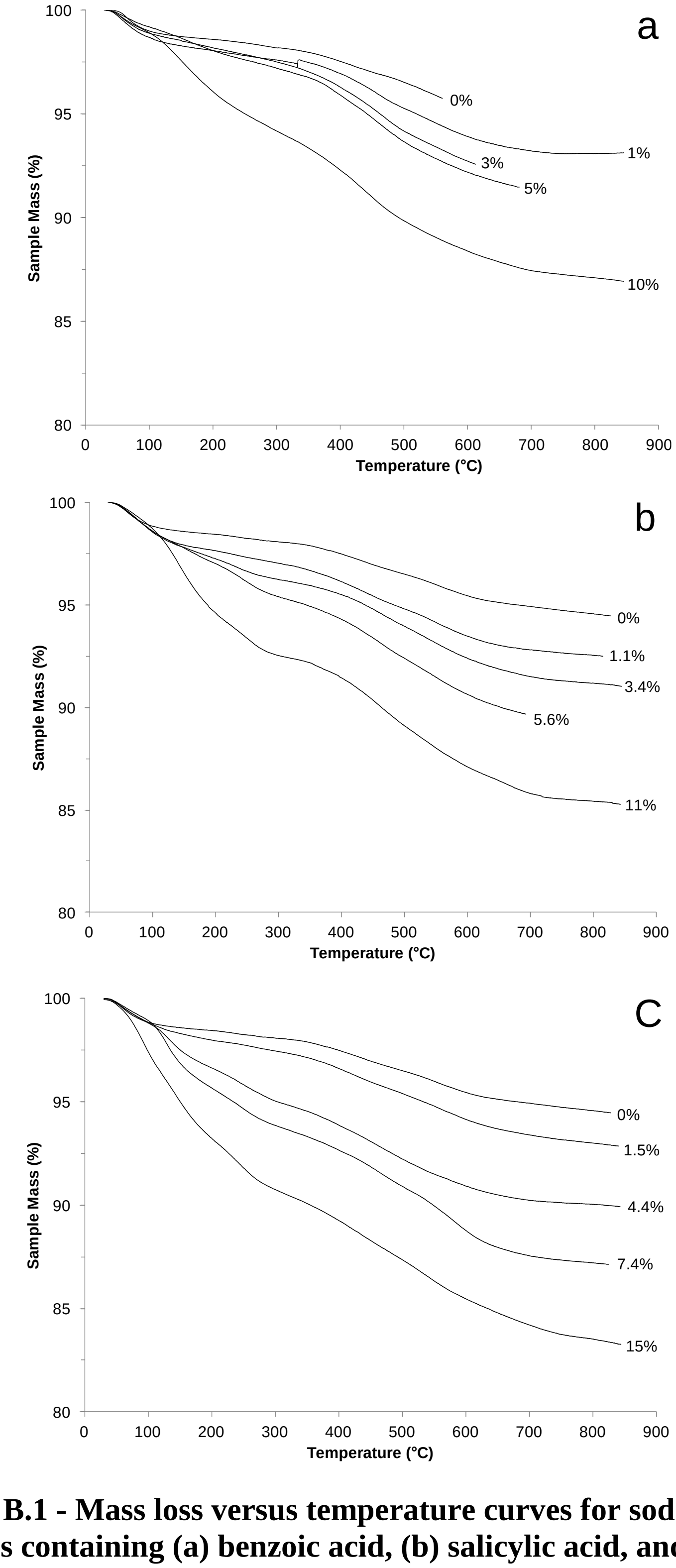

Figure B.1 - Mass loss versus temperature curves for sodium montmorillonite samples containing (a) benzoic acid, (b) salicylic acid, and (c) aspirin adsorbates. Sample loading percentages are indicated for each curve.

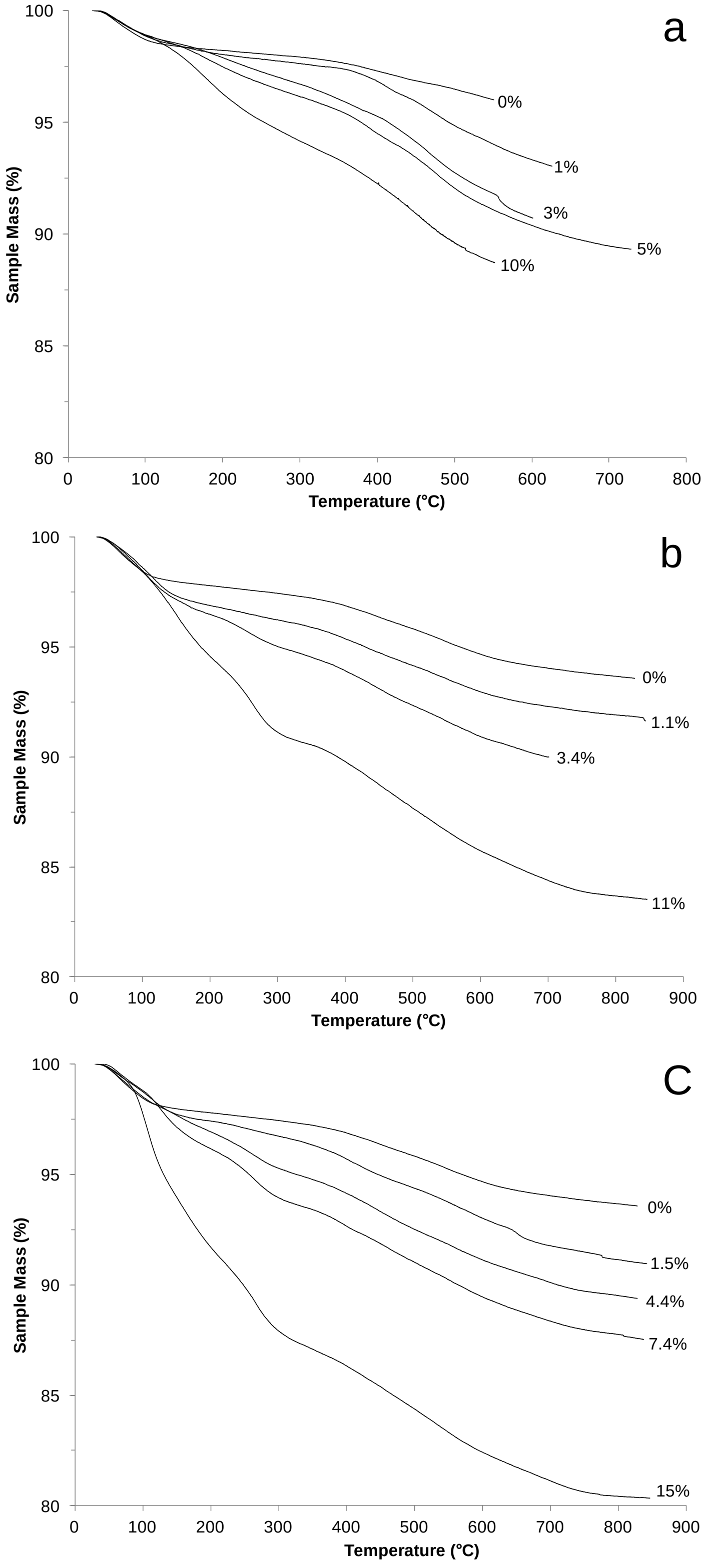

Figure B.2 - Mass loss versus temperature curves for calcium montmorillonite samples containing (a) benzoic acid, (b) salicylic acid, and (c) aspirin adsorbates. Sample loading percentages are indicated for each curve.

Appendix C : TGA Analyses in Air

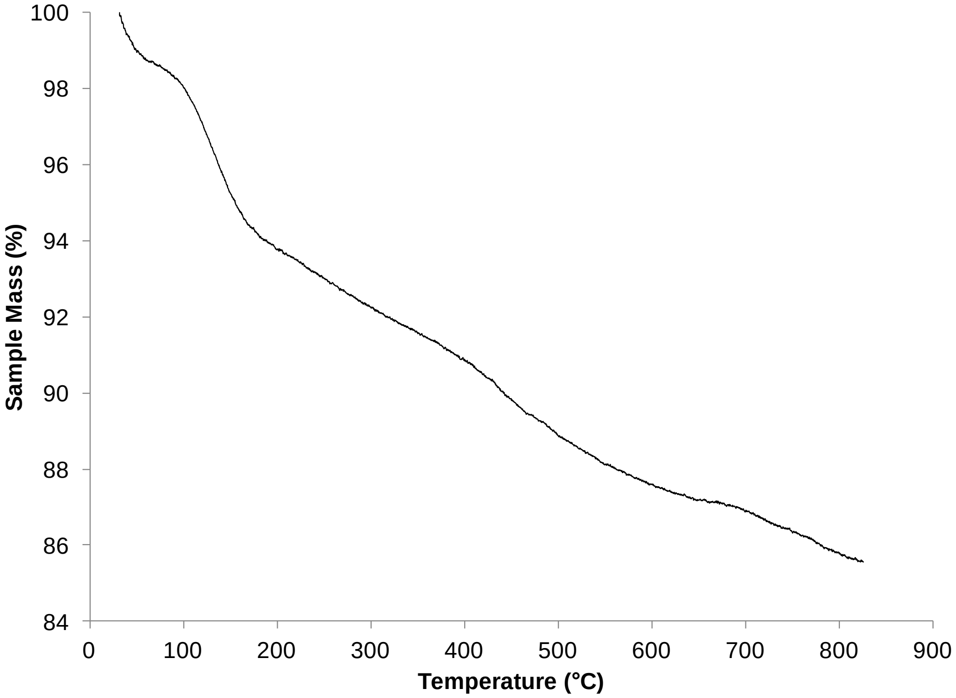

Figure C.1 – Mass loss versus temperature curve for 10% (w/w) benzoic acid/KMMT analyzed in air.

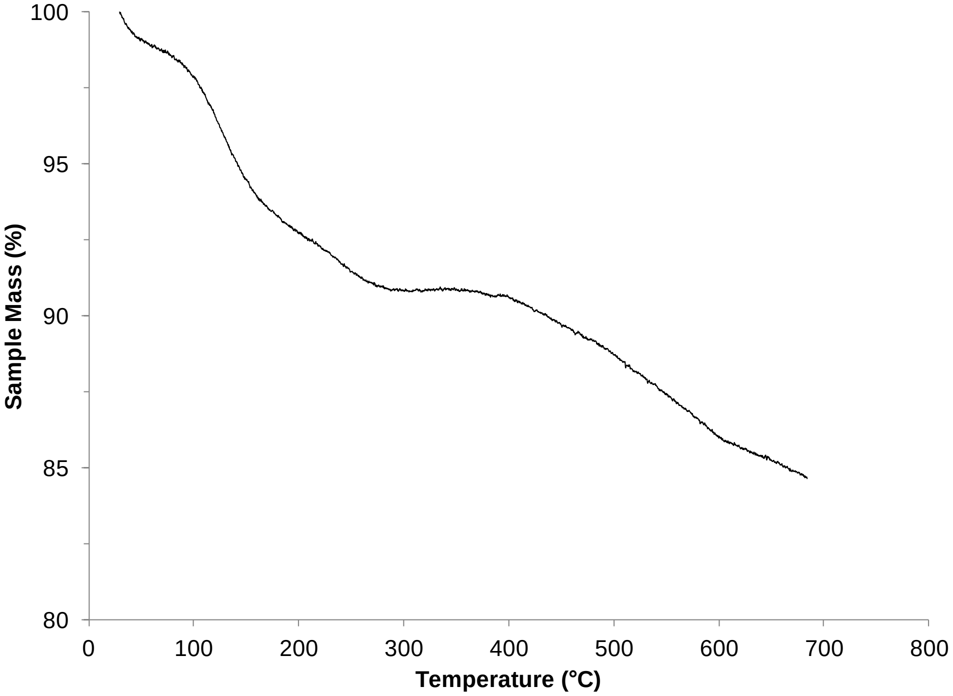

Figure C.2 – Mass loss versus temperature curve for 11% (w/w) salicylic acid/KMMT analyzed in air.

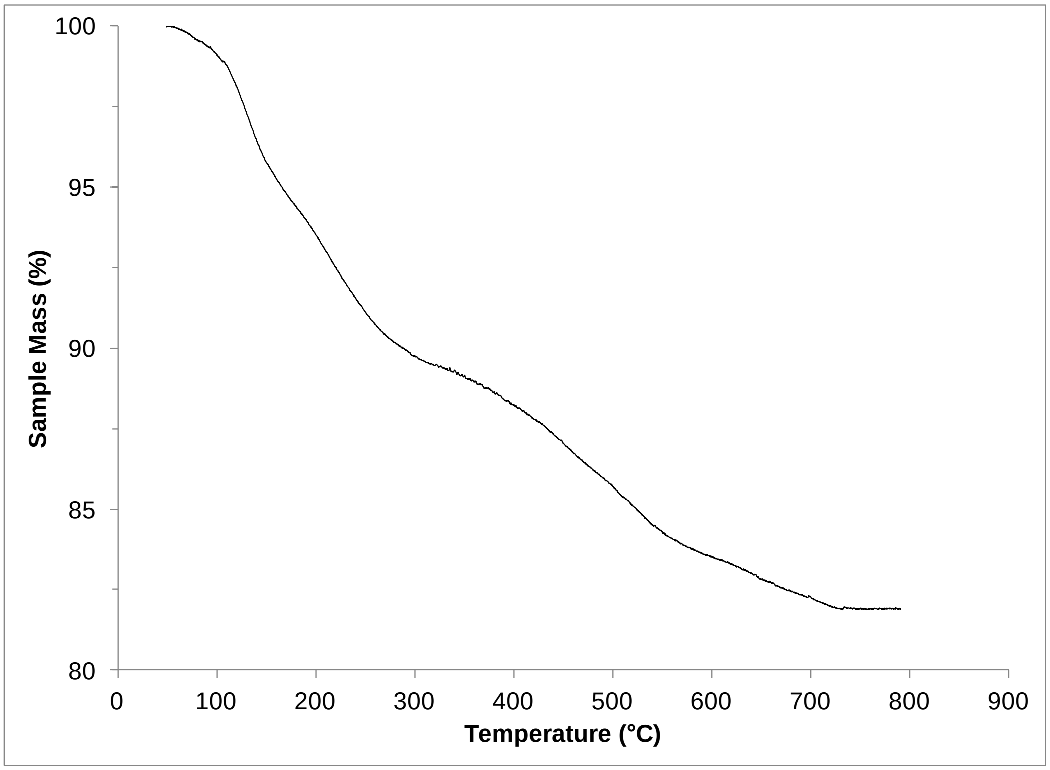

Figure C.3 – Mass loss versus temperature curve for 15% (w/w) acetylsalicylic acid/KMMT analyzed in air.

Appendix D : TG-MS Analyses of Silver-Diluted Samples for Comparison to VT-DRIFTS Results

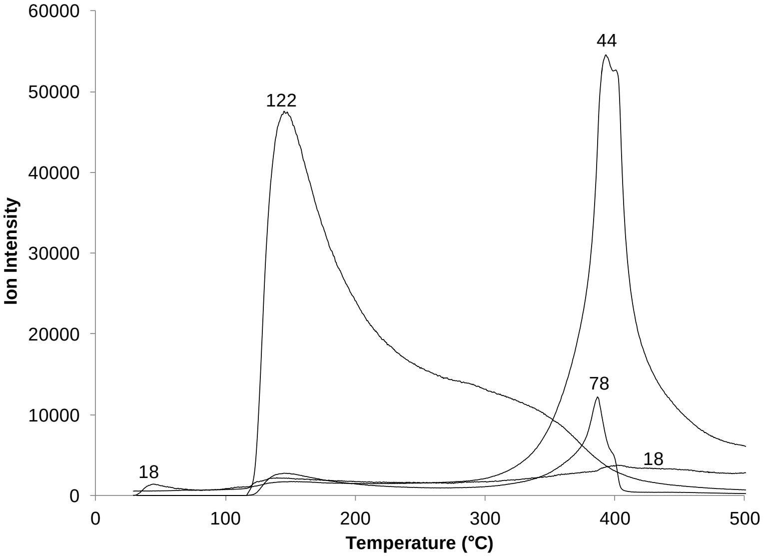

Figure D.1 - Mass spectrometric ion signal intensity profiles representing water (m/z 18), benzoic acid (m/z 122), benzene (m/z 78), and carbon dioxide (m/z 44) measured during TG-MS analysis of a KMMT sample containing 10% benzoic acid. The whole sample was diluted 5:95 (w/w) in silver powder.

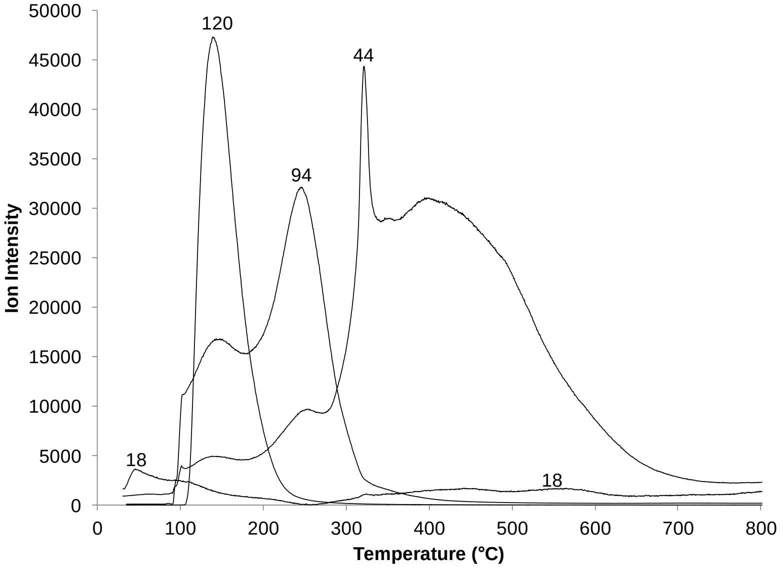

Figure D.2 - Mass spectrometric ion signal intensity profiles representing water (m/z 18), salicylic acid (m/z 120), phenol (m/z 94), and carbon dioxide (m/z 44) measured during TG-MS analysis of a KMMT sample containing 11% salicylic acid. The whole sample was diluted 5:95 (w/w) in silver powder.

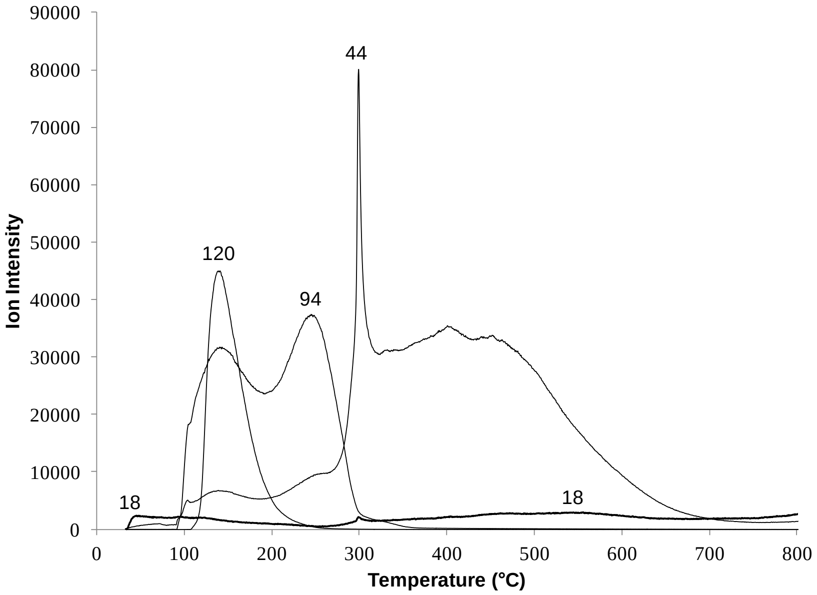

Figure D.3 - Mass spectrometric ion signal intensity profiles representing water (m/z 18), salicylic acid (m/z 120), phenol (m/z 94), and carbon dioxide (m/z 44) measured during TG-MS analysis of a NaMMT sample containing 11% salicylic acid. The whole sample was diluted 5:95 (w/w) in silver powder.

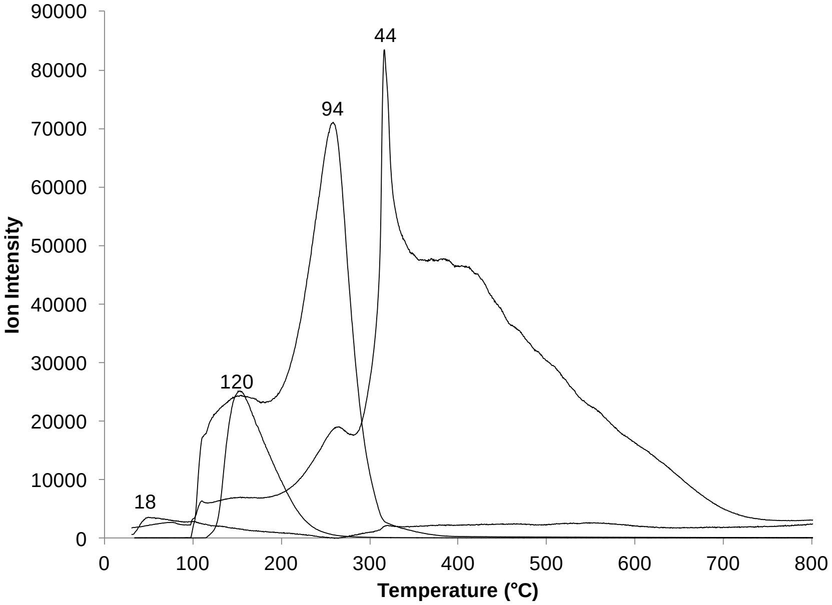

Figure D.4 - Mass spectrometric ion signal intensity profiles representing water (m/z 18), salicylic acid (m/z 120), phenol (m/z 94), and carbon dioxide (m/z 44) measured during TG-MS analysis of a CaMMT sample containing 11% salicylic acid. The whole sample was diluted 5:95 (w/w) in silver powder.

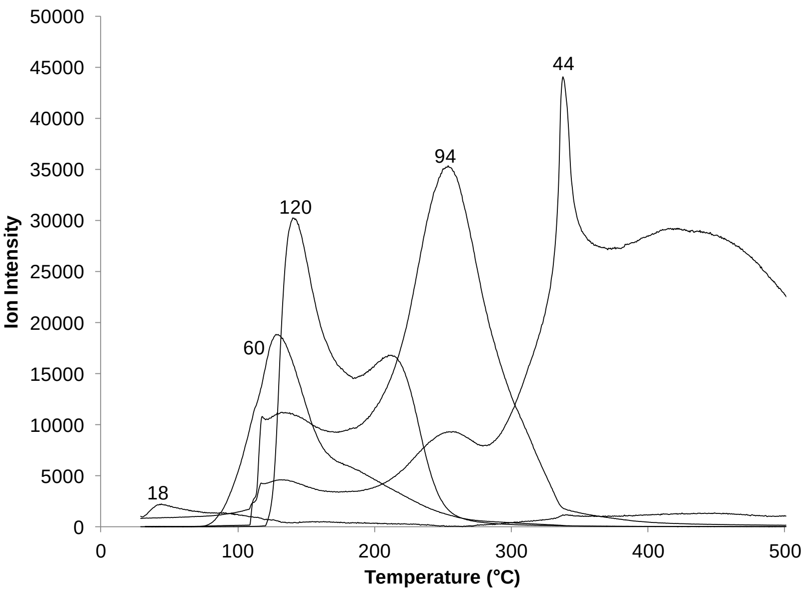

Figure D.5 - Mass spectrometric ion signal intensity profiles representing water (m/z 18), acetic acid (m/z 60), salicylic acid (m/z 120), phenol (m/z 94), and carbon dioxide (m/z 44) measured during TG-MS analysis of a KMMT sample containing 15% acetylsalicylic acid. The whole sample was diluted 5:95 (w/w) in silver powder.

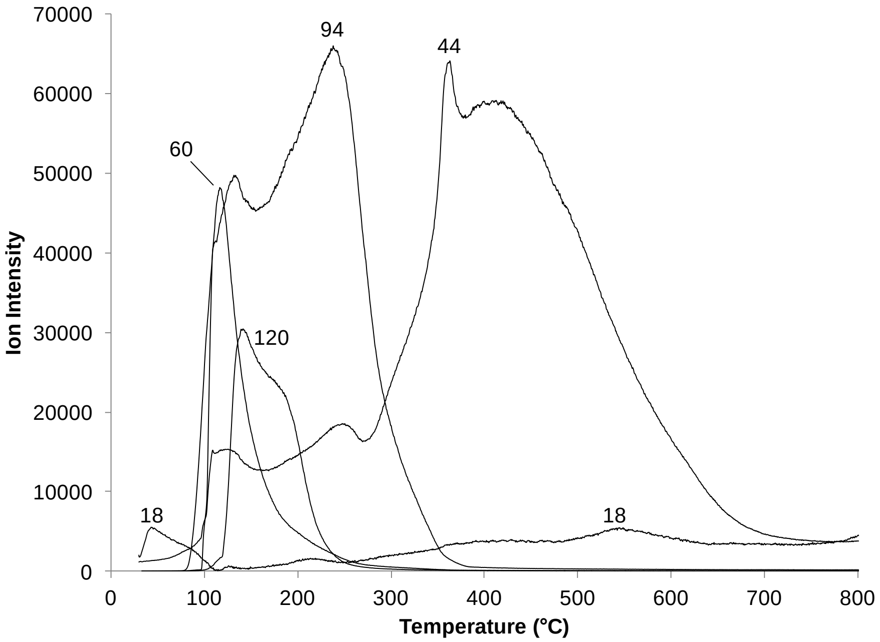

Figure D.6 - Mass spectrometric ion signal intensity profiles representing water (m/z 18), acetic acid (m/z 60), salicylic acid (m/z 120), phenol (m/z 94), and carbon dioxide (m/z 44) measured during TG-MS analysis of a NaMMT sample containing 15% acetylsalicylic acid. The whole sample was diluted 5:95 (w/w) in silver powder.

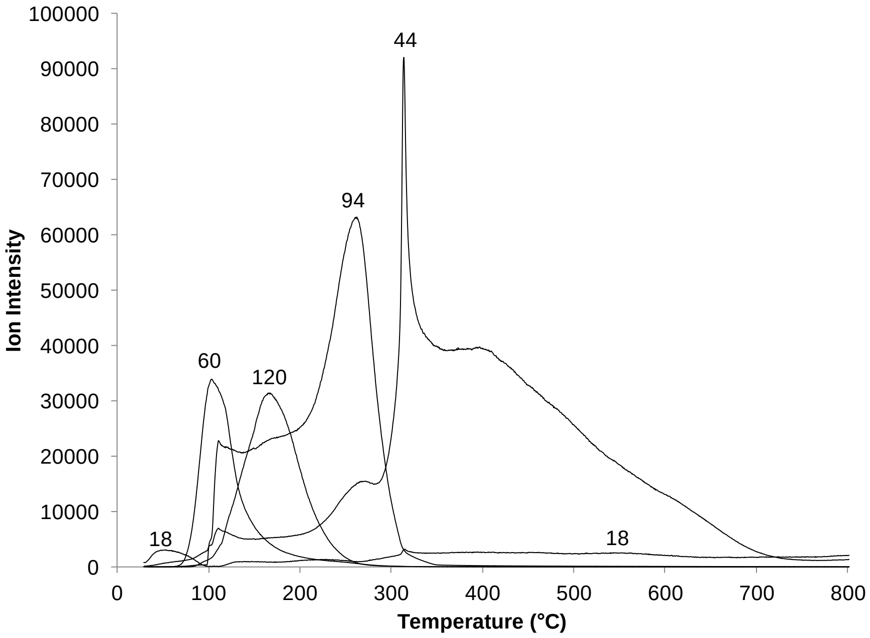

Figure D.7 - Mass spectrometric ion signal intensity profiles representing water (m/z 18), acetic acid (m/z 60), salicylic acid (m/z 120), phenol (m/z 94), and carbon dioxide (m/z 44) measured during TG-MS analysis of a CaMMT sample containing 15% acetylsalicylic acid. The whole sample was diluted 5:95 (w/w) in silver powder.